VERONIKA OBERSTEINER

Computational Modeling of Organic-Inorganic Nanomaterials
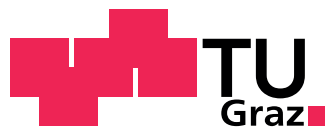
DISSERTATION

zur Erlangung des akademischen Grades

Doktorin der technischen Wissenschaften

eingereicht an der

Technischen Universität Graz

Technische Physik

Betreuer:

Ao.Univ.-Prof. Dipl.Ing. Dr.techn. Egbert Zojer

Institut für Festkörperphysik

Graz, Juni 2017

EIDESSTATTLICHE ERKLÄRUNG

Ich erkläre an Eides statt, dass ich die vorliegende Arbeit selbstständig verfasst, andere als die angegebenen Quellen/Hilfsmittel nicht benutzt, und die den benutzten Quellen wörtlich und inhaltlich entnommenen Stellen als solche kenntlich gemacht habe. Das in TUGRAZonline hochgeladene Textdokument ist mit der vorliegenden Dissertation identisch.

_____   _____

Datum   Unterschrift

Danksagung

In den letzten drei Jahren meiner Dissertation konnte ich nicht nur außerordentliche wissenschaftliche Erfahrungen sammeln sondern auch ganz besondere Menschen kennenlernen, die mich in dieser Zeit auf unterschiedlichste Weise unterstützt und motiviert haben.

Zu allererst möchte ich mich herzlichst bei meinem Betreuer Egbert Zojer bedanken, der mich in dieser Zeit mit großem Engagement begleitet und durch seine exzellente und individuelle Betreuung in jeder Hinsicht unterstützt hat. Ein weiteres großes Dankeschön möchte ich an Oliver Hofmann richten, der es mir ermöglichte in einem weiteren überaus spannenden Projekt mitzuwirken und mir zu jeder Zeit mit wertvollen Tipps zur Seite stand.

Vielen Dank auch an die gesamte Advanced Materials Modeling Arbeitsgruppe (*EgbertInnen* & Co) für die Unterstützung, das Feedback und die gemeinsame Zeit innerhalb und außerhalb der Univeristät. Ich habe es sehr genossen ein Teil dieses besonderen Teams bestehend aus Andreas, Anton, Aurelie, Christian, Daniel, Eduardo, Elsi, Georgii, Giulia, Iris, Jimmy, Karin, Lisi, Lukas, Markus, Michael, Natalia, Shashank, Simon und Thomas zu sein.

Bei Elisabeth Stern möchte ich mich für ihre stets lustige und auflockernde Art und die herzlichen Gespräche in der Zeit meiner Dissertation bedanken.

Für großartige Zusammenarbeit und konstruktives Feedback danke ich Daniel Wegner, Georg Huhs, Nick Papior, Reinhard Maurer und David Egger. Zudem möchte ich mich bei der gesamten Arbeitsgruppe von Karsten Reuter bedanken, die ich im Zuge eines zweiwöchigen Forschungsaufenthalts an der TU München besuchen durfte.

Die in meiner Dissertation durchgeführten Simulationen wurden zum größten Teil in externen Rechenzentren durchgeführt. An dieser Stelle möchte ich mich deshalb bei der Abteilung für Scientific Computing des Zentralen Informatikdiensts (ZID) der TU Graz, beim Vienna Scientific Cluster (VSC) und der Argonne Leadership Computing Facility (ALCF) für die zur Verfügung gestellten Ressourcen bedanken. Zudem danke ich dem Österreichischen Wissenschaftsfonds (FWF) für die Förderung meiner wissenschaftlichen Arbeit im Rahmen der Pojekte P24666-N20, P28631-N36 und P28051-N36.

Ein ganz besonderes Dankeschön möchte ich meiner gesamten Familie widmen die mich stets darin bestärkt hat Herausforderungen entschlossen anzunehmen und mir speziell in den letzten drei Jahren stabilen Rückhalt gegeben hat.

Nicht zuletzt möchte ich mich bei Daniel für die Unterstützung, den Rückhalt und den Zuspruch bedanken; für unzählige schöne Momente, für seine unvergleichlich lustige und liebevolle Art und die große Rücksichtnahme in herausfordernden Zeiten meines Physikstudiums.

Abstract

The modeling of organic-inorganic nanomaterials is becoming increasingly attractive in the fields of organic electronics and photovoltaics. Commonly used as valuable tool to provide explanation and interpretation of experimental results, computational simulations moreover enable the design and development of entirely new materials systems. Furthermore, their predictive power can be exploited to forecast materials properties even before they are experimentally synthesized. In this Thesis, several approaches towards materials modeling as well as prediction are presented. They are obtained by performing first-principle calculations at the level of density functional theory (DFT).

A major part of this Thesis is built upon the exploitation of so called *collective electrostatic effects*. These arise from the superposition of the electrostatic fields generated by a periodic assembly of dipole moments. The main consequence is an induced step in the electrostatic energy that shifts the energies of electronic states. Though emerging naturally in many systems, these effects are to date largely overlooked. Their existence is highlighted by investigating charge transport through molecular junctions that comprise either individual molecules or extended two-dimensional monolayers. On the basis of DFT combined with Non-Equilibrium Greens Function Techniques, a fundamental difference in the current-voltage characteristics between single molecules and monolayers is found. This is attributed to collective electrostatics originating from the dipole layer that arises at the organic-inorganic interface as well as from potential inter-molecular dipoles. The transport study is extended by using different docking groups between the molecules and the metal as well as differently sized clusters of molecules. While the said effects emerge naturally in the aforementioned systems, they can be intentionally exploited to realize materials with exceptional properties. By incorporating polar elements into bulk materials in an ordered fashion, it is possible to manipulate the electronic landscape in a controlled way. This conceptually new design strategy is proposed for the example of 3D covalent organic frameworks (COFs) linked via polar groups. For these materials spatially confined pathways for electrons and holes are generated holding potential for applications such as organic solar cells. The major advantage over existing design strategies for COFs is that the level offset as driving force for exciton dissociation is tunable.

In *any* such calculation the specific structure of the material is of major importance as it directly or indirectly determines all of its properties. Predicting structures from theory is of great interest in order to support and (in)validate experimental measurements. To take first steps towards materials prediction, a novel algorithm to predict the structure of surface-induced phases at organic-inorganic interfaces is developed. The approach combines a systematic discretization of the configuration space with an efficient exploration of the potential energy surface applying an iterative Monte Carlo procedure. The outcome is a set of energetically low-lying polymorphs. For the example of the small organic molecule tetracyanoethylene adsorbed on Au(111) the predicted global minimum is validated against experimental measurements providing an interpretation that could not be directly inferred from experimental data alone.

Kurzfassung

Die computerunterstützte Modellierung von organisch - anorganischen Nanomaterialien gewinnt unter anderem im Bereich der organischen Elektronik und Photovoltaik immer mehr an Bedeutung. Praktische Anwendungen erstrecken sich von der Aufklärung und Interpretation experimenteller Messungen bis hin zu Entwicklung und Design neuartiger Materialien. Darüber hinaus ermöglicht die Simulation theoretische Vorhersagen von Matrialeigenschaften noch vor der Materialsynthese. In der vorliegenden Arbeit werden verschiedene Ansätze zur Modellierung und Strukturvorhersage organisch-anorganischer Nanomaterialien präsentiert. Dies wird mit Hilfe quantenmechanischer Berechnungen basierend auf der Dichtefunktionaltheorie (DFT) erreicht.

Ein wesentlicher Teil dieser Arbeit basiert auf sogenannten *kollektiven elektrostatischen Effekten*. Diese entstehen in Materialien mit periodisch angeordneten Dipolen. Dadurch wird ein Sprung in der elektrostatischen Energie induziert, der die elektronischen Zustände verschiebt. In dieser Arbeit werden diese Effekte unter anderem im Bereich der molekularen Elektronik aufgezeigt. Transporteigenschaften durch einzelne Moleküle werden mit jenen durch selbstassemblierte Monolagen verglichen (mittels DFT und Nichtgleichgewichts Greenschen Funktionen). Der fundamentale Unterschied in den Strom-Spannungs Kennlinien ist auf kollektive Effekte von Dipolen am Interface zwischen Molekülen und Elektrode zurückzuführen. Diese Untersuchungen konzentrieren sich sowohl auf verschiedene Ankergruppen zwischen Molekül und Elektrode als auch auf verschieden große Cluster von Molekülen. Während kollektive elektrostatische Effekte in diesen Materialien auf natürliche Weise entstehen, können sie auch genutzt werden, um vollkommen neuartige Materialien zu entwickeln. Dieser innovative Designansatz wird am Beispiel von 3D kovalenten organischen Netzwerken demonstriert. Durch den gezielten, geordneten Einbau von polaren Gruppen in diese Materialien werden herausragende Eigenschaften erreicht. Je nach Architektur können vordefinierte Pfade für Ladunsgträger geschaffen werden. Dies könnte mögliche Anwendung in Solarzellen finden.

Für *jede* quantenmechanische Simulation ist die exakte Geometrie des zu beschreibenden Materials von ausschlaggebender Bedeutung. Sie bestimmt auf direkte oder indirekte Art praktisch jede seiner Eigenschaften. Dies betrifft auch organisch-anorganische Grenzflächen. Um dem Rechnung zu tragen, wird in der vorliegenden Arbeit ein neuartiger Algorithmus entwickelt um die Struktur von organisch-anorganischen Grenzflächen vorherzusagen. Die spezielle Herausforderung dabei liegt in der exponentiell wachsenden Anzahl an potentiellen Konfigurationen die sich hier aus der Anordnung mehrerer Moleküle auf der Oberfläche ergibt. Mittels systematischer Diskretisierung des Konfigurationsraums und anschließender effizienter Exploration über einen iterativen Monte Carlo Algorithmus, kann ein Satz an energetisch günstigsten Strukturen vorhergesagt werden. Am Beispiel des organischen Moleküls Tetracyanoethylen auf Au(111) wird das prognostizierte globale Minimum mit der experimentell gemessenen Struktur verglichen. Basierend darauf kann eine Interpretation geliefert werden, welche im vorliegenden Fall nicht aus rein experimentellen Daten gewonnen werden kann.

Structure of the Thesis

The following work is a *cumulative* PhD Thesis, which consists of peer-reviewed scientific articles to which I have extensively contributed in the course of the scientific work associated to my PhD studies. According to the structure suggested by the *Doctoral School of Physics* it consists of a general introduction putting the work into context, followed by the set of original publications which is completed by a summary. Furthermore, in this PhD Thesis additional unpublished data are added as an appendix directly after the publication they are associated to.

During the time of my PhD I prepared 5 manuscripts as the leading author. The first one (see Ref. [1]) was published in the first months of my PhD and is entirely connected to my Master Thesis. Therefore, it is not added here. Three manuscripts are enclosed as original publications together with their supplementary material in the main part of the Thesis. One manuscript is inserted as a draft.

It is deeply rooted in the nature of a scientific publication that several co-authors contribute to the underlying scientific content. Therefore, prior to each publication, extensive information on the contribution of each author is given.

List of Publications

PAPER I

Impact of Anchoring Groups on Ballistic Transport: Single Molecule vs Monolayer Junctions[2]

Veronika Obersteiner, David A. Egger, and Egbert Zojer

Journal of Physical Chemistry C, **2015**, 119 (36), 21198-21208

PAPER II

Molecular Junctions: Scaling of Charge Transport through Parallel Molecular Wires

Veronika Obersteiner, Georg Huhs, Nick Papior and Egbert Zojer

In preparation.

PAPER III

Electrostatic Design of 3D Covalent Organic Networks[3]

Veronika Obersteiner, Andreas Jeindl, Johannes Götz, Aurelie Perveaux, Oliver T. Hofmann, and Egbert Zojer

Advanced Materials, **2017**, in press.

PAPER IV

Structure Prediction for Surface-Induced Phases of Organic Monolayers

Veronika Obersteiner, Michael Scherbela, Lukas Hörmann, Daniel Wegner, and Oliver T. Hofmann

Submitted.

Contents

1 Introduction

Organic electronics is an increasingly appealing class of electronics aiming at augmenting energy- and cost-intensive silicon technology by materials based on organic molecules. Innovative organic materials are the key ingredients for flexible, lightweight and affordable future applications (*e.g.* organic light emitting diodes (OLED) for displays and lightings, organic field effect transistor (OFET) in integrated electronic circuits, organic sensors and batteries or organic photovoltaics). Improving the basic understanding of these materials is in the focus of the current Thesis, which deals with the quantum-mechanical simulation of organic-inorganic nanomaterials and their interfaces. In this introductory part a scientific background to the publications contained in the main part of this Thesis is provided as a short review of the existing literature. Furthermore, it addresses open questions that ought to be answered within this work.

The first part of the introduction is dedicated to so called *collective electrostatic effects* (Chapter 1.1). After explaining their origin and consequences for the electronic properties of materials on rather general grounds, their application and their potential are discussed on the bases of existing literature. In the following subsections two seemingly diverse topics, *i.e.* molecular electronics and covalent organic networks, are shortly reviewed as these are the subjects that PUBLICATION I to III are associated to. Their common ground is the application and exploitation of collective electrostatic effects.

Specifically, in section 1.1.1, the field of molecular electronics is historically reviewed and potential applications are discussed. In this context, several effects affecting charge transport properties through molecules are elaborated on with special emphasis on cooperative phenomena. While charge transport though single molecules is largely understood, the scaling towards ensemble devices is still a very disputed topic. To that aim collective electrostatic effects are pointed out in the course of an extensive coverage dependent charge transport study on molecular junctions with different packing densities (see PUBLICATION I). These considerations are then furthermore extended to the investigation of differently sized molecular clusters (see PUBLICATION II).

While the said collective electrostatic effects emerge naturally in the aforementioned systems, they are intentionally exploited to design entirely new materials in PUBLICATION III. These materials are based on covalent organic frameworks, which are introduced in section 1.1.2. Their general structure together with conventional design strategies are reviewed. Special emphasis is put on their potential application in photovoltaic devices as the proposed electrostatic design approach shows great potential for controlling exciton dissociation in solar cells.

All of the aforementioned systems properties depend heavily on the exact geometry of the underlying material. Understanding these structure-property relations is of great interest in order to predict materials with desired properties. As the exact structure is often not conceivable from pure experimental approaches, there is a request for global structure search techniques, which are the focus of the second part of the introduction, see Chapter1.2.

Section 1.2.1 motivates the need for efficient computational structure search and provides a short introduction into polymorphism at organic-inorganic interfaces. The so called *configuration explosion* being the main computational problem for these kind of optimization problems is introduced. In section 1.2.2, a brief overview of the currently existing methodological approaches to global structure prediction is given. While these mainly cover literature dealing with the prediction of crystals, biomolecules and clusters, in this Thesis first steps towards structure prediction at organic-inorganic interfaces are discussed (see PUBLICATION IV). The associated systems of interest, *i.e.* tetracyanoethylene on noble metals, are introduced in section 1.2.3.

All publications presented in this thesis rely on quantum-mechanical computer experiments. Hence, the last part of the introduction reviews the theoretical foundation of the simulations performed in this Thesis, see Chapter 1.3. Specifically, the general concept of density-functional theory (DFT) forming the basis of all included publications is presented (section 1.3.1). Subsequently, the combination of DFT with Non-Equilibrium Greens Function Techniques (NEGFT) is presented as an advantageous formalism to describe charge transport through nanoscopic systems (section 1.3.2). Besides a general overview of the theoretical concepts, the most relevant information for a practical calculation and the used codes are provided in the respective sections.

1.1 Collective Electrostatic Effects

When dealing with assemblies of molecular building blocks incorporating polar segments, so called collective electrostatic effects become relevant. These are cooperative phenomena arising simply due to the presence of neighboring polar entities. The resulting systems exhibit properties that can be markedly different to those of the individual components. Though being inherently apparent in many natural systems, these effects are to date largely overlooked. In the following, collective electrostatic effects are first introduced on rather general grounds, while their intriguing impact on the electronic properties of materials is then reviewed on basis of the current literature. In the consecutive subsections two organic-inorganic nanomaterials, *i.e.* molecular junctions as well as covalent organic frameworks (COFs), are introduced as these are the systems specific to PUBLICATION I - III.

Whenever a periodic arrangement of dipoles is introduced into a material, the electronic states above and below the dipole layer get permanently shifted with respect to each other. This is a consequence of so called collective electrostatic effects.[4–8] They can be nicely illustrated on the example of a self-assembled monolayer (SAM) containing dipolar terminal groups.[7] Fig. 1 shows the electrostatic energy of an individual biphenylthiol molecule with a terminal dipolar cyano group compared to that of the corresponding SAM reflecting the situation of a regularly ordered array of dipoles. As can be seen, the superposition of the electrostatic fields arising from the parallel arrangement of dipoles induces a sharp drop in the electrostatic energy, while the dipole of a single molecule disturbs the surrounding electrostatic energy only locally.[7]
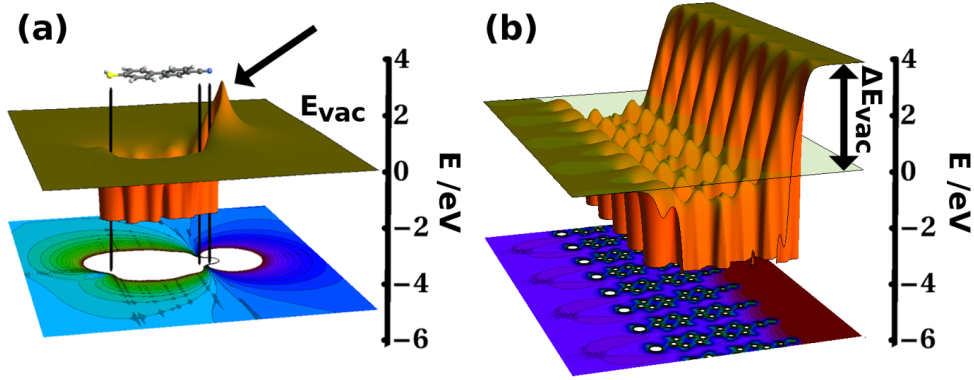
Figure 1: Collective Electrostatic Effects. Electrostatic energy of an individual biphenylthiol molecule with a terminal dipolar cyano group **(a)** compared to the corresponding self-assembled monolayer (SAM) consisting of parallel dipolar molecules **(b)**. The dipolar group in the isolated molecule disturbs the potential only locally as indicated by the arrow in (a). Due to the superposition of the electrostatic field arising from the periodic arrangement of dipoles in the case of the SAM (b) an overall shift, ΔE, in the elecrostatic energy is generated. Reproduced with permission from ref.[7], Copyright 2010 WILEY-VCH Verlag GmbH & Co. KGaA, Weinheim.

Mathematically, collective electrostatic effects can be understood by considering an infinite layer of dipoles in the simple picture of a plate capacitor where the different electrodes are the positively and negatively charged parts of the dipoles.[9] An exemplary charge density, ρ, is shown in the upper panel of Fig. 2. The electric field F can be obtained by integrating the corresponding one-dimensional Maxwell equation

$$\frac{dF(z)}{dz} = \frac{1}{\epsilon_0}\rho(z) \tag{1}$$

where ϵ_0 is the vacuum permittivity and z is the direction parallel to the dipole. The associated change in the electrostatic potential caused by the dipole layer can be obtained from

$$F(z) = -\frac{dV(z)}{d(z)} \tag{2}$$

where $V(z)$ multiplied by $-e$ yields the electrostatic energy (see bottom panel in Fig. 2). As can be seen, directly at the position of the dipole layer a jump in the electrostatic potential is induced. As discussed in detail in refs. [7] and [9], the magnitude of that step in the electrostatic energy, ΔE, due to the induced dipole layer with the dipole moment μ per surface area A can finally be derived by integrating Poisson's equations which then yields the Helmholtz equation

$$\Delta E = -e\Delta V = \frac{e\mu}{\epsilon_0 A}. \tag{3}$$

Hence, the magnitude of the induced energy shift is determined by the dipole moment as well as on the dipole density. Interestingly, the decay length of the electric field in the direction parallel to the dipoles ammounts to $d/(2\pi)$ which was demonstrated on the

3
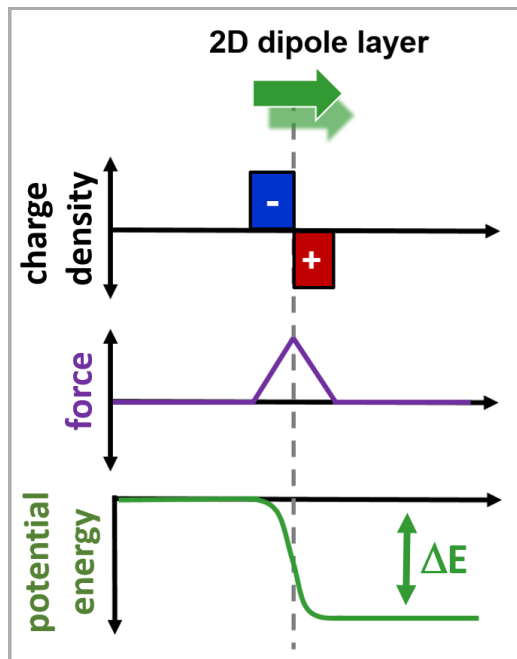
Figure 2: 2D Dipole Layer. Charge density, force and potential energy for electrons along the direction perpendicular to a single dipole layer. For details, see main text. Based on ref. [9].

example of a quadratic 2D array of discrete point dipoles with a mutual distance d.[10] Hence, while the electric field for an individual dipole reaches very far, the vertical decay length of a periodic arrangement of dipoles drops much more rapidly, *i.e.* it is an order of magnitude shorter than the intermolecular distance (as can also be qualitatively inferred from Fig. 1). Another cooperative effect that comes along when placing dipolar elements, is their mutual interaction via depolarization effects.[8,10] Neighboring polar segments give rise to an electric field, which depolarizes any one segment by inducing a dipole moment that counteracts its intrinsic dipole moment. These effects can be quite significant and were shown to be highly coverage dependent for self-assembled monolayers.[11,12] In the context of organic-inorganic nanomaterials, different sources of dipoles contribute to the aforementioned effects: (i) molecular dipoles being either deliberately embedded polar groups or polar terminal units and (ii) the interface dipole arising due to local charge redistribution whenever a molecule is bound to a substrate.

Originally, collective electrostatic effects were used to manipulate the work function at organic-inorganic interfaces.[8,10,13] In general, the work function of a pure metal surface is determined by the instrinsic bulk property of the metal as well as by a surface specific contribution caused by the electron density extending beyond the metal surface.[4] The latter gives rise to a dipole layer which is commonly referred to as *surface dipole* and results in a potential step across the metal surface. Adsorbing an organic monolayer onto the substrate changes the work function significantly.[13–15] First of all, the Pauli *pushback*[9] of the spilling electron cloud due to the presence of the molecules together with other charge rearrangements at the interface due to the bonding process give rise to a dipole layer which

is commonly termed as *bond dipole*. The second contribution is the dipole layer formed by either embedded dipoles or terminal groups of the used molecules. These two contributions can either add up or compensate each other, thereby offering a tuning handle of metal work functions by designing suitable SAMs and interfaces in order to control injection barriers in (opto)electronic devices. In this context, terphenyl-methanethiol derived SAMs with embedded polar pyrimidine groups where recently experimentally synthesized[16,17] exhibiting a sizable dipole moment of around $2 Debye$. In a combined experimental and theoretical study by Hehn et al. a continous tuning of the metal work function could be achieved by growing mixed SAMs consisting of these molecules with different orientations of the embedded dipolar groups.[18] Collective electrostatic effects were also shown to play an important role in the elucidation of X-ray photoelectron spectroscopy (XPS) measurements. By comparison of experimentally as well as theoretically obtained XPS data for thiolate-bonded SAMs, Taucher et al. could show that shifts in core-level binding energies measured by XPS are not only determined by the chemical environment of the atoms, but are also strongly affected by the potential shifts due to the interface dipole as well as embedded dipolar groups.[19]

The intriguing impact of collective electrostatic effects was recently significantly extended to exploit control over the electronic properties of complex SAMs by using a combination of polar elements and semiconducting units in the spirit of a molecular 'interface lego' toolbox.[20] By means of quantum-mechanical simulations, Kretz et al. nicely demonstrated, how collective electrostatic effects could be exploited to gain a precise control over the local eletronic structure and the localization of electronic states in order to build monolayer-based quantum cascades and quantum-well structures. These effects were successfully also used to locally pattern the electronic structure in 2D materials, namely by inserting polar boron nitride layers into graphene.[21]

One of the areas in this Thesis on which the impact of collective electrostatic effects is elaborated on is molecular electronics, see section 1.1.1. Typically investigated systems are so called molecular junctions, which consist of of a single molecules (often also a group of molecules) or a SAM sandwiched between two metal contacts. At each of these molecule-metal interfaces, interface dipoles emerge naturally in case of the SAM device. Hence, the said effects are expected to play a dominant role also in these systems. Indeed, as was first demonstrated by a theoretical charge transport study by Egger et al., two isomeric molecules with essentially identical energies of their frontier delocalized π-orbitals exhibit substantialy different current-voltage characteristics for the respective SAM-devices.[22] The current was shown to differ by an order of magnitude and moreover the charge-transport polarity was shown to switch. During my Master Thesis, these investigations were extended to a coverage-dependent charge transport analysis, clearly demonstrating the impact of collective electrostatic effects when going from a single molecule to the respective SAM.[2] This publication was finalized in the course of my PhD Thesis but is not included here. In PUBLICATION I enclosed in this Thesis this charge transport study is expanded to different docking groups. Differently sized clusters of molecules are finally investigated in order to discuss how the single molecule would essentially approach the SAM situation in the context of collective electrostatic effects. This is discussed in PUBLICATION II.

While in many of the aforementioned systems collective electrostatic effects emerge naturally at interfaces, in PUBLICATION III, these effects are deliberately exploited to electrostatically design novel materials. On the basis of covalent organic frameworks (see section 1.1.2) a novel design strategy is presented by inserting periodically arranged polar segments in order to manipulate the electronic landscape of 3D materials. The proposed materials could be potentially relevant for organic photovoltaics application.

1.1.1 Molecular Electronics

Molecular-scale electronics is the concept of creating functional electrical circuits on the basis of individual molecules or small molecular assemblies. It is currently a research area of focus because it not only meets the increasing technical demands of miniaturization, but moreover provides a versatile flexibility in chemical design. The primary theme in molecular electronics is the construction, measurement and thorough understanding of the transport mechanisms through electrical circuits comprising nanoscale collections of single molecules.

Historically, the interest in molecular-scale electronics grew in the 1970s, when the first effective self-assembly technique for organic molecules bound to solid substrate surfaces was developed.[23] In 1974, AVIRAM and RATNER introduced the visionary concept of using single molecules as molecular rectifiers.[24] Finally, in 1997, a collaboration of TOUR and REED led to what is known to be the first transport experiment through a single molecule.[25] Since then, many new experimental techniques were inveneted in order to produce robust and reproducible electronic devices that can be easily manufactured and integrated, see review [26] and ref. [27]. The fabrication techniques can be divided according to the production of either single molecule junctions or ensemble junctions consisting of several molecules in parallel, *i.e.* self-assembled monolayers (SAMs). The most common techniques to fabricate single molecule junctions are so called break junction (BJ) techniques in which molecular junctions are formed by breaking a metallic wire until a gap opens, which is then bridged by molecules.[28–31] An integration with the Scanning Tunneling Microscope (STM) or the Atomic Force Microscope (AFM) and the break junction strategy leads to the very common STM-BJ[32] technique and the conducting-probe AFM (CP-AFM)[33] technique. Since small variations of the contact geometry and conformation significantly affect the transport properties, these measurements are repeatedly performed to obtain reasonable statistics. Statistical fluctuations can be overcome by fabricating large are junctions where ensembles of $> 10^3$ molecules are arranged in parallel. These junctions are expected to be far more reproducible and integration into conventional electronics should be cheaper. However, as discussed in detail below, the scaling with the number of molecules is still a disputed topic. Successful strategies for forming ensemble molecular junctions are crossed-wire junctions[34] where an ensemble of molecules bridges the gap between two cylindric metal fibres. Furthermore, large-area junctions can be created by buffer interlayer based junctions[35] or liquid metal junctions[36].

Despite these considerable achievements during the past 20 years, there are still no commercially available molecular electronic devices. However, potential applications by integration into electrical circuits range from molecular wires[37,38] serving as charge transport

pathways, to diodes or rectifiers. The latter facilitate current flow in one bias direction realized either by assymetric molecules, *i.e.* donor-acceptor systems[24,39] or assymetric interfacial coupling using different electrodes[40] or different anchoring groups[41]. Single molecules can, moreover, be used as molecular switches,[42–45] where a conductance alternation can be obtained from changes in their physical properties upon exposure to external stimuli such as light, magnetic or electric fields. Besides these two-terminal devices, also transistors[46] to control the flow between two electrodes by applying a voltage to the third can be realized. Finally, there are first approaches towards using individual molecules as sensors.[47]

Molecular junctions can be structurally divided into the anchoring groups that connect to the external electrodes and the molecular backbones that functions as charge transport pathway, see Fig. 3. The conductance of a single molecule is a complex quantity because
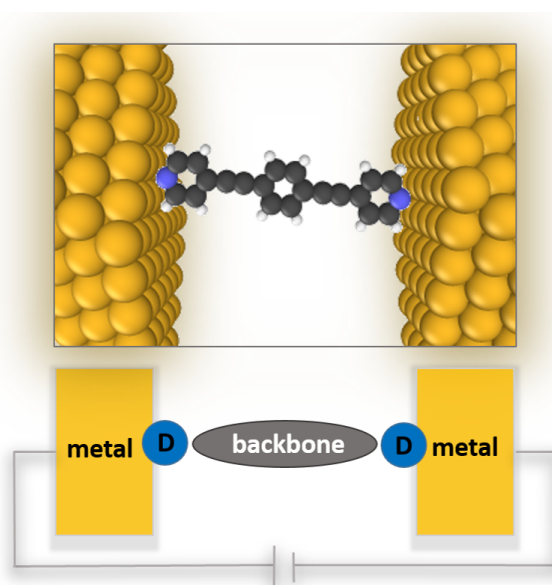
Figure 3: Molecular Junction. Schematic representation of a molecular junction consisting of a left and a right electrode (metal) and the organic part composed of the molecular backbone and the docking groups (D) to the metal. Typically used molecular backbones range from hydrocarbon chains (including saturated and conjugated species) to porphyrin arrays, carbon nanotubes and biological molecules such as DNA.

it is not only determined by the intrinsic molecular properties, but quite significantly by the details of the coupling to the electrodes. This can be illustrated by considering the conductance of a single molecule within a simplified picture, namely ballistic transport (for a detailed discussion see section 1.3.2). While in bulk materials, the macroscopic conductance is defined as $G = I/V$, in the microscopic picture of a single molecule G is proportional to the transmission probability of electrons to travel from one electrode to the other

$$G = \frac{2e^2}{h}T = G_0 \sum T_i \tag{4}$$

where e is the elementary charge, h is Planck's constant and T is the total transmission probability over all possible transmission pathways T_i associated with the molecular or-

bitals. $G_0 = 2e^2/h$ is the quantum of conductance. T itself is related to the transmission probability through the molecule as well as to the coupling strengths of the molecule to the left and right electrode. In the following, different effects affecting the final transport characteristics through molecular junctions such as (i) the interfacial coupling , (ii) the energy level alignment, (iii) the local environment, as well as (iv) collective effects due to the presence of neighboring molecules in the junctions are discussed.

(i) The Interfacial Coupling between the molecule and the metal is determined by the interaction type at the interface as well as by the exact contact geometry. The former results from the combination of the used electrode as well as the anchoring group. In general, covalent interactions, *i.e.* robust chemical bonds are preferred over weak interaction to ensure stability and reproducibility. Typically used anchoring groups in combination with a gold substrate include thiols, pyridines, isocyanides, cyanides, selenols, amines, carboxylic acids or fullerenes.[48,49] Their impact on the width of the transmissive features, which is a measure of the coupling strength (*i.e.* states get broadened due to hybridziation upon metal-SAM formation) is discussed in PUBLICATION I. Furthermore, the type of anchoring group strongly influences the charge rearrangements at the interface and in this way the bond dipole (see below). Besides the type of interface also the exact contact geometry plays a decisive role for the final current-voltage characteristics. It is determined by the specific docking site of the anchoring group[50] (*e.g.* on top, fcc hollow, bridge) and the structure of the electrode[51] (*i.e.* the orientation (*e.g.* (111) or (100)) as well as surface rearrangements.[52,53]

(ii)The Energy Level Alignment in a molecular junction is the alignment of the molecular energy levels, specifically the frontier states, *i.e.* the highest occupied molecular transmission channel (HOTC) and the lowest unoccupied transmission channel (LUTC) with respect to the Fermi levels E_F of the electrodes. It is the key parameter governing charge transport characteristics through molecular junctions. In particular, as can be seen in Fig. 4, the offsets ΔE_{LUTC} and ΔE_{HOTC} between the *closest* transmission channels and the Fermi level determines the charge injection barriers the charge carriers need to overcome in order to generate current. For symmetric junctions, depending on whether the LUTC or the HOTC is closer to the Fermi level, charge transport will be either dominated by holes or electrons. The level alignment is primarily determined by the intrinsic properties of the molecule, *i.e.* the ionization potential (IP) and the electron affinity (EA). Moreover, the band alignment is strongly affected by the type of anchoring group. In general, electron-donating groups such as amines lift frontier orbitals, thereby bringing the HOTC closer to E_F favoring hole transport (p-type), while in turn electron withdrawing groups such as pyridines promote electron transport (n-type). In PUBLICATION I the influence of different anchoring groups on the level alignment is elaborated in detail in the context of a coverage dependent transport study.

(iii) The Local Environment in a molecular junction is another factor impacting the conductance through molecules. These environmental parameters are external stimuli such as temperature[54], solvent, pH value, ions or dopants.
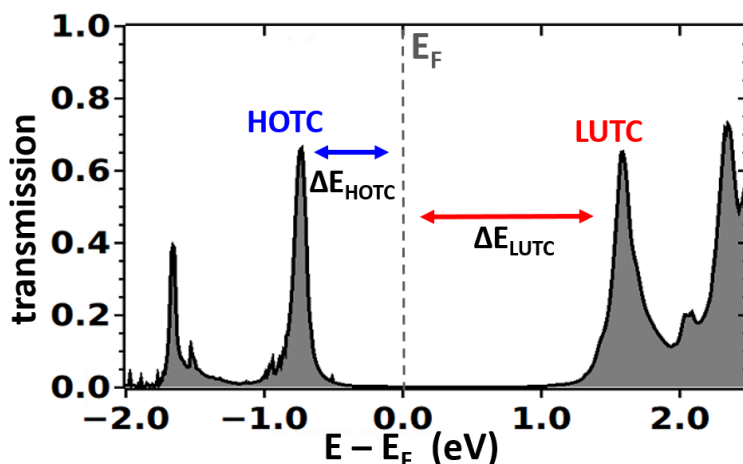
Figure 4: Energy Level Alignment. Schematic transmission probability as a function of energy illustrating the charge injection barriers ΔE_{HOTC} and ΔE_{LUTC} as energy offset between the highest occupied transmission channels (HOTC) and the lowest unoccupied transmission channels (LUTC) and the Fermi level E_F of the electrodes.

(iv) <u>Collective Effects</u>: One can expect on a rather general ground that the collective behaviour of surrounding molecules becomes important when going from single molecule junctions to the respective SAM devices. However, the scaling with the number of molecules is still a very disputed topic in the context of molecular electronics and is considered to be an *open question* in a recent comprehensive review from 2016.[26] Experimental as well as theoretical works reach quite contradicting results on how the conductance of a single molecule is related to that of multiple molecules in parallel. On the one hand, a common practice is to associate the conduction per molecule measured from monolayer junctions with that of the single molecule. This linear scaling was indicated in several experimental works.[32,34,55] On the other hand, the conduction of certain single molecule junctions was found to be orders of magnitudes larger than that of the corresponding monolayer conduction per molecule.[56] In an experimental work, Selzer et al. found that the conduction per molecule assembled in the SAM is similar to that of the corresponding individual molecules, but the differential conductance of the individual molecule increases more rapidly with bias and can become a thousand times larger than that of the SAM. They related these difference to electrostatic effects. Also, theoretical studies predict contradicting results.[57–60] The situation is insofar complicated as an experimental verification of these cooperative phenomena is difficult, as different groups report conductance values that potentially differ by orders of magnitude.[56] Moreover, in experiments it is often not possible to determine the number of molecules present in the junction.

Origins of cooperative phenomena in molecular electronics were mainly discussed in the context of quantum-interference phenomena.[61–63] In this Thesis special emphasis is put on the appearance of collective *electrostatic* effects. As mentioned in above, in the context of charge transport studies through molecular junctions the first theoretical work dealing with collective electrostatic effects was published by Egger et al.[22] For two iso-

meric molecules with essentially identical energies of their frontier delocalized π-orbitals, substantially different current-voltage characteristics for the respective Sam-devices were obtained. This was attributed to collective electrostatic effects arising at the interface between the molecules and the metal electrodes in combination with the dipoles originating from the molecules. Between the single molecule junction and the respective Sam device, the current was shown to differ by an order of magnitude and moreover the charge-transport polarity switches. In a consecutive work within my Master Thesis, these investigations were extended to a coverage-dependent charge transport analysis, clearly demonstrating the impact of collective electrostatic effects in these systems.[1] In Publication I enclosed in this Thesis the transport study is extensively expanded to different docking groups. Differently sized clusters of molecules are finally investigated in order to discuss how the single molecule would essentially approach the Sam situation. This is discussed in Publication II.

The transport studies performed in Publication I and II were obtained with atomistic simulations based on density-functional theory (Dft and non-equilibrium Greens function techniques (Negf). The underlying theoretical concepts are introduced in chapter 1.3.

1.1.2 Covalent Organic Frameworks

A class of materials that is attracting growing interest are so called porous organic frameworks (POFs). These are supramolecular materials in which organic as well as inorganic building blocks are assembled to create 3D bulk structures with outstanding properties such as (i) an exceptionally periodic and well-ordered arrangement, (ii) a supreme flexability due to versatile building blocks which allows for a controlled architecture and (iii) extremely high surface areas. POFs can be classified into COFs (Covalent-Organic Networks)[64–68] and MOFs (Metal-Organic Frameworks)[69–71] both of which initiated a rapidly growing field in chemistry and physics with a variety of promising applications. In the following, their general structure and composition are discussed. Then a short overview of their potential applications is given with special emphasis on COFs, as these are the materials our electrostatically designed covalent organic networks (see Publication III) come closest. Their connection to COFs and the main concept of the collective electrostatic design strategy are discussed in the end of this section.

As shown in Fig. 5a and b, COFs consist of a periodic arrangement of organic building blocks which are covalently bound to each other. They can be categorized into either 2D or 3D COFs. In 2D COFS the covalently bound framework is restricted to 2D sheets that are stacked on top of each other via π-stacking to form layered eclipsed structures representing periodically aligned columns. In contrast, 3D COFs extend this network by introducing building blocks in the third dimension. This results in large pores but looses the regular periodic columns. Depending on the symmetry of the used building blocks (*e.g.* porphyrin with C_4 symmetry or hexabenzocoronene with C_6 symmetry) and linking elements (*e.g.* boronate ester, imine, azine) a variety of different architectures such as hexagonal, rhombic or tetragonal-shaped COFs can be synthesized.[73] Composed of light-weight elements, they have low mass densities, possess high thermal stability and provide permanent porosity. MOFs, on the other hand, are porous crystalline materials
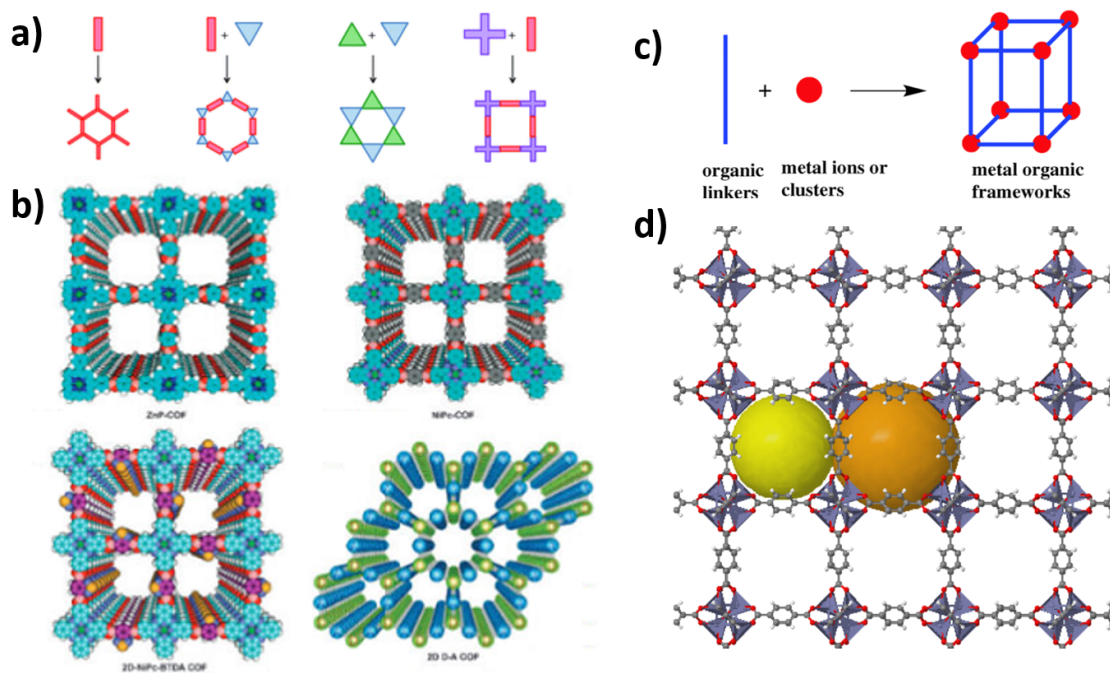
Figure 5: Covalent and Metal Organic Frameworks. **(a)** Building blocks and possible architectures for Covalent Organic Frameworks (COFs). **(b)** Schematic representation of typical π-stacked COFs. Reproduced from ref. [64] with permission of The Royal Society of Chemistry. **(c)** Illustration of the building blocks and structure of Metal Organic Frameworks (MOFs). Reprodcued from ref. [72] with permission of The Royal Society of Chemistry. **(d)** One of the most widely used MOFs: MOF-5 formed from Zn_4O nodes with 1,4-benzodicarboxylate linkers between the nodes. The spheres represent the pore size for gas storage. Taken from *www.chemtube3d.com/solidstate/MOF-MOF5.html*, *10.03.2017*.

based on classical coordination bonds between metal ions and organic linking elements, see Fig. 5c and d. A very promising approach to grow MOFs in a controlled is to use a layer-by-layer approach where MOFs are grown on a surface in a stepwise procedure termed as SurMOF.[74,75]

Applications of COFs

Since their discovery, COFs and MOFs have enjoyed extensive exploration with a variety of applications. In the following, a special focus is placed on the application of 2D COFs as these are the materials our electrostatic design idea is based on. There are a lot of recent recommendable reviews about COFs such as ref. [65], [68] or [76]. For MOF applications the interested reader is referred to ref. [71] and [70]. COFs exhibit a variety of interesting features. Due to their large surface areas and pore volumes they are ideal materials for gas storage and absorption.[77–79] Storage capabilities for gases, such as hydrogen, methane or carbon dioxide, have been widely investigated where the capacity was found to depend primarily on the components and topologies of the frameworks. As many of the synthesized COFs are photoconductive,[80–82] a special interest exists in their use in photovoltaics and optoelectronics.[83–87] Very recently, the first solar cell made out of pure covalent organic frameworks was published by constructing COFs as donor-acceptor bulk heterojunctions.[87]

Organic photovoltaics has promising potential as emission free and sustainable energy source. However, several challenges including limited efficiency or device stability need to be overcome to obtain 'competitive' organic solar cells. Key criteria for higher efficiency are high absorbance, efficient charge separation, low recombination as well as efficient charge transport and collection. The most widely used and currently most efficient systems employed to realize the active layer in an organic solar cell are donor-acceptor (D/A) heterojunctions. These significantly enhance charge separation compared to a single layer device.[88] They have been realized in different flavours ranging from a simple planar bilayer D/A heterojunction,[89] to blended bulk heterojunctions and targeted ordered interpenetrated D/A systems, successively increasing the efficiency of charge separation due to the significantly larger interface and a controlled morphology in the latter case. A schematic illustration of the level alignment achieved in such D/A bulk heterojunctions is shown in Fig. 6. When light gets absorbed by the donor an electron is excited from the valence band (VBM) to the conduction band (CBM). Thereby an exciton, *i.e.* an electron-hole pair is formed, which feels an attractive (screened) Coulomb force. To overcome this attractive force in order to generate free charge carriers a level offset, ΔE, is provided at the interface due to the different molecular properties of donor and acceptor. After dissociation, electrons and holes are transported as free charge carriers towards the electrodes.

COFs are ideally suited to mimic D/A bulk heterojunctions due to the well-defined and separated domains of donor and acceptor phases combined with an exceptionally large internal interface between those phases. Hence, they promise improved charge carrier transport, a low recombination rate, and efficient separation of the photo-generated exciton. The first working COF-based photovoltaic device was built in 2013 by Dogru et al.[84] They used tiophene building blocks serving as donors and fullerene acceptors are
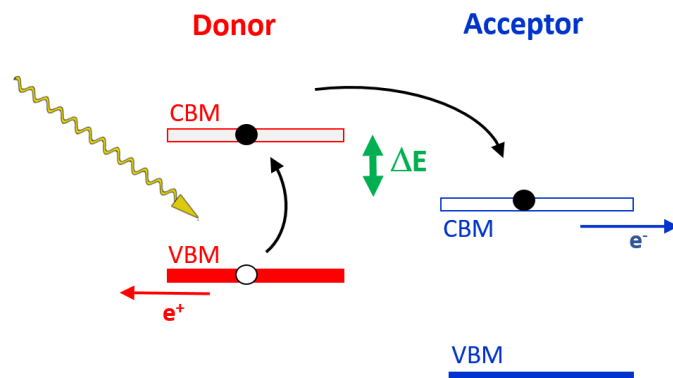
Figure 6: Donor-Acceptor Bulk Heterojunction. Schematic level alignment of the interface between donor and acceptor, *i.e.* relative position of the valence band maxima (VBM) and conduction band minima (CBM). The level offset, ΔE, provided as driving force for exciton dissociation is indicated by the green arrow. It is largely determined by the molecular properties, *i.e.* ionization potential (IP) and electron affinity (EA) of the used donor and acceptor.

infiltrated into the COF channels, thus forming a regular donor-acceptor 'host-guest' network, see Fig. 7a. Another closely related strategy that was discovered shortly after is
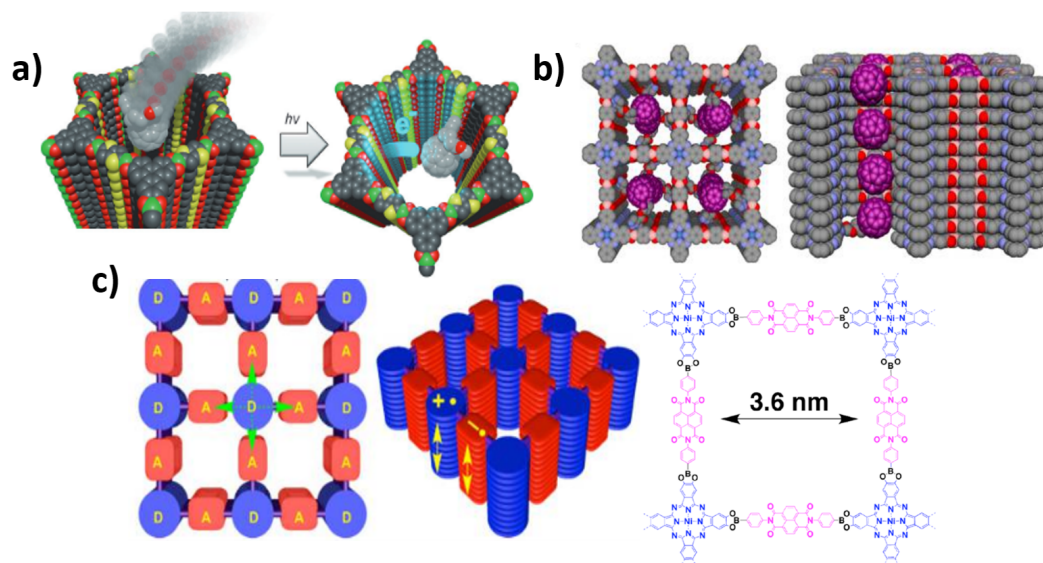

Figure 7: Photoconductive COFs. **(a)** First working COF-based photovoltaic device where tiophene building blocks serve as donors and fullerene acceptors will are infiltrated into the COF channels. Reproduced with permission from ref.[84]. Copyright 2013 WILEY-VCH Verlag GmbH & Co. KGaA, Weinheim. **(b)** Donor-acceptor COF via channel functionilization, *i.e.* electron donating COF and accepting fullerene. Reprinted with permission from ref.[85]. Copyright 2014 American Chemical Society. **(c)** First photovoltaic device with exclusively COF consisting of metallophtalocyanines as donor and diimide acceptor columns. Reprinted with permission from ref.[87]. Copyright 2015 American Chemical Society.

a donor covalently bound to the inner wall of an accepting COF, *i.e.*, wall functionalization[85] as shown in Fig. 7b. Compared to the design strategy in (a) where van der Waals interactions are the driving force, these materials are more stable due to the formed covalent bonds. Finally, in 2015, the first photovoltaic device with exclusively COF was published[87] using metallophtalocyanines donor and diimide acceptor columns, see Fig. 7c. Due to the regularly arranged columns of donor and acceptors these COFs exhibit an ideal mechanism for charge separation. The π-stacked columns of the layered donor-acceptor sheets provide pathways for electrons and holes,[82] facilitating charge transport along the stacking direction. The band alignment of these type-II D/A heterojunctions, *i.e.* the relative band offset between the local valence-band edges and conduction-band edges is primarily determined by the molecular properties of the individual donating and accepting segments.

Chemical vs. Electrostatic Design

Compared to the conventional chemical design approaches of COFs introduced so far, in this Thesis a fundamentally different design approach is pursued. The basic idea is to intentionally build dipolar elements into COF-like 3D bulk materials to exploit the resulting collective electroststatic effects in order to manipulate their electronic landscape, see PUBLICATION III. Thereby, an equivalent band offset as in the above mentioned D/A systems can be achieved. Figure 8 shows some of the designed systems. As basic building blocks zinc-porphyrin units are chosen, as they are widely used in MOFs and COFs.[90–93] Instead of the usually employed linkers we introduce polar linking groups as here exemplarily shown on the example of boron nitride, BN (note that the $B \equiv N$ linker is of somewhat hypothetical nature, but is used in this conceptional study to show that very large shifts are feasible for large dipole moments, in PUBLICATION III other linkers are introduced). Compared to conventional 2D COFs, in the third dimension they are not π-stacked on top of each other but linked via apolar linkers, such as bipyridine (see Fig. 8d). The reason for this is in detail discussed in Appendix A. By inserting periodic arrangements of dipoles into these covalent organic networks, different electrostatic pattern motifs are expected depending on the direction and orientation of the dipoles with respect to each other. Two examples are portrayed in Fig. 8: a striped structure (a) and a checkerboard structure (b). The expected energy landscape is indicated by the blue and red shaded areas. As discussed in detail in PUBLICATION III, due to the collective electrostatic effects arising upon the insertion of dipolar segments, the electronic states get localized in the respective stripes and are energetically shifted with respect to each other. Thereby, an equivalent band alignment as in the above mentioned D/A-bulk heterojunctions can be achieved. Interestingly, the amount of that shift depends on the dipole moment as well as on the density of the used dipolar linkers (*cf.* Helmholtz Eq. 3). This offers a major advantage over conventional D/A COFs, which can be illustrated when comparing the level alignment of the conventional 'chemical design' approach to the here proposed 'electrostatic design', see Fig. 9. While in the former the band offset is mainly determined by the molecular properties of donor and acceptor groups, for the electrostatic design the band offset between otherwise chemically identical building blocks is solely determined by the collective electrostatic effects of the inserted dipolar segments. In turn,
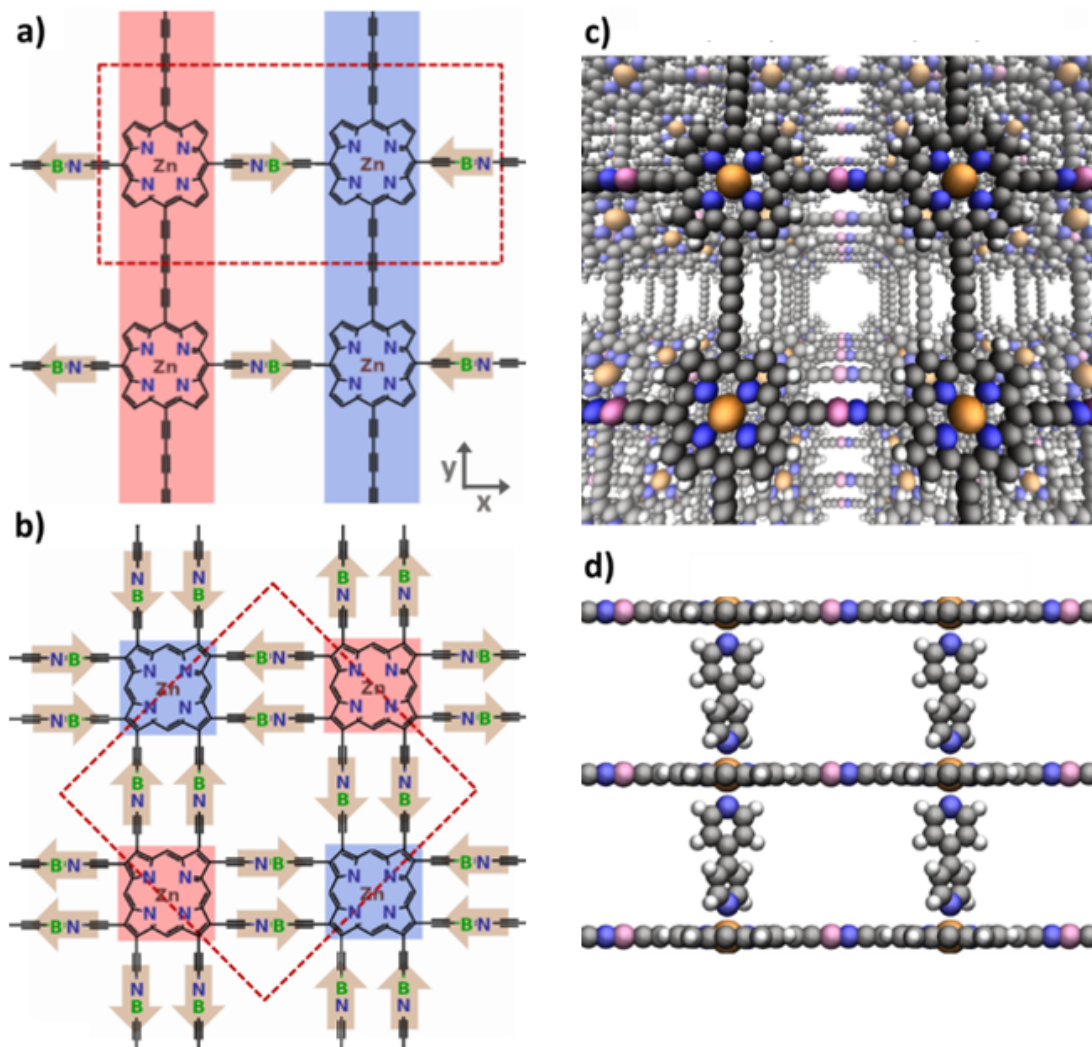
Figure 8: Electrostatically Designed Covalent Organic Network. Chemical structures of prototypical examples of electrostatically designed 3D covalent organic networks in **(a)** stripe architecture and **(b)** checkerboard structure. The red dashed lines indicate the unit cells used in the periodic DFT calculations. The arrows represent the directions of the dipole moments of the linking elements. The red (blue) shaded areas indicate regions for the expected lowered (raised) electrostatic energies for electrons. Besides the symmetry of the arrangement of the polar units the two displayed model systems also differ in their dipole densities. This is achieved by using singly (a) and doubly (b) linked structures. 3D representations of the model systems are shown in **(c)** top view and **(d)** side view, where 4,4'-bipyridine represents a typical apical linker.
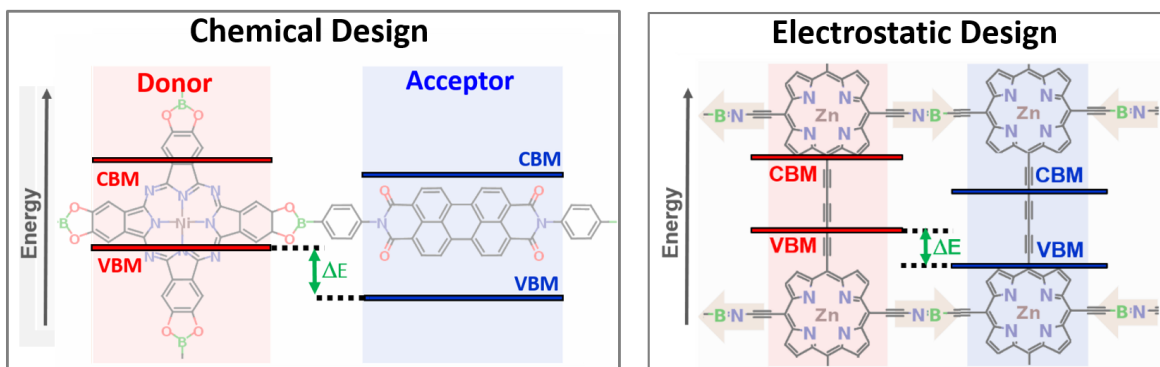
Figure 9: Chemical vs. Electrostatic Design. Energy level alignment of the heterojunction achieved by chemical design compared to the electrostatic design strategy. The band offset between VBMs (valence-band maxima) and CBMs (conduction-band minima), ΔE, is in the former case mainly determined by the molecular properties of donor (metallophtalocyanine) and acceptor (diimide). In notable contrast, for the electrostatic design strategy, it is solely determined by the collective electrostatic effects that arise by introducing polar elements (here boron nitride) between otherwise chemical identical segments (here porphyrin chromophores).

for the electrostatic design, the band offset as driving force for exciton dissociation can be tuned by changing the type of polar linker or the dipole density. These tuning handles are in detail discussed in PUBLICATION III. (Note that for the chemical design (Fig. 9a) the used boronate ester linker also has a small dipole of around $0.16 Debye$ (calculated for an isolated singly linked porphyrin dimer, *i.e.* without considering depolarization effects) and is, hence, expected to induce an electrostatic shift, which was shown to counteract the D/A level offset in these systems, see Bachelorthesis of Christoph Dlapa.)

The electronic structure calculations performed in PUBLICATION III were obtained with atomistic simulations based on density-functional theory (DFT). The underlying theoretical concepts are introduced in chapter 1.3.

1.2 Global Structure Search

Knowing the specific structure of any material is of crucial importance as it directly or indirectly determines pretty much all of its properties. Besides the chemical composition, the way its single constituents arrange, *i.e.* the polymorph the material assumes, strongly influences its mechanical, optical[94], electronic[95] or thermal[96] properties. While thermodynamics states that in thermodynamic equilibrium a material forms the structure with the lowest free energy, in many cases, several different energetically low lying competing polymorphs exist. They can become stable due to different external conditions such as pressure or temperature. Due to intricate interactions resulting in complex potential energy landscapes, it is commonly a priori not assessable which polymorph the material will assume. Hence, computational structure search is of increasing interest in order to predict a set of energetically lowest lying polymorphs.

While structure search and polymorphism are extensively discussed in the context of molecules, crystals or clusters, only limited progress has been made for describing polymorphic forms at surfaces and interfaces. First steps towards filling this gap are part of this Thesis. In the following, a general introduction into polymorphism at organic-inorganic interfaces and the so called configuration explosion as the main computational challenge, are discussed. Thereafter, a brief overview of the currently existing methodological approaches to global structure prediction is given. Finally, the systems of interest, *i.e.* tetracyanoethylene (TCNE) on several different metallic substrates, are introduced. Within this Thesis the structure prediction code SAMPLE was developed to explore the potential energy surface at organic-inorganic interfaces. PUBLICATION IV focuses on its application for the example of TCNE/Au(111). Appendix C specifies on related issues for the system TCNE/Cu(111) and provides a more detailed information on the SAMPLE procedure.

1.2.1 The Configuration Explosion

In the 1970s WALTER MCCRONE has stated that "every compound has different polymorphic forms, and that, in general, the number of forms known for a given compound is proportional to the time and money spent in research on that compound".[97] Moreover, as stated in 1995 by THRELFALL, one third of organic substances show polymorphism under normal pressure conditions.[98] Specifically, when depositing monolayers and thin films of organic molecules on inorganic substrates, the interface between the two fundamentally different components gives rise to a particularly rich and intricate polymorphism, which results in so called surface-induced phases.[99,100] The interplay between intermolecular and substrate-molecule interactions induces many mechanisms such as van der Waals interactions, electrostatic interactions as well as charge-transfer that jointly exist for these systems. These surface-induced phases exhibit structures that are markedly different from those observed in the bulk. Famous semiconducting representatives exhibiting polymorphsm are pentacene, rubrene, TIPS-pentacene or sexitiophene.[100] The exact arrangement of the molecules with respect to the surface, *i.e.* flat lying or upright standing molecules and the orientation with respect to each other, *i.e.* tilt angle or packing density, have a large impact on the charge transport characteristics of the final device (such as an organic field-effect transistor).[101] Slight changes in the crystal packing can

have large effects on the electronic properties, as charge transport is highly sensitive to the intermolecular π-orbital overlap, as was shown for the example of TIPS-pentacene thin film transistors, where the hole mobility in a non-equilibrium polymorph was measured to be an order of magnitude higher than in the equilibrium form.[102] A molecule that also shows rich polymorphim is tetracyanoethylene (TCNE),[103–105] which is used in this Thesis as model system to develope and demonstrate the structure search algorithm. As was shown by Scanning Tunneling Microscopy (STM) studies, TCNE adsorbs very differently on coinage metal substrates ranging from straight chains of flat lying molecules on Cu(111) to ordered triangular structures of upright standing molecules for Au(111).[103] (see section 1.2.3 for more details).

Finding polymorphs at organic-inorganic interfaces is a necessary step for a detailed understanding of their properties and potential applications. Structure prediction can be used to aid experimental measurements supporting their interpretation. Specifically, for organic-inorganic interfaces a purely experimental approach to determine the interface geometry is often not feasible, as most experimental techniques convey only partial or ambiguous information. Hence, computational simulations are becoming increasingly important to aid the interpretation. Beyond that, global structure search offers the power to predict materials properties even before the systems are synthesized. This paves the way for computational materials design.

Despite its importance and great potential, theoretical polymorph prediction is far from trivial. "One of the continuing scandals in the physical sciences is that it remains impossible to predict the structure of even the simplest crystalline solids from their chemical composition". So wrote the chemist JOHN MADDOX in 1988 (see ref. [106]). He was bemoaning the lack of a computational method to predict, how molecules will arrange in the solid state. From a computational point of view, structure prediction can be considered as a global optimization problem, *i.e.* the problem of finding the global minimum of the energy landscape. The potential energy surface (PES) of a system is a complex high-dimensional function of the atomic coordinates. Fig. 10 shows a very simplified scheme of a PES consisting of several local minima together with one global minimum. The main difficulty arises from the huge number of possible minima on the multidimensional PES, which increases exponentially with the size of the system.[107] Due to the associated exponential explosion problem one quickly ends up with several thousand to hundreds of thousand different configurations.

Of fundamental interest is without doubt the global minimum, which constitutes the most stable polymorph. However, finding a set of energetically lowest lying polymorphs is also of significant interest, as metastable polymorphs might be observed in experiment as well (due to finite temperature or kinetic effects). They are, thus, additionally in the focus of interest. Hence, global structure prediction faces a twofold computational challenge. In order to find a set of energetically lowest lying polymorphs an efficient sampling of the configuration space needs to be accompanied by a huge accuracy of the corresponding energy ranking. The latter necessitates a method that yields the total energy for a given configuration with high precision. While in the following an overview of typically applied global optimization schemes is given, the theoretic concepts of the underlying electronic

18
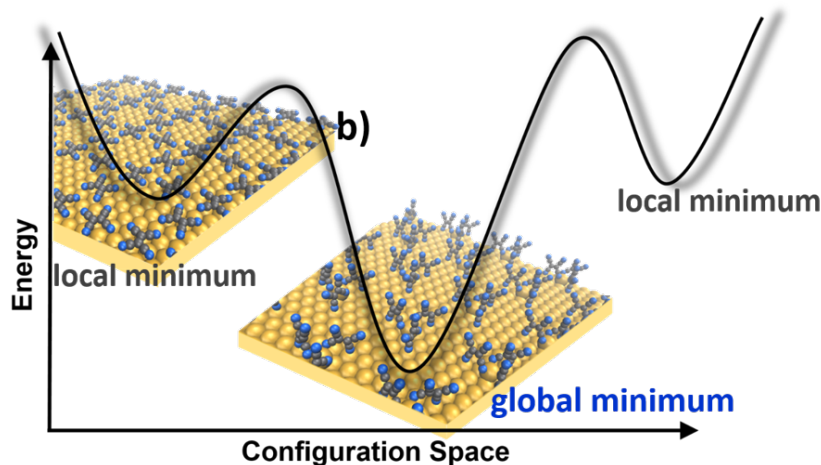
Figure 10: Potential Energy Surface for Organic-Inorganic Interfaces. A schematic PES consisting of several local minima together with the global minimum for the example of TCNE/Au(111).

structure methods, *i.e.* density-functional theory (DFT) is introduced in section 1.3.

1.2.2 Global Optimization Schemes

Numerous approaches have been suggested to solve the global optimization problem. With applications in many different scientific fields, the corresponding literature is widely spread ranging from physics to chemistry, mathematics and biology. By far the greatest potential, however, is found in predicting structures of crystals, clusters or biomolecules. Applying a variety of different methods ranging from Monte Carlo or Molecular Dynamics based techniques such as simulated annealing[108], basin-hopping[109] or minima hopping[110] to evolutionary methods such as genetic algorithms[111], tremendous progress has been made during the last decade. In the following, some of the most widely used techniques are explicitly discussed. Hereby, special emphasis is put on the Basin-Hopping approach as this is the method to which our developed SAMPLE procedure (see PUBLICATION IV) comes closest. For detailed information on a variety of the applied methods, the interested reader is referred to ref. [112].

Simulated Annealing

The most famous and one of the first developed classical optimization schemes is the simulated annealing algorithm.[108,113] It is based on simple concepts arising from physical annealing in metallurgy, where upon heating and controlled cooling, the material crystallizes in an ordered fashion with the energy reaching the global minimum. Though, if the temperature is decreased too rapidly or when the initial temperature is too low, the material may freeze into a disordered glass or a crystalline system containing defects. Similar to this process, in simulated annealing, an artificial temperature is slowly decreased in the hope that the system will eventually come to rest at the global potential energy minimum. Starting from an arbitrary configuration, the system is continually perturbed

using either a Monte Carlo (MC) scheme, *i.e.* a chain of configurations is generated in a stochastic way via discrete step walkers, or a Molecular Dynamics (MD) scheme, *i.e.* Newton's equations of motion are integrated. This provides a natural way of following the evolution of a system in time.

In MC simulated annealing, the configuration is updated applying (quasi-)random displacements of atoms or groups of atoms via so called trial moves and the Metropolis-Hastings[114] scheme is typically used to determine whether the Monte Carlo step is accepted or rejected. Based on the difference in the total energy of the computed structure with respect to the last accepted one, the move is accepted or rejected according to Boltzmann's acceptance probability:

$$p_{acc} = min\left[1, exp\left(\frac{-(E_{current} - E_{last})}{k_B T}\right)\right] \tag{5}$$

Hence, the suggested step is always accepted if its energy is lower than the last accepted one, $E_{current} < E_{last}$. For $E_{current} > E_{last}$ the new structure is only accepted if $p_{acc} > r$ where r represents a random number between 0 and 1. Note that this acceptance criterion can also be replaced by a Fermi-function like distribution (fast annealing) or the Tsallis distribution[115,116]. The initial temperature is chosen such that the acceptance probability in the Metropolis criterion is high enough to allow the system to overcome barriers between local minima on the PES. Hence, it is possible to move uphill as well as downhill along the PES, providing a chance to escape from a local minimum energy in favor of finding a better, more global one. The consecutive decrease in temperature (*e.g.* linear or exponentially) favors downhill moves on the PES while disfavoring jumps between local minima. With ongoing simulation time it, thus, gets more and more unlikely to jump between minima and move uphill, with a great probability to end up in the global minimum upon a smooth reduction of the temperature.

In MD simulated annealing the structure evolves following Newtonian equations of motion.

$$\mathbf{F} = m.\frac{d\mathbf{v}(t)}{dt} \tag{6}$$

The force can either be obtained ab-initio or it is adjusted to the specific system by so called force fields[117]. The latter often applies a velocity-verlet algorithm,[118] which updates the velocities at the same time step as positions. Reducing the temperature of the system affects the velocity in the average kinetic energy of the particles during the simulation. Physically motivated MD is not more realistic than random displacements in MC simulations when going to longer simulations, as was demonstrated for the example of Lennard Jones systems.[119]

Basin-Hopping

Basin-Hopping is a very powerful MC technique for the determination of the global minimum, that was first described by WALES and DOYE.[109] It is applied to many realistic systems, such as molecular clusters and very recently also to interface structures.[120] Com-

pared to MC simulated annealing its additional key ingredient is a local structure relaxation after every trial move. As can be seen in Fig. 11, thereby, the values of the PES within one basin are replaced by the associated local minima and the PES (black line) is transformed into a set of interpenetrating staircases (red line). Specifically, starting from
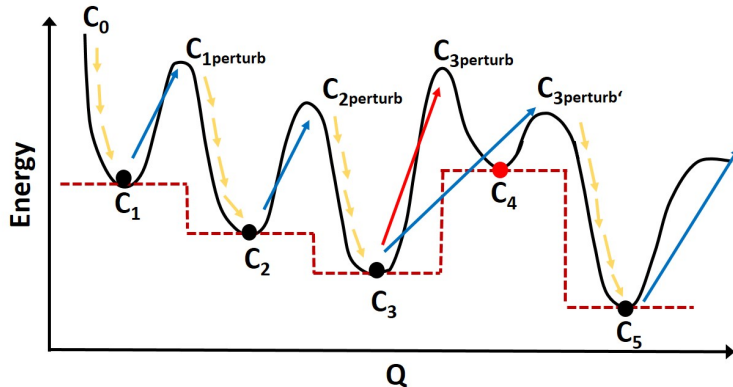
Figure 11: Schematic Illustration of the Basin-Hopping Method. The model energy surface (solid black line) is transformed into a collection of staircases (dashed red line) by several hops: Starting from an initial conformation C_0 several random trial moves (blue and red arrows) to perturbed conformations $C_{iperturb}$ are performed. Each trial move is followed by a local structure relaxation (yellow arrows) to the local minimum conformation C_i. The blue (red) arrows indicate hops that are accepted (rejected). See main text for detailed information.

a certain (often randomly chosen) initial conformation C_0 several random trial moves (blue and red arrows) to perturbed conformations $C_{iperturb}$ are performed. In classical Basin-Hopping the trial moves suggest to apply these perturbations are random displacements of atoms, thereby provoking changes in bond lenghts and bond angles. The choice of coordinates was demonstrated to have a large impact on the efficiency of the Basin-Hopping approach.[120,121] For of a silicon cluster,[121] as well as for methane adsorbed on Ag(111),[120] internal coordinates were shown to result in a superior performance compared to standard optimization moves based on Cartesian coordinates. As already mentioned, each trial move is followed by a local structure relaxation (yellow arrows in Fig. 11) to the local minimum conformation C_i. Typically, the Metropolis-Hastings criterion (see Eq.5) is used for acceptance or rejection with the temperature for the Boltzmann criterion kept constant. Several different Basin-Hopping runs starting from randomly chosen starting configurations are performed with a finite number of steps, in order to sample different parts of the PES.

Within this Thesis, the SAMPLE (Surface Adsorbate Polymorph Prediction with Little Effort) approach was developed for exploring the PES at organic-inorganic interfaces. As discussed in detail in PUBLICATION IV, it is a global structure prediction algorithm inspired by a Monte Carlo based Basin-Hopping scheme. In contrast to classical Basin-Hopping we do not perform random trial moves, but set up a neighborhood for each configuration according to system-dependent selection rules. Only within this neighbourhood the next configuration (hop) is chosen randomly. Moreover, we apply an efficient

discretization procedure such that the perturbed configuration is already very close to a local minimum, ensuring that the geometry optimization that follows each hop is highly efficient (in contrast to the situation shown in Fig. 11 where the perturbed conformation needs a large number of steps to relax to its closest local minimum). Acceptance and rejection is implemented via the Metropolis-Hastings criterion and the temperature is varied in each step according to the flooding technique. Details are discussed in Appendix C.

Minima Hopping

Minima-Hoppping[110] is in principle a similar method to Basin-Hopping, where hops from one local minimum to the next are performed, but with the main difference that the random displacements are replaced by MD trajectories. Furthermore, instead of the Metropolis criterion the next configuration is accepted by simple thresholding, *i.e.* the step is accepted if the new local minimum energy rises by less than a threshold energy, E_{diff}, compared to the former configuration. E_{diff} is continuously adjusted during the simulation, *i.e.* it is decreased in case of acceptance whereas it is increased upon rejection, so that half of the configurations will be accepted. Small values of E_{diff} are optimal to go down on the PES, while larger values are needed to jump out of a funnel. The continuous modifications of E_{diff} forces the algorithm to explore parts of the configuration space that is currently searched over. In order to keep track of all visited configurations, the Minima-Hopping method introduces an interesting feature which is a history list consisting of all the minima visited previously. In this list, the configurations are identified only by their energy. Introducing the history list enables the pushing of the configuration space towards parts of the PES that were not visited before. It has to be mentioned, that, of course, different configurations on different parts on the PES could potentially have very similar energies. Hence, the tracking on basis of the energy alone does not guarantee that the algorithm will evolve towards parts of the PES that have not been explored before. In PUBLICATION IV, we include a similar but more effective way of a history list. As described in detail in Appendix C, the systematic discretization of the configuration space, allows us to introduce a unique labeling of all configurations. Thereby, the history list not only includes the energy of already visited configurations but additionally the geometry.

Genetic Algorithm

Inspired by the mechanism of natural evolution, the genetic algorithm approach[122,123] is the most popular representative of the so called evolutionary techniques for global structure determination. Genetic algoritms were first developed by JOHN HOLLAND[124] and are stochastic global optimization methods based on the Darwinistic principle, *i.e.* survival of the fittest. Contrary to the methods described so far, the starting point is a *population* of several different structures instead of a single starting configuration. The procedure is illustrated in Fig. 12. Symbolically, each structure is represented by a box of four constituents labeled from 1 to 3. In this simplified example the starting population consists of three conformations. After a local geometry optimization, within this population two *parents* are picked selected on the basis of their energy according to their *fitness* (often by applying the roulette wheel selection[125]). According to system-specific *crossover* symmetry rules these parents are mated to breed a certain number of *children*. This crossover is
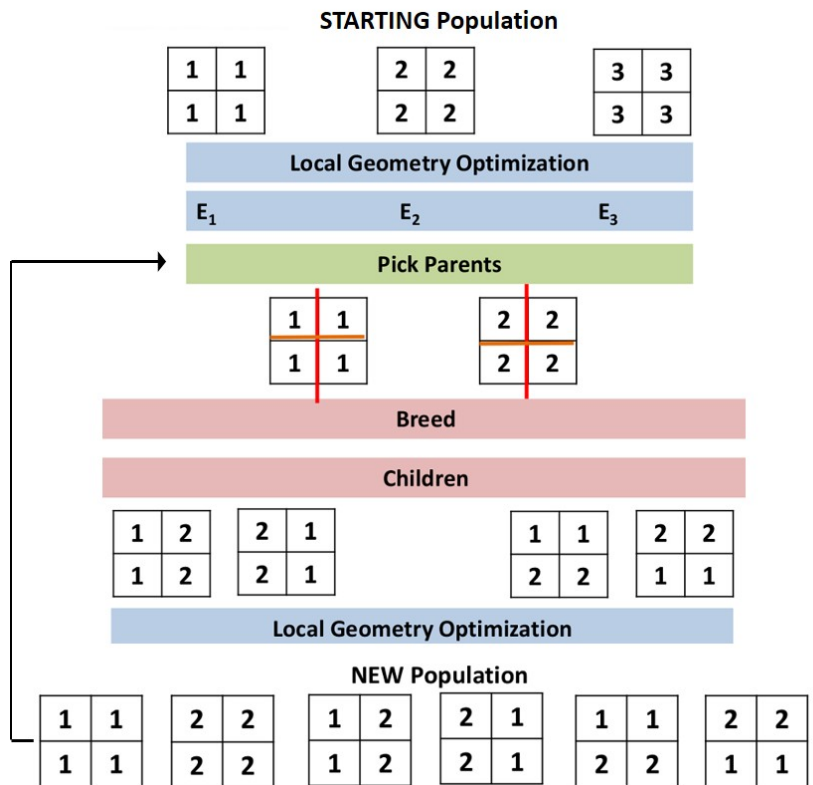
Figure 12: Schematic Illustration of a Genetic Algorithm. The starting point is a population of structures (symbolically, each structure is indicated as a box consisting of four constituents). After a local geometry optimization two *parents* are chosen. By mating these *parents* according to some optional symmetry rules (mirror planes are indicated in this example as orange and red lines) several *children* are bred. After local geometry optimizations, these *children* together with their *parents* form a new population and the iterative process starts again. See main text for more details.

chosen in a way that specific structural properties are preserved. In the example shown in Fig. 12 two symmetry axes (red and orange lines) are defined and children are born by swapping the components along the mirror plane. After a local geometry optimization the new population consists of parents as well as children and the process starts again. In order to maintain diversity during this evolutionary procedure a key ingredient of genetic algorithms is to introduce *mutations* by sporadic arbitrary changes in the compositions.

Apart from the basic types of global optimization schemes introduced here, several modification and extensions have been suggested. However, no general rule of preference to a specific algorithm exists, as the efficiency of classical global optimization methods is highly system dependent. There are many technical aspects that influence the performance of any global sampling technique, such as the choice of initial geometry, the ways of disturbing the configuration during the trial move, the definition of acceptance criteria or the electronic structure methods employed for optimizing geometries and obtaining the energies and forces.

As all of the above-described methods were historically developed to predict structures of biomolecules, crystals or clusters, they are in a large part dedicated to gas-phase structures or periodic bulk structures containing a single entity. However, the application of global structure search to systems with several molecules per unit cell was just recently demonstrated to be quite successfull in the 6$^{\text{th}}$ blind test of organic crystal structure prediction methods.[126] Moreover, there are applications of structure prediciton for bulk interfaces in multicomponent systems. Applying genetic algorithm non-stochiometric grain boundaries for the ternary oxide $SrTiO_3$ were predicted.[127] Furthermore, a similar genetic algorithm was applied to predict the atomic structures at solid-solid interfaces.[128] Recently, a virtual screening approach based on machine learning was applied to predict the atomic configuration of bulk interfaces.[129] Global structure search of organic-inorganic *interfaces* with *several moelcules* per unit cell is quite rarely addressed. There are some works dealing with the prediction of single molecules on surfaces. The Basin-Hopping method was applied to metallic and hydrogenated silicon clusters in gas phase and adsorbed on surfaces,[121] which was recently extended to trans-β-ionylideneacetic acid adsorbed on a Au(111) surface and methane adsorbed on a Ag(111)surface.[120] Very recently, there have been some attempts to describe self-assembly processes at organic-inorganic interfaces with several molecules per unit cell.[102,130–134] These methods mostly rely on force-field Molecular Dynamics.[130–132] and, often, they only account for intermolecular interactions (either obtained from gas-phase data fitting[134] or via atomistic models[133]) while the interactions of the molecules on the surface are neglected. However, especially for hybrid organic-inorganic interfaces where charge transfer between molecules and metals is apparent, the interactions between the (charged) molecules drastically change upon adsorption.

In this Thesis, a novel algorithm to predict a set of energetically lowest lying polymorphs of organic-inorganic interfaces is suggested (see PUBLICATION IV), that is purely *ab-initio*. It is specifically designed to treat interfaces with several molecules in the unit cell and fully accounts for substrate- as well as molecule-molecule interactions directly obtained from DFT. The model systems to validate the developed approach are introduced in the next section.

1.2.3 System of Interest

The model system we choose to apply on global structure prediction is the organic molecule tetracyanoethene (TCNE, C_6N_4, see Fig. 14a) adsorbed on metal substrates. Due to its electron pulling cyano groups TCNE is known to be a very strong electron acceptor with a large electron affinity. Therefore, it readily forms charge-transfer complexes with metallic substrates.[135,136] For a global structure study, TCNE is in particular interesting as it forms very different surface-induced phases on various metallic substrates,[103,104] all of which exhibit structures that are markedly different from those observed in the bulk.[137,138]

Experimentally, bulk TCNE has two resolved molecular crystalline phases at ambient pressure,[137,139] both of which are shown in Fig. 13. A cubic phase that reversibly transforms into a monoclinic phase when heated to temperatures higher than $320K$.[139] In the
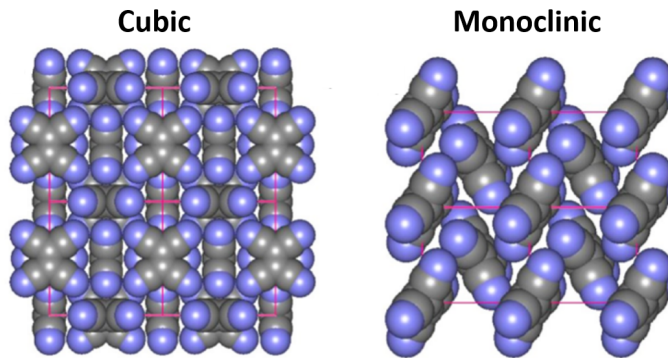
Figure 13: TCNE Bulk Structue. Cubic and monoclinic polymorphs of TCNE. The central molecules are surrounded by 12 nearest neighbors. The figure is partly reproduced from ref. [140] with permission of The Royal Society of Chemistry

cubic phase, the molecules orient mutually perpendicular to each other, whereas in the monoclinic phase they are aligned in planes to form chainlike zig-zag structures (similar to a herringbone arrangement). When depositing TCNE on metallic substrates, the resulting surface-induced phases exhibit structures that are markedly different from those observed in the bulk. This can be inferred from the Scanning Tunneling Microscopy (STM) images shown in Fig. 14. As can be seen, on Cu(100) TCNE orders in straight chains of flat lying molecules, whereas for TCNE on Ag(111) a network of flat lying molecules connected by silver adatoms is formed.[104] Another strikingly different behavior is observed for TNCE on Au(111). This system forms a complex pattern of ordered triangular structures exhibiting a non-orthogonal unit cell including three TCNE molecules. Interestingly, on the gold surface, the TCNE molecules do not appear in the expected flat-lying fashion but have been suggested to be tilted onto their sides.[103] In their paper Wegner et al.[103] qualitatively explain these different orientations and structures by a combination of charge-transfer and lattice-mismatch leading to different degrees of intermolecular versus molecule-substrate interactions. Specifically, from an electrostatic perspective, the upright standing arrangement on Au(111) facilitates TCNE molecules to maximize their quadrupole interaction,
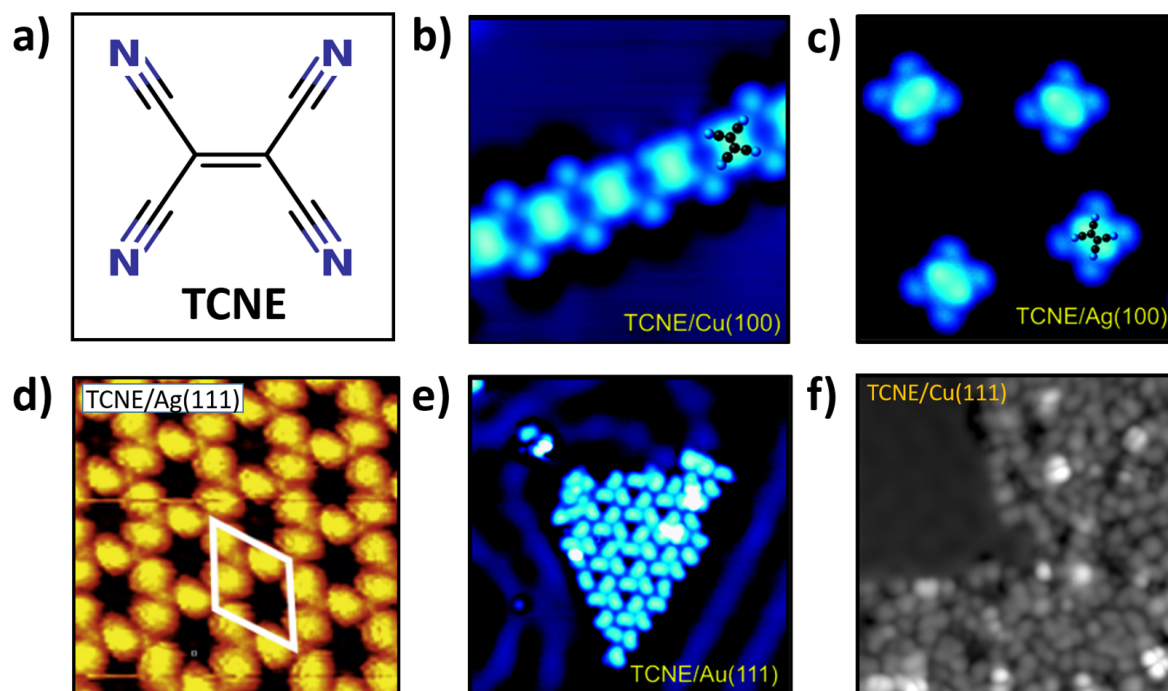
Figure 14: TCNE on Noble Metals. **(a)** Chemical structure of TCNE (tetracyanoethene, C_6N_4) **(b)-(f)** Experimental STM result of TCNE adsorbed on **(b)** Cu(100), reprinted in part with permission from ref. [103] (Copyright 2017 American Chemical Society) **(c)** Ag(100), reprinted in part with permission from ref. [103], **(d)** Ag(111), reprinted in part from ref. [104] with permission of AIP Publishing, **(e)** Au(111), reprinted in part with permission from ref. [103] and **(f)** Cu(111), private communication with D. Wegner. STM was operated in constant current mode and the films were grown at room temperature.

i.e. electronegative cyano groups pointing towards electropositive C=C centers. Moreover, as gold has the largest work function among the discussed metal substrates, it is less likely to establish a strong charge transfer bond by donating electrons to the molecules. In turn, the smaller work function of Ag(111) enables weak charge transfer to the molecules. These are therefore pinned flat to the surface and repel each other due to their negative charge. On Cu(100), a very strong chemical bond is formed while the lattice constant is smaller compared to silver. During initial growth, molecules diffuse until they hit a step edge where nitriles can connect to Cu atoms of the upper terrace.[103] As also shown in Fig. 14, on Cu(111) TCNE molecules grow in a disordered fashion. The strong metal-molecule interaction tends to pin the molecules flat to the surface while a mismatch of lattice and molecular symmetries prevents ordered self-assembly. This interpretation is supported by observations of different charge states that occur simultaniously for TCNE/Cu(111).[141] Moreover, several energetically similar local adsorption structures of TCNE/Cu(111) were found in a separate STM study.[142] Still, all these considerations are qualitative interpretations.

The peculiarity of TCNE forming distinctively different structures on different surfaces, makes it an interesting candidate for a global structure study. Furthermore, TCNE is a rather small molecule consisting of only 10 atoms, therefore perfectly suited for the current study as one of the major limiting factors in *any* global structure prediction technique is the computational cost of the underlying electronic structure method (this is in particular decisive for larger unit cells containing several molecules). In PUBLICATION IV we predict the structure of TCNE/Au(111) applying the SAMPLE algorithm, while in Appendix C the TCNE/Cu(111) system is discussed.

1.3 Methodological Aspects

In this Thesis computational simulations of organic-inorganic nanomaterials are performed. For an accurate description of the electronic structure of these complex many-body systems at the nanoscale a quantum-mechanical approach is essential. Due to the comparably large systems comprising several hundreds of atoms, the method of choice is Density-Functional Theory (DFT) providing the best compromise between accuracy and performance. All electronic structure calculations contained in PUBLICATION I - IV are obtained on the basis of state-of-the-art DFT. An overview of the underlying principles is given in the first part of this chapter. A very popular extension of DFT is its combination with Non-Equilibrium Greens Function Techniques (NEGF) in order to describe charge transport in nanoscale devices. This formalism is utilized in PUBLICATION I & II and its basic concepts are discussed in the second part of this chapter. One of the main challenges in *any* structure search approach (as the one in PUBLICATION IV) is the large number of calculations for often comparably large systems. In search of computationally less expensive alternatives to DFT, a possible option is offered by Density Functional Tight Binding (DFTB). Rooted in first principles via DFT but combined with semi-empirical tight binding concepts, it enormously reduces computational cost at the expense of accuracy. Its basic ideas and comparison to DFT are given in Appendix D.

1.3.1 Density Functional Theory

The ultimate goal in any electronic structure method is the solution of the time-independent Schrödinger equation for the many-electron wave function Ψ,

$$\hat{H}\Psi(\mathbf{r}_1, \cdots, \mathbf{r}_N, \mathbf{R}_1, \cdots, \mathbf{R}_M) = E\Psi(\mathbf{r}_1, \cdots, \mathbf{r}_N, \mathbf{R}_1, \cdots, \mathbf{R}_M) \tag{7}$$

where $\hat{H}$ is the Hamiltonian for a molecular system containing M nuclei and N electrons which are situated at positions $\mathbf{r}_i$ and $\mathbf{R}_I$, respectively.

$$\hat{H} = -\frac{\hbar^2}{2m_e}\sum_{i=1}^{N}\nabla_i^2 - \frac{\hbar^2}{2}\sum_{I=1}^{M}\frac{1}{M_I}\nabla_I^2 - \sum_{i=1}^{N}\sum_{I=1}^{M}\frac{Z_I e^2}{|\mathbf{r_i} - \mathbf{R_I}|} + \frac{1}{2}\sum_{i=1}^{N}\sum_{\neq j}^{N}\frac{e^2}{|\mathbf{r_i} - \mathbf{r_j}|} + \frac{1}{2}\sum_{I=1}^{M}\sum_{\neq J}^{M}\frac{Z_I Z_J e^2}{|\mathbf{R_I} - \mathbf{R_J}|} \tag{8}$$

The first two terms of $\hat{H}$ describe the kinetic energies of the electrons and the nuclei. The three remaining terms represent the attractive electrostatic interaction between nuclei and electrons and the repulsive potential due to electron-electron interactions and nucleus-nucleus interactions. A very common simplification of the Hamiltonian can be achieved by applying the BORN-OPPENHEIMER approximation,[143] *i.e.* the electrons are considered in the field of the much heavier nuclei, which are fixed in space. Thereby, the kinetic energy of the nuclei is eliminated while their mutual electrostatic interaction turns into a constant. The problem for the electronic system reduces into

$$\hat{H} = \hat{T} + \hat{V}_{int} + \hat{V}_{ext} \tag{9}$$

with $\hat{T}$ being the kinetic energy of the electrons, $\hat{V}_{int}$ the electron-electron interaction and $\hat{V}_{ext}$ the external potential acting on the electrons. Still, the many-electron wave function depends on the coordinates of all N electrons in the system. However, in 1964,

HOHENBERG and KOHN formulated two theorems[144] that reduce the complexity in an advantageous way. The main statement is that the ground state properties of an interacting many-electron system are uniquely determined by an electron density $n(\mathbf{r})$ which is a scalar object only depending on $\mathbf{r}$. The total energy of the electronic system can be expressed as a functional of the electron density $n(\mathbf{r})$.

$$E[n(\mathbf{r})] = T[n(\mathbf{r})] + E_{int}[n(\mathbf{r})] + \int d\mathbf{r} V_{ext}(\mathbf{r}) n(\mathbf{r}) \tag{10}$$

The first two terms include all internal energies (kinetic and potential) of an interacting electron system and can be summarized into the HOHENBERG-KOHN functional $F_{HK}[n(\mathbf{r})]$. The latter term describes the interaction of the electron density with the external potential created by the nuclei. For any V_{ext}, the exact ground state energy is the global minimum of the energy functional and the density that minimizes the functional is the exact ground state electron density. However, the exact form of the energy functional is not known. The major problem is the description of the kinetic energy as a function of the electron density. This issue was addressed by KOHN and SHAM[145] and made DFT practically feasible. They introduced a fictitious system of N non-interacting electrons that have the same ground state density as the fully interacting system. Thereby, the complex interacting many-body system is replaced by an auxiliary non-interacting one and the problem is simplified to treating independent-particle equations where all complicated terms are comprised into the so called exchange-correlation functional. Auxiliary orbitals ϕ_i are introduced which relate to the ground state density as

$$n(\mathbf{r}) = \sum_i |\phi_i(\mathbf{r})|^2. \tag{11}$$

The functional of the whole electronic system can be formulated as

$$E[n(\mathbf{r})] = T_S[n(\mathbf{r})] + E_{Hartree}[n(\mathbf{r})] + \int d\mathbf{r} V_{ext} n(\mathbf{r}) + E_{xc}[n(\mathbf{r})] \tag{12}$$

where $T_S[n(\mathbf{r})]$ is the kinetic energy functional of the non-interacting auxiliary electron system moving in an effective KOHN-SHAM potential V_{KS}.

$$T_S[n(\mathbf{r})] = \frac{1}{2} \sum_i \int d\mathbf{r} \langle \phi_i | \nabla | \phi_i \rangle = \frac{1}{2} \sum_i \int |\nabla \phi_i|^2 \tag{13}$$

$E_{Hartree}[n(\mathbf{r})]$ describes the classical Coulomb interaction energy of the electron density $n(\mathbf{r})$.

$$E_{Hartree}([n(\mathbf{r})]) = \frac{1}{2} \sum_{ij} d\mathbf{r} d\mathbf{r}' \frac{|\phi_i(\mathbf{r})|^2 |\phi_j(\mathbf{r}')|^2}{|\mathbf{r} - \mathbf{r}'|} = \frac{1}{2} \int d\mathbf{r} \frac{n(\mathbf{r}')}{|\mathbf{r} - \mathbf{r}'|} \tag{14}$$

Eq.12 defines the exchange-correlation energy, $E_{xc}[n(\mathbf{r})]$, which includes all many-body effects that are not described by the other three contributions. By minimizing the total energy functional with respect to the electron density one finally ends up with the non-

interacting KOHN-SHAM equations

$$\left(-\frac{1}{2}\nabla^2 + V_{KS}(\mathbf{r})\right)\phi_i(\mathbf{r}) = \epsilon_i\phi_i(\mathbf{r}) \tag{15}$$

with the effective KS-potential

$$V_{KS}(\mathbf{r}) = V_{ext}(\mathbf{r}) + V_{Hartree}(\mathbf{r}) + V_{xc}(\mathbf{r}) \tag{16}$$

Eq.15 represents a set of single-particle Schödinger equations, where solutions are Ks-orbitals ϕ_i with energies ϵ_i. In practice, one starts with an initial guess for the electron density, from which the Ks-potential (Eq.16) is determined. Then, the KS-equations (Eq.15) are solved for this potential, which results in a new electron density calculated from the KS-orbitals (Eq.11). This process is iteratively repeated until a certain convergence criterion is met. The Ks-scheme is an *exact* mapping of the N-electron problem to N one-electron problems.

Exchange-Correlation Functionals

Using the KOHN-SHAM ansatz, the remaining unknown part of the functional is the exchange-correlation XC functional, for which many different approximations have been proposed. The simplest approximation is the LDA approach (Local Density Approximation)

$$E_{xc}^{LDA}[n(\mathbf{r})] = \int d\mathbf{r} n(\mathbf{r}) e_{xc}^{hom}(n(\mathbf{r})) \tag{17}$$

where e_{xc}^{hom} is the XC energy per particle for a homogeneous electron gas. It only depends on the electron density and is exact for the uniform electron gas. However, as many systems (such as molecules) do not exhibit a uniform distribution of their electrons, a more accurate approximation can be achieved by including the generalized gradient of the electron density, $|\nabla n(\mathbf{r})|/n(\mathbf{r})$, which is done in the GGA[146] approach (Generalized Gradient Approximation).

$$E_{xc}^{GGA}[n(\mathbf{r})] = \int d\mathbf{r} n(\mathbf{r}) e_{xc}(n(\mathbf{r}), \nabla n(\mathbf{r})) \tag{18}$$

The most widely used form for this approach is the Perdew-Burke-Ernzerhof (PBE)[146] functional, which is also applied in this Thesis. The next step beyond GGA are meta-GGA functionals which include second and higher derivatives of the electron density in the exchange correlation functional.[147] Despite its apparent approximative character, (semi)-local KS DFT yields rather accurate pedictions for many different physical observables of materials.[148] Still, there are also some known deficiencies such as the self-interaction error (SIE).[148,149] In the Hartree energy in Eq.14, for $i = j$, the electron interacts with itself. The impact of the SIE becomes particularly decisive when simulating systems with localized electrons. Because the SIE is always positive it raises the energy of localized states and favors delocalization instead[150–152] (*cf.* PUBLICATION III). Hybrid functionals are approximations to the XC energy functional that incorporate a portion of exact exchange from Hartree-Fock theory partly correcting the SIE. Such a functional that has shown to

give good results for molecules is the B3LYP[153] functional, which mixes LDA, GGA and Hartree-Fock like exchange. Another common functional is PBE0[154], being the hybrid equivalent to PBE, which mixes 25% of Hartree-Fock exchange to the PBE functional.

$$E_{XC}^{PBEh} = \frac{1}{4}E_X^{exact} + \frac{3}{4}E_X^{PBE} + E_C^{PBE} \qquad (19)$$

These hybrid functionals are computationally very costly as they include long range Hartree-Fock for exact exchange. Screened hybrid functionals, such as the Heyd-Scuseria-Ernzerhof (HSE)[155] functional limit the exact exchange to the short range by applying a range separation parameter ω.

$$E_{XC}^{HSE} = \frac{1}{4}E_X^{HF,SR}(\omega) + \frac{3}{4}E_X^{PBE,SR}(\omega) + E_X^{PBE,LR}(\omega) + E_C^{PBE} \qquad (20)$$

Exchange is thereby subdivided into long range and short range and only the short range part for exact exchange is used. For $\omega = 0$, HSE degenerates to PBE0 while for $\omega \to \infty$, it converges to PBE. With $\omega = 0.2$, the HSE06[155] functional is obtained, which was used in PUBLICATION III. Adjusting ω such that a physical constraint is fullfilled leads to so called optimally tuned range separated hybrid (OT-RSH) functionals,[156,157] which where already successfully applied to a variety of systems.[158–160]

Van der Waals Forces

Van der Waals (vdW) interactions are non-local attractive interactions between instantaneous and induced multipoles arising from charge density fluctuations. For long distances between the atoms, they are described by a $1/R^6$ characteristics with an atomic separation R. Long-range vdW forces are of key importance in the context of understanding the interaction of a metal with large π-conjugated molecules, as the latter contain an easily polarizable π-electron system, as well as for example of π-stacked layers in covalent organic frameworks (*cf.* section 1.1.2). To account for vdW interactions in DFT they are typically included in different flavors as energy corrections outside of the self-consistent routine. While in the following, vdW implementations used in this Thesis are discussed, the interested reader is referred to recent reviews of these and other methods.[161–166]

DFT+vdW^{TS} is a pairwise additive correction method developed by Tkatchenko and Scheffler[167] in which the interaction of two atoms is considered separately from the rest of the system and screening effects are neglected. The additive energy term E_{vdW} for an atom pair A and B is calculated in terms of the interatomic distance R_{AB}, the vdW radii of each atom R_A^0 and R_B^0 and the vdW coefficients C_6^{AB}.

$$E_{vdW} = -\frac{1}{2}\sum_{A,B} f_{damp}(R_{AB}, R_A^0, R_B^0)C_6^{AB}R_{AB}^{-6} \qquad (21)$$

A Fermi-type damping function is included to avoid R_{AB}^{-6} singularities at short distances. R_{AB} and C_6^{AB} arre obtained from the electronic ground-state density by Hirshfeld-volume partitioning.[168] The vdW^{TS} method was used in PUBLICATION III.

DFT+vdW$^{\text{surf}}$ is an extension of the pairwise vdW$^{\text{TS}}$ method developed by Ruiz et al.[169] in order to describe the interaction of molecules with *surfaces*. It additionally includes Coulomb screening effects of a metal substrate applying the Lifshitz-Zaremba-Kohn theory[170]. This approach was shown to result in a very accurate description of the binding distances for PTCDA on Ag(111)[169] and is a very common method to describe the vdW interactions at metal-organic interfaces. The vdW$^{\text{surf}}$ method was applied in PUBLICATION IV.

DFT+MBD is the Many-Body-Dispersion method[171] developed by Tkatchenko et al. which is one of the approaches which includes dispersion beyond pairwise correction. The long-range correlation energy is computed through the coupled Harmonic oscillator model Hamiltonian where vdW interactions can be treated to all orders beyond the pairwise vdW$^{\text{TS}}$ or vdW$^{\text{surf}}$ method. This method has been demonstrated to compare very well to experimental values for a broad range of molecules on surfaces.[166,172] In a comprehensive study by Maurer et al., theoretical DFT+MBD results for 23 adsorption heights and 17 adsorption energies werde found to only deviate by 0.06 Å and 0.16 eV on average when compared to experiment.[166] MBD was also applied in PUBLICATION IV where qualitative differences compared to vdW$^{\text{surf}}$ in the energetic ordering of the polymorphs for TCNE/Cu(111) are observed.

DFT in Practice

The practical input for *any* electronic structure calculation using DFT consists of (a first guess) of the coordinates of all involved atoms in the unit cell (in case of periodic calculations) as well as the specific settings of all parameters, such as the used functional, basis set or the vdW scheme. Most calculations in this Thesis are performed on periodic systems. In case of 2D systems, *i.e.* molecules on surfaces, the repeated slab approach is applied in order to mimic the 2D systems in a fully periodic code.[7] As can be seen in Fig. 15, in the repeated-slab approach consecutive replicas of the unit cell are decoupled from each other by introducing a large vacuum gap in the z-direction. Moreover, a dipole correction is applied to compensate the electrostatic field created by the system.[173]

For the DFT calculations performed in this Thesis, three different programs have been applied, namely the Vienna Ab Initio Simulation Package, `VASP`[174], the Spanish Initiative for Electron Simuations with Thousands of Atoms, `SIESTA`[175] and the Fritz-Haber Institute *ab-initio* molecular simulation package, `FHI-aims`[176]. They mainly differ in the type of representation for the basis functions together with the respective treatment of core and valence electrons. In particular, in `VASP` orbitals are expressed in plane-wave basis sets while the interactions between core and valence electrons are described by the projected-augmented wave method (PAW)[177] which is an advancement of the pseudopotential method. `SIESTA`, on the other hand, uses strictly localized atomic orbitals, which is a necessary prerequisite for the descritpion of charge transport properties in the `Tran-SIESTA`[178] extension. `FHI-aims` is a full-potential, all-electron code applying numerically tabulated atomic-centered basis functions. In principle, all of these methods should give equally accurate results, provided well overconverged numerical settings are used. For
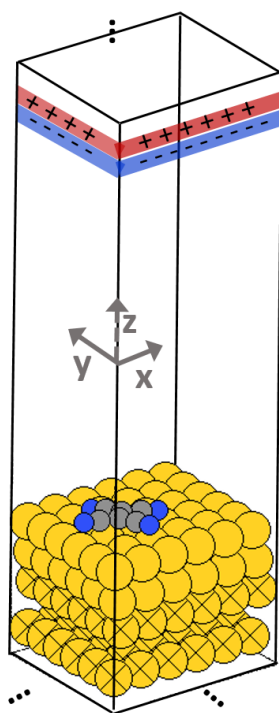
Figure 15: Repeated Slab Approach. Illustration of the repeated slab approach to mimic organic/inorganic surfaces in a 3D-periodic code on the example of TCNE on Au(111). To decouple consecutive unit cells in z dimension a large vacuum has to be introduced and a dipole correction is applied by inserting an artificial dipole layer (red and blue bars) to compensate the electrostatic field created by the system.

`VASP` and `FHI-aims` this was recently demonstrated in a comperative study in which 71 elemental crystals were compared applying 15 common DFT codes.[179] For all `SIESTA` calculations performed in this Thesis the PAO.EnergyShift, which specifies the spatial confinement of the atomic orbitals was modified such that the observed trends in the density of states meet the results obtained from `VASP` (for further details see the Supplementary Information of ref. [1]). The specific settings for the calculations performed in this Thesis can be found in the Methods section as well as the Supporting Information of the respective publication.

1.3.2 Greens Function Techniques

The most widely used formalism to describe ballistic transport in nanocontacts is the Landauer approach.[180] It is a theoretical model in which electrons are regarded as non-interacting particles, neglecting any inelastic scattering events and transferring the charge transport problem into a scattering problem. Hence, transport properties like current-voltage characteristics or electrical conductance get related to the transmission probability for an electron to cross the system. Within the Landauer approach, the current through a molecular wire connected to two metallic leads at different chemical potential μ_L and μ_R can be expressed as

$$I(V) = \frac{2e}{h} \int T(E)[f(E - \mu_L) - f(E - \mu_R)]dE. \tag{22}$$

Here, $f(x)$ is the Fermi-Dirac occupation function at 300 K and $\mu_{L/R} = E_F \pm (eV/2)$ with e the elementary charge, E_F the Fermi energy, and V the voltage.

To obtain an expression for the transmission function $T(E)$, Non-Equilibrium Greens Function Techniques (NEGF) can be combined with DFT. The main idea is to partition the molecular junction into semi-infinite electrodes serving as electron reservoirs and a central region, see Fig. 16. The main advantage is the possibility to decompose also the associated Hamiltonian into different parts. The incorporation of the influence of the infinitely extended leads on the finite size central region is then treated as a combination of DFT and Greens function techniques. Within this approach, the transmission function entering the current-voltage characteristics in Eq.22 can be expressed as

$$T(E) = \sum_k \omega_k Tr(\mathbf{G}_C^\dagger \mathbf{\Gamma}_R \mathbf{G}_C \mathbf{\Gamma}_L). \tag{23}$$

Here, $\mathbf{G}_C$ is the retarded Greens function of the central region and $\mathbf{\Gamma}_{L/R} = i(\mathbf{\Sigma}_{L/R} - \mathbf{\Sigma}_{L/R}^\dagger)$ are the coupling matrices to the electrodes, with $\mathbf{\Sigma}_{R/L}$ being the self-energy of left and right electrodes. The weight of lateral k-points is given by ω_k. The Greens function of the central region is obtained as

$$\mathbf{G}_C^R = (E^+ \mathbf{S}_C - \mathbf{H}_C - \mathbf{\Sigma}_L - \mathbf{\Sigma}_R)^{-1} \tag{24}$$

which is calculated by extracting the Hamilton matrix $\mathbf{H}_C$ and the overlap matrix $\mathbf{S}_C$ of the central region (by standard DFT), as well as the self energies $\mathbf{\Sigma}_{L/R}$ including all
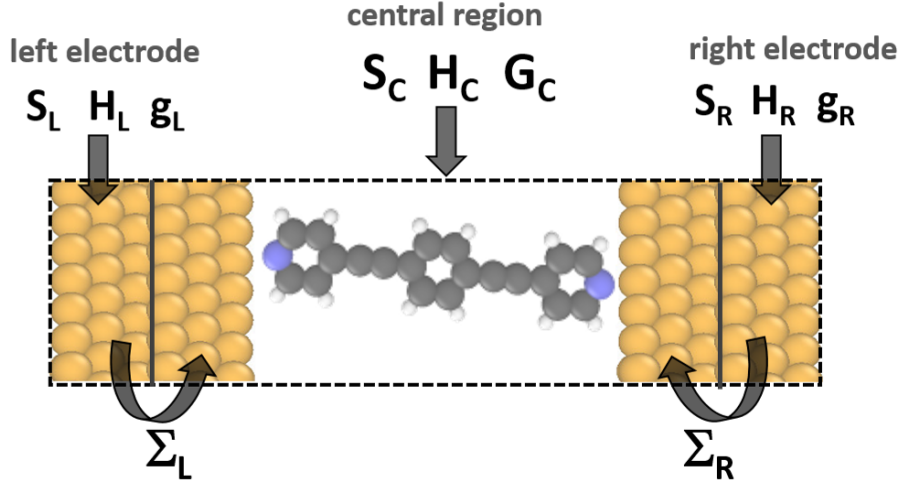
Figure 16: Scattering Approach. Decomposition of a molecular junction into the finite sized central region (black dashed box) and the semi-infinite left and right electrode respectively. All objects entering the transmission function in Eq.23 are indicated. For details see main text.

the effects coming from the coupling between central region and the leads. These are separately obtained for both electrodes as

$$\mathbf{\Sigma}_L = \boldsymbol{\tau}_L^\dagger \mathbf{g}_L \boldsymbol{\tau}_L \tag{25a}$$

$$\mathbf{\Sigma}_R = \boldsymbol{\tau}_R^\dagger \mathbf{g}_R \boldsymbol{\tau}_R \tag{25b}$$

where $\mathbf{g}_L = (E^+\mathbf{S}_L - \mathbf{H}_L)^{-1}$ and $\mathbf{g}_R = (E^+\mathbf{S}_R - \mathbf{H}_R)^{-1}$ are the retarded Greens functions of the isolated semi-infinite left and right leads, also called surface Greens functions of the electrodes uncoupled to the device. $\boldsymbol{\tau}_{R/L}$ determines the coupling of the central region to the surface Greens function corresponding to the surface atoms. They are caclulated using an efficient iterative method proposed by Sancho et al.[181]

DFT-NEGF in Practice

In this Thesis two different codes were applied to obtain the transport characteristics of molecular junctions, namely `TranSIESTA`[182] which is a generally available transport extension of the aforementioned `SIESTA` code and `SIESTA`$_{\text{TS}}$ which was developed by Georg Heimel and David A. Egger and is not officially available. In principle, `SIESTA`$_{\text{TS}}$ takes the same steps as `TranSIESTA` but omits the self-consistent Greens function cycle of the density matrix and only works for zero-bias. In general, for both of the codes, three consecutive calculations are performed: (i) the *bulk* calculation to obtain the Hamiltonian and overlap matrices together with the information to calculate the surface Greens function, (ii) the *central region* calculation to obtain the Hamiltioan and overlap matrices of the central region(as well as the density and energy density matrix in the case of `TranSI-ESTA`), and finally (iii) the determination of the transmission function according to Eq.23. A detailed description of the individual steps for both codes can be found in ref. [183].

2 Publications

2.1 Impact of Anchoring Groups on Ballistic Transport

2.1.1 Author Contribution

E. Zojer conceived the idea to use different anchoring groups for molecular junctions in order to demonstrate their effect on charge transport properties when varying the coverage between single molecules and self-assembled monolayers. V. Obersteiner performed all calculations and primary analysis of the data. The data were interpreted by all authors. The used $SIESTA_{TS}$ code which is an extension to $SIESTA$, facilitating the calculation of the transmission functions, was written by G. Heimel and D. A. Egger. V. Obersteiner wrote the first version of the manuscript and prepared all figures. The manuscript was improved in close cooperation with E. Zojer and D. A. Egger. The project was supervised by E. Zojer.

The following paper is published in the Journal of Physical Chemistry C and inserted here as original publication together with the Supporting Information. Reprinted with permission from "Obersteiner, V.; Egger, D. A.; Zojer, E. Impact of Anchoring Groups on Ballistic Transport: Single Molecule vs Monolayer Junctions, *J. Phys. Chem. C.* 2015, 119, 21198-21208". Copyright 2015 American Chemical Society.

Note that this paper is based on work I did within my Master Thesis that was, however, extensively extended during the time of my PhD. The paper entirely connected to my Master Thesis, see Ref. [1], was finished during the course of my PhD but is not included in this Thesis.

2.1.2 Original Article

# Impact of Anchoring Groups on Ballistic Transport: Single Molecule vs Monolayer Junctions

Veronika Obersteiner,[†] David A. Egger,[†,‡] and Egbert Zojer*[,†]

[†]Institute of Solid State Physics, NAWI Graz, Graz University of Technology, Petersgasse 16, 8010 Graz, Austria
[‡]Department of Materials and Interfaces, Weizmann Institute of Science, Rehovoth 76100, Israel

Ⓢ *Supporting Information*

ABSTRACT: Tuning the transport properties of molecular junctions by chemically modifying the molecular structure is one of the key challenges for advancing the field of molecular electronics. In the present contribution, we investigate current−voltage characteristics of differently linked metal−molecule−metal systems that comprise either a single molecule or a molecular assembly. This is achieved by employing density functional theory in conjunction with a Green's function approach. We show that the conductance of a molecular system with a specific anchoring group is fundamentally different depending on whether a single molecule or a continuous monolayer forms the junction. This is a consequence of collective electrostatic effects that arise from dipolar elements contained in the monolayer and from interfacial charge rearrangements. As a consequence of these collective effects, the "ideal" choice for an anchoring group is clearly different for monolayer and single molecule devices. A particularly striking effect is observed for pyridine-docked systems. These are subject to Fermi-level pinning at high molecular packing densities, causing an abrupt increase of the junction current already at small voltages.
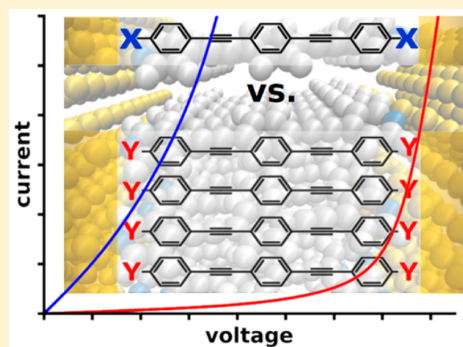
■ INTRODUCTION

Electronic devices in which individual molecules or a molecular assembly are used as semiconducting components constitute a promising approach for ultimate miniaturization.[1−3] One of the key challenges in realizing such "molecular electronics" is a microscopic understanding of charge transport through metal−molecule−metal systems. An efficient way of tuning the transport properties of molecular devices is exploiting the enormous versatility of organic chemistry that is mainly achieved by chemical substitutions within the molecular backbone[4] and via specific side groups. Another commonly used "molecular design" approach is to control charge transport in molecular junctions by changing the anchoring group linking the molecule and the metal.[5−7] This, on the one hand, offers the possibility to tune the properties of the individual molecules, i.e., the ionization potential (IP) and electron affinity (EA). After all, from a molecular perspective, the anchoring group acts as yet another electron donating or accepting substituent. On the other hand, when assembling molecules into an actual junction, the choice of the anchoring chemistry strongly affects the coupling strength between the metal and the electrodes, crucially impacting the chemical stability of the device as well as its charge transport properties.[8−32]

One of the first and to date most studied anchoring groups in gold-based junctions is thiol (−SH),[8−10] mostly because of the strong covalent S−Au bond and the efficient electronic coupling associated with it. The properties of thiolate-bonded

molecular junctions were, however, also shown to be quite sensitive to the binding geometry.[11] Furthermore, the S−Au bond seems to have some disadvantage compared to, e.g., the Se bond to coinage metals.[12] In fact, the structural details of the S−Au bond are strongly disputed in the literature,[13−15] suggesting that a coexistence of several different geometries might be especially relevant for thiol-Au bonded junctions causing a wide spread of experimentally measured conductances.[16−18] Thus, alternative anchoring groups have been studied extensively both theoretically and experimentally. These include, for example, pyridines[10,19−21], isocyanides (−NC),[7,22,23] cyanides (−CN),[5,10,22] the above-mentioned selenolates (−Se),[24,25] amines (−NH$_2$),[10,26−28] carboxyl-acids (−COOH),[26,29] and fullerenes (C$_{60}$).[30−32] These investigations showed that, depending on their donor and acceptor character, anchoring groups can have a profound impact on the level alignment,[9] i.e., the relative energetic position of the HOMO (highest occupied molecular orbital) and the LUMO (lowest unoccupied molecular orbital) with respect to the metal Fermi level. In the coherent transport regime, this determines the tunneling barrier for charge carriers and is thus of key importance in molecular electronics.[33,34] Chemical trends of conductance and junction stability were investigated by Hong et al.[10] for tolane molecules attached to gold via different

anchor groups. The conductance was found to decrease following the sequence SH > NH$_2$ > Pyr ≫ CN, while the junction formation probability followed the chemical trend Pyr > SH > NH$_2$ > CN. Interestingly, a recent combined theoretical and experimental study of porphyrin single molecule junctions[35] found a sequence in conductance that is different, namely, Pyr > NH$_2$ > SO$_3$ > CN > COOH. Note that these investigations focused on single molecule junctions, whereas a systematic study on docking dependent transport for full monolayer junctions is currently missing. One can, however, expect on rather general grounds that the collective behavior of surrounding molecules becomes important when going from a single molecule to a SAM.[36−48] Notably, it has recently been demonstrated that tuning the "electrostatic environment" allows for strong rectification in single-molecule junctions.[49] Furthermore, we have shown that intramolecular collective electrostatic effects are an important source of such "collectivity" in molecular junctions and that they can drastically affect the level alignment and with it important electrical characteristics.[50,51] As these electrostatic effects arise from the combined electric fields of neighboring molecules, they are especially relevant for differently linked junctions, since binding to the leads in virtually all cases involves the formation of a polar bond. Therefore, additional electric fields are generated by charge rearrangements due to metal−organic interactions. Additionally, the anchor groups themselves are often highly polar. As a consequence, collective electrostatic effects are present in virtually every multimolecular junction.

Here, we present an extensive theoretical analysis on how these additional fields caused by intramolecular polar bonds and the metal−molecule bonding impact the electronic and transport properties of molecular assemblies bonded to gold electrodes.[50,51] The focus is on the variations of collective electrostatics for commonly used anchoring groups, namely, thiol, methylthiol, isocyanide and pyridine. We will demonstrate that it is not only the "chemistry" of a specific anchoring group that determines the transport properties of molecular junctions, but also the local electrostatic environment of a molecule that plays a similarly decisive role. Most importantly, this can result in fundamentally different chemical trends in the transport properties of SAMs and single-molecule junctions, where it needs to be clarified to what extent they depend on the specific docking chemistry. This ultimately raises the question to what extent chemical design of only the molecular properties can control the characteristics of actual molecular junctions.

System Setup and Theoretical Methods. In our calculations, we study molecular junctions based on "Tour-wire"-type[52] molecules, i.e., 1,2-bis(2-phenylethynyl)benzene attached to gold electrodes via thiolate (−S), methylthiolate (−CH$_2$S), isocyanide (−NC), and pyridine (−Pyr) anchor groups (see Figure 1a). These molecules differ in the electron donating/accepting properties due to the different anchoring groups, which changes the associated local dipoles, as well as in the bonding mechanism with the gold leads.

For the corresponding metal−molecule−metal junctions, we consider different molecular packing densities Θ. These span the range between the two limiting cases represented by the (periodically repeated) unit cells shown in Figure 1b and c, where the latter models a single molecule and the former a densely packed monolayer: we use one molecule in a (2 × 2) Au(111) surface unit-cell to model the Θ = 1 case (i.e., a densely packed SAM), and reduce the packing density gradually by expanding the cell laterally and removing all except one
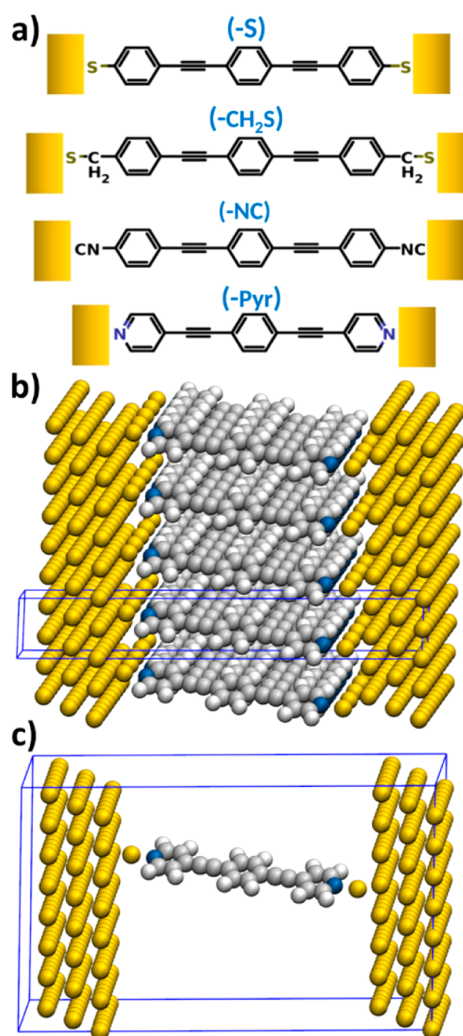
Figure 1. (a) Schematic representation of the chemical structure of the investigated molecules with thiolate (−S), mehtylthiolate (−CH$_2$S), isocyanide (−NC), and pyridine (−Pyr) anchoring groups, respectively; (b) structure of the densely packed (Θ = 1) (−Pyr$_{ad}$) junction and (c) the corresponding model system for the single-molecule situation (Θ = 1/16). The unit cells are indicated as blue boxes.

molecule. With this procedure, molecular packing densities of Θ = 1/2, 1/4, 1/8, and 1/16 are realized. The latter corresponds to a single molecule per 8 × 8 surface unit-cell of gold (for more details see Supporting Information). This we consider as the single-molecule junction limit, an assessment supported by the analysis of the changes in the electrostatic energy due to the bond formation discussed below. The metallic leads are represented by three layers of Au(111) on each side of the junction (i.e., six layers of Au separating periodic replicas of the molecules/monolayers). We optimized the structure of the SAM-based junctions (at full packing density, Θ = 1) including the innermost gold layers, and also relaxed the dimensions of the junction in the transport direction to allow for a more systematic structural setup. The geometry was not reoptimized at lower molecular packing densities, as the impact on the junction properties is expected to be minor and in this way we can also isolate the role of collective electrostatic effects. A detailed description of the
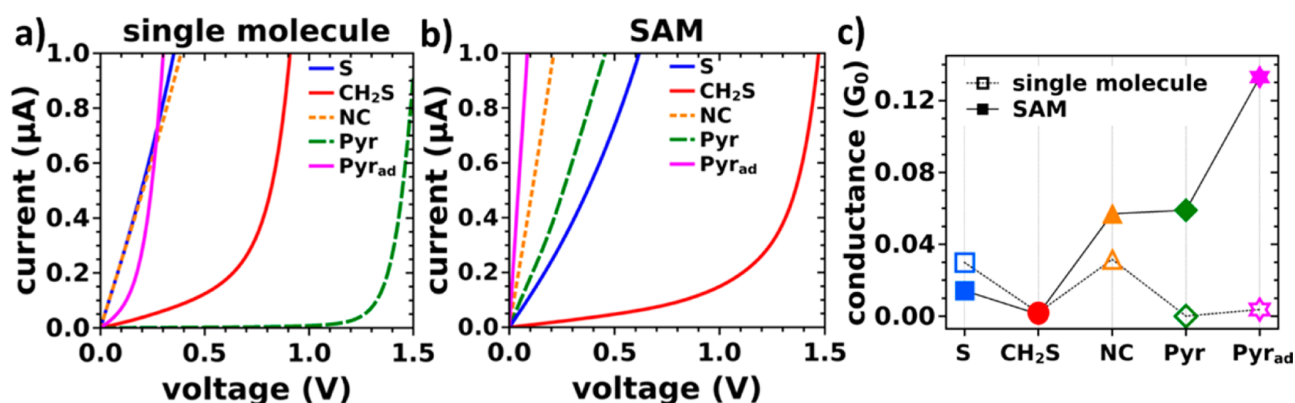
Figure 2. Calculated current–voltage characteristics of the (−S), (−CH$_2$S), (−NC), (−Pyr), and (−Pyr$_{ad}$) systems for (a) the model for a single molecule junction (i.e., a packing density of $\Theta = 1/16$) and (b) for a SAM with $\Theta = 1$; (c) corresponding zero-bias conductance $G(E_F) = T(E_F) \cdot G_0$ for single molecule junctions (open symbols) and full monolayer junctions (closed symbols). G_0 here refers to the quantum of conductance that corresponds to $2e^2/h$.

geometry-optimization process employed for such junctions can be found in the Supporting Information of ref 51.

For the thiolate anchoring group, the sulfur atom was found to be situated close to the fcc hollow site, while for the methylthiolate a docking position between fcc hollow and bridge was observed, in accordance with previous findings.[53] The optimization for the isocyanide anchoring group also led to a docking position between fcc hollow and bridge. In the case of the pyridine anchoring group we investigated two different adsorption geometries, because the pyridine linker is characterized by a double-peak conductance signature corresponding to two distinctly different binding geometries that are present predominantly in the junction.[21] The lower conductance feature corresponds to a vertical geometry, and the higher conductance value to a geometry where the molecule is significantly tilted and the electrode separation is smaller than the molecular length. Quek et al. further demonstrated that switching between these two conductance states can be achieved reversibly through repeated junction elongation and compression.[54] We modeled the vertical "low-conductance" pyridine structure (tilted by 5° relative to the surface normal and denoted as (−Pyr)) by a standard planar gold geometry, where after optimization the nitrogen atom is found in an on top position. A tilting of the pyridine docked molecule is energetically very costly for a flat Au surface; to overcome gold–hydrogen steric repulsion,[20] we studied a pyridine-docked molecule in the presence of an ad atom added to an fcc hollow site as a second structure. This results in a "high conductance" structure, tilted by 15° and denoted as (−Pyr$_{ad}$). Note that depending on the specific docking sites chosen for the electrodes and influenced also by the relative alignment of the electrodes in the experiment, of course other (higher) tilt angles are also conceivable, but the two geometries studied here already provide fundamental insight into the peculiarities of transport through pyridine docked systems (vide infra).

Geometry optimizations and electronic structure calculations were performed applying periodic boundary conditions within the framework of density functional theory (DFT) using the VASP[55] code. We employed the Perdew-Burke-Enzerhof PBE[56] exchange-correlation functional and a plane-wave basis set (cutoff: ca. 20 Ry). Geometries were optimized for the full packing density, $\Theta = 1$, by applying the conjugate gradient scheme[57] as implemented in VASP. Charge-transport calcu-

lations were done in a three-step procedure combining DFT and nonequilibrium surface Green's functions[58] to calculate I-V curves from (zero-bias) transmission functions in the Landauer-Büttiker formalism.[59,60] First, we used a locally modified version of the DFT based code SIESTA,[61] where we applied a double-ζ polarized orbital basis set (DZP) in conjunction with a "PAO.EnergyShift" of 0.001 Ry, for extracting the Hamilton and overlap matrix of a region comprising the molecule and three gold layers at each side (a detailed discussion of why for the present study this choice of the "PAO.EnergyShift" is crucial in conjunction with the standard DZP basis functions of SIESTA can be found in ref 51). Successively, using recursive Green's functions we computed the self-energies of the electrodes. Finally, we obtained the zero-bias transmission function $T(E)$ and used it to calculate the current–voltage characteristics $I(V)$ within the Landauer-Büttiker formalism as

$$I(V) = \frac{2e}{h} \int T(E)[f(E - \mu_{\text{left}}) - f(E - \mu_{\text{right}})] \, dE \tag{1}$$

Here, $f(x)$ is the Fermi–Dirac occupation function at 300 K and $\mu_{\text{left/right}} = E_F \pm (eV/2)$, with E_F the Fermi energy, e the elementary charge, and V the voltage. Further details regarding the implementation of this approach can be found in the Supporting Information of ref 51. The zero-bias conductance $G(E_F)$ also discussed in the following was calculated as $G(E_F) = T(E_F) \cdot G_0$, where $T(E_F)$ is the value of the zero-bias transmission function T at E_F, and $G_0 = (2e^2/h)$ is the quantum of conductance.

Bonding-induced charge rearrangements are defined as the difference between the charge density of the full metal–molecule–metal junction, ρ_{sys}, and the sum of densities of the isolated noninteracting subsystems, $\Delta\rho = \rho_{\text{sys}} - (\rho_{\text{mono}} + \rho_{\text{slab}})$. ρ_{slab} is the charge density of the electrodes and ρ_{mono} the charge density of the free-standing monolayer. In the thiolates the charge density of the H-layers also has to be included.[62,63] The changes in the electrostatic energies due to metal–molecule bonding are calculated as differences of the electrostatic energies of the individual systems obtained from the VASP calculations. XCrySDen,[64] VMD,[65] Mayavi2,[66] and Ovito[67] were used for graphical visualization.

■ RESULTS

Transport Characteristics of Single Molecule and Monolayer Junctions. The calculated current–voltage (I–V) characteristics for the differently linked molecular junctions are shown in Figure 2a for transport through single molecules (i.e., at $\Theta = 1/16$, vide supra).

Not surprisingly, we find significant differences in the current per molecule as a function of the docking chemistry. For the (−S) and (−NC) single molecule junctions, a pronounced increase of the current already at small bias voltages is observed. This indicates a strong hybridization of molecular states with states in the metal−electrode close to E_F resulting in good metal−molecule coupling. In contrast, for the (−CH$_2$S), (−Pyr), and (−Pyr$_{ad}$) single molecule junctions, a significant increase of the current is seen only for higher voltages. This is indicative of a weaker coupling between the (−CH$_2$S), (−Pyr), and (−Pyr$_{ad}$) molecules and the metal electrodes. Overall, we identify the following sequence for the current in the single-molecule junction in the studied geometry at small voltages of up to 0.25 V: S ≈ NC > Pyr$_{ad}$ > CH$_2$S ≫ Pyr.

The situation changes markedly at full packing density (see Figure 2b; current−voltage characteristics for intermediate situations are contained in the Supporting Information). While the (−CH$_2$S) SAM still exhibits a close to exponential (I−V) characteristic with the onset of significant current shifted to even higher voltages, in all other systems an abrupt rise of the current with voltage is observed. This means that the performance of different anchoring groups for the single molecule and the SAM situation is very different. This is most pronounced for the (−Pyr) system, where a slowly, roughly exponentially growing current in the single molecule junction is replaced by an immediately increasing one in the respective SAM device. Hence, the ideal anchoring group for obtaining a large current per molecule is different in the case of the SAM-junctions, where we obtain the following sequence (see Figure 2b): Pyr$_{ad}$ > NC > Pyr > S ≫ CH$_2$S.

As can be seen from Figure 2c, these trends are also reflected in the zero-bias conductance $G(E_F)$ (see also the enlarged image of the small bias region of Figure 2a contained in the Supporting Information). Notably, for the isocyanide (−NC) and both pyridine linked junctions, the zero-bias conductance per molecule is strongly increased when going from the single molecule to the SAM, while for the junction based on the thiolate anchoring group (−S) we find a decrease of $G(E_F)$. For the methylthiolate-based system (−CH$_2$S) the change in conductance between single molecule and SAM device is comparably small (increase from 0.001 G_0 at $\Theta = 1$ to 0.002 G_0 at $\Theta = 1/16$).

These results show that it depends on the molecular packing density which anchoring group yields the highest conductance.

Evolution of Transmission Functions with Molecular Packing Density. Current−voltage characteristics are related to transmission functions via the Landauer-Büttiker formula (cf. eq 1). Therefore, the above-discussed trends can be directly traced back to the respective transmission functions. They offer an initial handle to better understand the results presented above and are shown in Figure 3 for all investigated systems as a function of the molecular packing density Θ. Solid, darkly shaded curves correspond to the SAM situation, $\Theta = 1$, and dotted, lightly shaded curves to the respective single molecule case, $\Theta = 1/16$. Gray lines represent packing densities in between, namely, $\Theta = 1/2$, $\Theta = 1/4$, and $\Theta = 1/8$. They are
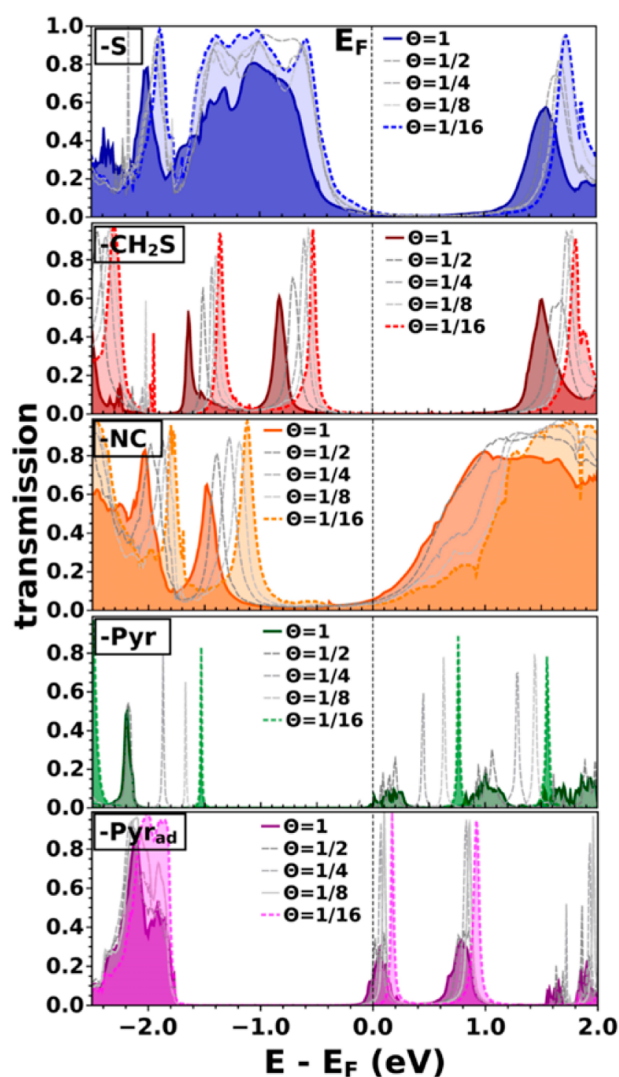
Figure 3. Calculated (zero-bias) transmission functions of the (−S), (−CH$_2$S), (−NC), (−Pyr), and (−Pyr$_{ad}$) systems at different packing densities Θ ($\Theta = 1$ (SAM): darkly shaded, solid lines. $\Theta = 1/16$ (single molecule): lightly shaded, dotted lines. The Fermi level E_F is used as the energy reference.

included here to better visualize the typically rather smooth packing density-dependent evolution of the electronic structure of the junctions.

The following discussion first concentrates on the single molecule situation: When comparing the transmission functions of the differently linked systems we find two important differences. First, the energetic positions of the transmissive states with respect to the metal Femi level E_F drastically change when changing the anchoring group. Electron-donating linker groups, i.e., thiolate and methylthiolate, lift the frontier orbital energies, bringing the HOMO closer to E_F. Therefore, for (−CH$_2$S) and (−S) we find a pronounced p-type current with holes as the dominant charge carriers. Electron-withdrawing anchoring groups such as (−NC) and (−Pyr) push the frontier orbital energies down with respect to E_F, thus reducing the difference between the LUMO and E_F, thereby promoting an n-type current. The second apparent difference when comparing the differently docked systems is
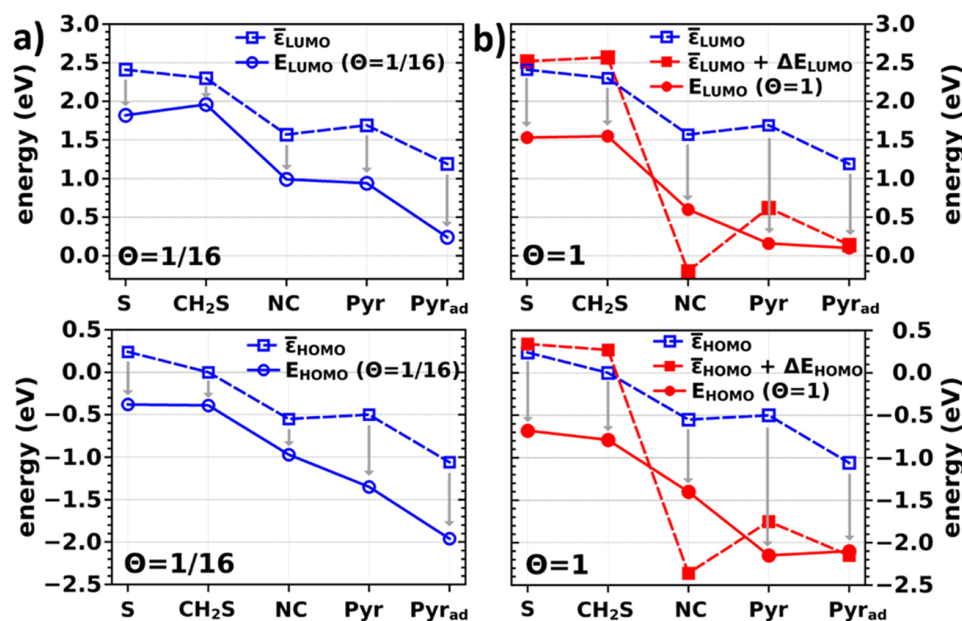
Figure 4. (a) Energies of the molecular frontier orbitals, $\overline{\varepsilon}_{HOMO}$ (top) and $\overline{\varepsilon}_{LUMO}$ (bottom), of the isolated molecule corrected by the work-function of the electrodes (see text for details) and level alignment in the single molecule junction, E_{HOMO} ($\Theta = 1/16$) and E_{LUMO} (Θ 1/16) as a function of the anchoring group used. Note that for Pyr_{ad} the work function of the Au substrate including the adatoms has been considered. (b) $\overline{\varepsilon}_{HOMO}$ (top) and $\overline{\varepsilon}_{LUMO}$ (bottom), of the isolated molecule compared to the situation in the hypothetical free-standing monolayer; $\overline{\varepsilon}_{HOMO} + \Delta E_{HOMO}$ (top) and $\overline{\varepsilon}_{LUMO} + \Delta E_{LUMO}$ (bottom) and level alignment in the monolayer junction, E_{HOMO} ($\Theta = 1$)/E_{LUMO} ($\Theta = 1$) for all studied anchoring groups.

the width of the transmissive features. For the ($-$S) and the ($-$NC) system we find particularly broad and highly transmissive π-HOMO and π-LUMO-derived states. The pronounced broadening of these states is also seen in the density of states, which means that it is characteristic of the electronic structure of this molecule–metal interface and can be associated with a pronounced molecule–metal hybridization. Indeed, the width of the transmission states is a measure of the molecule–metal coupling strength,[1,68] which together with the small tunneling barrier explains the pronounced current for the ($-$S) and ($-$NC) systems. These results indicate that ($-$NC) and ($-$S) terminated molecules are especially promising for highly conductive single-molecule junctions. When introducing a methyl group between the thiolate and the conjugated backbone, the coupling between the extended states in the metal and the transmissive π-orbitals of the molecule is significantly reduced, resulting in a narrowing of the HOMO-related $T(E)$ peak in ($-$CH$_2$S). Correspondingly, the current per molecule also decreases for the ($-$CH$_2$S) anchoring group compared to ($-$S), cf. Figure 2a. This finding is in agreement with several single molecule transport measurements,[69−72] where methyl spacers were shown to reduce the conductance by several orders of magnitude.[69] Similarly, Danilov et al.[71] suggested a change of the transport mechanism from strong coupling with coherent tunneling for ($-$S) to weak coupling with sequential tunneling and Coulomb blockade behavior for ($-$CH$_2$S) due to the insertion of the CH$_2$ spacer.

Compared to the systems discussed so far, ($-$Pyr) shows extraordinarily narrow HOMO and LUMO derived peaks at Θ = 1/16 that are both >1 eV away from E_F. This explains the strongly reduced current for the ($-$Pyr) single molecule junction, a finding that is again in agreement with the literature, as this pyridine configuration reflects the low conductance situation, where the molecule is vertically arranged between the two electrodes.[21,54,73] When introducing an adatom in the

junction geometry ($-$Pyr$_{ad}$) the molecule tilts and the overlap between the Au s-states and the molecular π-system is increased[54] resulting in a somewhat increased lead to molecule coupling. Moreover, the transmissive states in the single-molecule situation (Figure 3) are shifted toward the Fermi level compared to the ($-$Pyr) system, which is also reflected in an increased current (see Figure 2a).

When we increase the packing density from the single molecule limit to the densely packed SAM, ($\Theta = 1$; darkly shaded, solid lines in Figure 3), the relevant transmission features strongly shift to lower energies for all investigated systems. The exact amount of this energy shift depends on the system, and its origin will be explained in detail below. The broadening of $T(E)$ hardly changes in the case of ($-$S), ($-$CH$_2$S), and ($-$NC) junctions when increasing the packing density. For the ($-$Pyr) and ($-$Pyr$_{ad}$) systems, however, the very sharp features observed at the single molecule level broaden significantly in the SAM structure. This indicates that the metal−molecule coupling is qualitatively different for the single molecule and densely packed layer scenario of the pyridine-docked systems. The broadening concurs with the downward-shift of the LUMO-derived feature in $T(E)$ until it aligns with the Fermi level; for ($-$Pyr$_{ad}$) the Fermi energy even cuts through the corresponding transmission peak. This is a manifestation of Fermi-level pinning,[74−76] which due to the vanishing electron-injection barrier gives rise to the steep and immediate increase of the current observed for the pyridine linked SAM junctions (see Figure 2b). The origin of this Fermi-level pinning situation will be explained in detail below.

Relation between Level Alignment in the Junction and the Properties of the Individual Molecules. To understand the shifts of the transmission functions when changing anchoring groups and molecular packing densities, it is useful to perform an in-depth analysis of the location of the electronic states in the molecular systems relative to the states

Table 1. Interface Energetics[a]

	ΔE_{HOMO}	ΔE_{LUMO}	ΔE_{BD}	E_{corr}^{HOMO}	E_{corr}^{LUMO}	E_{HOMO}	E_{LUMO}
			$\Theta = 1$				
−S	0.10	0.10	−1.03	0.01	0.05	−0.68	1.53
−CH₂S	0.27	0.27	−1.04	−0.02	0.02	−0.79	1.55
−NC	−1.81	−1.77	1.00	−0.04	−0.20[b]	−1.40	0.60
−Pyr	−1.07	−1.07	−0.29	−0.11	−0.17	−2.15	0.16
−Pyr$_{ad}$	−1.09	−1.05	0.37	−0.32	−0.41	−2.10	0.10
			$\Theta = 1/16$				
−S	0.00	0.00	−0.24	−0.38	−0.35	−0.38	1.82
−CH₂S	0.00	0.00	−0.19	−0.20	−0.15	−0.39	1.96
−NC	0.00	0.00	−0.14	−0.28	−0.44	−0.97	0.99
−Pyr	0.00	0.00	−0.19	−0.48	−0.56	−1.35	0.94
−Pyr$_{ad}$	0.00	0.00	−0.51	−0.39	−0.44	−1.96	0.24

[a]Quantities characterizing the energetic shift of the electronic states between single molecules and molecules as part of a monolayer junction (cf., eqs 3a and 3b) for (−S), (−CH₂S), (−NC), (−Pyr), and (−Pyr$_{ad}$) junctions at full packing density, $\Theta = 1$, and at the single molecule limit, $\Theta = 1/16$. ΔE_{HOMO} and ΔE_{LUMO} are the energetic shifts of the centers of the HOMO- and LUMO-derived bands due to the formation of a free-standing monolayer. ΔE_{BD} is the bond dipole upon junction formation; E_{corr}^{HOMO} and E_{corr}^{LUMO} are correction energies, and E_{HOMO} and E_{LUMO} are the energetic positions of the peaks of the π-HOMO and π-LUMO derived bands relative to the Fermi level in the complete junctions. All quantities are given in eV. The values for the molecule-derived quantities ε_{HOMO} and ε_{LUMO} and the corresponding energies realigned relative to the Fermi level of the electrodes $\overline{\varepsilon}_{Homo}$ and $\overline{\varepsilon}_{LUMO}$ can be found in the Supporting Information. [b]Note that this value has a significant uncertainty as it is difficult to determine because the frontier unoccupied states are spread over a wide energy range (see also ref 62).

in the electrodes. The level alignment in the junction is given by the energetic positions of the peaks of the π-HOMO and π-LUMO (respectively, the corresponding bands in the SAM) relative to the Fermi level. These quantities are denoted as E_{HOMO} and E_{LUMO}. They are obtained from the densities of states projected onto the molecular region (including a Gaussian broadening). Their determination becomes somewhat ill-defined in strongly hybridized cases such as the (−S) HOMO and (−NC) LUMO.[62] In a first approximation, we can attempt to understand the dependence of E_{HOMO} and E_{LUMO} on the molecular packing densities from three properties: (i) the energies of the frontier π-orbitals of the molecules in the gas phase (ε_{HOMO} and ε_{LUMO}), (ii) the work function of the clean Au(111) electrode (Φ), and (iii) the change in the energies of the molecular states due to intermolecular and molecule−metal interactions. The latter is denoted as $\delta E_{HOMO}(\Theta)$ and $\delta E_{LUMO}(\Theta)$ for the HOMO- and LUMO-derived states, respectively. This yields the following equations for the Θ-dependent energy level alignment in the junction, $E_{HOMO}(\Theta)$ and $E_{LUMO}(\Theta)$:

$$E_{HOMO}(\Theta) = \varepsilon_{HOMO} + \Phi + \delta E_{HOMO}(\theta)$$
$$= \overline{\varepsilon}_{HOMO} + \delta E_{HOMO}(\theta) \tag{2a}$$

$$E_{LUMO}(\Theta) = \varepsilon_{LUMO} + \Phi + \delta E_{LUMO}(\theta)$$
$$= \overline{\varepsilon}_{LUMO} + \delta E_{LUMO}(\theta) \tag{2b}$$

In passing, we note that including the work function of the electrodes in this analysis is necessary, as the relevant energy reference in the junction is the Fermi energy determined by the leads, while molecular orbitals are typically given relative to the vacuum level. The "realigned" quantities are denoted as $\overline{\varepsilon}_{HOMO}$ and $\overline{\varepsilon}_{LUMO}$. $\overline{\varepsilon}_{HOMO}$, $\overline{\varepsilon}_{LUMO}$, and $E_{HOMO}(\Theta)$ and $E_{LUMO}(\Theta)$ are plotted in Figure 4 for the various molecules at full and lowest packing densities. At this point it should be mentioned that the values reported in Figure 4 have been derived from our DFT results, i.e., they include all effects that arise from the molecular packing density up to the level of the employed PBE functional (in particular, collective electrostatic effects in the focus of the

present paper). Renormalization occurring within the molecular films and molecule−metal renormalization effects are, however, not accounted for in our (semi)local DFT calculations.[77]

When comparing the dotted and solid blue lines in Figure 4a, we find a reasonably close correlation between the properties that can be inferred from the isolated molecules alone, i.e., $\overline{\varepsilon}_{HOMO}$ and $\overline{\varepsilon}_{LUMO}$, and the level alignment in the complete single molecule junction, $E_{HOMO}(\Theta = 1/16)$ and $E_{LUMO}(\Theta = 1/16)$ display a similar relative evolution. Thus, variations in the energetic positions of the transmission maxima can primarily be regarded as a consequence of a change in the molecular properties due to the chemical substitution with docking moieties. Still, it should be kept in mind that the bonding to the metal, which within our approximate framework for the single-molecule case is the only reason for finite values of $\delta E_{HOMO}(\Theta = 1/16)$ and $\delta E_{LUMO}(\Theta = 1/16)$ (cf., gray arrows), shifts the unoccupied states toward E_F and the occupied ones away from it. This has immediate consequences for the transport and is intertwined with its polarity, as will be discussed below.

To better understand the SAM situation ($\Theta = 1$), it is useful to employ a Gedanken experiment often used for analyzing the properties of self-assembled monolayers,[62,63] namely, splitting the transition from the isolated molecule to the densely packed SAM into two steps: the formation of a hypothetical free-standing monolayer followed by the bonding of that monolayer to the substrate (where the latter in the case of thiolates also means eliminating the H atoms of the anchoring group). Consequently, $\delta E_{HOMO}(\Theta)$ and $\delta E_{LUMO}(\Theta)$ can be partitioned into

$$\delta E_{HOMO}(\Theta) = \Delta E_{HOMO}(\Theta) + \Delta E_{BD}(\Theta) + E_{corr}^{HOMO}(\Theta) \tag{3a}$$

$$\delta E_{LUMO}(\Theta) = \Delta E_{LUMO}(\Theta) + \Delta E_{BD}(\Theta) + E_{corr}^{LUMO}(\Theta) \tag{3b}$$

In this way, the energetic shifts of the states upon advancing from the isolated molecule to the monolayer bonded to two electrodes are viewed as a combination of (i) an energetic shift of the centers of the HOMO- and LUMO-derived bands due to the formation of a free-standing monolayer at a certain
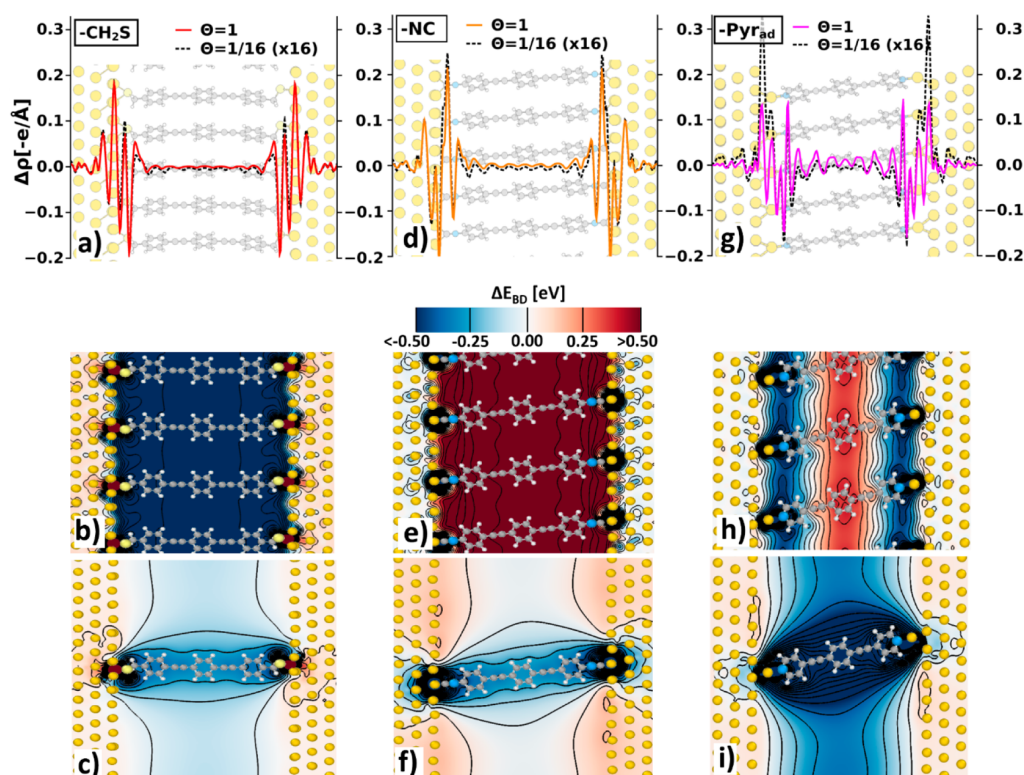
Figure 5. (a,d,g) (x,y)-integrated charge rearrangements per molecule, $\Delta\rho$, along transport direction at full ($\Theta = 1$, solid lines) and lowest ($\Theta = 1/16$, dashed, black lines) packing density for ($-CH_2S$), ($-NC$), and ($-Pyr_{ad}$); (b,e,h) contour plot of the change in the electrostatic energy in the plane of the molecule due to metal−molecule bonding, ΔE_{BD}, at full packing density, $\Theta = 1$, for ($-CH_2S$), ($-NC$), and ($-Pyr_{ad}$); (c,f,i) equivalent plots at the lowest considered packing density, $\Theta = 1/16$. Isolines are drawn every 0.1 eV in the range from -2 eV to 2 eV.

molecular packing density Θ ($\Delta E_{HOMO}(\Theta)$ and $\Delta E_{LUMO}(\Theta)$); (ii) the modification of the energy landscape resulting from the charge rearrangements due to the bond formation between the molecules and the electrodes expressed as the bond-dipole, $\Delta E_{BD}(\Theta)$; (iii) correction energies E_{corr}^{HOMO} and E_{corr}^{LUMO}, quantifying the change of the energy of the electronic eigenstates due to the charge rearrangements and resulting electrical fields. Effects (i) and (ii) are effectively largely electrostatic, while (iii) is a quantum-mechanical effect, which is typically small in densely packed systems due to the confinement of the energy gradients to the immediate interface region.[62] The latter is observed also here (cf., Table 1) with the exception of ($-Pyr_{ad}$), which is an expected consequence of Fermi-level pinning (vide infra).

The results of the two-step Gedanken experiment are illustrated in Figure 4b and the relevant energies are summarized in Table 1. They shall be discussed in the following for the ($-CH_2S$), ($-S$), and ($-NC$) junctions. For pyridine-linked molecular junctions, the underlying physics changes drastically. Thus, they will be explained separately. The origin of ΔE_{HOMO} and ΔE_{LUMO} are collective electrostatic effects that arise from the superposition of the fields generated by the polar anchoring groups at both ends of the free-standing molecular assemblies. They change the electrostatic energy and with it the energies of the frontier orbitals within the free-standing monolayer with the magnitude of the effect proportional to the dipole density.[13] By definition, $\Delta E_{HOMO}(\Theta)$ and $\Delta E_{LUMO}(\Theta)$ vanish in the case of isolated molecules. As can be seen from Table 1, thiolate ($-S$) and methylthiolate ($-CH_2S$) linked molecules show an upward shift of the states in the

monolayer compared to the isolated molecule, whereas for isocyanide ($-NC$) and pyridine, downward shifts of up to 1.8 eV are observed. This can also be retraced in Figure 4b, where we find pronounced differences in energy when comparing the blue open squares (isolated molecules) with the red filled ones (free-standing SAMs). As a consequence, we find no correlation between the molecular and monolayer properties. The particularly large shifts for isocyanide and pyridine are mostly attributed to a vertical alignment of the dipoles in these anchoring groups compared to a more tilted orientation of thiol and methylthiol dipoles.

The bonding-induced shift of the energy landscape (contribution (ii)) is a consequence of charge-rearrangements, $\Delta\rho$, either due to the formation of bonds between the anchoring groups and the metal surface (in the case of pyridines and isocyanides) or due to a replacement of S−H by S−Au bonds (in the case of the thiolates[78]). The magnitude of the total step in the electrostatic energy due to the metal−molecule bond is typically referred to as "bond dipole", ($\Delta E_{BD}(\Theta)$), and especially at high packing densities depends on the chemical nature of the anchoring group.[62] The spatially resolved change in the electrostatic energy due to the charge rearrangements are shown in Figure 5 for several examples. In the case of ($-CH_2S$) and ($-NC$) (as well as in the thiolate case not shown here), $\Delta\rho$ for the isolated molecule and SAM situation is well localized at the metal−molecule interface (see Figure 5a and d). Here, one essentially deals with a succession of charge depletions and accumulations rather than with a single dipole.[62]

At full packing density this behavior of $\Delta\rho$ results in a rigid and abrupt shift of the electrostatic energy at the immediate metal−SAM interface and in an essentially flat energy surface in between as shown in Figure 5b and e. The abruptness of that energetic jump is, on one hand, due to the localization of the charge rearrangements (vide supra) and, on the other hand, a consequence of collective electrostatics: the decay length of the electric field of a regular 2D arrangement of dipoles is nearly an order of magnitude smaller than the interdipole distance.[42] As can be inferred from Figure 5b and e, in the case of (−CH$_2$S) the bond dipole shifts the orbitals down in energy, while it shifts them up for (−NC). These observations can also be retraced in Table 1, where ΔE_{BD} is listed as the shift of the electrostatic energy in the middle of the junction (see Supporting Information for a graphical illustration).

As ΔE_{HOMO} and ΔE_{LUMO} are small for (−S) and (−CH$_2$S), in these systems ΔE_{BD} dominates the level alignment in the junction at $\Theta = 1$. Conversely, for (−NC) we find a strong shift to negative energies due to collective effects within the free-standing monolayer (vide supra) that is partially compensated by a strong positive shift by the bond dipole. The latter is primarily a consequence of the electron-density depletion in the top metal layer and the electron accumulation at the C atoms resulting in a dipole layer opposing the − NC dipoles. The details of the charge rearrangements can be understood from the specifics of the bond formation between the − NC groups and the Au substrate, explained in detail in the Supporting Information. Overall, the particularly strong dipole of the − NC group, on one hand, triggers a particularly large ΔE_{HOMO} and ΔE_{LUMO}, but, on the other hand, also causes a very strong compensating ΔE_{BD}. As a consequence, the fairly good correlation of the relative trends of $\bar{\varepsilon}_{HOMO}$ and ΔE_{HOMO}, respectively, $\bar{\varepsilon}_{LUMO}$ and ΔE_{LUMO} is recovered in Figure 4b (comparing open blue rectangles and full red circles). The shift between the two evolutions caused by the collective electrostatic effects is, however, much larger than in the case of the single-molecule junctions.

Discussing the single-molecule junction limit (i.e., $\Theta = 1/16$) in the framework of the above Gedanken experiment provides us with certain additional insights, but also has its limitations, as will become evident below. The shape of the plane-integrated charge rearrangements remains similar but the magnitude changes (Figure 5a and d). These charge-rearrangements are localized in the vicinity of the anchoring groups. As the density of those groups is much lower at the interface, the modifications of the electrostatic energy in the single molecule case (Figure 5c and f) are fundamentally different from those in the SAMs (Figure 5b and e).[31] Most importantly, no abrupt energetic jumps in the regions of the interfaces occur that would result in a massive and rigid shift of the molecular states. As a consequence, the values of ΔE_{BD} remain small (see Table 1). In contrast to the full coverage case, where the sign of the change in electrostatic energy depends on the anchoring group, for the single-molecule limit it is always negative. The more extended variations of the electrostatic energy in the direction perpendicular to the metal surface result in a quite significant modification of the molecular eigenstates. This results in the correction energies becoming rather large, i.e., in the range of 0.3−0.4 eV (see Table 1), which hints towards severe limitations of describing bonding-induced effects in terms of only the bond-dipole for a highly dilute monolayer.

Fermi Level Pinning. For the pyridine docked molecular junctions (−Pyr) and (−Pyr$_{ad}$) a different behavior is observed.

This is a consequence of Fermi-level pinning,[74−76] which occurs here especially at full packing density. Phenomenologically, one can consider a system in the regime of Fermi-level pinning when in the combined electrode−molecule (SAM)−electrode system the Fermi level cuts through a peak in the density of states that is associated either with the HOMO- or, in the present case, LUMO-derived bands. As a consequence, the corresponding peak of the DOS is very close to E_F, as shown for the pyridine-docked SAMs by the red circles in Figure 4b. Whether such a situation occurs in a SAM depends on (i) molecular properties (here the electron affinity approximated by the position of the LUMO realigned to account for the metal work-function, i.e., $\bar{\varepsilon}_{LUMO}$), (ii) the shift of the molecular bands due to the formation of the (free-standing) monolayer, and (iii) the bond-dipole caused by the formation of the chemical bond between the anchoring group and the metal electrodes. Notably, (ii) and (iii) differ between isolated molecules and SAMs due to the collective electrostatic effects discussed above.

In the case where considering all these effects the LUMO-derived bands would come to lie below E_F, additional charge rearrangements are triggered to re-establish thermodynamic equilibrium. These are no longer confined to the immediate interface region, but extend onto the molecular backbone as shown in Figure 5g for (−Pyr$_{ad}$) (this also occurs in the case of (−Pyr) not shown here). Interestingly, the extended charge rearrangements are mostly not associated with charge transfer between the metal and the molecular π-system, as usually observed for flat-lying adsorbates in the case of Fermi-level pinning.[74,79,80] Rather, they correspond to a (local) polarization of the molecules[75] (see plots of the net charge transfer in the Supporting Information). For the resulting changes in the electrostatic energy at $\Theta = 1$ (see Figure 5h), one observes an abrupt jump to negative values directly at the interface between the metal and the molecule, as in the thiolates. Deeper into the layer the extended charge rearrangements, however, cause a significant energy gradient, yielding a large positive change of the electrostatic energy in the center of the (−Pyr$_{ad}$) SAM. As a consequence, the concept of a single bond-dipole describing a rigid shift of the overall energy landscape upon bonding cannot be applied here. Thus, the values of ΔE_{BD} in Table 1, calculated as shifts of the plane-averaged electrostatic energy in the middle of the junction, are no longer particularly meaningful. The differences in the level alignment between (−Pyr) and (−Pyr$_{ad}$) stem from the reduced work-function of the Au-surface covered with Au adatoms (4.71 eV compared to the 5.18 eV for flat Au(111)) and the differences in chemical bonding mentioned in the description of the system setup.[54] This triggers Fermi-level pinning already at relatively low packing densities in the presence of adatoms (see Figure 3); in fact (−Pyr$_{ad}$) even at ($\Theta = 1/16$) can be considered to be at the onset of Fermi-level pinning. This is confirmed by the more massive interfacial charge rearrangements in that system compared to (−Pyr). It also results in the comparably steep rise of the current for bias voltages above 0.2 eV (see Figure 2a).

■ DISCUSSION

With all ingredients in hand, we can now reconsider the relation between chemical trends due to different anchoring groups, their impact on level alignment, and the actual transport properties. As discussed above, for the single molecule junctions the molecular trends induced by the substitution with electron withdrawing, respectively, donating

anchoring groups essentially prevail. This is a consequence of the comparably small energetic shifts due to the metal−molecule bonding. They are caused by comparably weak energy shifts in the molecular region in conjunction with the resulting changes in the molecular eigenstates (E_{corr}), which are always negative. The situation changes dramatically in the densely packed monolayer, where collective electrostatic effects come into play that significantly shift the states in the monolayers. Interestingly, the shifts of the electrostatic energy caused by (i) the monolayer formation and (ii) the metal−SAM bonding add up such that the net effect is a strong shift of the states in all SAMs to lower energy compared to E_F. This shift is of roughly comparable magnitude and, most importantly, in all cases significantly larger than the shift for the single-molecule junction.

As a consequence, when comparing single-molecule and SAM junctions, the (zero-bias) transmission functions in the latter case are always shifted to smaller energies compared to E_F. Whether this then results in a decrease or an increase of the current per molecule depends on whether the transmissive channels at low bias arise from occupied or unoccupied states, i.e., whether hole or electron currents dominate. Consequently, the current per molecule decreases for the SAM case in (−S) and (−CH$_2$S), as there the increase of the barrier for holes is the relevant effect. Conversely, in (−NC) and both pyridine linked junctions, the decreased barrier for electrons at $\Theta = 1$ results in an increase of the current per molecule. As a second effect, the coupling and hybridization at the metal−molecule interface obtained from the widths of the transmission peaks significantly influences the current, where strongly coupled junctions like (−S) and (−NC) are advantageous.

CONCLUSIONS

In conclusion, the relative energetic trends obtained for the orbital energies of the studied molecules with various anchoring groups by and large translate into trends in the level alignment of single-molecule as well as SAM-junction cases. A direct estimation of the junction properties solely on the basis of the molecular properties, however, remains difficult, if not impossible. This is a consequence of collective electrostatic effects that trigger a massive overall shift between the orbital energies in the single molecule and the SAM case. This yields an enormous increase or decrease of the junction current depending on the type of majority carriers. For pyridine-linked junctions the situation is further complicated by Fermi Level Pinning, which changes the metal−molecule bonding and the resulting energetic shifts especially at high packing densities. Thus, in such junctions a particularly steep increase of the current with rising bias voltage is observed, an effect that can be of particular interest for certain molecular electronics applications.

ASSOCIATED CONTENT

Ⓢ Supporting Information

The Supporting Information is available free of charge on the ACS Publications website at DOI: 10.1021/acs.jpcc.5b06110.

> Details on the variation of molecular packing densities, $(I–V)$ − characteristics and transmission functions for all packing densities, packing dependent peak positions of HOMO- and LUMO-derived bands (obtained from PDOS) for all investigated systems, cumulative charge transfer and bond dipole for all anchoring groups, the

values for the molecule-derived quantities $\overline{\varepsilon}_{HOMO}$ and $\overline{\varepsilon}_{LUMO}$, and a detailed description of the bond formation between (−NC) and Au substrate (PDF)

AUTHOR INFORMATION

Corresponding Author
*E-mail: egbert.zojer@tugraz.at.

Notes
The authors declare no competing financial interest.

REFERENCES

(1) Cuevas, J. C.; Scheer, E. *Molecular Electronics−An Introduction to Theory and Experiment*; World Scientific Publishing: Singapore, 2010.

(2) Song, H.; Reed, M. A.; Lee, T. Single Molecule Electronic Devices. *Adv. Mater.* **2011**, *23*, 1583−1608.

(3) McCreery, R. L.; Yan, H.; Bergren, A. J. A Critical Perspective on Molecular Electronic Junctions: There Is Plenty of Room in the Middle. *Phys. Chem. Chem. Phys.* **2013**, *15*, 1065−1081.

(4) Venkataraman, L.; Park, Y. S.; Whalley, A. C.; Nuckolls, C.; Hybertsen, M. S.; Steigerwald, M. L. Electronics and Chemistry: Varying Single-Molecule Junction Conductance using Chemical Substituents. *Nano Lett.* **2007**, *7*, 502−506.

(5) Lörtscher, E.; Cho, C. J.; Mayor, M.; Tschudy, M.; Rettner, C.; Riel, H. Influence of the Anchor Group on Charge Transport through Single-Molecule Junctions. *ChemPhysChem* **2011**, *12*, 1677−1682.

(6) Hihath, J.; Tao, N. The Role of Molecule−Electrode Contact in Single-Molecule Electronics. *Semicond. Sci. Technol.* **2014**, *29*, 054007.

(7) Leary, E.; La Rosa, A.; González, M. T.; Rubio-Bollinger, G.; Agraït, N.; Martin, N. Incorporating Single Molecules into Electrical Circuits. The Role of the Chemical Anchoring Group. *Chem. Soc. Rev.* **2015**, *44*, 920−942.

(8) Ulman, A. Formation and Structure of Self-Assembled Monolayers. *Chem. Rev.* **1996**, *96*, 1533−1554.

(9) Zotti, L. A.; Kirchner, T.; Cuevas, J. C.; Pauly, F.; Huhn, T.; Scheer, E.; Erbe, A. Revealing the Role of Anchoring Groups in the Electrical Conduction Through Single-Molecule Junctions. *Small* **2010**, *6*, 1529−1535.

(10) Hong, W.; Manrique, D. Z.; Moreno-Garcia, P.; Gulcur, M.; Mishchenko, A.; Lambert, C. J.; Bryce, M. R.; Wandlowski, T. Single Molecular Conductance of Tolanes: Experimental and Theoretical Study on the Junction Evolution dependent on the Anchoring Group. *J. Am. Chem. Soc.* **2012**, *134*, 2292−2304.

(11) Lee, M. H.; Speyer, G.; Sankey, O. F. Electron Transport through Single Alkane Molecules with Different Contact Geometries on Gold. *Phys. Status Solidi B* **2006**, *243*, 2021−2029.

(12) Shaporenko, A.; Cyganik, P.; Buck, M.; Terfort, A.; Zharnikov, M. Self-Assembled Monolayers of Aromatic Selenolates on Noble Metal Substrates. *J. Phys. Chem. B* **2005**, *109*, 13630−13638.

(13) Heimel, G.; Rissner, F.; Zojer, E. Modeling the Electronic Properties of π-Conjugated Self-Assembled Monolayers. *Adv. Mater.* **2010**, *22*, 2494−2513.

(14) Vericat, C.; Vela, M. E.; Benitez, G.; Carro, P.; Salvarezza, R. C. Self-Assembled Monolayers of Thiols and Dithiols on Gold: New

Challenges for a Well-Known System. *Chem. Soc. Rev.* **2010**, *39*, 1805−1834.

(15) Häkkinen, H. The Gold-Sulfur Interface at the Nanoscale. *Nat. Chem.* **2012**, *4*, 443−455.

(16) Ulrich, J.; Esrail, D.; Pontius, W.; Venkataraman, L.; Millar, D.; Doerrer, L. H. Variability of Conductance in Molecular Junctions. *J. Phys. Chem. B* **2006**, *110*, 2462−2466.

(17) Müller, K. H. Effect of the Atomic Configuration of Gold Electrodes on the Electrical Conduction of Alkanedithiol Molecules. *Phys. Rev. B: Condens. Matter Mater. Phys.* **2006**, *73*, 045403.

(18) Li, C.; Pobelov, I.; Wandlowski, T.; Bagrets, A.; Arnold, A.; Evers, F. Charge Transport in Single Au| Alkanedithiol| Au Junctions: Coordination Geometries and Conformational Degrees of Freedom. *J. Am. Chem. Soc.* **2008**, *130*, 318−326.

(19) Xu, B.; Xiao, X.; Tao, N. J. Measurements of Single-Molecule Electromechanical Properties. *J. Am. Chem. Soc.* **2003**, *125*, 16164−16165.

(20) Pérez-Jiménez, Á. J. Uncovering Transport Properties of 4, 4′-Bipyridine/Gold Molecular Nanobridges. *J. Phys. Chem. B* **2005**, *109*, 10052−10060.

(21) Kamenetska, M.; Quek, S. Y.; Whalley, A. C.; Steigerwald, M. L.; Choi, H. J.; Louie, S. G.; Nuckolls, C.; Hybertsen, M. S.; Neaton, J.; Venkataraman, L. *Conductance and Geometry of Pyridine-Linked Single-Molecule Junctions. J. Am. Chem. Soc.* **2010**, *132*, 6817−6821.

(22) Lang, N. D.; Kagan, C. R. The Role of Chemical Contacts in Molecular Conductance. *Nano Lett.* **2006**, *6*, 2955−2958.

(23) Koga, J.; Tsuji, Y.; Yoshizawa, K. Orbital Control of Single-Molecule Conductance Perturbed by π-Accepting Anchor Groups: Cyanide and Isocyanide. *J. Phys. Chem. C* **2012**, *116*, 20607−20616.

(24) Patrone, L.; Palacin, S.; Charlier, J.; Armand, F.; Bourgoin, J. P.; Tang, H.; Gauthier, S. Evidence of the Key Role of Metal-Molecule Bonding in Metal-Molecule-Metal Transport Experiments. *Phys. Rev. Lett.* **2003**, *91*, 096802.

(25) Yasuda, S.; Yoshida, S.; Sasaki, J.; Okutsu, Y.; Nakamura, T.; Taninaka, A.; Takeuchi, O.; Shigekawa, H. Bond Fluctuation of S/Se Anchoring Observed in Single-Molecule Conductance Measurements Using the Point Contact Method with Scanning Tunneling Microscopy. *J. Am. Chem. Soc.* **2006**, *128*, 7746−7747.

(26) Chen, F.; Li, X.; Hihath, J.; Huang, Z.; Tao, N. Effect of Anchoring Groups on Single-Molecule Conductance: Comparative Study of Thiol-, Amine-, and Carboxylic-Acid-Terminated Molecules. *J. Am. Chem. Soc.* **2006**, *128*, 15874−15881.

(27) Venkataraman, L.; Klare, J. E.; Tam, I. W.; Nuckolls, C.; Hybertsen, M. S.; Steigerwald, M. L. Single Molecule Circuits with Well-Defined Molecular Conductance. *Nano Lett.* **2006**, *6*, 458−462.

(28) Fagas, G.; Greer, J. C. Tunnelling in Alkanes Anchored to Gold Electrodes via Amine End Groups. *Nanotechnology* **2007**, *18*, 424010.

(29) Sheng, W.; Li, Z. Y.; Ning, Z. Y.; Zhang, Z. H.; Yang, Z. Q.; Guo, H. Quantum Transport in Alkane Molecular Wires: Effects of Binding Modes and Anchoring Groups. *J. Chem. Phys.* **2009**, *131*, 244712.

(30) Rogero, C.; Pascual, J. I.; Gomez-Herrero, J.; Baro, A. M. Resolution of Site-Specific Bonding Properties of C60 Adsorbed on Au (111). *J. Chem. Phys.* **2002**, *116*, 832−836.

(31) Martin, C. A.; Ding, D.; Sørensen, J. K.; Bjørnholm, T.; van Ruitenbeek, J. M.; van der Zant, H. S. Fullerene-Based Anchoring Groups for Molecular Electronics. *J. Am. Chem. Soc.* **2008**, *130*, 13198−13199.

(32) Leary, E.; González, M. T.; Van Der Pol, C.; Bryce, M. R.; Filippone, S.; Martín, N.; Agraït, N. Unambiguous One-Molecule Conductance Measurements Under Ambient Conditions. *Nano Lett.* **2011**, *11*, 2236−2241.

(33) Xue, Y.; Datta, S.; Ratner, M. A. Charge Transfer and "Band Lineup" in Molecular Electronic Devices: A Chemical and Numerical Interpretation. *J. Chem. Phys.* **2001**, *115*, 4292−4299.

(34) Lindsay, S. M.; Ratner, M. A. Molecular Transport Junctions: Clearing Mists. *Adv. Mater.* **2007**, *19*, 23−31.

(35) Li, Z.; Smeu, M.; Ratner, M. A.; Borguet, E. Effect of Anchoring Groups on Single Molecule Charge Transport through Porphyrins. *J. Phys. Chem. C* **2013**, *117*, 14890−14898.

(36) Yaliraki, S. N.; Ratner, M. A. Molecule-Interface Coupling Effects on Electronic Transport in Molecular Wires. *J. Chem. Phys.* **1998**, *109*, 5036−5043.

(37) Magoga, M.; Joachim, C. Conductance of Molecular Wires Connected or Bonded in Parallel. *Phys. Rev. B: Condens. Matter Mater. Phys.* **1999**, *59*, 16011.

(38) Salomon, A.; Cahen, D.; Lindsay, S.; Tomfohr, J.; Engelkes, V. B.; Frisbie, C. D. Comparison of Electronic Transport Measurements on Organic Molecules. *Adv. Mater.* **2003**, *15*, 1881−1890.

(39) Kushmerick, J. G.; Naciri, J.; Yang, J. C.; Shashidhar, R. Conductance Scaling of Molecular Wires in Parallel. *Nano Lett.* **2003**, *3*, 897−900.

(40) Selzer, Y.; Cai, L.; Cabassi, M. A.; Yao, Y.; Tour, J. M.; Mayer, T. S.; Allara, D. L. Effect of Local Environment on Molecular Conduction: Isolated Molecule versus Self-Assembled Monolayer. *Nano Lett.* **2005**, *5*, 61−65.

(41) Cahen, D.; Naaman, R.; Vager, Z. The Cooperative Molecular Field Effect. *Adv. Funct. Mater.* **2005**, *15*, 1571−1578.

(42) Liu, R. U. I.; Ke, S. H.; Baranger, H. U.; Yang, W. Intermolecular Effect in Molecular Electronics. *J. Chem. Phys.* **2005**, *122*, 044703.

(43) Natan, A.; Kronik, L.; Haick, H.; Tung, R. T. Electrostatic Properties of Ideal and Non-ideal Polar Organic Monolayers: Implications for Electronic Devices. *Adv. Mater.* **2007**, *19*, 4103−4117.

(44) Landau, A.; Kronik, L.; Nitzan, A. Cooperative Effects in Molecular Conduction. *J. Comput. Theor. Nanosci.* **2008**, *5*, 535−544.

(45) Agapito, L. A.; Cao, C.; Cheng, H. P. First-Principles Determination of the Effects of Intermolecular Interactions on the Electronic Transport through Molecular Monolayers. *Phys. Rev. B: Condens. Matter Mater. Phys.* **2008**, *78*, 155421.

(46) Reuter, M. G.; Solomon, G. C.; Hansen, T.; Seideman, T.; Ratner, M. A. Understanding and Controlling Crosstalk between Parallel Molecular Wires. *J. Phys. Chem. Lett.* **2011**, *2*, 1667−1671.

(47) Reuter, M. G.; Seideman, T.; Ratner, M. A. *Molecular Conduction through Adlayers: Cooperative Effects Can Help or Hamper Electron Transport. Nano Lett.* **2011**, *11*, 4693−4696.

(48) Galperin, M.; Nitzan, A. Cooperative Effects in Inelastic Tunneling. *J. Phys. Chem. B* **2013**, *117*, 4449−4453.

(49) Capozzi, B.; Xia, J.; Adak, O.; Dell, E. J.; Liu, Z. F.; Taylor, J. C.; Neaton, J. B.; Campos, L. M.; Venkataraman, L. Single-molecule diodes with high rectification ratios through environmental control. *Nat. Nanotechnol.* **2015**, *10*, 522−527.

(50) Egger, D. A.; Rissner, F.; Zojer, E.; Heimel, G. Polarity Switching of Charge Transport and Thermoelectricity in Self-Assembled Monolayer Devices. *Adv. Mater.* **2012**, *24*, 4403−4407.

(51) Obersteiner, V.; Egger, D. A.; Heimel, G.; Zojer, E. Impact of Collective Electrostatic Effects on Charge Transport through Molecular Monolayers. *J. Phys. Chem. C* **2014**, *118*, 22395−22401.

(52) Bumm, L. A.; Arnold, J. J.; Cygan, M. T.; Dunbar, T. D.; Burgin, T. P.; Jones, L.; Allara, D. L.; Tour, J. M.; Weiss, P. S. Are Single Molecular Wires Conducting? *Science* **1996**, *271*, 1705−1707.

(53) Heimel, G.; Romaner, L.; Brédas, J. L.; Zojer, E. Odd-Even Effects in Self-Assembled Monolayers of ω-(Biphenyl-4-yl) Alkanethiols: a First-Principles Study. *Langmuir* **2008**, *24*, 474−482.

(54) Quek, S. Y.; Kamenetska, M.; Steigerwald, M. L.; Choi, H. J.; Louie, S. G.; Hybertsen, M. S.; Neaton, J. B.; Venkataraman, L. Mechanically controlled binary conductance switching of a single-molecule junction. *Nat. Nanotechnol.* **2009**, *4*, 230−234.

(55) Kresse, G.; Furthmüller, J. Efficient Iterative Schemes for ab Initio Total-Energy Calculations Using a Plane-Wave Basis Set. *Phys. Rev. B: Condens. Matter Mater. Phys.* **1996**, *54*, 11169−11186.

(56) Perdew, J. P.; Burke, K.; Ernzerhof, M. Generalized Gradient Approximation Made Simple. *Phys. Rev. Lett.* **1996**, *77*, 3865−3868.

(57) Teter, M. P.; Payne, M. C.; Allan, D. C. Solution of Schrödinger's equation for large systems. *Phys. Rev. B: Condens. Matter Mater. Phys.* **1989**, *40*, 12255−12263.

(58) Sancho, M. P. L.; Sancho, J. M.; Sancho, J. M. L.; Rubio, J. Highly Convergent Schemes for the Calculation of Bulk and Surface Greens Functions. *J. Phys. F: Met. Phys.* **1985**, *15*, 851−858.

(59) Büttiker, M.; Imry, Y.; Landauer, R.; Pinhas, S. Generalized Many-Channel Conductance Formula with Application to Small Rings. *Phys. Rev. B: Condens. Matter Mater. Phys.* **1985**, *31*, 6207−6215.

(60) Xue, Y.; Datta, S.; Ratner, M. A. First-Principles Based Matrix Green's Function Approach to Molecular Electronic Devices: General Formalism. *Chem. Phys.* **2002**, *281*, 151−170.

(61) Soler, J. M.; Artacho, E.; Gale, J. D.; García, A.; Junquera, J.; Ordejón, P.; Sánchez-Portal, D. The SIESTA Method for ab Initio Order-N Materials Simulation. *J. Phys.: Condens. Matter* **2002**, *14*, 2745−2779.

(62) Heimel, G.; Romaner, L.; Zojer, E.; Brédas, J. L. Toward Control of the Metal-Organic Interfacial Electronic Structure in Molecular Electronics: A First-Principles Study on Self-Assembled Monolayers of π-Conjugated Molecules on Noble Metals. *Nano Lett.* **2007**, *7*, 932−940.

(63) Rusu, P. C.; Brocks, G. Work Functions of Self-Assembled Monolayers on Metal Surfaces by First-Principles Calculations. *Phys. Rev. B: Condens. Matter Mater. Phys.* **2006**, *74*, 073414.

(64) Kokalj, A. XCrySDen - A New Program for Displaying Crystalline Structures and Electron Densities. *J. Mol. Graphics Modell.* **1999**, *17*, 176−179.

(65) Humphrey, W.; Dalke, A.; Schulten, K. VMD: visual molecular dynamics. *J. Mol. Graphics* **1996**, *14*, 33−38.

(66) Ramachandran, P.; Varoquaux, G. Mayavi: 3D Visualization of Scientific Data. *Comput. Sci. Eng.* **2011**, *13*, 40−51.

(67) Stukowski, A. Visualization and Analysis of Atomistic Simulation Data with OVITO The Open Visualization Tool. *Modell. Simul. Mater. Sci. Eng.* **2010**, *18*, 015012.

(68) Van Dyck, V.; Geskin, V.; Kronemeijer, A. J.; de Leeuw, D. M.; Cornil, J. Impact of Derivatization on Electron Transmission through Dithienylethylene-based Photoswitches in Molecular Electronics. *Phys. Chem. Chem. Phys.* **2013**, *15*, 4392−4404.

(69) Xiao, X.; Xu, B.; Tao, N. J. Measurement of Single Molecule Conductance: Benzenedithiol and Benzenedimethanethiol. *Nano Lett.* **2004**, *4*, 267−271.

(70) Moth-Poulsen, K.; Patrone, L.; Stuhr-Hansen, N.; Christensen, J. B.; Bourgoin, J. P.; Bjørnholm, T. Probing the Effects of Conjugation Path on the Electronic Transmission through Single Molecules using Scanning Tunneling Microscopy. *Nano Lett.* **2005**, *5*, 783−785.

(71) Danilov, A.; Kubatkin, S.; Kafanov, S.; Hedegård, P.; Stuhr-Hansen, N.; Moth-Poulsen, K.; Bjørnholm, T. Electronic Transport in Single Molecule Junctions: Control of the Molecule-Electrode Coupling through Intramolecular Tunneling Barriers. *Nano Lett.* **2008**, *8*, 1−5.

(72) Van Dyck, C.; Geskin, V.; Cornil, J. Fermi Level Pinning and Orbital Polarization Effects in Molecular Junctions: The Role of Metal Induced Gap States. *Adv. Funct. Mater.* **2014**, *24*, 6154−6165.

(73) Kim, T.; Darancet, P.; Widawsky, J. R.; Kotiuga, M.; Quek, S. Y.; Neaton, J. B.; Venkataraman, L. Determination of Energy Level Alignment and Coupling Strength in 4, 4′-Bipyridine Single-Molecule Junctions. *Nano Lett.* **2014**, *14*, 794−798.

(74) Braun, S.; Salaneck, W. R.; Fahlman, M. Energy-Level Alignment at Organic/Metal and Organic/Organic Interfaces. *Adv. Mater.* **2009**, *21*, 1450−1472.

(75) Ma, Z.; Rissner, F.; Wang, L.; Heimel, G.; Li, Q.; Shuai, Z.; Zojer, E. Electronic Structure of Pyridine-Based SAMs on Flat Au (111) Surfaces: Extended Charge Rearrangements and Fermi Level Pinning. *Phys. Chem. Chem. Phys.* **2011**, *13*, 9747−9760.

(76) Heimel, G.; Zojer, E.; Romaner, L.; Brédas, J. L.; Stellacci, F. Doping Molecular Wires. *Nano Lett.* **2009**, *9*, 2559−2564.

(77) Neaton, J. B.; Hybertsen, M. S.; Louie, S. G. Renormalization of Molecular Electronic Levels at Metal-Molecule Interfaces. *Phys. Rev. Lett.* **2006**, *97*, 216405.

(78) Wang, L.; Rangger, G. M.; Ma, Z.; Li, Q.; Shuai, Z.; Zojer, E.; Heimel, G. Is there a Au-S Bond Dipole in Self-Assembled Monolayers on Gold? *Phys. Chem. Chem. Phys.* **2010**, *12*, 4287−4290.

(79) Koch, N. Organic Electronic Devices and their Functional Interfaces. *ChemPhysChem* **2007**, *8*, 1438−1455.

(80) Rohlfing, M.; Temirov, R.; Tautz, F. S. Adsorption Structure and Scanning Tunneling Data of a Prototype Organic-Inorganic Interface: PTCDA on Ag (111). *Phys. Rev. B: Condens. Matter Mater. Phys.* **2007**, *76*, 115421.

2.1.3 Supporting Information

Supporting Information to

Impact of Anchoring Groups on Ballistic Transport:

Single Molecule vs. Monolayer Junctions

Veronika Obersteiner†, David A. Egger †, ‡, and Egbert Zojer †

† Institute of Solid State Physics, NAWI Graz, Graz University of Technology, Petersgasse 16, 8010 Graz, Austria

‡ Department of Materials and Interfaces, Weizmann Institute of Science, Rehovoth 76100, Israel

Additional Data

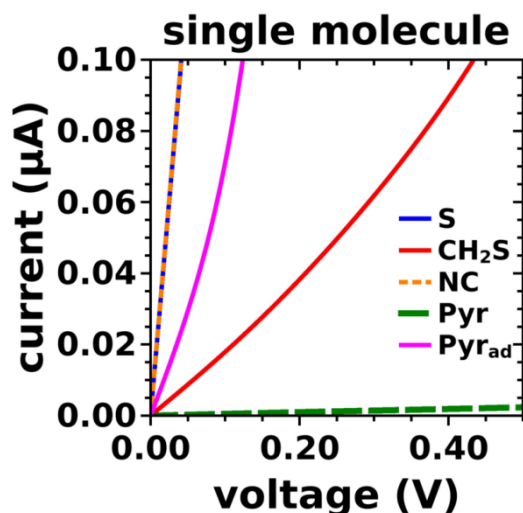## 1. Variation of the molecular packing density

The density of the molecules bridging the electrodes was varied by increasing the size of the unit cell and consecutively removing molecules. Figure S1 a-e shows the different unit cells for molecular packing densities of $\Theta=1$, 1/2, 1/4, 1/8 and 1/16, respectively. For example, the 50% packing density, $\Theta=1/2$, was achieved by doubling the (2x2) surface unit cell in x-direction and deleting one molecule. The gold atoms situated laterally in-between the remaining molecule were set to their bulk atomic positions (eliminating surface reconstructions due to thiolate-Au bonds in regions, where molecules have been removed). Lower packing densities were generated by alternately doubling the unit cells in y- and x-direction, in all cases retaining only one molecule per unit cell. For all packing densities, the molecules are kept in the equilibrium geometry found for $\Theta=1$.
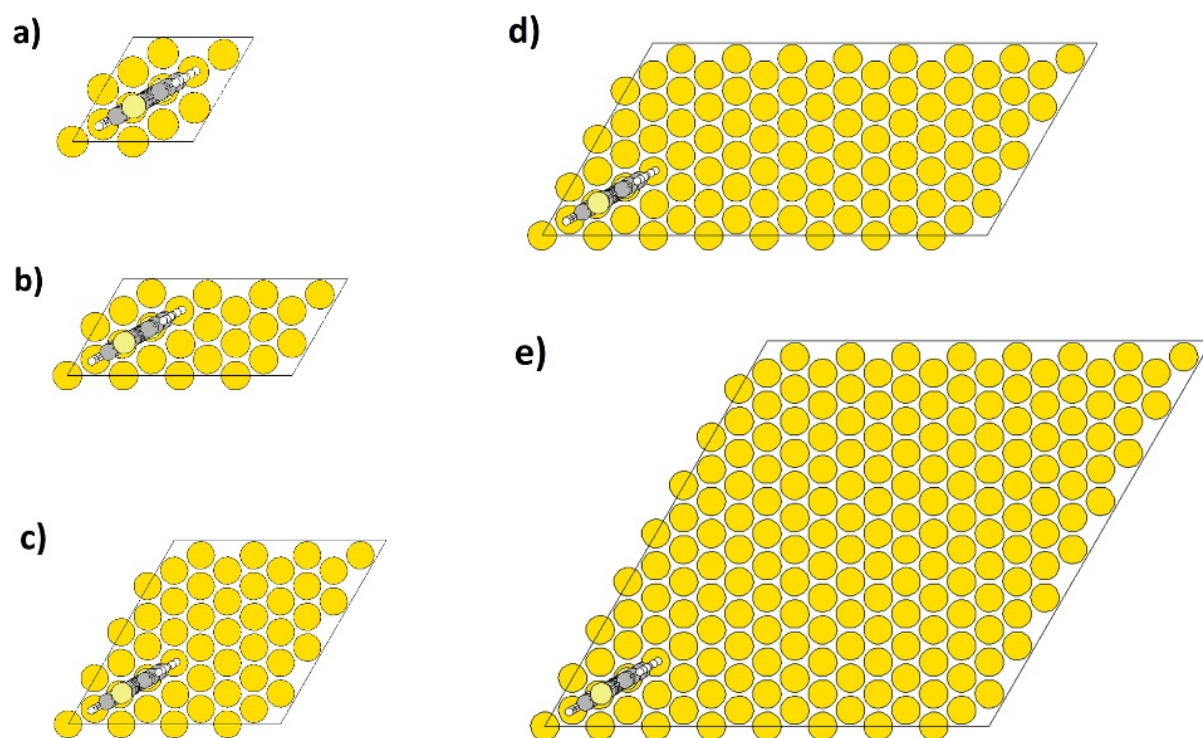
Figure S1: Top view of molecular junctions without their top electrodes at different molecular packing densities of **(a)** $\Theta=1$, **(b)** $\Theta=1/2$, **(c)** $\Theta=1/4$, **(d)** $\Theta=1/8$, and **(e)** $\Theta=1/16$.

2. Current-Voltage Characteristics

Figure S2 shows the current-voltage characteristics of the investigated systems for the single molecule junction in a voltage range between 0 V and 0.50 V. At 0.2 V we can identify a sequence of currents following: $S \approx NC > Pyr_{ad} > CH_2S > Pyr$. This sequence is the same as for the zero-bias conductance $G(E_F) = T(E_F) \cdot G_0$ shown in Figure 2 of the main text. The values for $G(E_F)$ are summarized in Table S1.


Figure S2: *: Calculated current-voltage characteristics of the (–S), (-CH$_2$S), (-NC), (-Pyr) and (-Pyr$_{ad}$) systems for the model of a single molecule junction with a packing density $\Theta = 1/16$ This figure is a zoom of Figures 2a) of the main manuscript.*

Table S1: *Zero-bias conductance $G(E_F) = T(E_F) \cdot G_0$ for full monolayer junctions, $\Theta = 1$ and single molecule junctions, $\Theta = 1/16$. G_0 here refers to the quantum of conductance that corresponds to $2e^2/h$.*

	$G(E_F)$ [G_0] at Θ=1	$G(E_F)$ [G_0] at Θ=1/16
(-S)	0.014	0.030
(-CH$_2$S)	0.001	0.002
(-NC)	0.057	0.032
(-Pyr)	0.059	6e-05
(-Pyr$_{ad}$)	0.133	0.004

Figure S3 shows the voltage dependent current per molecule for the investigated systems at different molecular packing densities Θ, ranging from full monolayer, Θ=1, to Θ=1/2, Θ=1/4, Θ=1/8 and finally the single molecule situation, Θ=1/16.
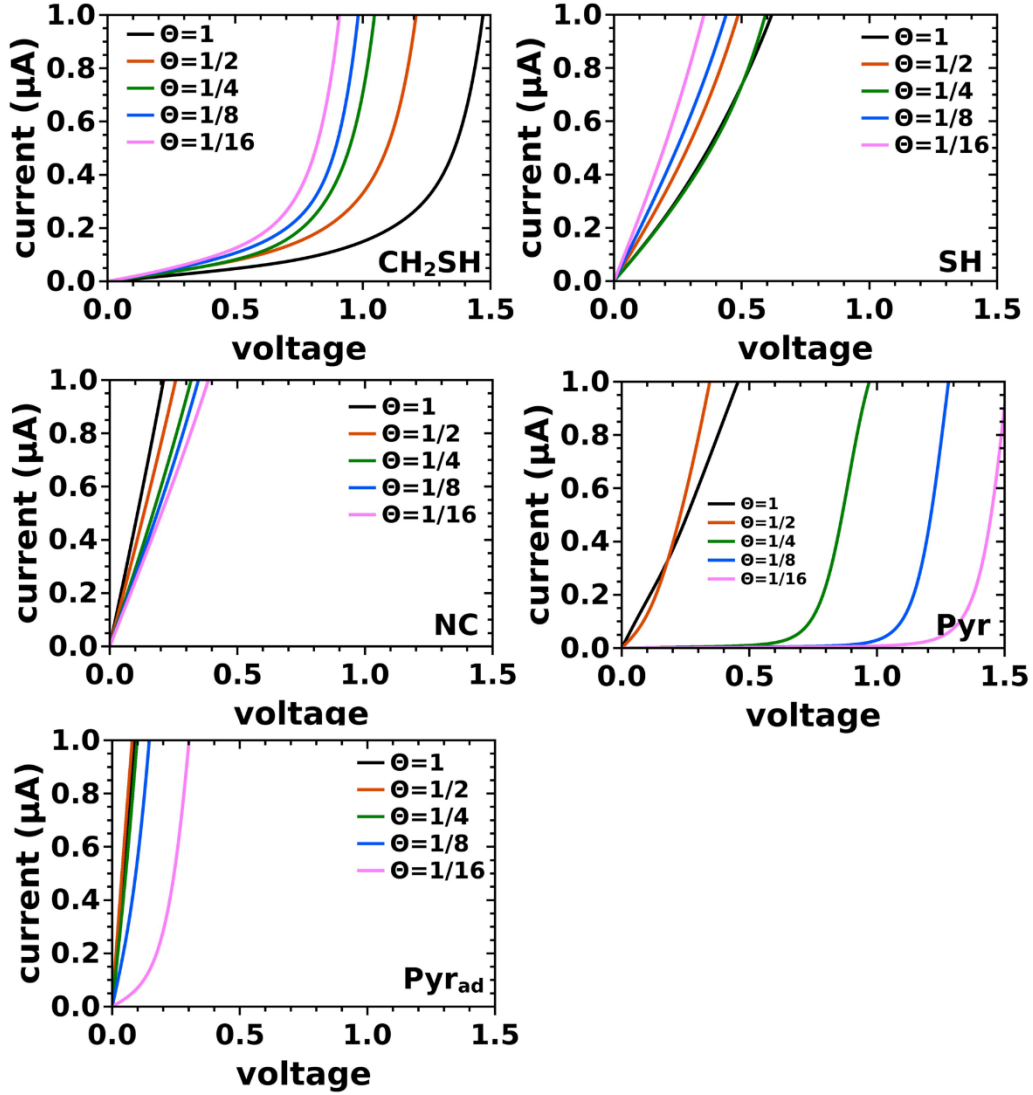
Figure S3: Voltage dependent current per molecule for (-CH2SH), (-SH), (-NC), (-Pyr) and (-Pyr$_{ad}$) junctions at different molecular packing densities Θ derived from the transmission functions via the Landauer equation.

3. Cumulative charge transfer

Further insight into the implications of the charge rearrangements can be obtained by integrating Δρ over the transport direction, z: $Q(z) = \int_0^z \Delta\rho(z')dz'$. This yields the total amount of transferred charge per unit cell from left to right of a plane at z . Figure S4 shows the cumulative charge transfer of the investigated systems at the highest an lowest considered packing densities. Dashed grey lines indicate the positions of the innermost gold layers. Note that whenever Q(z) reaches zero that means that no net charge is transferred across the plane at z. The triangular shapes of Q(z) in the molecular regions at Θ=1/16 with the zero-crossing in the middle of the junction are indicative of a polarization of the molecular backbones arising from the molecule metal interaction. The wiggles at Θ=1 for (-Pyr) and (-

Pyr_{ad}) along the molecular backbones indicate short-range polarization effects due to Fermi-level pinning.
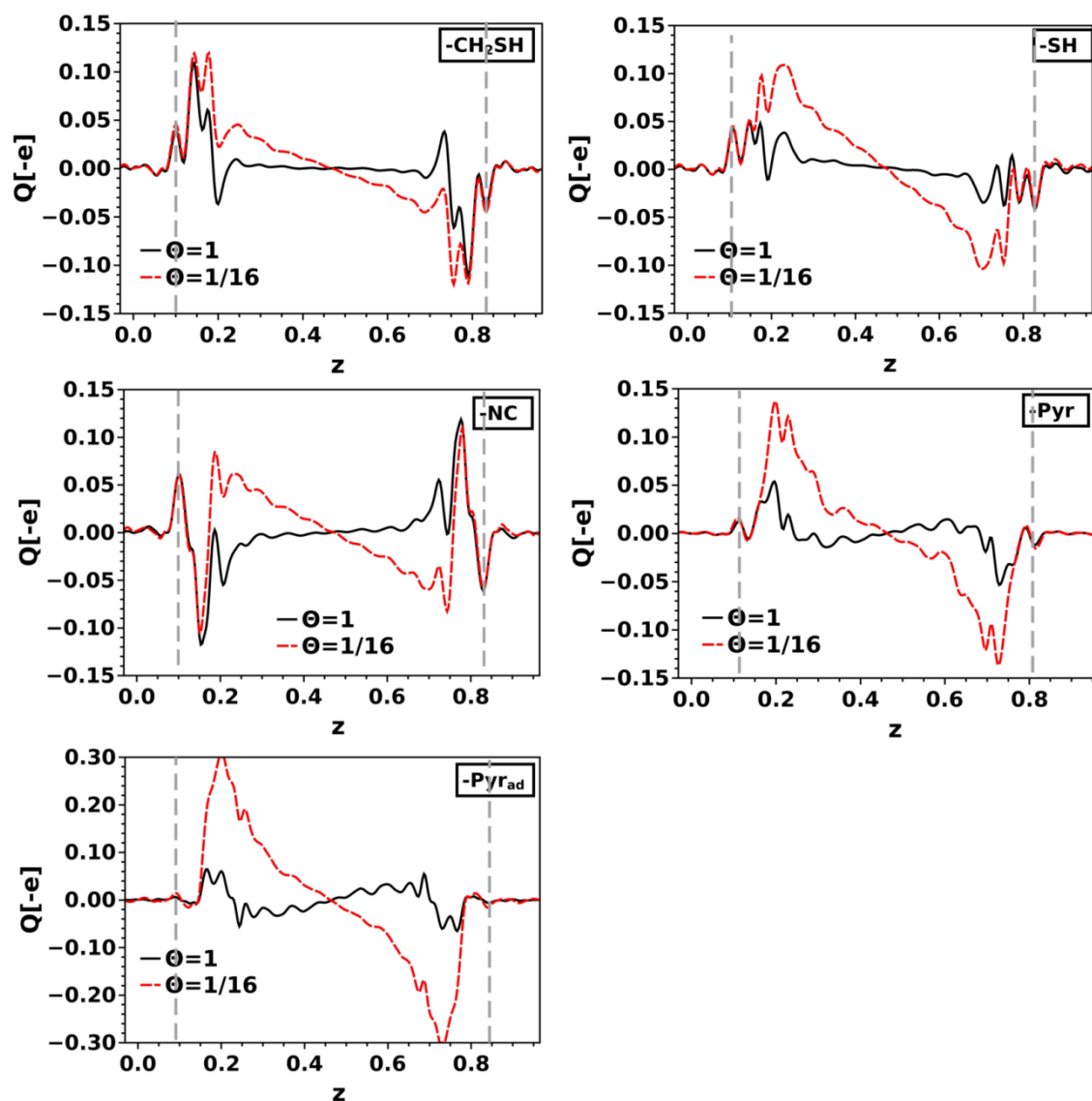
Figure S4: Cumulative charge transfer Q for all investigated molecular junctions with different docking groups: (-CH₂S), (-S), (-NC), (-Pyr) and (-Pyr_ad) at different packing densities Θ.

4. Evolution of the Bond Dipole with Packing Density

Figure S5 shows the (x-y)-plane averaged change in the electrostatic energy due to metal-molecule bonding of all investigated systems at different molecular packing densities Θ. The corresponding contour plots in the plane of the molecules can be found in the main text in Figure 5. The values for ΔE_{BD} in Table 1 of the main text are obtained from these plane-averaged quantities as the value in the center of the molecular junction.
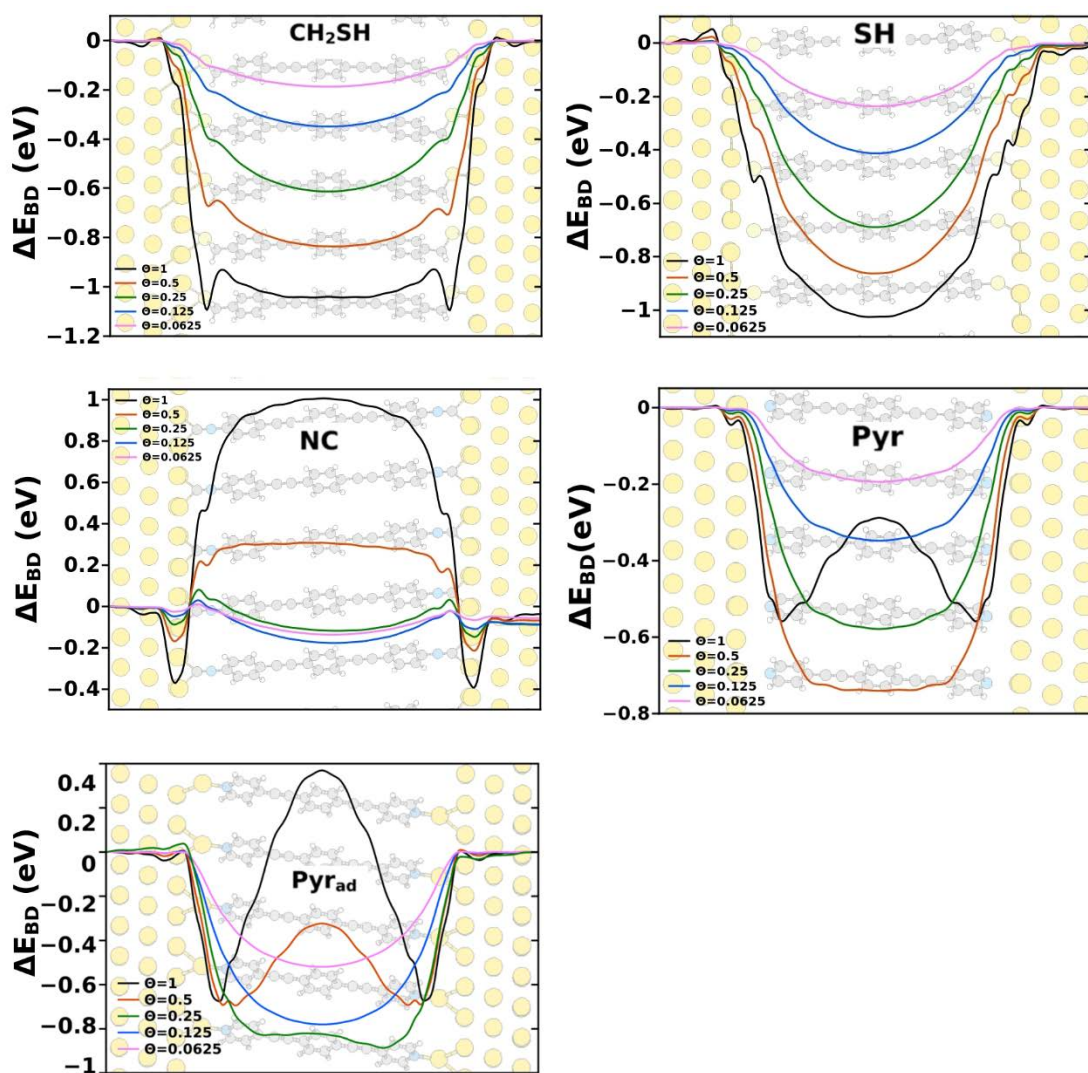
Figure S5: *Bond dipole ΔE_{BD} for all investigated molecular junctions with different docking groups: (-CH$_2$S), (-S), (-NC), (-Pyr) and (-Pyr$_{ad}$) at different packing densities Θ.*

## 5. Molecular Properties of investigated systems

Table S2: *Energies of the frontier π-orbitals of the isolated molecules, ε_{HOMO} and ε_{LUMO}, relative to the vacuum level realigned considering the work function of the electrodes (details see main manuscript), obtained from VASP calculations for the lowest molecular packing density at $\Theta=1/16$ for (-CH$_2$S), (-S), (-NC), (-Pyr) and (-Pyr$_{ad}$) systems.*

	-S	-CH$_2$S	-NC	-Pyr	-Pyr$_{ad}$
ε_{HOMO} [eV]	-4.94	-5.18	-5.73	-5.86	-5.77
ε_{LUMO} [eV]	-2.77	-2.88	-3.61	-3.49	-3.52

|	-S	-CH$_2$S	-NC	-Pyr	-Pyr$_{ad}$
$\bar{\epsilon}_{HOMO}$ [eV]	0.24	0.00	-0.55	-0.68	-1.06
$\bar{\epsilon}_{LUMO}$ [eV]	2.41	2.30	1.57	1.69	1.19

6. Bond Formation between (-NC) anchoring group and Au substrate

Figure S6 shows the 3D isodensity representation of the charge rearrangements of the isocyanide linked system at highest packing density. Blue/red regions show electron depletion/accumulation. Black arrows indicate the position of the N and C atom. These charge rearrangements at the interface can be associated with the bond-formation between the –NC group and Au ,where electrons are redistributed from the C lone pair to the region between the C atom and the two closest Gold atoms (red regions between the Carbene and the Au-surface).At the same time, the strong electron depletion at the Nitrogen atom (blue lobe between the nitrogen and the carbene) is indicative of a partial transformation from a (N-C) triple to a double bond. This interpretation is supported by the observation that the N-C bond elongates upon adsorption (1.18 Å in the gas phase molecule and 1.22 Å after bonding).
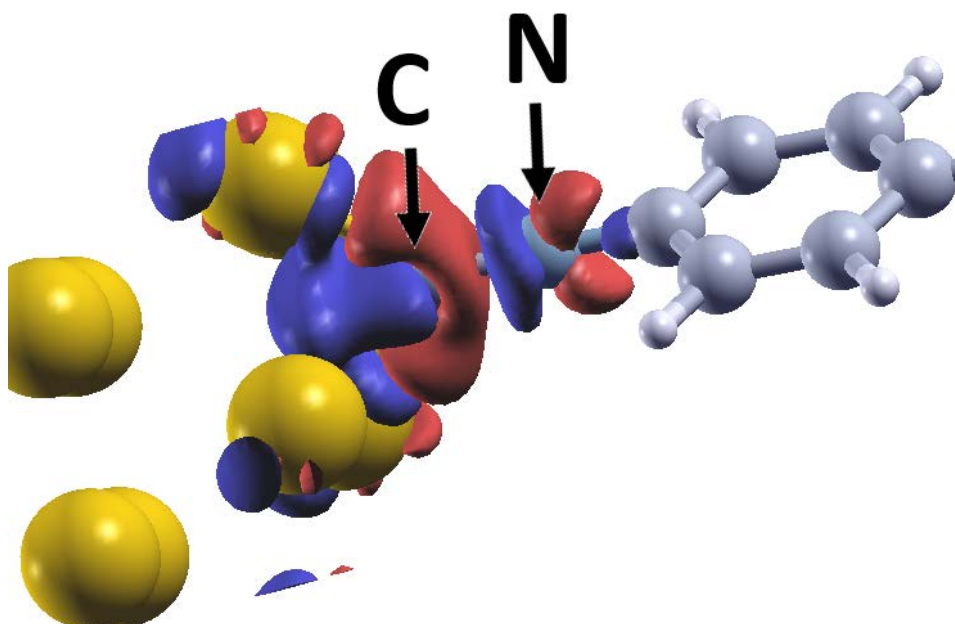

Figure S6: *3D isodensity representation of the charge rearrangements of the metal-molecule interface of the (-NC) system at highest packing density. Blue means charge depletion, red means charge accumulation.*

7. Packing Dependent Peak Positions of HOMO- and LUMO-Derived Bands for all Investigated Systems
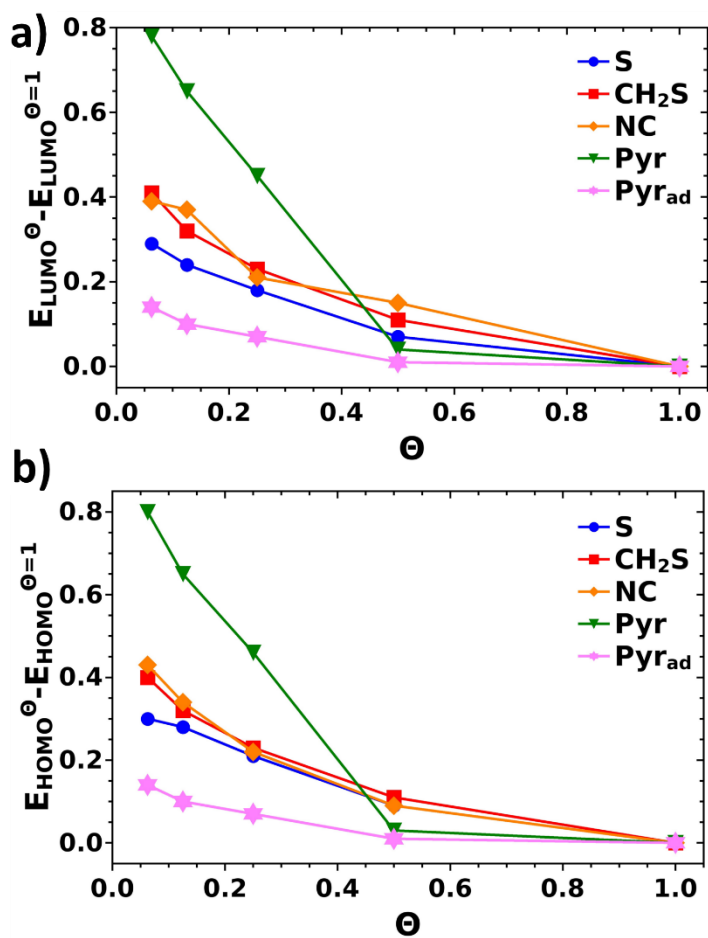
Figure S7: *Packing dependent peak positions of (a) HOMO- and (b) LUMO-derived bands (obtained from PDOS) for all investigated systems, aligned with respect to the energies for full packing density Θ=1.*

8. Packing Dependent Transmission Function for all Investigated Anchoring Groups
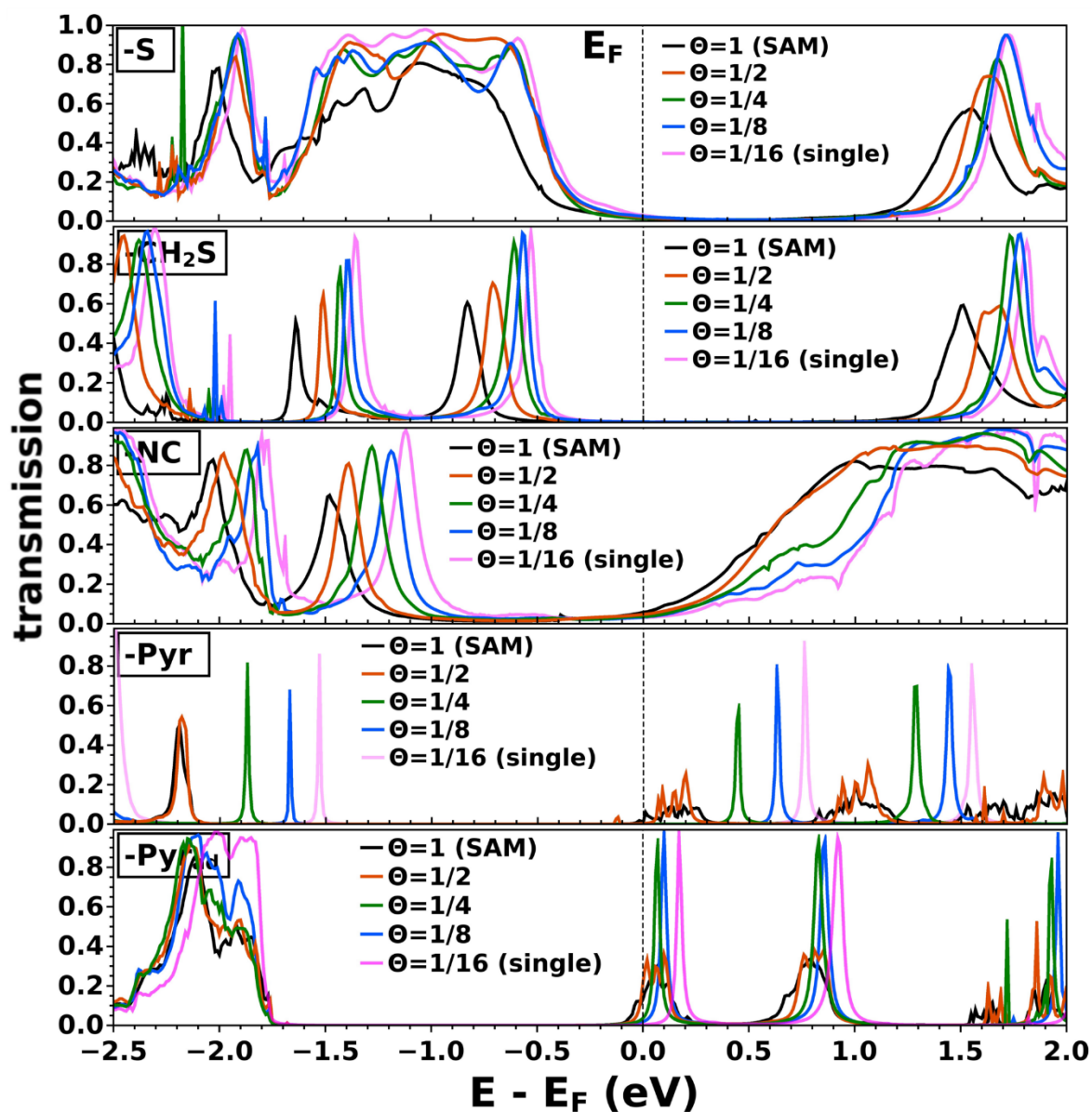
Figure S8: *Calculated (zero-bias) transmission functions of the (–S), (-CH$_2$S), (-NC), (-Pyr) and (-Pyr$_{ad}$) systems at different packing densities Θ. The Fermi level E_F is used as the energy reference.*

2.2 Scaling of Charge Transport through Parallel Molecular Wires

2.2.1 Author Contribution

The idea of performing transport calculations on clusters of molecules first arose in a discussion with Emmanuel Lörtscher and is an extension of the investigations performed in PUBLICATION I. While in the latter the difference in charge transport characteristics between individual molecules and self-assembled monolayers is demonstrated by varying the packing density of the molecules, here, differently sized clusters of molecules are investigated, which appears as a more realistic scenario for comparison to experiments. V. Obersteiner set up and optimized all the systems and performed the electronic structure calculations applying the `VASP` code. G. Huhs performed all transport calculations applying the `TranSIESTA` code. N. Papior provided significant technical insight into the transport calculations. The current status of the manuscript is a draft, which was produced by V. Obersteiner and improved by E. Zojer. E. Zojer supervised the project.

Note that this paper is based on work I did within my Master Thesis that was, however, extensively extended during the time of my PhD. The paper entirely connected to my Master Thesis, see Ref. [1], was finished during the course of my PhD but is not included in this Thesis.

2.2.2 Current Draft of the Publication

Molecular Junctions: Scaling of Charge Transport through Parallel Molecular Wires

Veronika Obersteiner[1]‡, Georg Huhs[2]‡, Nick Papior[3], and Egbert Zojer[1],*

[1]Institute of Solid State Physics, NAWI Graz, Graz University of Technology, Petersgasse 16, 8010 Graz, Austria

[2]Department of Computer Applications in Science and Engineering, Barcelona Supercomputing Center, Carrer de Jordi Girona 29, 08034 Barcelona, Spain

[3]Department of Micro- and Nanotechnology (DTU Nanotech), Technical University of Denmark, DK-2800 Kgs. Lyngby, Denmark

ABSTRACT

Metal-molecule-metal junctions are the constitutive components of molecular electronics circuits. A microscopic understanding of charge transport through these systems is essential for advancing the field. In the present contribution, we aim at understanding the collective behavior of molecular wires in parallel, bridging the gap between single molecule and large-area molecular electronics. On the basis of first-principles charge-transport simulations in conjunction with electrostatic considerations, we explicitly calculate the "scaling" of charge-transport with an increasing number of molecules forming clusters within the junction. We show that transport in clusters becomes highly inhomogeneous with pronounced edge effects due to molecules in locally different electrostatic environments. The associated collective electrostatic effects appear already for comparably small cluster sizes and largely affect the scaling of charge-transport that is found to be far from linear.

Molecular electronics aims at realizing electronic devices by contacting nanoscale assemblies of molecules between metallic electrodes.[1,2] A key goal is to meet the increasing technical demands of miniaturization. Beyond that, new device types are thought after, exploiting the enormous variety of conceivable systems arising from the flexibility of chemical design. Molecular electronics can be divided into two branches, namely single molecule junctions[3,4] and large-area molecular ensemble junctions[5,6] comprising thousands of molecules in parallel or even extended monolayers. While there has been tremendous progress in understanding charge-transport in each of these fields, the transition between single molecule and monolayer junctions is hardly ever addressed.

The main conceptual difference between a molecular to an ensemble (respectively, monolayer) junction, is that in the latter case the collective interaction of individual molecules becomes important. It determines the "scaling" of charge-transport properties with the *number of molecules* involved in the transport process. In this context, experimental as well as theoretical works reach quite contradicting results on how the conductance of a single molecule is related to that of multiple molecules in parallel. While in some experimental works,[7–9] the conductance per molecule was observed to scale directly with the number of molecules in the monolayer,[9] in other cases the current per molecule in single molecule junctions was found to be orders of magnitudes larger than in the monolayer case.[10] Also, several theoretical studies,[11–16] reported that collective effects can "help or hamper"[13] charge-transport trough molecular junctions. When discussing collectivity, one generally has to distinguish between effects originating mostly from quantum-mechanical interactions, such as quantum interference effects,[15–18] and effects caused by mere electrostatics due to polar elements within the junction (so-called, collective electrostatic effects).[19–21] The latter generally arise from the combined electric fields of

periodically assembled neighboring dipoles and significantly affect the electrostatic-potential energy landscape.[22–25] In molecular junctions they emerge "naturally" from polar docking groups and from interface dipoles arising due to the bonding of the molecules to the leads, and can be intentionally triggered by incorporating polar elements into the molecular backbones.[20] They crucially affect the alignment between the molecular transport channels and the Fermi level of the metal, which massively changes the current per molecules, potentially even switching the charge-transport polarity.[19,20] Collective electrostatic effects have also been found to shift measured transition voltages in monolayer junctions and through the spatial localization of charge-transporting states they can even cause rectification.[26,27]

In this letter, we contribute to filling the gap between molecular and monolayer junctions by explicitly calculating the evolution of the charge-transport characteristics with an increasing number of molecules forming clusters within the junction. The results obtained for the clusters are compared to the behavior of single molecule and monolayer junctions. The focus is here on the above-mentioned collective electrostatic effects. On the basis of first-principles quantum transport simulations for junctions containing up to sixteen molecules and electrostatic considerations for larger clusters, we show (i) that collective electrostatic effects appear already for comparably small cluster sizes, (ii) that transport in clusters becomes highly inhomogeneous with pronounced edge effects due to molecules in different electrostatic environments, and (iii) that the scaling of charge-transport with the number of molecules is typically far from linear with the actual evolution depending on the specific system at hand.

In our calculations, we study molecular junctions that are based on the prototypical "Tour-wire"[28] molecule, i.e., 1,2,-bis(2-phenylethynyl)benzene bonded to Au electrodes via the

commonly used anchoring groups pyridine (-Pyr), thiolate (-S) and isocyanide (NC), see Figure 1a.
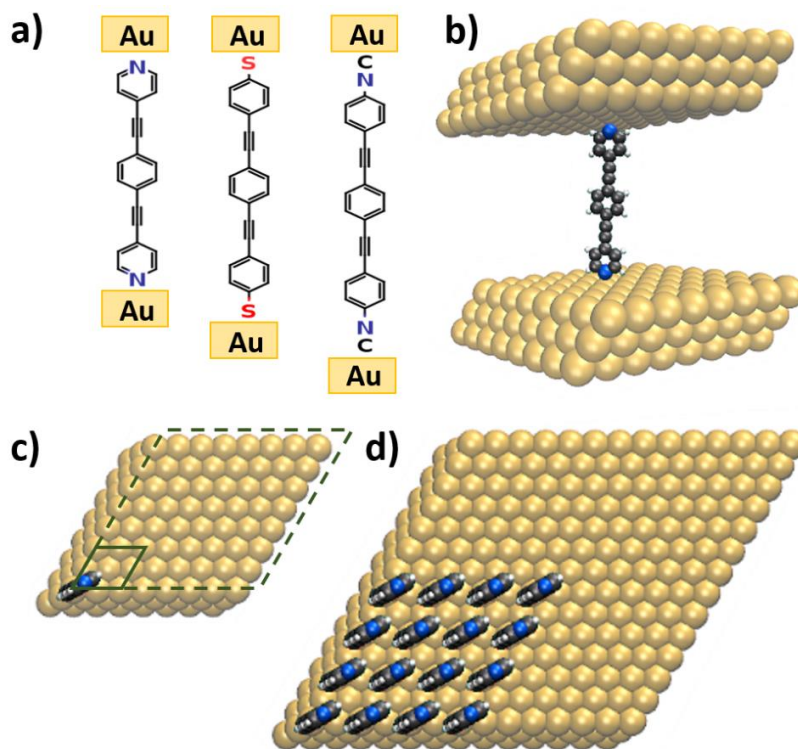
Figure 1. (a) Chemical structure of the investigated molecular junctions, i.e. 1,2,-bis(2-phenylethynyl)benzene bonded to Au electrodes via commonly used anchoring groups, such as pyridine (-Pyr), thiolate (-S) and isocyanide (NC). (b) Model systems to simulate the single molecule junction employing periodic boundary conditions. (c) Top view of single molecule junction (dashed box) and the monolayer junction (solid box). (d) Top view of a cluster comprising sixteen molecules.

The type of anchoring group is known to have a profound impact on the degree of coupling between molecules and leads[29] as well as on the level alignment,[30–32] i.e. the relative energetic position of the transmission channels with respect to the Fermi level. Electron donating

anchoring groups (such as thiolate) shift the highest occupied transport channels closer to the Fermi level, thereby, promoting p-type current, while electron withdrawing groups (pyridine and isocyanide) trigger transport through the lowest unoccupied transmission channels (i.e., n-type current). In terms of collective electrostatic effects, for monolayer junctions, energetic shifts due to dipoles of the anchoring groups, which differ in magnitude and orientation, and due to different interfacial charge rearrangements causing different bond dipoles, need to be considered, as discussed in detail in Ref. [21].

For all systems, we first simulate the two limiting cases of a single molecule and a densely packed monolayer, where the former is modeled by a comparably sparse monolayer, as we employ periodic boundary conditions. For the densely packed monolayer we use one molecule in a p(2x2) Au(111) surface unit cell (see solid box in Figure 1c), while the single molecule is modeled by one molecule in a (8x8) Au(111) surface unit cell (i.e., at 1/16 coverage; see dashed box in Figure 1c). The metallic leads are represented by three layers of Au(111) on each side of the junction. To set up the geometries for differently sized clusters of molecules, we start from the single molecule unit cell and consecutively add molecules while enlarging the unit cell such that the distance between the clusters remains the same as in the nominal single-molecule limit. Thereby, we generate clusters of 1, 2, 3, 4, 9 and 16 molecules (see Figure 1d). Note that 16 molecules together with the gold electrodes comprise ~1700 atoms per unit cell, which constitutes a computational upper limit for our quantum-mechanical calculations, see Supporting Information.

To determine the electronic properties of the systems and optimize their geometries, we performed band-structure calculations within the framework of density-functional theory (DFT) using the VASP[33] code in conjunction with the PBE[34] functional and a plane-wave basis set (cut-

off: ca. 20 Ry). We optimized the structure of the monolayer junction according to the procedure described in Ref. [20]. The geometries of the individual clusters were not optimized due to the size of the systems and as no significant changes in molecular conformation are expected considering that the molecules are suspended between two electrodes. To obtain current-voltage characteristic and zero-bias transmission functions we combined DFT with non-equilibrium Greens function (NEGF) techniques applying the recently improved version of the TRANSIESTA[35] code. We employed the double-ζ polarized orbital basis set (DZP) accompanied by a PAO.EnergyShift of 0.001 Ry, which we found to be crucial to correctly describe the evolution of the energy level alignment with molecular coverage (see the Supporting Information of Ref. [20] for detailed tests). The zero-bias conductance, $G(E_F)=T(E_F) \cdot G_0$, was evaluated as the value of the zero-bias transmission function T at the Fermi level E_F; $G_0=(2e^2/h)$ is the quantum of conductance. Xcrysden[36] and VMD[37] were used for graphical visualization. For full details on the applied computational methodology and numerical parameters used in our calculations, see the Supporting Information.

To discuss the main effects we choose the pyridine linked system shown in Figure 1a. This choice is motivated by the fact that the comparably weak coupling between the pyridines and the electrodes[38,39,21] allows a clear distinction between well-resolved transport channels. The other systems are compared to the pyridine-linked system below. The calculated current-voltage (I-V) characteristics for the differently sized pyridine-linked clusters are shown in Figure 2a together with the results for the single molecule and monolayer limits. Overall, one observes a roughly exponentially increasing current with an onset that shifts to smaller voltages with increasing cluster size. For the monolayer an immediate and steep increase is obtained.
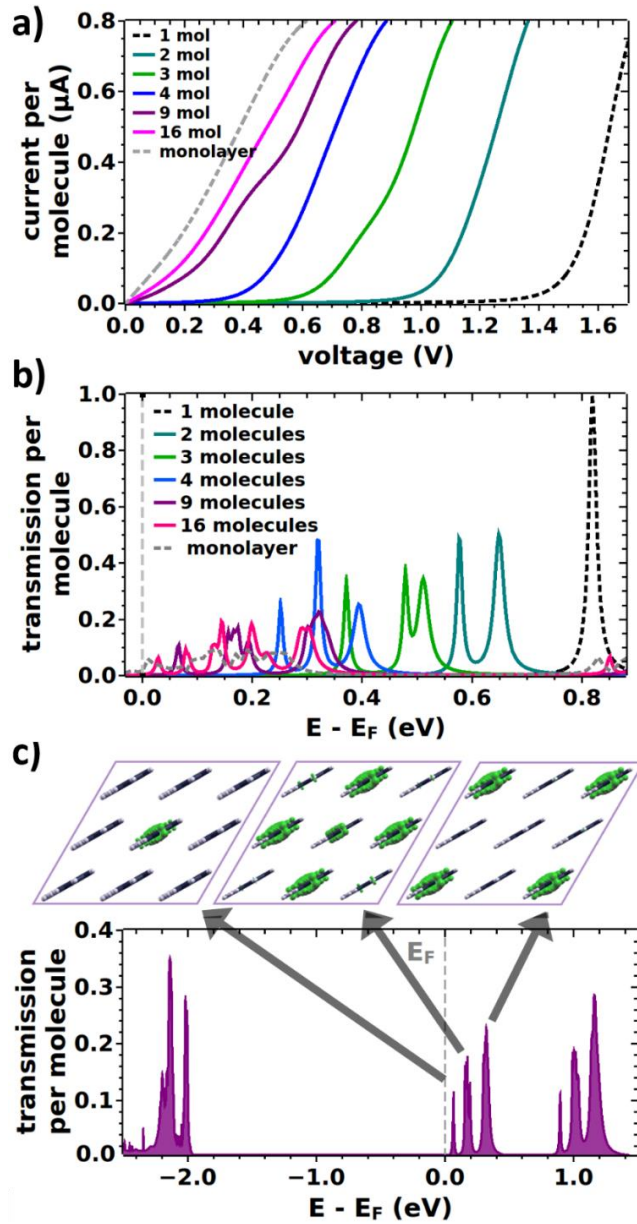
***Figure 2**. (a) Calculated current-voltage characteristics for the pyridine linked junction for different cluster sizes (1, 2, 3, 4, 9, and 16 molecules) and the monolayer junction. (b) Corresponding (zero-bias) transmission functions in the energy range of the lowest unoccupied transmission channels. The Fermi level, E_F, is used as the reference energy. (c) Transmission function for the pyridine linked cluster containing nine molecules. The insets*

show the local density of states (as obtained from VASP with an isovalue of 0.03 per Å³)

associated to the three lowest unoccupied transmission channels (calculated for the following

energy windows: 0.0-0.1 eV, 0.1-0.3 eV and 0.3-0.5 eV).

To understand that evolution, it is useful to analyze the (zero-bias) transmission functions, which directly reflect the energetic alignment of molecular transport channels with respect to the Fermi level of the electrodes. These are shown in Figure 2b in the energetic range of the unoccupied states, as those are the dominant conductance channels for the pyridine-linked junction. As can be seen, for the single molecule junction (black line), the lowest unoccupied transmission channel is represented by a narrow peak at around 0.8 eV. For two molecules in the junction, it splits and the lower-energy feature is shifted by as much as 0.22 eV. Upon further increasing the number of molecules in the cluster this trend continues and for the pyridine-docked system, at 16 molecules, a situation similar to that in the monolayer is recovered. For 16 molecules in the junction, the transmission features spread out over a wide energy range (ca. 0.3 eV) and the net shift between the lowest-energy transmission feature in the single molecule limit and the 16 molecule cluster amounts to 0.8 eV.

The shift is a consequence of a change of the electrostatic energy in the region of the molecules caused by the electrical fields of the pyridine- and bond-dipoles, which, when reducing the coverage of the monolayer, has been shown to be directly proportional to the dipole density (including coverage-dependent depolarization effects).[21] For the clusters, the situation is, however, qualitatively different from a mere reduction of the dipole density, as here the number and position of neighbors varies for different molecules. This, however, also means that the electrostatic energy landscape to which different molecules are exposed, varies. As a consequence, also the energetic positions of the transmission channels of the molecules vary

within the cluster. This (rather than a quantum-mechanical coupling) is responsible for the emergence of multiple peaks, as we show explicitly for the 9-molecule cluster in Figure 2c. For that cluster, the transmission features group into three main peaks centered at 0.05, 0.2 and 0.4 eV. For those peaks we display the local density of states (LDOS) in the top region of Figure 2c. There, one clearly sees that the lowest-energy feature is mostly associated with transport through the central molecule. This molecule is surrounded by eight neighboring molecules with their associated dipoles and, hence, the electrostatically-induced shift is largest. The next feature can be associated primarily with molecules at the edges of the cluster, while the molecules at the corners have the smallest number of neighboring molecules and, consequently, experience also the smallest fields resulting in the least shifted transmission feature.

These data show that collective electrostatic effects do shift transmission features also in clusters in analogy to the situation in a monolayer, but, on top of that, there are pronounced edge-effects. This is also clearly visible in Figure 3a, where we plot the energy of the transmission feature derived from the lowest unoccupied orbital that is closest to the Fermi level (i.e., the feature associated with the central molecule) as a function of cluster size (filled squares). The energies of the corresponding peaks furthest from E_F (i.e., feature associated with border molecules) are shown as open circles. One clearly sees that for the energy associated with the central molecule approaches E_F more quickly, which results in a continuous increase of the energy range in which transmission features exist (shaded area).
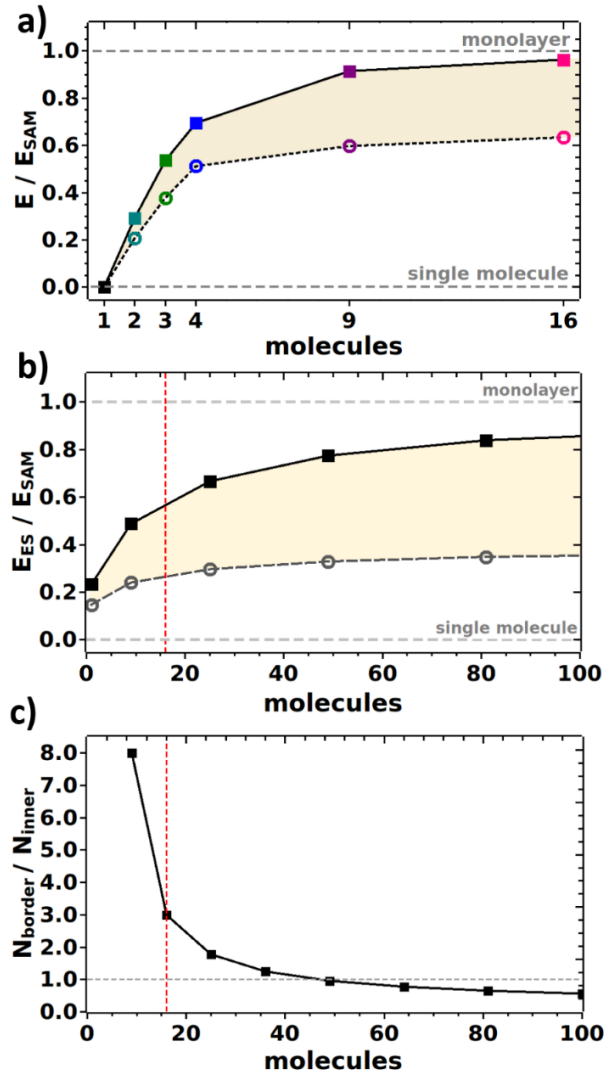
Figure 3. *(a) Energy of the transmission features derived from the lowest unoccupied transmission channels (as obtained from Figure 2b) relative to the energy of the monolayer, E_{SAM}, for an increasing number of molecules in the cluster for the pyridine-linked junction. Closed squares (open rings) refer to electrostatically most (least) shifted states, i.e. central (border) molecules in the cluster, cf. Figure 2c. (b) Electrostatic energy, E_{ES}, of the central (squares) and a boarder dipole (rings) in the middle of two opposite square 2D point dipole arrays, for increasing number of point dipoles (molecules). The energies are given relative to*

the monolayer energy, E_{SAM} (c) Ratio of the number of border molecules to molecules inside the cluster for increasing number of molecules (dipoles) in the cluster.

To further analyze that situation and to extend the discussion to much larger clusters, we devised a simple electrostatic point dipole model. In this, we described the electrostatic situation by two opposite square 2D dipole arrays, where each array comprises N point dipoles, which mimic the dipoles due to the docking groups including the bond dipoles. Then, we calculated the shift in electrostatic energy an electron would experience in the middle of the two arrays, E_{ES}, at the position of the central molecule as well as at the position of a border molecule. Figure 3b shows these energies relative to the corresponding energies for a continuous monolayer for increasing cluster size. These data confirm several of the trends discussed already above for the small clusters calculated quantum-mechanically: The energy at the position of the central molecule gradually shifts towards the monolayer limit. The shift at the position of one of the molecules at the border of the cluster is much smaller and saturates at < 40% of the shift obtained in the monolayer. This again clearly highlights the boundary effects that are expected for transport through a molecular cluster. Consequently the spread in energetic positions of the transmission channels keeps increasing (cf. shaded area in Figure 3a and 3b). In extended clusters, this effect is somewhat offset by the fact that upon increasing the cluster size, the ratio of molecules (dipoles) at the border of the cluster relative to molecules inside the cluster drops dramatically, as seen in Figure 3c. These trends are also confirmed by the following experimental observation, where a huge difference in the current between a single-molecule junction and a ~10 nm wide array (which is ~ 20 times larger than the typical intermolecular distances in such junctions, i.e. around 400 molecules) is found,[40] while much smaller differences between a 10nm and a 10mm wide junction were observed.[41]

While the qualitative conclusions from the electrostatic model match those of the quantum-mechanical calculations for the cluster consisting of the pyridine-docked molecules, there is also one fundamental difference: While in the quantum-mechanical simulations the monolayer limit is nearly reached for the 16-molecule cluster, much larger structures are needed in the electrostatic model. A possible reason for this discrepancy are depolarization effects.[23,25] These are expected to be less pronounced for border molecules, hence, the average dipole per molecule is larger for small clusters and should decrease with increasing cluster size. While these effects are fully accounted for in our quantum-mechanical calculations they are not considered in the electrostatic point dipole model. Another potential reason lies in an electronic peculiarity of the pyridine docking group: For pyridine-docked junctions, the lowest unoccupied transport channels frequently aligns with E_F,[21,42] an effect known as Fermi-level pinning.[43,44] In the present case that means that for clusters containing more than 16 molecules, the electrostatically induced trend of a shift of transmission features to lower energies would continue, but this would result in unoccupied states lying below the Fermi level. Thus, in thermodynamic equilibrium either charge is redistributed (typically in flat-lying molecules)[45] or the adsorbate layer is polarized (usually in upright-standing monolayers)[44] with the consequence that the electronic states in the monolayer get aligned with the metal Fermi level.

After discussing the pyridine-linked system, we compare these results to thiolate-, and isocyanide-linked junctions. A complication in those systems is that the transmission peaks become very broad due to the strong coupling of the docking atoms to the junction. This makes a determination of the positions of transmission peaks difficult, if not impossible. However, to obtain quantitative trends also for these systems, we calculate the (zero-bias) conductance, $G(E_F)$, per molecule. The results are plotted for increasing cluster size and compared to the

monolayer conductance in Figure 4. For both systems, the conductance per molecule is significantly different for the single molecule and the monolayer. Moreover, the evolution with cluster size follows opposite trends such that in the case of the thiolate-bonded junction the conductance per molecule decreases when approaching the monolayer, while it increases for the isocyanide-linked junction. In contrast to the pyridine linked junction, where the cluster containing 16 molecules was already very close to the monolayer limit due to Fermi level pinning, for these systems the conductance for the 16 molecule cluster reaches around 70-80% of the shift of the monolayer.
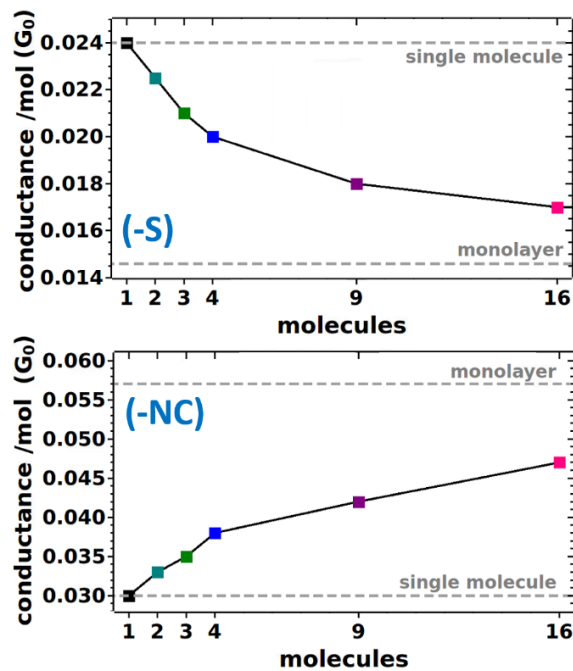
Figure 4. *Calculated zero-bias conductance per molecule, obtained from the calculated transmission function as $G(E_F) = T(E_F).G_0$, for the thiolate (-S) and the isocyanide (-NC) linked molecular junctions for an increasing number of molecules in the cluster. For*

comparison, the two limits of the single molecule and the monolayer junction are indicated (grey dotted lines). $G_0 = 2e^2/h$ refers to the quantum of conductance.

In conclusion, we performed first-principles charge-transport calculations through molecular clusters of increasing size in order to bridge the gap between single molecule und large-area molecular junctions. We explicitly calculated the "scaling" of molecular wires in parallel with a particular focus on collective electrostatic effects which emerge naturally due to the combined electric fields of the bond dipoles at the interface between the molecules and the leads. We showed that collective electrostatic effects appear already at very small cluster sizes and strongly affect the current-voltage characteristics. Compared to extended monolayers, in clusters, charge-transport becomes highly inhomogeneous with pronounced edge effects associated with molecules in locally different electrostatic environments. Supported by electrostatic considerations for larger clusters, we could demonstrate that the scaling of charge-transport with the number of molecules is far from linear. The actual evolution depends strongly on the system at hand and can be complicated by system-specific effects such as Fermi level pinning.

Corresponding Author

*egbert.zojer@tugraz.at

References

1. Cuevas, J. C. & Scheer, E. *Molecular electronics: an introduction to theory and experiment*. (World Scientific, 2010).
2. Xiang, D., Wang, X., Jia, C., Lee, T. & Guo, X. Molecular-Scale Electronics: From Concept to Function. *Chem. Rev.* **116,** 4318–4440 (2016).
3. Nichols, R. J. & Higgins, S. J. Single-Molecule Electronics: Chemical and Analytical Perspectives. *Annu. Rev. Anal. Chem.* **8,** 389–417 (2015).
4. Metzger, R. M. Unimolecular Electronics. *Chem. Rev.* **115,** 5056–5115 (2015).
5. Akkerman, H. B., Blom, P. W. M., de Leeuw, D. M. & de Boer, B. Towards molecular electronics with large-area molecular junctions. *Nature* **441,** 69–72 (2006).
6. Vilan, A., Aswal, D. & Cahen, D. Large-Area, Ensemble Molecular Electronics: Motivation and Challenges. *Chem. Rev.* **117,** 4248–4286 (2017).
7. Cui, X. D. *et al.* Reproducible Measurement of Single-Molecule Conductivity. *Science* **294,** 571–574 (2001).
8. Xu, B. & Tao, N. J. Measurement of Single-Molecule Resistance by Repeated Formation of Molecular Junctions. *Science* **301,** 1221–1223 (2003).
9. Kushmerick, J. G., Naciri, J., Yang, J. C. & Shashidhar, R. Conductance Scaling of Molecular Wires in Parallel. *Nano Lett.* **3,** 897–900 (2003).
10. Salomon, A. *et al.* Comparison of Electronic Transport Measurements on Organic Molecules. *Adv. Mater.* **15,** 1881–1890 (2003).
11. Magoga, M. & Joachim, C. Conductance of molecular wires connected or bonded in parallel. *Phys. Rev. B* **59,** 16011–16021 (1999).
12. Lang, N. D. & Avouris, P. Electrical conductance of parallel atomic wires. *Phys. Rev. B* **62,** 7325–7329 (2000).
13. Reuter, M. G., Seideman, T. & Ratner, M. A. Molecular Conduction through Adlayers: Cooperative Effects Can Help or Hamper Electron Transport. *Nano Lett.* **11,** 4693–4696 (2011).
14. Reuter, M. G., Solomon, G. C., Hansen, T., Seideman, T. & Ratner, M. A. Understanding and Controlling Crosstalk between Parallel Molecular Wires. *J. Phys. Chem. Lett.* **2,** 1667–1671 (2011).
15. Vazquez, H. *et al.* Probing the conductance superposition law in single-molecule circuits with parallel paths. *Nat. Nanotechnol.* **7,** 663–667 (2012).
16. Galperin, M. & Nitzan, A. Cooperative Effects in Inelastic Tunneling. *J. Phys. Chem. B* **117,** 4449–4453 (2013).
17. Guédon, C. M. *et al.* Observation of quantum interference in molecular charge transport. *Nat. Nanotechnol.* **7,** 305–309 (2012).

18. Dubi, Y. Transport Through Self-Assembled Monolayer Molecular Junctions: Role of In-Plane Dephasing. *J. Phys. Chem. C* **118,** 21119–21127 (2014).

19. Egger, D. A., Rissner, F., Zojer, E. & Heimel, G. Polarity Switching of Charge Transport and Thermoelectricity in Self-Assembled Monolayer Devices. *Adv. Mater.* **24,** 4403–4407 (2012).

20. Obersteiner, V., Egger, D. A., Heimel, G. & Zojer, E. Impact of Collective Electrostatic Effects on Charge Transport through Molecular Monolayers. *J. Phys. Chem. C* **118,** 22395–22401 (2014).

21. Obersteiner, V., Egger, D. A. & Zojer, E. Impact of Anchoring Groups on Ballistic Transport: Single Molecule vs Monolayer Junctions. *J. Phys. Chem. C* **119,** 21198–21208 (2015).

22. Cahen, D., Naaman, R. & Vager, Z. The Cooperative Molecular Field Effect. *Adv. Funct. Mater.* **15,** 1571–1578 (2005).

23. Natan, A., Kronik, L., Haick, H. & Tung, R. T. Electrostatic Properties of Ideal and Non-ideal Polar Organic Monolayers: Implications for Electronic Devices. *Adv. Mater.* **19,** 4103–4117 (2007).

24. Blumenfeld, M. L., Steele, M. P. & Monti, O. L. A. Near- and Far-Field Effects on Molecular Energy Level Alignment at an Organic/Electrode Interface. *J. Phys. Chem. Lett.* **1,** 145–148 (2010).

25. Monti, O. L. A. Understanding Interfacial Electronic Structure and Charge Transfer: An Electrostatic Perspective. *J. Phys. Chem. Lett.* **3,** 2342–2351 (2012).

26. Kovalchuk, A. *et al.* Transition voltages respond to synthetic reorientation of embedded dipoles in self-assembled monolayers. *Chem. Sci.* **7,** 781–787 (2015).

27. Kovalchuk, A. *et al.* Dipole-induced asymmetric conduction in tunneling junctions comprising self-assembled monolayers. *RSC Adv.* **6,** 69479–69483 (2016).

28. Bumm, L. A. *et al.* Are Single Molecular Wires Conducting? *Science* **271,** 1705–1707 (1996).

29. Dyck, C. V., Geskin, V., Kronemeijer, A. J., Leeuw, D. M. de & Cornil, J. Impact of derivatization on electron transmission through dithienylethene-based photoswitches in molecular junctions. *Phys. Chem. Chem. Phys.* **15,** 4392–4404 (2013).

30. Xue, Y., Datta, S. & Ratner, M. A. Charge transfer and 'band lineup' in molecular electronic devices: A chemical and numerical interpretation. *J. Chem. Phys.* **115,** 4292–4299 (2001).

31. Lindsay, S. M. & Ratner, M. A. Molecular Transport Junctions: Clearing Mists. *Adv. Mater.* **19,** 23–31 (2007).

32. Zotti, L. A. *et al.* Revealing the Role of Anchoring Groups in the Electrical Conduction Through Single-Molecule Junctions. *Small* **6,** 1529–1535 (2010).

33. Kresse, G. & Furthmüller, J. Efficient iterative schemes for *ab initio* total-energy calculations using a plane-wave basis set. *Phys. Rev. B* **54,** 11169–11186 (1996).

34. Perdew, J. P., Burke, K. & Ernzerhof, M. Generalized Gradient Approximation Made Simple. *Phys. Rev. Lett.* **77,** 3865–3868 (1996).

35. Papior, N. R., Lorente, N., Frederiksen, T., García, A. & Brandbyge, M. Improvements on non-equilibrium and transport Green function techniques: The next-generation TRANSIESTA. *Comput. Phys. Commun.* **212,** 8–24 (2017).

36. Kokalj, A. XCrySDen—a new program for displaying crystalline structures and electron densities. *J. Mol. Graph. Model.* **17,** 176–179 (1999).

37. Humphrey, W., Dalke, A. & Schulten, K. VMD: Visual molecular dynamics. *J. Mol. Graph.* **14,** 33–38 (1996).

38. Quek, S. Y., Choi, H. J., Louie, S. G. & Neaton, J. B. Length Dependence of Conductance in Aromatic Single-Molecule Junctions. *Nano Lett.* **9,** 3949–3953 (2009).

39. Kamenetska, M. *et al.* Conductance and Geometry of Pyridine-Linked Single-Molecule Junctions. *J. Am. Chem. Soc.* **132,** 6817–6821 (2010).

40. Selzer, Y. *et al.* Effect of Local Environment on Molecular Conduction: Isolated Molecule versus Self-Assembled Monolayer. *Nano Lett.* **5,** 61–65 (2005).

41. Sangeeth, C. S. S. *et al.* Comparison of DC and AC Transport in 1.5–7.5 nm Oligophenylene Imine Molecular Wires across Two Junction Platforms: Eutectic Ga–In versus Conducting Probe Atomic Force Microscope Junctions. *J. Am. Chem. Soc.* **138,** 7305–7314 (2016).

42. Van Dyck, C. & Ratner, M. A. Molecular Junctions: Control of the Energy Gap Achieved by a Pinning Effect. *J. Phys. Chem. C* **121,** 3013–3024 (2017).

43. Braun, S., Salaneck, W. R. & Fahlman, M. Energy-Level Alignment at Organic/Metal and Organic/Organic Interfaces. *Adv. Mater.* **21,** 1450–1472 (2009).

44. Ma, Z. *et al.* Electronic structure of pyridine -based SAMs on flat Au(111) surfaces: extended charge rearrangements and Fermi level pinning. *Phys. Chem. Chem. Phys.* **13,** 9747–9760 (2011).

45. Edlbauer, H., Zojer, E. & Hofmann, O. T. Postadsorption Work Function Tuning via Hydrogen Pressure Control. *J. Phys. Chem. C* **119,** 27162–27172 (2015).

2.3 Electrostatic Design of 3D Covalent Organic Networks

2.3.1 Author Contribution

E. Zojer conceived the idea to incorporate polar elements into 3D covalent organic networks to exploit collective electrostatic effects in 3D materials. Supervised by E. Zojer and V. Obersteiner, A. Jeindl and J. Götz performed first preliminary studies on molecular clusters and simple periodic systems during their Bachelor Theses. V. Obersteiner hugely expanded the range of studied systems and overcame all technical challenges that were encountered especially when using hybrid functionals in conjunction with periodic boundary conditions for the comparably large systems studied here. She also analyzed the data in close cooperation with E. Zojer and O. Hofmann. A. Perveaux did some calculations for the fluorinated system as well as for the cascade systems. O. T. Hofmann provided significant technical support. V. Obersteiner wrote the first version of the manuscript, prepared all figures and together with E. Zojer compiled the paper. E. Zojer supervised the project.

2.3.2 Original Article

Article type: Communication

Electrostatic Design of 3D Covalent Organic Networks

Veronika Obersteiner, Andreas Jeindl, Johannes Götz, Aurelie Perveaux, Oliver T. Hofmann, and Egbert Zojer[*]

Institute of Solid State Physics, NAWI Graz, Graz University of Technology, Petersgasse 16, 8010 Graz, Austria

*egbert.zojer@tugraz.at

Abstract

An innovative strategy for electrostatically designing the electronic structure of 3D bulk materials is proposed to control charge carriers at the nanoscale. This is achieved by shifting the electronic levels of chemical identical semiconducting elements through the periodic arrangement of polar functional groups. For the example of covalent organic networks, by first-principles calculations, the resulting collective electrostatic effects are shown to allow a targeted manipulation of their electronic landscape such that spatially confined pathways for electrons and holes can be realized. Mimicking donor-acceptor bulk heterojunctions, the new materials hold high promise for photovoltaic applications. The distinct advantage over the conventional approach of splitting excitons through chemically distinct donor and acceptor units is that here the magnitude of the band offset can be continuously tuned by varying dipole densities. A particularly promising feature of the suggested strategy is its structural versatility, which also enables the realization of more complex quantum structures such as quantum-cascades and quantum-checkerboards.

We portray an innovative strategy for designing the electronic structure of 3D materials, where we use polar functional groups to control the energy landscape and localization of electronic states. The approach is discussed for the prototypical example of bulk heterojunctions. These are commonly applied in organic solar cells as active layers responsible for dissociating the photogenerated excitons. Bulk heterojunctions consist of phase separated electron donating (D) and accepting (A) regions. An approach for achieving a sensitive control over their nano-morphology is incorporating the donating and accepting elements into Covalent-Organic Frameworks (COFs). In this way, D/A bulk heterojunctions with a maximized internal interface can be realized, in which a periodic and well-controlled arrangement of the organic building blocks is ensured by covalent bonds. [1–8] Traditional design strategies for realizing donor-acceptor COFs either use a donor covalently bound to the inner wall of an accepting COF (i.e., wall functionalization)[6] or they rely on constructing the walls from alternatingly donating and accepting functional units.[3,4,7,8] The π-stacked columns of the layered donor-acceptor sheets then provide pathways for electrons and holes,[1] facilitating charge transport in the stacking direction. The alignment of the electronic states in such type-II heterostructures, i.e. the offsets between the local valence- and conduction-band edges, is usually determined by changing the ionisation energy and electron affinity of the individual donating and accepting segments. [5,6,9,10]

In the present contribution, we employ a fundamentally different strategy for controlling the energetic positions and localization of electronic states: We employ chemically identical building blocks as nominally donating and accepting units, but achieve an equivalent band offset as in the D/A systems through so-called collective electrostatic effects. These occur when assembling periodic arrays of polar groups within a material in an ordered fashion. Then the superposition of their electric fields dramatically changes the energy landscape.[11–16] Such an approach has recently been suggested for manipulating the electronic states within graphene[17] and semiconducting self-assembled monolayers (SAMs) on metal substrates.[18] First proof of principle experiments on SAMs have already confirmed the induced potential step within the monolayer[16] and its significant impact on ballistic charge transport through the SAMs.[19]

Here we go decisively beyond these approaches, showing how electrostatic design can be used to control charges at a nanoscopic level in bulk materials with the ultimate goal to

locally control exciton dissociation and to realize confined pathways for electrons and holes. The distinct advantage over the above-discussed donor-acceptor based bulk heterostructures is that electrostatic design allows a quasi-continuous tuning of the offset between energy levels by varying the dipole density. This can be very useful for solar cells consisting of organic chromophores, as this offset is the driving force for overcoming the often considerable exciton binding energies. At the same time, the level offset needs to be small enough to avoid an excessive loss of energy to the creation of phonons. By a suitable design of the polar sections, electrostatic design also allows the realization of much more complex energy landscapes. As prototypical examples for those, we discuss 3D quantum-cascades and quantum-checkerboards.

The suggested approach is not restricted to a specific class of materials, as it solely relies on the superposition of the electric fields generated by an ordered array of dipolar elements. In fact, it can be applied to any type of structure (be it organic or inorganic) in which regular arrangements of dipolar functional groups can be realized. Therefore, in the present paper we focus on conceptually and structurally simple systems, in which the energetic shifts due to collective electrostatic effects can be seen most clearly without any interference from complex functional elements. Thus we here discuss the electrostatic design idea on the basis of 3D networks consisting of identical semiconducting units (i.e.., chromophore segments). The collective electrostatic effects are realized by a periodic arrangement of linking units containing a dipolar element.

In this way, complex energy landscapes of electronic states can be realized. Prototypical examples of the resulting structures are shown in **Figure 1**. We choose (zinc)-porphyrin units as classical semiconducting chromophores, as they are frequently used in COF-based systems. [20–27] and are also commonly employed in organic solar cells.[28,29] Depending on the specific position of the porphyrin in the structure and the linking direction, they are connected either by triacetylene groups (apolar and chosen to avoid any steric complications) or by linkers in which the central acetylene group is replaced by a polar unit. For the example shown in Figure 1 this is 1,3-difluorobenzene (*F*); other polar linkers will be discussed below. Depending on the orientation of the dipolar elements (indicated by the brown arrows) and their arrangement one can create a number of different architectures of varying complexity. Two prototypical arrangements are the "stripe structure" and the "checkerboard structure" shown in Figure 1. We refrain from including functional groups containing reversible bonds like boronates or imines into the linkers of our model systems in

4

order to keep the systems simple and not to divert from the main effects, even though in practice such elements are useful for achieving a high degree of crystallinity.[9] As far as electrostatic design is concerned, their primary impact is an amplification or a reduction of the energetic shifts depending on whether their intrinsic dipoles are arranged parallel or antiparallel to those of the main polar units of the linkers.

In the third dimension, which is usually referred to as the stacking direction, we introduce vertical linkers that connect the zinc atoms of porphyrin units of subsequent layers (see Figure 1c). We specifically choose 1,4 –diazobicycle[2.2.2]octane (*DABCO*) and 4,4'-bipyridine as they are commonly used linkers for metal organic frameworks (MOFs). [30–33] Moreover, in several instances they have been used to link zinc-porphyrin units. [34–36]

The band alignment in the above-described systems solely depends on the electrostatically triggered energetic shift between chemically identical semiconducting elements (the porphyrins), one can identify two major handles to tune the energetic offset: (i) one can either vary the magnitude of the *dipole moment* per in-plane linker by changing the polar group; (ii) alternatively, one can change the *linker density*. Notably, the two handles are not fully independent, as increasing the linker density reduces the dipole moment per linker due to depolarization effects.[10, 32–34]
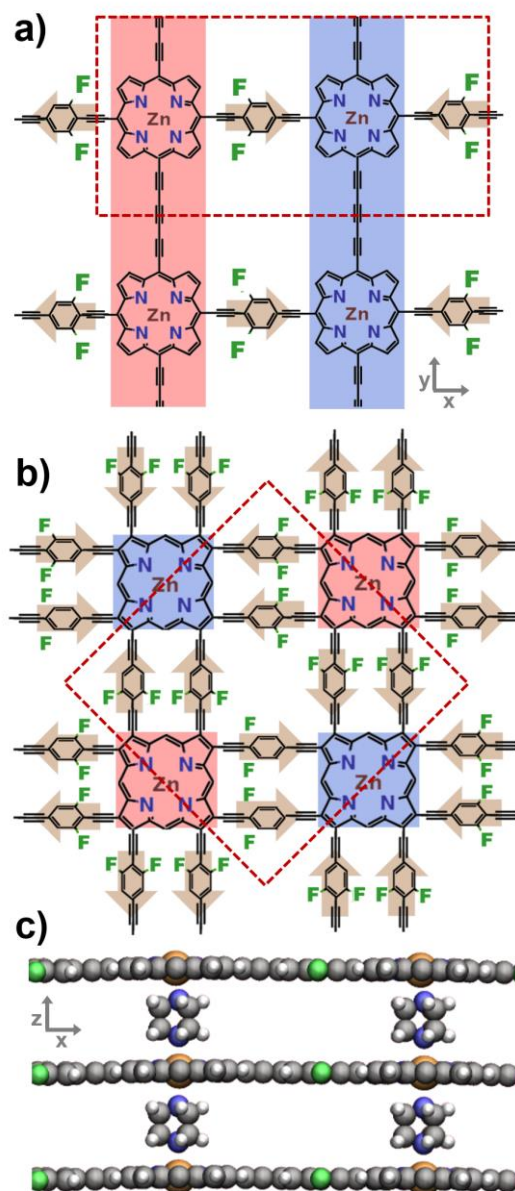
Figure 1: *Chemical structures of prototypical examples of electrostatically designed covalent organic networks: (**a**) stripe architecture and (**b**) checkerboard structure. The red dashed lines indicate the unit cells used in the periodic DFT calculations. The arrows represent the directions of the dipole moments of the linking elements. The red (blue) shaded areas indicate regions where lowered (raised) electrostatic energies for electrons are expected. Besides the symmetry of the arrangement of the polar units the two displayed model systems also differ in their dipole densities. This is achieved by using singly (**a**) and doubly (**b**) linked structures (for more details see main text). A 3D representation of the model system is shown in (**c**), where 1,4 –diazobicycle[2.2.2]octane (DABCO) represents a typical vertical linker. Color code for the atoms: grey =C, white=H, blue=N, orange=Zn, green=F.*

To change the polarity of the linking groups we consider 1,3-dichlorobenzene (*CL*), pyrimidine (*PYR*), 1,3-difluorobenzene (*F*), and boron nitride (*BN*). They exhibit dipole moments of 0.56, 1.43, 1.94 and 6.86 Debye when calculated for an isolated singly linked porphyrin dimer. The differences between the various linkers are reduced when including them into the networks due to the above-mentioned depolarization effects, an effect that is fully accounted for in our periodic-boundary condition calculations.. The B≡N linker is of hypothetical nature, but is still included here to show that very large shifts are feasible for large dipole moments. More realistic ways for achieving such large dipole moments would, for example, be multiple repetitions of the other polar elements.

The modification of the linker density can be achieved in two different ways: First, the distance in stacking direction can be changed by increasing the length of the vertical linker from *DABCO* to *BIPYRIDINE*. Additionally, varying between single- and double-linking of porphyrin units (cf., Figure 1 a and b) is a viable scenario considering that both linking motifs have been discussed in literature. [40–42]

To adopt a consistent nomenclature we introduce systematic abbreviations for the different model systems following the scheme *[vertical linker]_[#polar linkers]_[architecture]*. In that spirit the material shown in Figure 1a is referred to as *DABCO_1F_stripe* and the one in Figure 1b is denoted as *DABCO_2F_checkerboard* (in both cases assuming that DABCO linkers form the connection in the third dimension). The chemical structures of all systems can be found in Figure S5 (Supporting Information).

To present the general idea and discuss the underlying physics, we choose the *DABCO_1F_stripe* system as shown in Figure 1a. The corresponding contour plot of the electrostatic energy for an electron in a plane perpendicular to the stacking direction is shown in Figure 2. One clearly sees the expected division into stripes of high and low energy due to the superposition of the electric fields of the dipolar 1,3-difluorobenzene (*F)* linkers. An interesting observation in this context is the relatively abrupt change of the energy, which is fully consistent with the work of Natan et al.[13], who showed that the decay length of the field of a 2D array of point dipoles is nearly an order of magnitude shorter than the inter-dipole distance.
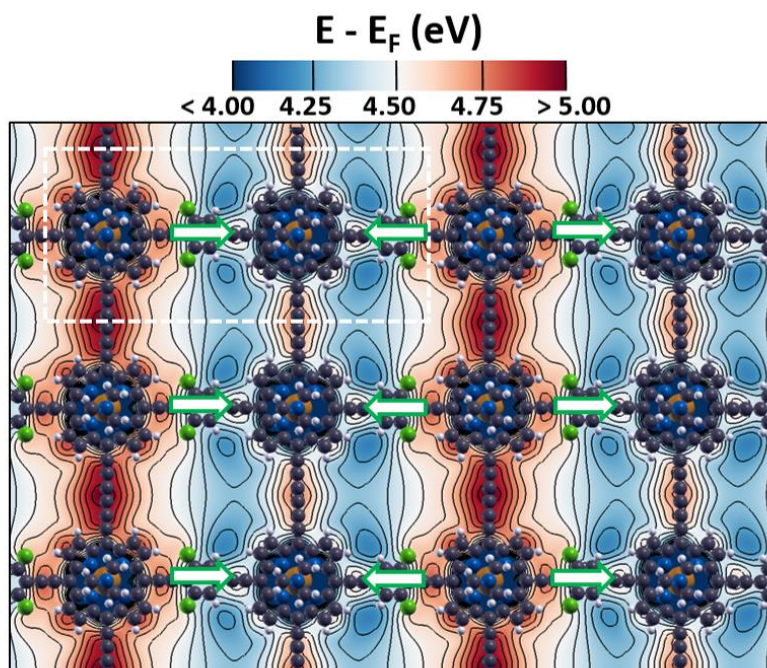
Figure 2. *Contour plot of the electrostatic energy of an electron for the DABCO_1F_stripe system in a plane perpendicular to the stacking direction (approximately 2.5 Å away from the molecular plane to avoid extensive variations near the nuclei). The electrostatic energy is given relative to the Fermi level. Isolines are drawn every 0.15 eV. The arrows represent the directions of the dipole moments of the linking elements. Color code for the atoms: grey =C, white=H, blue=N, orange=Zn, green=F.*

To evaluate the consequences of these potential variations, it is useful to perform an in-depth analysis of the location of the electronic states in the 3D periodic system. In the absence of dipolar units, electronic states extend in both spatial directions due to the strong electronic coupling within the linked porphyrin plane. This is manifested in strongly dispersing bands in X- and Y-direction with band widths of 0.5 eV, see Figure S4 (Supporting Information). When introducing dipolar elements, this coupling is broken due to the electrostatically induced energetic shifts, diminishing the band width in the direction parallel to the dipoles to less than 0.1 eV. Hence, as can be seen from the schematic band alignment contained in Figure 3a, the electronic states should localize in the respective stripes and they should be energetically shifted with respect to each other.
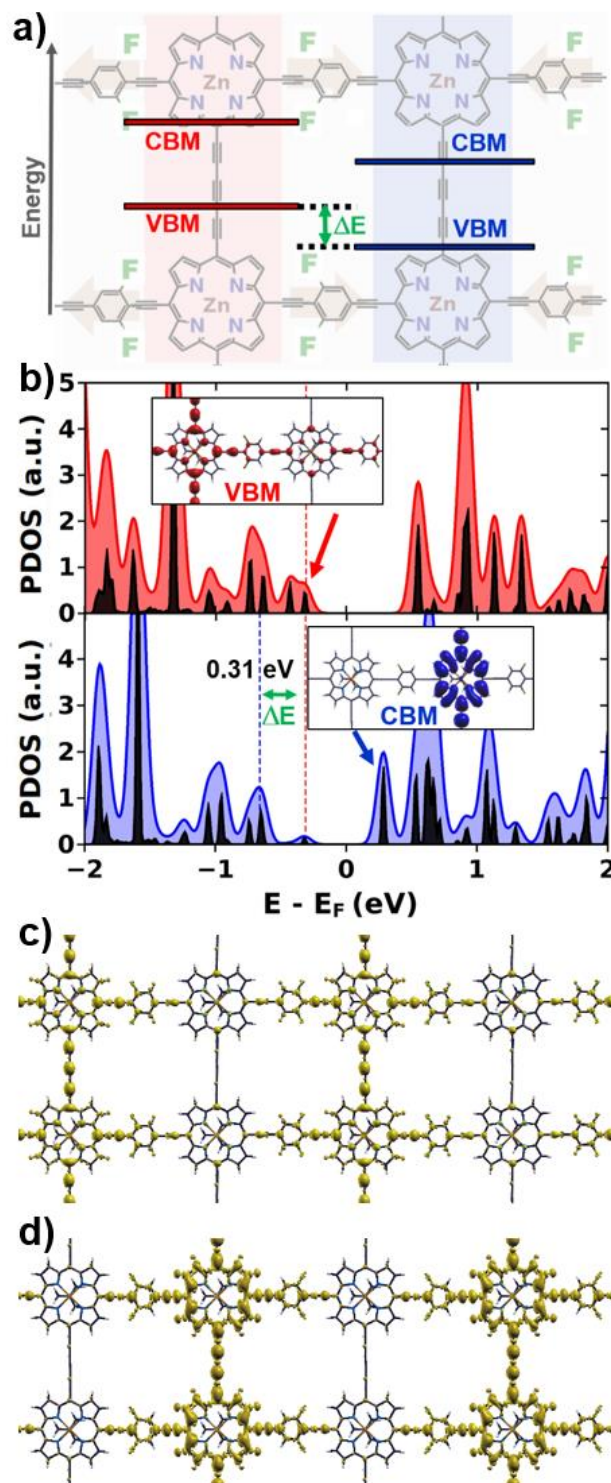
Figure 3. *(a) Energy level alignment of the heterojunction achieved by electrostatic design for the DABCO_1F_stripe system. The band offset between VBMs (valence-band maxima) and CBMs (conduction-band minima) of electrostatically shifted stripes is indicated by ΔE. (b) Density of states projected onto different parts of the unit cell for the DABCO_1F_stripe system; top panel: DOS projected onto the high electrostatic energy*

9

side, i.e. red region in (a); bottom panel: DOS projected onto the low electrostatic energy side, i.e. blue region on (a). The energy is aligned to the Fermi level. The black lines represent the projected density of states (PDOS) obtained directly from the calculations with a Gaussian broadening of 0.01 eV while the red and blue shaded areas show the PDOS with a Gaussian broadening of 0.05 eV applied in a post-processing routine, serving as a guide to the eye. Isodensity plots of the Gamma-point states of the valence and conduction bands are included as insets (isovalue of 0.03 states per Å ^{3}). (c) and (d) show 3D isodensity plots of the charge density differences between the neutral system and the equivalent positively (c) and negatively (d) charged DABCO_1F_stripe system. An isovalue of 0.0004 electrons per Å^3 was used. More quantitative information independent of the choice of the isodensity value can be obtained by plotting the plane averaged charge density difference, see Figure S6 in the Supporting Information. There we also report the results of a Mulliken population analysis, which fully confirms the trends inferred from Figure 3c.

As shown in Figure 3b, these expectations are fully met in the present system, as can be inferred from the densities of states (DOS) projected onto regions with different electrostatic energy (the regions shaded in blue and red in Figure 3a). One observes an essentially rigid shift of the projected DOSs amounting to 0.31 eV. This shift represents the band offset between the local valence-band maxima VBM, respectively, conduction-band minima CBM of two consecutive stripes (cf., Figure 3a). As the stripes are chemically identical, this offset is solely determined by the fields arising from the polar 1,3-difluorobenzene (*F)* linking groups. In the Supporting Information we included a section highlighting the collectivity of the effect and showing that mesomeric effects caused by the fluorine atoms do not significantly impact the situation. The fact that the frontier bands below and above the Fermi level are localized in different spatial regions can be clearly seen from the corresponding local densities of states (LDOSs) plotted as insets in Figure 3b. This suggests that in these electrostatically designed covalent networks, pathways for electrons and holes should be decoupled from each other.

To verify that, we studied the localization of excess electrons and holes in the system by either adding or removing 0.1 electrons per unit cell (containing two porphyrin units). Such local excess charges could result either from exciton dissociation or from carrier

injection at electrodes. The charge density differences between the neutral and charged systems are shown in Figure 3c and d. They nicely correlate with the isodensity plots of the LDOSs of the frontier states (insets of Figure 3b). This is insofar remarkable, as the localization of the charges occurs without considering the strong electron-phonon coupling in organic semiconductors (often also termed polaronic effects), which usually drive spatial localization of charge carriers in such materials.

Exciton binding energies in organic semiconducting materials have been reported to range from a few tenths of an eV up to several eV. [43–45] As a driving force for dissociating these excitons into separate charge carriers, one usually exploits the offset of the energy levels in type-II bulk heterojunctions. Consequently, this offset needs to be sufficient for ensuring efficient exciton dissociation. At the same time, it should not be too large as this would result in an unnecessary dissipation of energy and, thus, in a reduction of the achievable open-circuit voltage, when using the materials in solar cells. In this context, a significant advantage of the electrostatic design strategy over changing the chemical nature of the semiconducting units is that it offers a comparably straightforward way of quasi continuously tuning the shift of the energy levels in the nominally electron accepting and donating sections. As mentioned already above, this can be achieved by tuning the dipole density either through varying the dipole moment of the linkers, the number of linkers between porphyrin units, or the spacing between the layers. As shown in Figure 4, in this way we are indeed capable of significantly varying the band-offset for the considered systems.
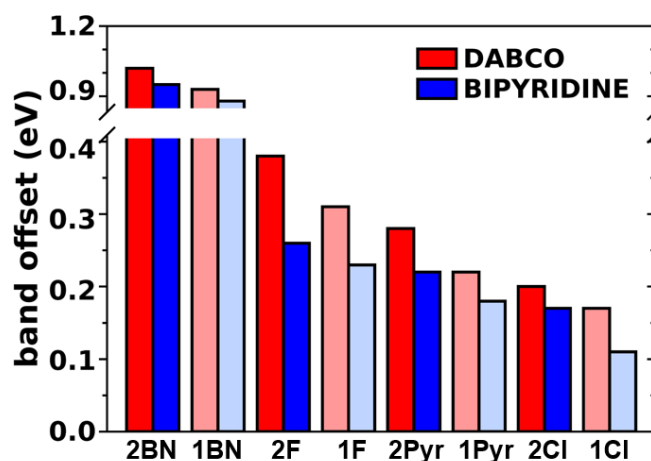
Figure 4. *Band offset, ΔE, between VBMs and CBMs of electrostatically different stripes achieved by collective electrostatic design. ΔE can be quasi continuously tuned between*

0.11 to 1.02 eV depending on the used dipolar elements and linker densities. The used polar linkers are 1,3-dichlorobenzene (CL), pyrimidine (PYR), 1,3-difluorobenzene (F), and boron nitride (BN). Pale bars refer to singly-linked structures, while solid bars refer to the doubly-linked equivalents. The chemical structures of all systems can be found in Figure S5 (Supporting Information). The values for ΔE are taken from the PDOS plots shown in Figure S7-S10 and summarized in Table S2 in the Supporting Information.

Electrostatic design also allows the realization of a multitude of complex quantum structures, where the checkerboard architecture introduced in Figure 1b is only one example. The corresponding contour plot of the electrostatic energy is shown in Figure 5a. The obtained band offset (0.47 eV for *DABCO_2F_checkerboard*) and the projected densities of states are similar to the stripe structure, but here, carrier transport within the sheets is largely suppressed. This can be gauged from the observation that the band-dispersion essentially vanishes both in the X and Y-directions. I.e., compared to the striped structure, now also the band width in Y-direction is reduced from 0.15 (0.35) eV to 0.00 (0.15) eV for the valence and conduction bands, respectively (see Figure S11 in the Supporting Information).
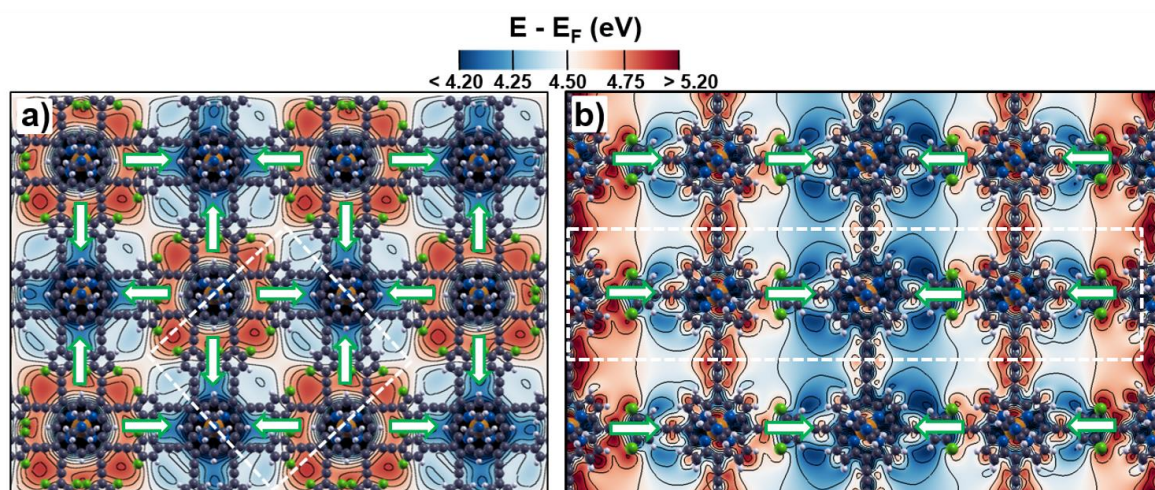
Figure 5. *Contour plot of the electrostatic energy for (a) the DABCO_2F_checkerboard system and (b) the BIPYRIDINE_1F_cascade system in a plane perpendicular to the stacking direction, approximately 2.5 Å away from the molecular plane to avoid extensive variations in the energy near the nuclei. The energy is given relative to the respective Fermi level. Isolines*

are drawn every 0.15 eV. Unit cells are indicated as dashed white boxes. The arrows represent the directions of the dipole moments of the linking elements. Color code for the atoms: grey =C, white=H, blue=N, orange=Zn, green=F.

Another interesting structure that is much more difficult to realize with conventional strategies is the quantum cascade architecture, which is shown in Figure 5b for the example of *BIPYRIDINE_1F_cascade* (the corresponding chemical structure is shown in Figure S12, Supporting Information). Compared to the stripe topology discussed above, where the dipoles in the linking groups connecting successive stripes point in opposite directions, here the dipole orientation of the linkers switches only after several (in the displayed system after two) stripes. This creates an energetic staircase, as can again be inferred from the electrostatic energy shown in Figure 5b. The electronic states follow the characteristics of the energy landscape resulting in a subsequent shift of about 0.3 eV between the band edges in subsequent regions (see Figure S13, Supporting Information). In this way, the highest and lowest energy stripes (and consequently also the states at the corresponding band edges) are well separated in space. Such a structure could, for example, help minimizing recombination losses in photovoltaic cells.

In conclusion, based on first-principle calculations, we have shown that electrostatic design is a highly promising approach for manipulating the electronic properties of bulk materials. To illustrate how charges can be controlled at the nanoscale through ordered arrangements of polar units, we studied 3D covalent organic networks and discussed their properties primarily in view of their potential applications in photovoltaics. Through electrostatic design we achieve an energy-level offset between otherwise chemically identical semiconducting segments. This is in stark contrast to conventional donor-acceptor COFs, where chemically distinct building blocks provide the donor and acceptor functionality needed to dissociate excitons. Through the inclusion of polar building blocks into the networks, we are able to manipulate the electronic landscape in a controlled way, achieving spatially confined pathways for electrons and holes. Varying the dipole density in the considered systems offers the possibility to continuously tune the magnitude of the band offset over a wide energy range. Changing the position and orientation of the introduced dipolar elements allows the design of architectures with conceptually different potential distributions, such as stripes, checkerboards or quantum-cascades. These aspects endow the

electrostatic design approach with significant potential for the realization of materials with novel properties far beyond the organic networks discussed here.

Experimental Section

To determine the electronic structure of the systems and optimize their geometries, we performed band-structure calculations within the framework of density-functional theory (DFT) using the Fritz-Haber-Institute *ab initio* molecular simulations (FHI-*aims*) code. [46] We applied the Perdew-Burke-Ernzerhof (PBE)[47] exchange-correlation functional augmented with the Tkatchenko-Scheffler scheme[48] to account for van der Waals interactions for geometry optimization and the hybrid functional HSE06[49] for single point calculations. We applied a converged set of light basis functions at the tier2 level and a 2 x 4 x 20 Monkhorst-Pack k-point grid for all studied systems in stripe architecture. For the checkerboard structure we used a converged k-point grid of 4 x 4 x 20. Full details on the applied computational methodology (in particular also the pursued geometry optimization procedure) and numerical parameters used in our calculations are contained in the Supporting Information. The latter also contains a discussion on how the electronic structure of the materials is changed when employing the PBE (i.e. a generalized gradient approximation based functional) instead of the hybrid HSE06 functional. VMD[50], XCrySDen[51] and Mayavi2[52] were used for graphical visualization.

Supporting Information

Supporting Information is available from the Wiley Online Library or from the author.

Acknowledgements

References

[1]   X. Feng, L. Chen, Y. Honsho, O. Saengsawang, L. Liu, L. Wang, A. Saeki, S. Irle, S. Seki, Y. Dong, D. Jiang, *Adv. Mater.* **2012**, *24*, 3026.

[2]   M. Dogru, M. Handloser, F. Auras, T. Kunz, D. Medina, A. Hartschuh, P. Knochel, T. Bein, *Angew. Chem.* **2013**, *125*, 2992.

[3]   S. Jin, X. Ding, X. Feng, M. Supur, K. Furukawa, S. Takahashi, M. Addicoat, M. E. El-Khouly, T. Nakamura, S. Irle, S. Fukuzumi, A. Nagai, D. Jiang, *Angew. Chem. Int. Ed.* **2013**, *52*, 2017.

[4]   S. Jin, K. Furukawa, M. Addicoat, L. Chen, S. Takahashi, S. Irle, T. Nakamura, D. Jiang, *Chem. Sci.* **2013**, *4*, 4505.

[5]   M. Dogru, T. Bein, *Chem Commun* **2014**, *50*, 5531.

[6]   L. Chen, K. Furukawa, J. Gao, A. Nagai, T. Nakamura, Y. Dong, D. Jiang, *J. Am. Chem. Soc.* **2014**, *136*, 9806.

[7]   M. Calik, F. Auras, L. M. Salonen, K. Bader, I. Grill, M. Handloser, D. D. Medina, M. Dogru, F. Löbermann, D. Trauner, A. Hartschuh, T. Bein, *J. Am. Chem. Soc.* **2014**, *136*, 17802.

[8]   S. Jin, M. Supur, M. Addicoat, K. Furukawa, L. Chen, T. Nakamura, S. Fukuzumi, S. Irle, D. Jiang, *J. Am. Chem. Soc.* **2015**, *137*, 7817.

[9]   N. Huang, P. Wang, D. Jiang, *Nat. Rev. Mater.* **2016**, *1*, 16068.

[10] S.-Y. Ding, W. Wang, *Chem Soc Rev* **2013**, *42*, 548.

[11] D. Cahen, R. Naaman, Z. Vager, *Adv. Funct. Mater.* **2005**, *15*, 1571.

[12] A. Natan, Y. Zidon, Y. Shapira, L. Kronik, *Phys. Rev. B* **2006**, *73*, 193310.

[13] A. Natan, L. Kronik, H. Haick, R. T. Tung, *Adv. Mater.* **2007**, *19*, 4103.

[14] G. Heimel, F. Rissner, E. Zojer, *Adv. Mater.* **2010**, *22*, 2494.

[15] O. L. A. Monti, *J. Phys. Chem. Lett.* **2012**, *3*, 2342.

[16] T. Abu-Husein, S. Schuster, D. A. Egger, M. Kind, T. Santowski, A. Wiesner, R. Chiechi, E. Zojer, A. Terfort, M. Zharnikov, *Adv. Funct. Mater.* **2015**, *25*, 3943.

[17] G. J. Kraberger, D. A. Egger, E. Zojer, *Adv. Mater. Interfaces* **2015**, *2*, n/a.

[18] B. Kretz, D. A. Egger, E. Zojer, *Adv. Sci.* **2015**, *2*, n/a.

[19] A. Kovalchuk, T. Abu-Husein, D. Fracasso, D. A. Egger, E. Zojer, M. Zharnikov, A. Terfort, R. C. Chiechi, *Chem. Sci.* **2016**, *7*, 781.

[20] E.-Y. Choi, P. M. Barron, R. W. Novotny, H.-T. Son, C. Hu, W. Choe, *Inorg. Chem.* **2009**, *48*, 426.

[21] A. Nagai, X. Chen, X. Feng, X. Ding, Z. Guo, D. Jiang, *Angew. Chem. Int. Ed.* **2013**, *52*, 3770.

[22] X. Ding, X. Feng, A. Saeki, S. Seki, A. Nagai, D. Jiang, *Chem. Commun.* **2012**, *48*, 8952.

[23] B. J. Burnett, P. M. Barron, W. Choe, *CrystEngComm* **2012**, *14*, 3839.

[24] M. C. So, S. Jin, H.-J. Son, G. P. Wiederrecht, O. K. Farha, J. T. Hupp, *J. Am. Chem. Soc.* **2013**, *135*, 15698.

[25] N. Huang, X. Chen, R. Krishna, D. Jiang, *Angew. Chem.* **2015**, *127*, 3029.

[26] X. Chen, J. Gao, D. Jiang, *Chem. Lett.* **2015**, *44*, 1257.

[27] H. Wang, H. Ding, X. Meng, C. Wang, *Chin. Chem. Lett.* **2016**, *27*, 1376.

[28] C. W. Tang, *Appl. Phys. Lett.* **1986**, *48*, 183.

[29] M. G. Walter, A. B. Rudine, C. C. Wamser, *J. Porphyr. Phthalocyanines* **2010**, *14*, 759.

[30] J. Kesters, P. Verstappen, M. Kelchtermans, L. Lutsen, D. Vanderzande, W. Maes, *Adv. Energy Mater.* **2015**, *5*, 1500218.

[31] O. Shekhah, H. Wang, M. Paradinas, C. Ocal, B. Schüpbach, A. Terfort, D. Zacher, R. A. Fischer, C. Wöll, *Nat. Mater.* **2009**, *8*, 481.

[32] J. Zhuang, J. Friedel, A. Terfort, *Beilstein J. Nanotechnol.* **2012**, *3*, 570.

[33] B. Liu, O. Shekhah, H. K. Arslan, J. Liu, C. Wöll, R. A. Fischer, *Angew. Chem. Int. Ed.* **2012**, *51*, 807.

[34] Z. Wang, J. Liu, H. K. Arslan, S. Grosjean, T. Hagendorn, H. Gliemann, S. Bräse, C. Wöll, *Langmuir* **2013**, *29*, 15958.

[35] P. N. Taylor, H. L. Anderson, *J. Am. Chem. Soc.* **1999**, *121*, 11538.

[36] C. A. Hunter, M. N. Meah, J. K. M. Sanders, *J. Am. Chem. Soc.* **1990**, *112*, 5773.

[37] E. Iengo, E. Zangrando, R. Minatel, E. Alessio, *J. Am. Chem. Soc.* **2002**, *124*, 1003.

[38] D. Cornil, Y. Olivier, V. Geskin, J. Cornil, *Adv. Funct. Mater.* **2007**, *17*, 1143.

[39] D. Deutsch, A. Natan, Y. Shapira, L. Kronik, *J. Am. Chem. Soc.* **2007**, *129*, 2989.

[40] L. Romaner, G. Heimel, E. Zojer, *Phys. Rev. B* **2008**, *77*, 045113.

[41] P. N. Taylor, J. Huuskonen, R. T. Aplin, H. L. Anderson, J. Huuskonen, G. Rumbles, E. Williams, *Chem. Commun.* **1998**, 909.

[42] I. Hisaki, S. Hiroto, K. S. Kim, S. B. Noh, D. Kim, H. Shinokubo, A. Osuka, *Angew. Chem. Int. Ed.* **2007**, *46*, 5125.

[43] T. Tanaka, A. Osuka, *Chem Soc Rev* **2015**, *44*, 943.

[44] M. Knupfer, *Appl. Phys. A* **2003**, *77*, 623.

[45] A. Dkhissi, *Synth. Met.* **2011**, *161*, 1441.

[46] P. K. Nayak, *Synth. Met.* **2013**, *174*, 42.

[47] V. Blum, R. Gehrke, F. Hanke, P. Havu, V. Havu, X. Ren, K. Reuter, M. Scheffler, *Comput. Phys. Commun.* **2009**, *180*, 2175.

[48] J. P. Perdew, K. Burke, M. Ernzerhof, *Phys. Rev. Lett.* **1996**, *77*, 3865.

[49] A. Tkatchenko, M. Scheffler, *Phys. Rev. Lett.* **2009**, *102*, 073005.

[50] J. Heyd, G. E. Scuseria, M. Ernzerhof, *J. Chem. Phys.* **2003**, *118*, 8207.

[51] W. Humphrey, A. Dalke, K. Schulten, *J. Mol. Graph.* **1996**, *14*, 33.

[52] A. Kokalj, *J. Mol. Graph. Model.* **1999**, *17*, 176.

[53] P. Ramachandran, G. Varoquaux, *Comput. Sci. Eng.* **2011**, *13*, 40.

The electrostatic design of 3D covalent organic networks is presented as an innovative strategy to mimic donor-acceptor bulk heterojunctions. Periodic arrangements of polar building blocks are used to locally shift the energies of the electronic states and to spatially confine the frontier wavefunctions. In this way a driving force for exciton dissociation is realized without the need for using distinct semiconducting units.

V. Obersteiner, A. Jeindl, J. Götz, A. Perveaux, Oliver T. Hofmann, and E. Zojer[*]

Electrostatic Design of 3D Covalent Organic Networks
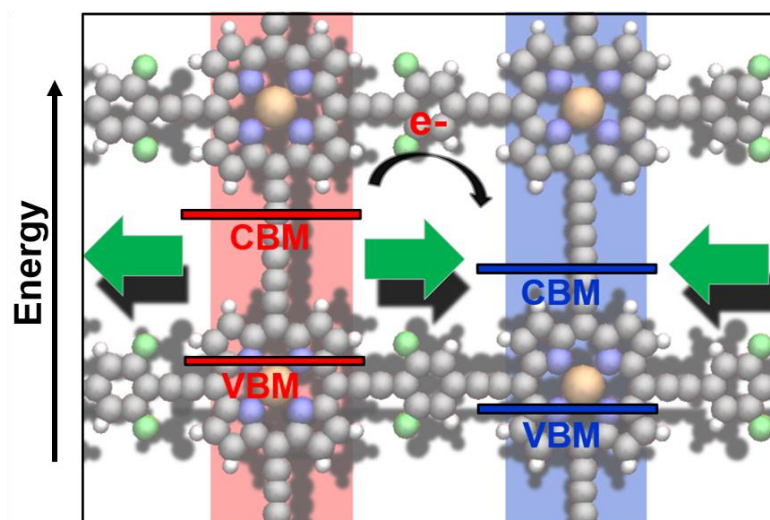
2.3.3 Supporting Information

Supporting Information

Electrostatic Design of 3D Covalent Organic Networks

Veronika Obersteiner, Andreas Jeindl, Johannes Götz, Aurelie Perveaux, Oliver T. Hofmann, and Egbert Zojer[*]

I. Methodological aspects

As described in the main text, dispersion corrected DFT calculations were performed applying the FHI-aims code). For all calculations we used a converged set of basis functions as shipped with the "light" defaults at the tier2 level and a 2 x 4 x 20 and 4 x 4x 20 Monkhorst-Pack k-point grid for the stripe and checkerboard structure respectively. For the cascade structure a converged k-point grid of 1x2x20 was used. The convergence criteria for the self-consistent cycles were set to the default values of 10^{-5} e/Bohr³ for the charge density and 10^{-6} eV for the total energy respectively. The Gaussian smearing occupation scheme[1] was used with a width of 0.01 eV. The density of states was afterwards calculated using a Gaussian broadening with a width of 0.05 eV. To consistently quantify the energetic shift in the PDOS due to collective electrostatic effects we identified the peak corresponding to the highest occupied state in the unbroadened PDOS in both regions, as can be seen from Figure 2b. The Fermi level was set to the center of the band gap. As we are including Zinc as the central atoms of the porphyrin units we included relativistic effects within the atomic ZORA approximation[2].

(a) Geometry Optimization

Geometry optimizations were performed at the PBE level using the trust radius method enhanced version of the Broyden-Fletcher-Goldfarb-Shanno optimization algorithm with a tolerance of 10^{-2} eV/ Å, until the remaining forces were smaller than 10^{-4} eV/ Å. As the geometry optimization for the 3D networks includes the relaxation of every atom as well as the optimization of the unit cell size, we applied a three-step procedure to find the equilibrium structure for each system in stripe architecture. As a first step, we optimized the individual building blocks of the networks, i.e. the porphyrin monomers in gas phase as well as the corresponding dimers consisting of two porphyrins and the different linking units. From these geometries we then built the unit cells for periodic calculations of the 3D networks and performed single point calculations for different stacking distances in z-direction in steps of 0.1 Å including the vertical linkers. By fitting the resulting energies with the Birch-Murnaghan equation of states,[3,4] we derived a structure close to the minimum. As a last step, a full geometry optimization including the relaxation of all unit vector lengths (with fixed angles) was performed. Exemplary, for the *BIYPR_1BN_stripe* system we an optimized unit cell of 32.52 Å x 16.18 Å x 11.84 Å. An exact calculation of the full vibrational spectrum as is customarily done when optimizing the structures of small molecules would be computationally exceedingly demanding requiring millions of core-hours on contemporary computational resources. Therefore, we adopted an alternative strategy: We studied the

impact of a slip of consecutive layers (reflected here by the angle of the unit cell vector perpendicular to the plane of the layers) on the total energy, as this is expected to be the geometric parameter with respect to which the above-described procedure is most likely to result in a saddle point rather than a minimum of the potential-energy surface. This test showed that the orthogonal unit cell within the chosen numerical settings does correspond to a minimum, but that this minimum is comparably shallow (tilting the axis by 4° and then reoptimizing all other geometric parameters increased the total energy of the system by 16 meV).

(b) HSE calculations

After optimizing the geometries at the PBE level we performed single point calculation applying the HSE06 functional. First of all, this methodology allows to mitigate the well-known self-interaction error in (semi)local DFT [5,6] which is in particular important here, as it changes the order of the orbitals in the energetic vicinity of the gap for some of the systems. This is a consequence of differently localized orbitals experiencing a different self-interaction error. Moreover, as PBE is known to underestimate the HOMO-LUMO band gap, applying HSE we can accordingly increase it and, thereby, avoid a spurious overlap of conduction and valence band edges of the differently shifted regions when applying large dipole densities. In our calculations, applying the PBE functional we obtain a HOMO-LUMO gap of the porphyrin building blocks of only 1.94 eV, which is increased to 2.56 eV when applying HSE06. Both values are reasonably close to the optical gap, experimentally found at 2.16 eV. [7] They, however, still significantly underestimate the fundamental gap, as the latter was calculated to be 5.52 eV. Here it needs to be kept in mind that the resulting exciton binding energy of 3.36 eV is significantly reduced in the periodic material due to screening effects. Also the degree of localization of the exciton influences its binding energy, but a detailed discussion of such effects goes beyond the scope of the present paper. In passing, we note that a full geometry optimization at the level of HSE is not affordable due to the huge computational cost associated with the use of hybrid functionals in conjunction with periodic boundary conditions.

For the sake of comparison, in Figure S1 we show the calculated density of states for the *DABCO_1F_stripe* system. One clearly sees that the electrostatically induced shift prevails

independent of the used functional. As discussed before, the global band gap is reduced from 0.6 eV for the HSE06 calculations to 0.3 eV for PBE.
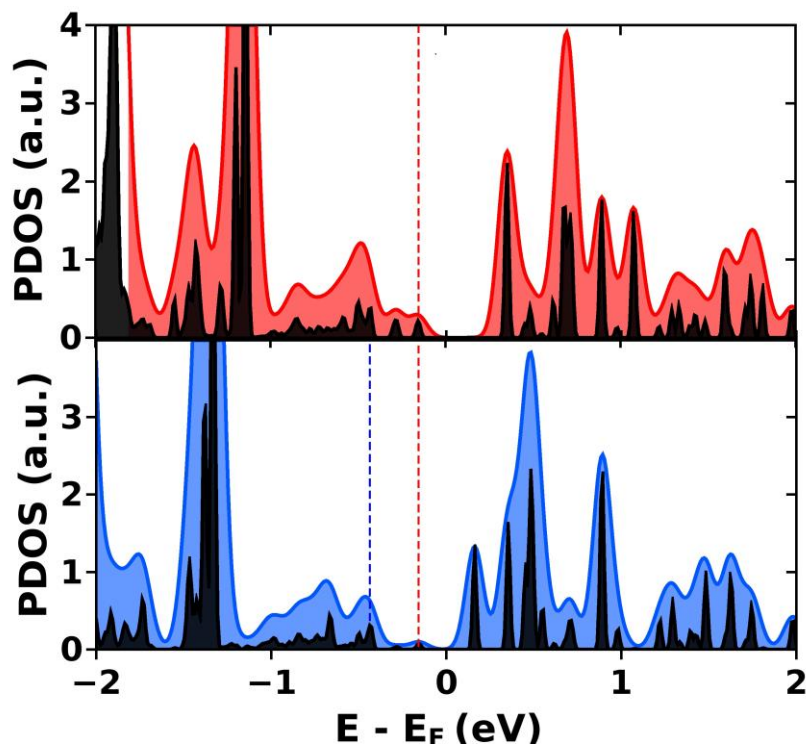
Figure S1: Density of states projected onto different parts of the unit cell for the *DABCO_1F_stripe* system calculated at the PBE level; top panel: DOS projected onto the high electrostatic energy side, i.e. red region in (a); bottom panel: DOS projected onto the low electrostatic energy side, i.e. blue region on (a). The energy is aligned to the Fermi level. The black lines represent the projected density of states (PDOS) obtained directly from the calculations with a Gaussian broadening of 0.01 eV while the red and blue shaded areas show the PDOS with a Gaussian broadening of 0.05 eV applied in a post-processing routine, serving as a guide to the eye.

(c) Charging the System

In order to simulate how an additional extra charge would distribute over the unit cell we charged the system by a positive and negative amount of 0.1 electrons per unit cell which is then neutralized by introducing a homogenous background charge density. We want to state that this creates a somehow artificial situation as we do not account for electron-phonon coupling by geometry optimizing a supercell containing at least one charge. Unfortunately, this is still far beyond current computational capabilities even when using efficient GGA functionals. As electron-phonon coupling (polaronic effects) would increase the localization

of the charges this means that our calculations represent a lower boundary to the actually achievable charge localization.

(d) Collectivity of the electrostatic shifts and impact of mesomeric effects due to the fluorine substituents

To evaluate to what extent the observed energetic shifts are caused by the periodic arrangement of the polar linkers, we also calculated the energetic offsets of isolated porphyrin units bearing polar substituents. These are shown in Figure S2. The asymmetry in the frontier orbitals between systems with fluorine atoms in meta and ortho positions relative to the porphyrin macrocycle (the blue and red segments in the main manuscript) amounts to 0.09 eV (0.18 eV) when attaching one (two) 1,3-difluorobenzene units. This shift is significantly smaller than the 0.31 eV computed for the periodic arrangement of dipoles; i.e., the collectivity in the system with periodically aligned dipoles strongly amplifies the shift. This leaves the question, to what extent the asymmetry in the isolated systems might be caused by mesomeric effects due to the fluorine atoms. To test that, we studied a system with a 1,3-bis(trifluoromethyl)benzene instead of the 1,3-difluorobenzene substituent. For the dipolar elements (F / CF_3), the modified Swain-Lupton constants for the resonance contributions of the groups differ not only in magnitude, but also in sign (R = -0.39 for F and R = 0.16 for CF_3). [8] This means that the mesomeric effect for F mitigates the electron-withdrawing nature of the substituent, while for CF_3, the mesomeric effect amplifies it. In this context it is important to keep in mind that the mesomeric effect of a substitutent is important if it is located in ortho- or para-positino, but essentialy void if the substitutent is located in meta position. . Nevertheless, the obtained asymmetry of the frontier orbitals due to the different location of the substituent in the non-periodic system prevails. In fact, its magnitude even increases, which we attribute to an increase of the local dipole moment. An increase of the dipole moment (respectively, the dipole density) is also seen, when calculating the periodic system, where the shift of the DOS's projected on the red and blue regions also increases from 0.31 eV to 0.35 eV (see Figure S 3) . A negligible mesomeric effect of the fluorine atom is further confirmed by the again equivalent asymmetry in frontier orbital energies, when breaking the conjugation between the difluorobenzene and the porphyrine by an aliphatic linker (see last system in Figure S2).
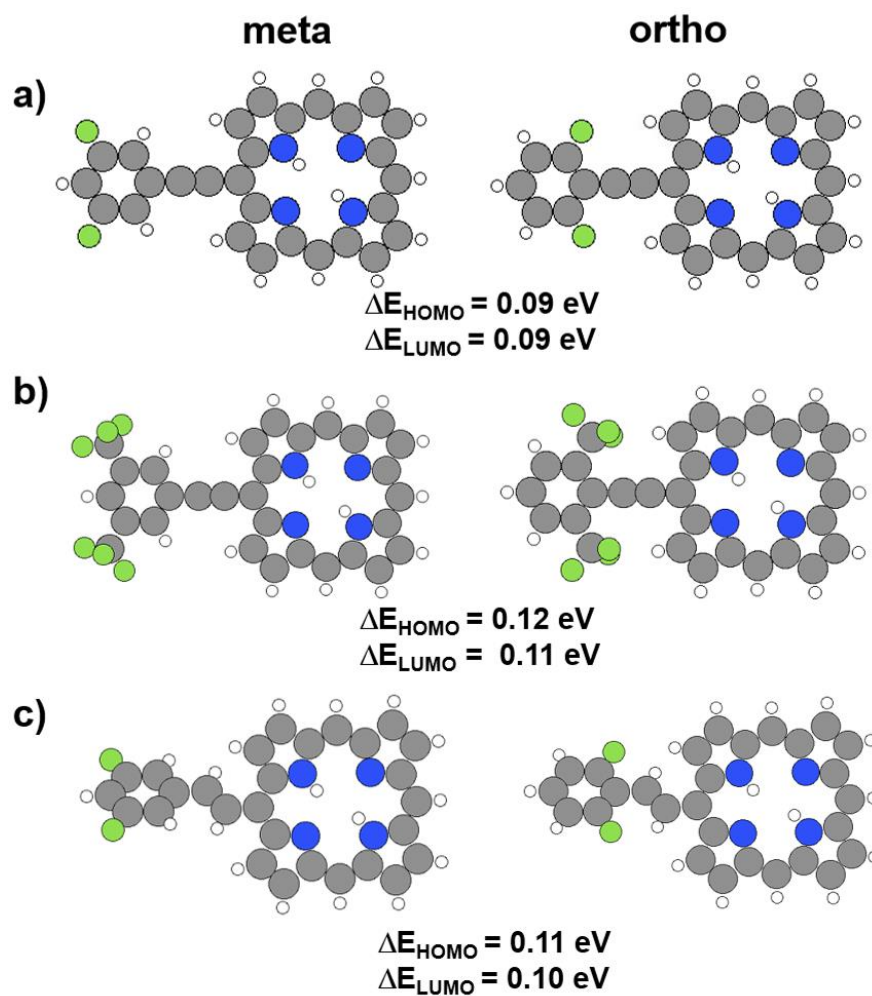
Figure S2. Structures and frontier orbital energy differences for isolated porphyrin units bearing polar substituents linked in 2 (left panels) and 4 (right panels) positions: (a) 1,3-difluorobenzene connected via an ethinyl unit; (b) 1,3-bis(trifluoromethyl)benzene connected via an ethinyl unit (c) 1,3-difluorobenzene connected via an ethyl unit.
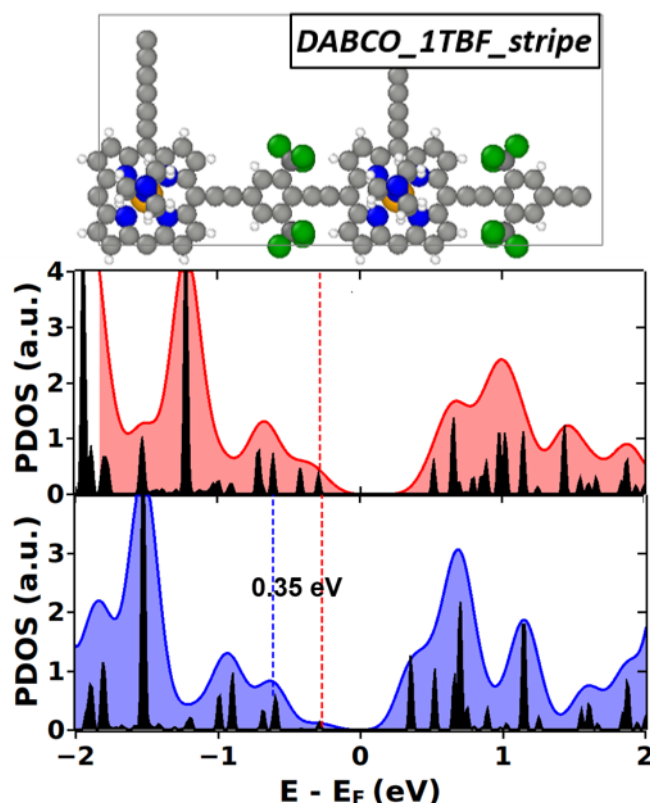
Figure S3. Density of states projected onto different parts of the unit cell for the DABCO_1TBF_stripe system, i.e. PDOS projected onto the red, high energy side (up) and the blue, low potential energy side (bottom). The energy is aligned to the Fermi level. Black lines represent the PDOS with a Gaussian smearing of 0.01 eV while the red and blue shaded areas show the PDOS with a Gaussian broadening of 0.1 eV, serving as a guide to the eye.

(e) Band structures

The band structures of the reference system without any dipolar elements and the *DABCO_1F_stripe* system are shown in Figure S4. In the absence of dipolar units, electronic states extend in both spatial directions (X and Y) due to the strong electronic coupling within the linked porphyrin plane. When introducing dipolar elements this coupling is broken due to the electrostatically induced energetic shifts. Therefore, the strongly dispersing bands in X- and Y-direction with band widths of 0.5 eV in the case of the reference system (a) are reduced in the direction parallel to the dipoles (X) to less than 0.1 eV for the system including dipoles (b). For the reference case the LUMO and LUMO+2 (belonging to the strongly dispersing bands) are essentially degenerate and delocalized over the whole system. The corresponding states in the structures containing polar elements are localized to the individual stripes.

Therfore, they are significantly shifted in energy due to the collective electrostatic effects. The reason for the small dispersion in Z direction is the separation of the π-electron systems by the *BIPYR* linkers.
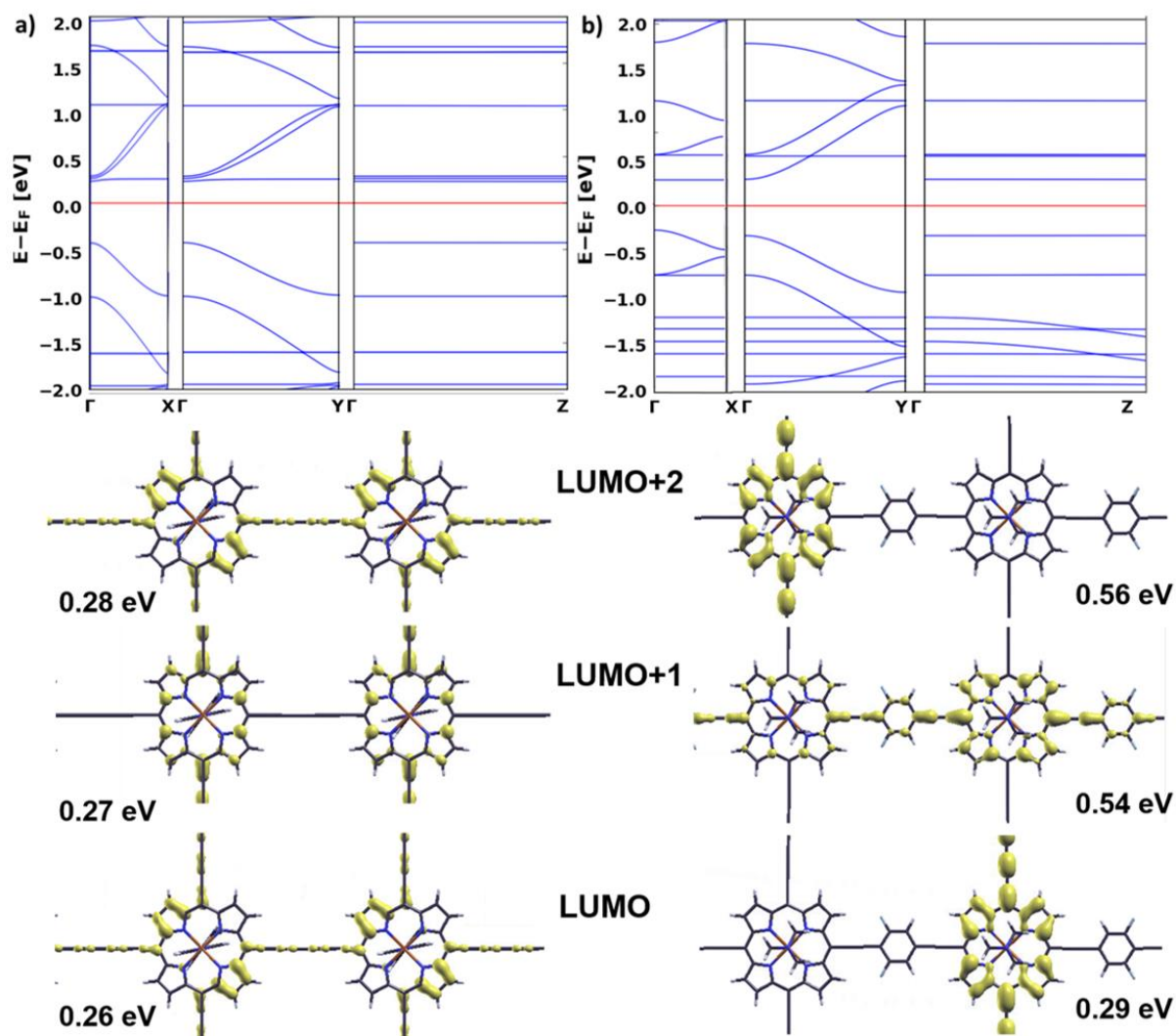
Figure S4. Band structure along X, Y and Z direction (the directions are indicated in Figure 1 and Figure S5) for the reference system without any dipolar elements **(a)** and the *DABCO_1F_stripe* system **(b)** with the corresponding isodensity plots of the Gamma-point states for the three lowest lying unoccupied states (isovalue of 0.005 states per $Å^3$) . Their energies are given with respect to the Fermi level.

II. Supporting Tables and Figures
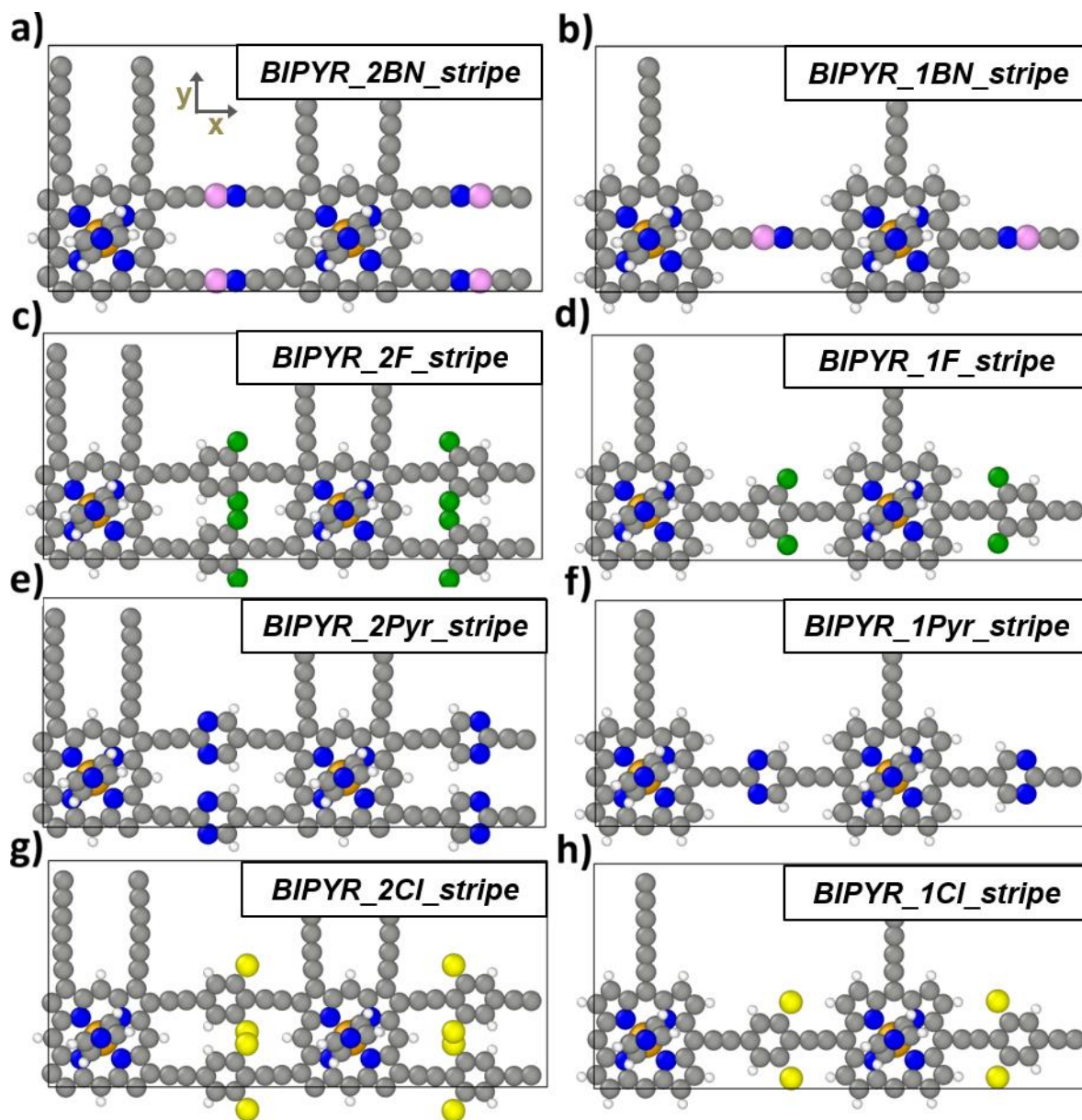
Figure S5: Chemical structure of all investigated systems in stripe architecture (top view).

Color code: grey=C, white = H, pink=B, blue=N, green = F, yellow=Cl, orange=Cu.
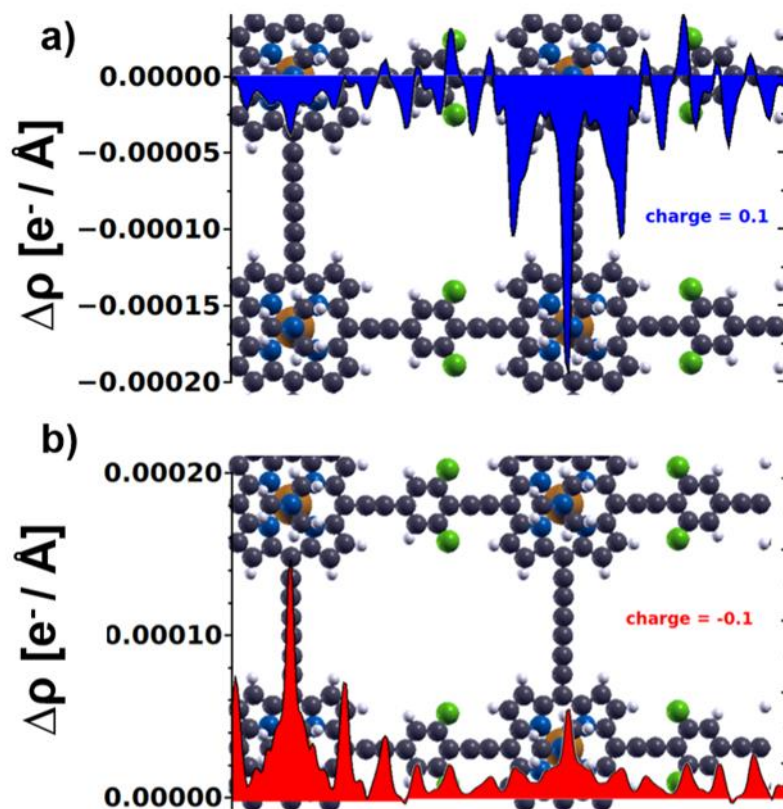
Figure S6. (y,z)- plane averaged charge density difference between neutral and (a) positively and (b) negatively charged *DABCO_1F_stripe* system respectively. While the information on the spatial distribution of charge-density changes is reduced in this representation compared to the isodensity plots shown in the main manuscript, it provides more quantitative information as the shape of the plot is not affected by the choice of the isodensity value. In both cases, we find localization of charges in agreement with the isodensity plots in Figure 3b.

Table S1. Changes in the Mulliken charges of the different sections upon positively and negatively charging DABCO_1F_stripe system. Charges are given in multiples of the elementary charge; the total charge is 0.1 e, respectively -0.1 e per unit cell (the remaining charge is found on the difluorinated benzene).

	0.1 e total charge	-0.1 e total charge
region highlighted in red (porphyrines, triacetylene linker + DABCO)	0.053 e	-0.016 e
region highlighted in red + adjacent acetylene segments	0.063 e	-0.025 e
region highlighted in blue (porphyrines, triacetylene linker + DABCO)	0.015 e	-0.062 e
region highlighted in red + adjacent acetylene segments	0.025 e	-0.064 e
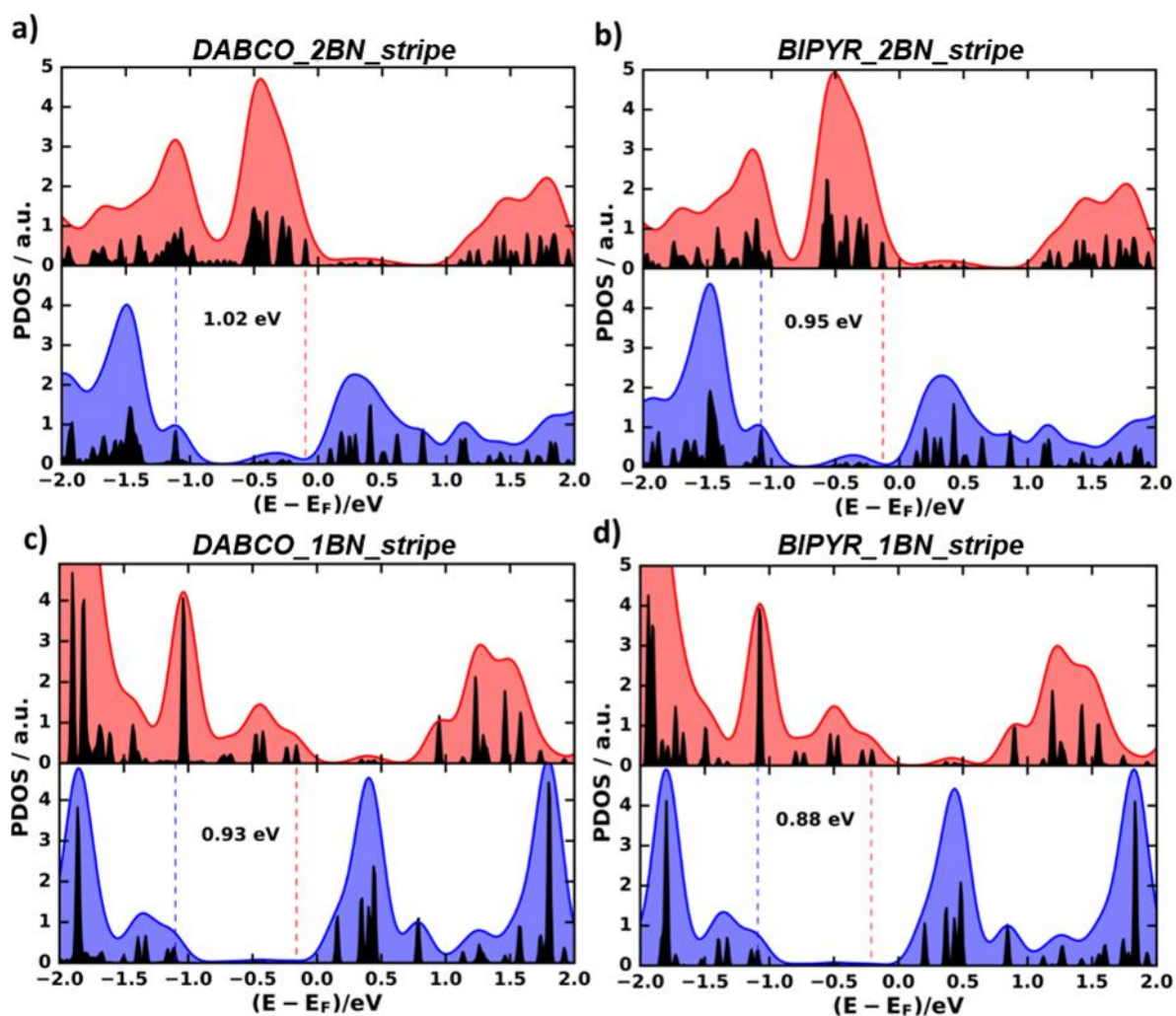
Figure S7. Density of states projected onto different parts of the unit cell of all BN containing stripe systems, i.e. PDOS projected onto the red, high energy side (up) and the blue, low potential energy side (bottom). The energy is aligned to the Fermi level. Black lines represent the PDOS with a Gaussian smearing of 0.01 eV while the red and blue shaded areas show the PDOS with a Gaussian broadening of 0.1 eV, serving as a guide to the eye. The values for the band offset with respect to the HOMO as well as LUMO positions are summarized in Supplementary Table 1.
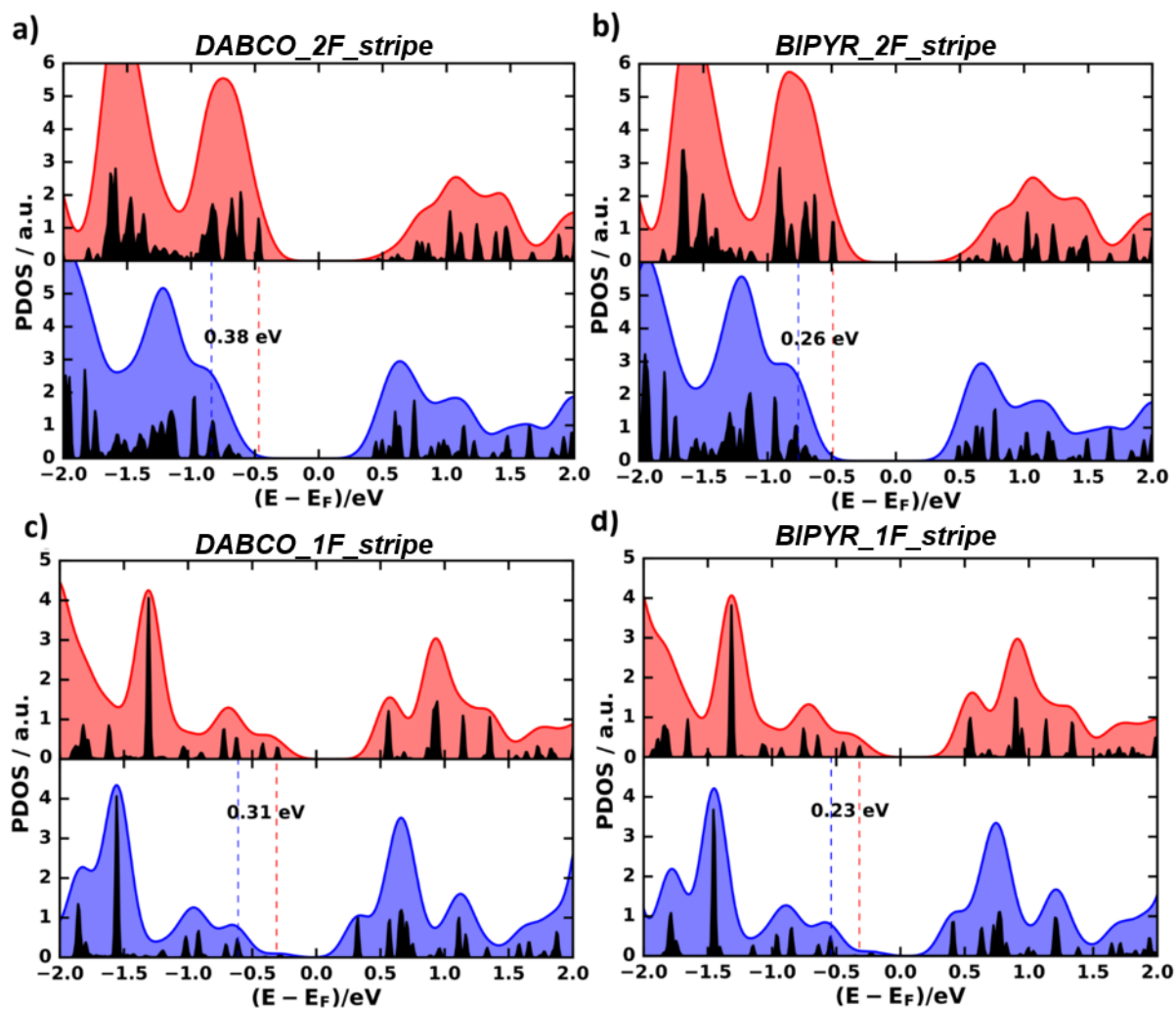
Figure S8. *Density of states projected onto different parts of the unit cell of all F containing stripe systems, i.e. PDOS projected onto the red, high energy side (up) and the blue, low potential energy side (bottom). The energy is aligned to the Fermi level. Black lines represent the PDOS with a Gaussian smearing of 0.01 eV while the red and blue shaded areas show the PDOS with a Gaussian broadening of 0.1 eV, serving as a guide to the eye. The values for the band offset with respect to the HOMO as well as LUMO positions are summarized in Supplementary Table 1.*
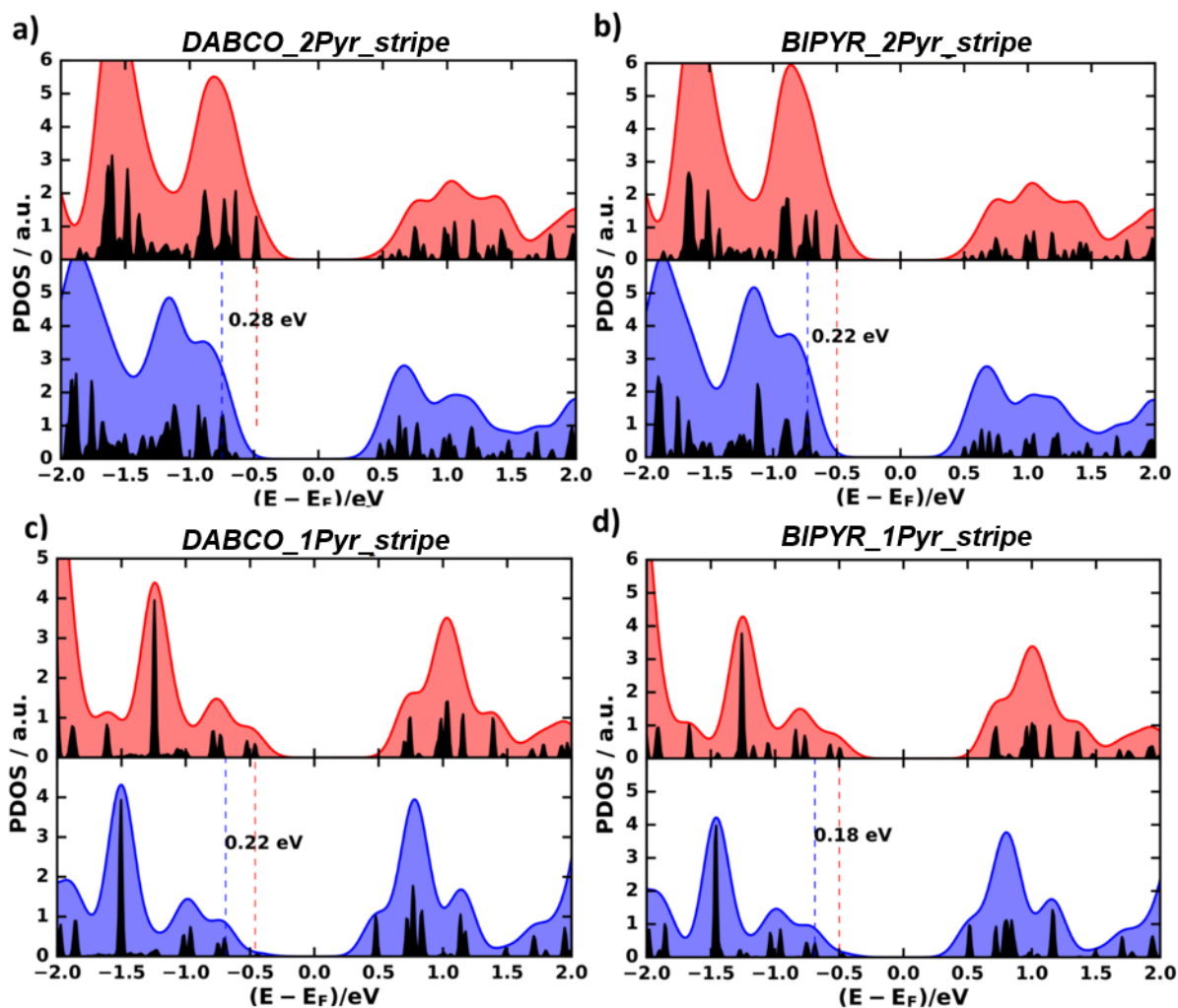
Figure S9. Density of states projected onto different parts of the unit cell of all Pyr containing stripe systems, i.e. PDOS projected onto the red, high energy side (up) and the blue, low potential energy side (bottom). The energy is aligned to the Fermi level. Black lines represent the PDOS with a Gaussian smearing of 0.01 eV while the red and blue shaded areas show the PDOS with a Gaussian broadening of 0.1 eV, serving as a guide to the eye. The values for the band offset with respect to the HOMO as well as LUMO positions are summarized in Supplementary Table 1.
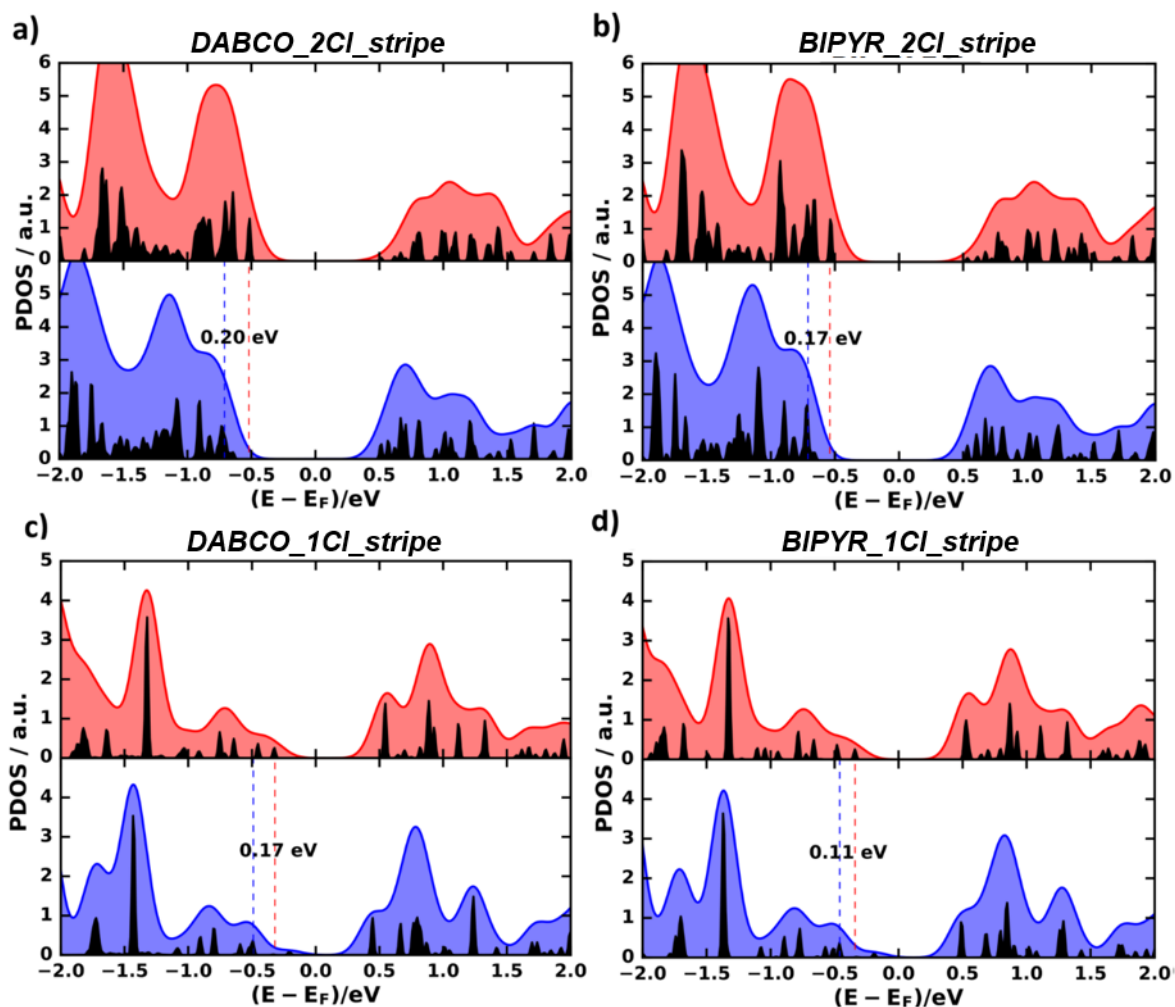
Figure S10. Density of states projected onto different parts of the unit cell of all Cl containing stripe systems, i.e. PDOS projected onto the red, high energy side (up) and the blue, low potential energy side (bottom). The energy is aligned to the Fermi level. Black lines represent the PDOS with a Gaussian smearing of 0.01 eV while the red and blue shaded areas show the PDOS with a Gaussian broadening of 0.1 eV, serving as a guide to the eye. The values for the band offset with respect to the HOMO as well as LUMO positions are summarized in Supplementary Table 1.

Table S2. *Energetic shift (in eV) between HOMOs and LUMOs of consecutive stripes,*
ΔE$_{HOMO}$ and ΔE$_{LUMO}$ respectively, taken from the peak positions in the calculated PDOS shown
in Figures S7-10.

	DABCO 2BN	DABCO 1BN	DABCO 2F	DABCO 1F	DABCO 2Pyr	DABCO 1Pyr	DABCO 2Cl	DABCO 1Cl
ΔE$_{HOMO}$	1.02	0.93	0.38	0.31	0.28	0.22	0.20	0.17
ΔE$_{LUMO}$	1.01	0.79	0.33	0.32	0.27	0.23	0.20	0.12
	BIPYR 2BN	BIPYR 1BN	BIPYR 2F	BIPYR 1F	BIPYR 2Pyr	BIPYR 1Pyr	BIPYR 2Cl	BIPYR 1Cl
ΔE$_{HOMO}$	0.95	0.88	0.26	0.23	0.22	0.18	0.17	0.11
ΔE$_{LUMO}$	1.04	0.70	0.25	0.21	0.17	0.20	0.1	0.07
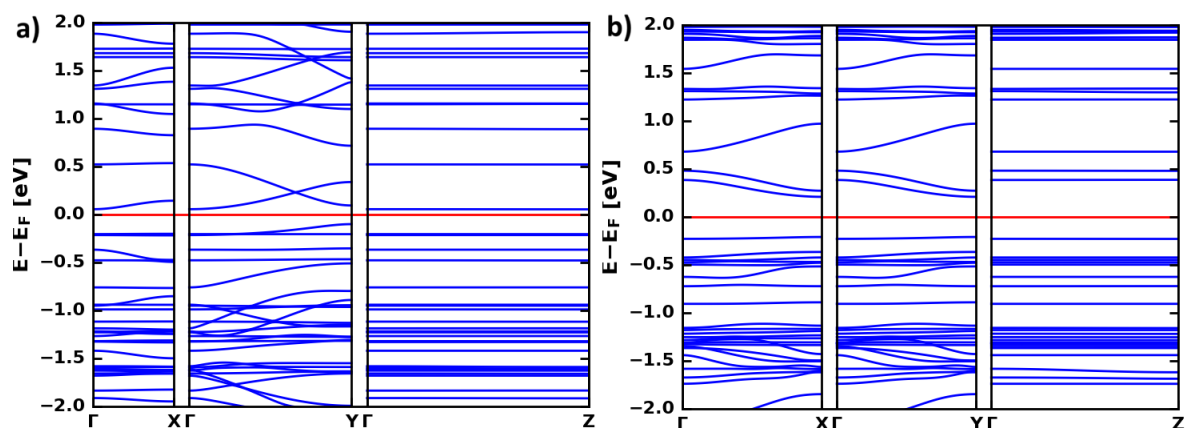
Figure S11. Bandstructure along X, Y and Z direction for BIPYR_2BN_stripe in **a)** stripe
architecture and **b)** checkerboard architecture at the PBE level. We find that the dispersion in
Y direction is largely suppressed in case of the checkerboard structure. The band width in Y-
direction is reduced from 0.15 (0.35) eV to 0.00 (0.15) eV for the VBM (CBM) respectively.
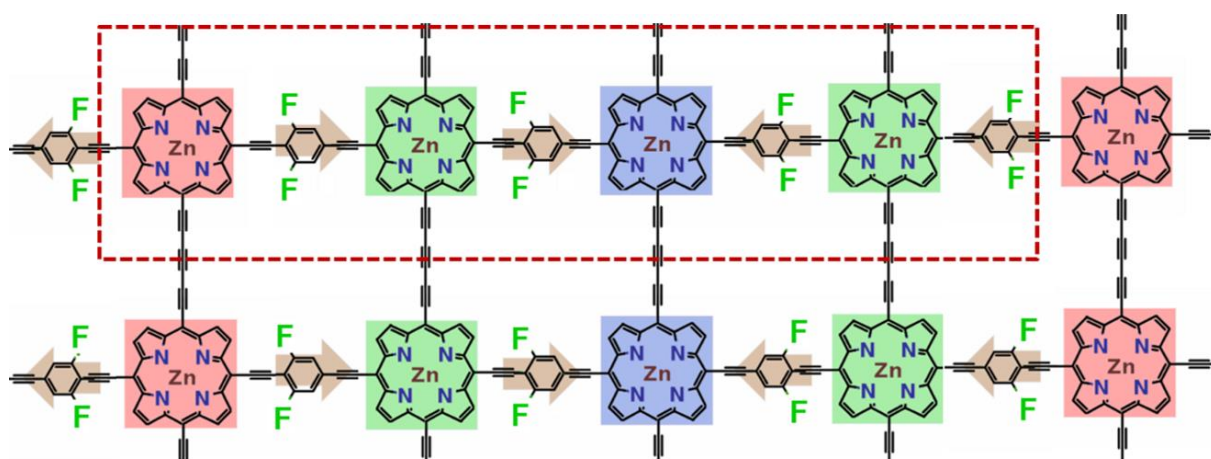
Figure S12. Chemical Structure of BIPYR_1F_cascade in cascade-like architecture.
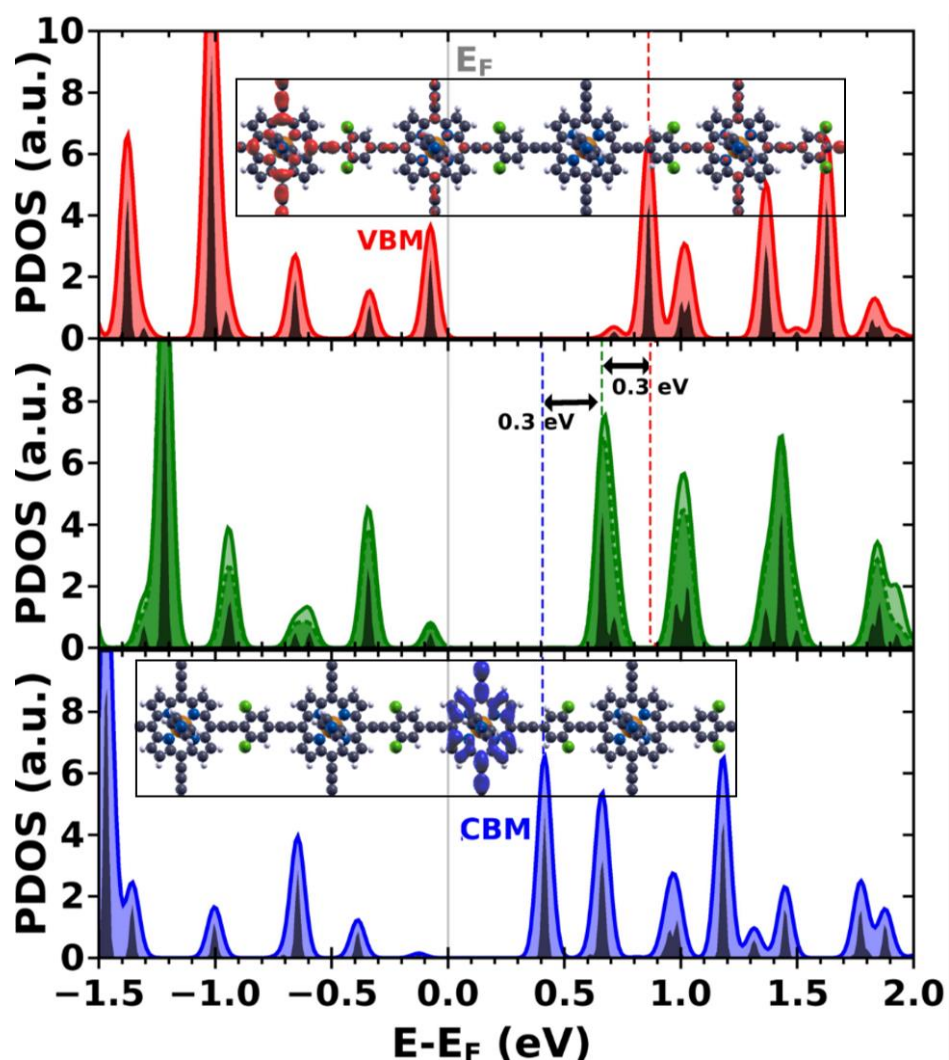
Figure S13. Density of states projected onto different parts of the unit cell for the BIPYR_1F_cascade system; top panel: DOS projected onto the high electrostatic energy region (red region in Figure S12); middle panel: DOS projected onto the middle

electrostatic energy region (green region in Figure S12); bottom panel: DOS projected onto the low electrostatic energy region (blue region in Figure S12). The energy is aligned to the Fermi level. The black lines represent the PDOS obtained directly from the calculation with a Gaussian smearing of 0.01 eV while the red and blue shaded areas show the PDOS with a post-processed Gaussian broadening of 0.03 eV, serving as a guide to the eye. Gamma-point states of VBM and CBM are inserted as local density of states (LDOS) plots with an isovalue of 0.03 electrons per Å ^{3}.

References

[1] C.-L. Fu, K.-M. Ho, *Phys. Rev. B* **1983**, *28*, 5480.

[2] V. Blum, R. Gehrke, F. Hanke, P. Havu, V. Havu, X. Ren, K. Reuter, M. Scheffler, *Comput. Phys. Commun.* **2009**, *180*, 2175.

[3] F. D. Murnaghan, *Proc. Natl. Acad. Sci. U. S. A.* **1944**, *30*, 244.

[4] F. Birch, *Phys. Rev.* **1947**, *71*, 809.

[5] J. P. Perdew, *Phys. Rev. B* **1981**, *23*, 5048.

[6] S. Kümmel, *Rev. Mod. Phys.* **2008**, *80*, 3.

[7] A. J. McHugh, M. Gouterman, C. Weiss, *Theor. Chim. Acta* **1972**, *24*, 346.

[8] C. Hansch, A. Leo, R. W. Taft, *Chem. Rev.* **1991**, *91*, 165.

III. Appendix: Geometric parameters of all studied materials

The following lists contain the full geometrical information of all studied systems (in the format of the geometry.in file of FHI-aims). The lines starting with "lattice vector" contain the lattice vectors in Cartesian coordinates in Å. The following lines starting with "atom" contain the Cartesian coordinates (again in Å) and atom types of all atoms contained in the basis (respectively, unit cell).

DABCO_1F_stripe system: *geometry.in* for FHI-aims

```
lattice_vector     35.67269807      0.00000000     -0.00000000
lattice_vector     -0.00000000     16.10365688     -0.00000000
lattice_vector      0.00000000     -0.00000000      7.64808444
atom     25.08257263      0.98424915      0.06302594 C
atom     24.39321919      2.25277824      0.05080544 C
atom     22.84566932      0.70258132      0.04398762 C
atom     24.11525210      0.01648427      0.05857776 C
atom     21.57224144      0.05818097      0.03626619 C
atom     20.29735489      0.70127621      0.03073474 C
atom     19.02762416      0.01442797      0.02300918 C
atom     18.05949054      0.98180501      0.02293017 C
atom     18.74686756      2.25100124      0.02990416 C
atom     18.10693265      3.52328890      0.03061932 C
atom     18.74572026      4.79631835      0.03203510 C
atom     20.29524246      6.34714088      0.03398995 C
atom     19.02496218      7.03315450      0.03189283 C
atom     18.05743392      6.06512796      0.03057003 C
atom     21.56998161      6.99083427      0.03522642 C
atom     22.84388013      6.34731886      0.03765704 C
atom     24.11316454      7.03403530      0.04151764 C
atom     24.39262542      4.79781240      0.04383573 C
atom     25.08116819      6.06678155      0.04549621 C
atom     25.03215899      3.52543186      0.05046623 C
atom      7.24398002      6.04267171      0.03819494 C
atom      6.27791418      7.01169479      0.04170501 C
atom      5.00897492      6.32585323      0.04897956 C
atom      6.55618303      4.77401935      0.04370929 C
atom      3.73656520      6.97168443      0.05304976 C
atom      2.46167118      6.32912448      0.05551373 C
atom      1.19318662      7.01694483      0.06138820 C
atom      0.22551592      6.04915433      0.06273298 C
atom      0.91032229      4.77924488      0.05762038 C
atom      0.26789562      3.50805874      0.05965993 C
atom      0.90686919      2.23523766      0.05873369 C
atom      0.21986763      0.96649769      0.06372501 C
atom      1.18600846     -0.00295141      0.06214514 C
atom      2.45572063      0.68272078      0.05609128 C
atom      3.72975582      0.03823875      0.05312575 C
atom      5.00347957      0.68177331      0.04867315 C
atom      6.55377827      2.23084875      0.04340815 C
atom      6.27119116     -0.00628392      0.04109433 C
atom      7.23908352      0.96096169      0.03761003 C
atom      7.19638559      3.50181630      0.04157543 C
atom      4.38762821      4.70146230      3.09817229 C
atom      4.37177955      2.29582932      3.09789271 C
atom      2.30169196      3.51219907      3.09872588 C
atom      2.30301941      3.51198574      4.65415424 C
atom      4.37297608      2.29590772      4.65131495 C
atom      4.38878505      4.70101953      4.65155606 C
atom     22.27114509      2.35456906      3.08558577 C
atom     20.15014621      3.48017139      3.08246038 C
atom     20.14881508      3.48065392      4.63780393 C
atom     22.27049194      2.35494115      4.63885773 C
```

2.3.4 Appendix A - π-Stacked Networks

In this chapter the characteristics of π-stacked 3D covalent organic networks are presented. In contrast to the above discussed systems (PUBLICATION III), the vertical linkers in stacking direction are removed and the individual layers are stacked on top of each other via π-π-stacking, *i. e.* via non-covalent, attractive interactions between aromatic systems containing π-orbitals. These π-stacked covalent organic networks fully reflect the set-up of traditional 2D covalent organic frameworks (COFs), but additionally include polar linking groups. Note that the layers were stacked in the exact eclipsed configuration directly on top of each other, while for many COFs a slight offset of $1.5 - 2.8\mathring{A}$ between the layers is found.[184]

Interlayer Distance
First of all, the impact of the interlayer distance on the electronic properties of the 3D covalent organic networks is investigated. Figure 17a shows the band structure along X, Y, and Z direction for the π-stacked zinc-porphyrin network including polar BN groups. This is compared to the equivalent system comprising the bipyridine linker in stacking direction, see Fig.17b. For the π-stacked system a large dispersion in stacking direction
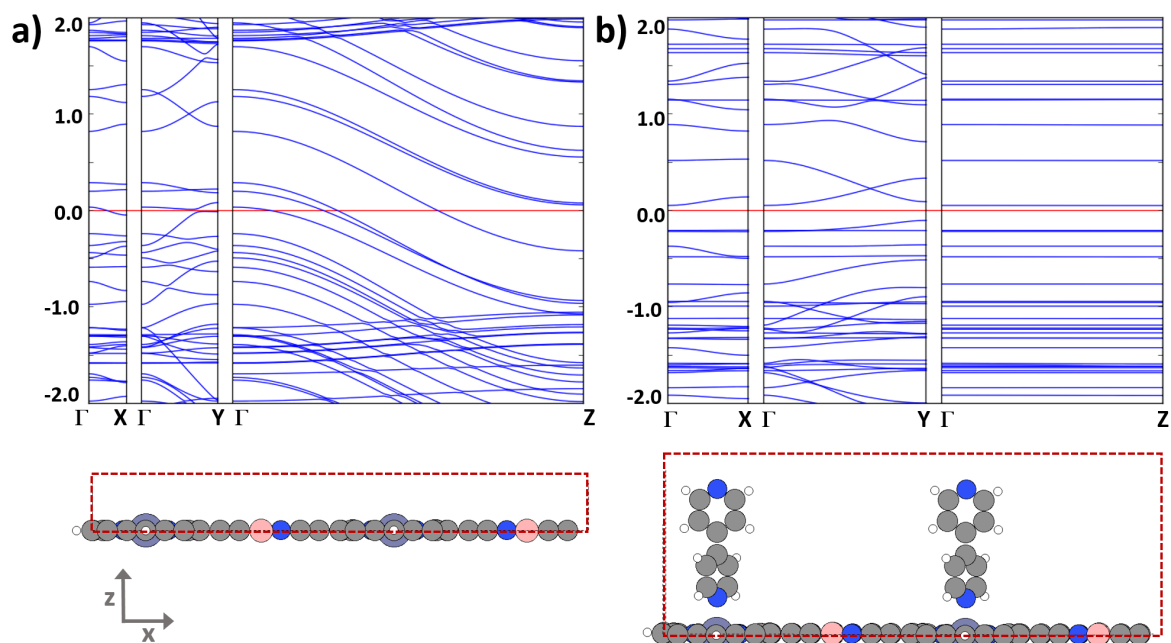
Figure 17: Band Structure for Different Interlayer Distances. **(a)** Band structure along X, Y and Z direction for the π-stacked zinc-porphyrin network including polar BN groups obtained at the level of PBE. **(b)** Equivalent band structure for the bipyridine linked zinc-porphyrin network. The dispersion in Z direction of around $1.2eV$ for the π-stacked system vanishes when increasing the interlayer distance by introducing the bipyridine linker in stacking direction.

$(\Gamma \rightarrow Z)$ of around $1.2eV$ is observed. This is attributed to a large transfer integral along the stacking direction due to the close distance between the layers of around $3.49\mathring{A}$.

This interlayer spacing is in the typical range of the $3.3 - 3.5 \mathring{A}$ measured for conventional COFs.[185,186] The strongly overlapping bands in Z-direction lead to a gap closure in these systems. However, when introducing spacer elements in stacking direction, as for example the bipyridine linker shown in Fig. 17b, the interlayer distance is increased to $11.8 \mathring{A}$ and the dispersion in stacking direction disappears. The π-stacked situation does not conceptually prevent electrostatic design, but the overall situation becomes more involved, as the overlap of the bands counteracts the electrostatically induced shifts.

Stability

In order to investigate the binding characteristics of these π-stacked COFs in more detail, the binding energy of the corresponding dimers is calculated. Figure 18 shows the dimer structure used for the calculations in gas-phase. The interlayer distance, d_{stack}, is set to the one obtained from the optimized periodic geometry. The binding energy, E_{bind}, be-
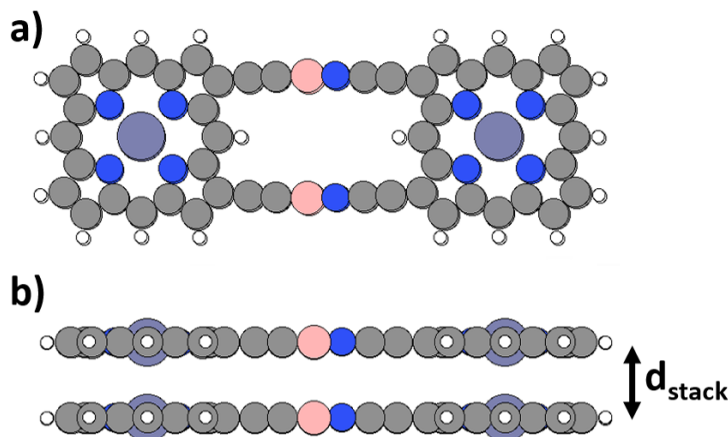
Figure 18: π-Stacked Porphyrin Dimers. Top **(a)** and side **(b)** view of the porphyrin dimers as calculated in Tab. 1. The stacking distance as obtained from the periodic calculations is indicated as d_{stack}.

tween the layers is obtained as the difference in total energy of a dimer and a monomer in gas-phase. We compare the zinc-porphyrin system linked via polar BN groups, abbreviated as Zn_Por_BN, to systems where (i) the central metal atom of the porphyrin segment is either removed or replaced by Paladium or Platinum, and (ii) where the polar $B \equiv N$ groups are replaced by $C \equiv C$. The corresponding binding energies are summarized in Tab. 1 together with the stacking distance and the dipole moment for the monomer and dimer, respectively. For the "reference system" without polar groups and without a central metal atom, Por_CC, the binding energy amounts to $\sim 1.76 eV$. Upon inserting polar BN elements, Por_BN, it gets slightly reduced by $0.03 eV$. When inserting a metal in the center of the porphyrin segments, the binding energy strongly increases. The exact value largely depends on the type of the metal. The platinum system, Pt_Por_BN, exhibits the largest binding energy of $2.28 eV$ and is, hence, expected to form the most stable networks.

Depolarization Effects

As introduced in section 1.1, whenever dipoles are cooperatively arranged, so called depolarization effects become apparent.[8,10] Their main effect is to reduce the dipole moment

Table 1: π-Stacked Porphyrin Dimers. E_{bind} is the binding energy calculated as the difference in total energy between the dimer and the monomer in gasphase (more negative is more binding). d_{stack} is the optimized interlayer distance in stacking direction as obtained from the periodic systems. μ_{mono} and μ_{dimer} are the dipole moments for the monomer and dimer structures in gasphase. Note that these values were obtained at the PBE level and therefore the dipole moment for the *Zn_Por_BN* monomer differs compared to the HSE value reported in PUBLICATION III.

	Por_CC	**Por_BN**	**Zn_Por_BN**	**Pt_Por_BN**	**Pd_Por_BN**
$\mathbf{E_{bind}[eV]}$	-1.76	-1.73	-1.88	-2.28	-2.15
$\mathbf{d_{stack}[\mathring{A}]}$	3.47	3.47	3.43	3.48	3.49
$\mathbf{\mu_{mono}[Debye]}$	0.00	8.18	8.28	8.03	8.13
$\mathbf{\mu_{dimer}[Debye]}$	0.00	12.64	12.82	12.33	12.54

of the individual components due to the electric fields generated by neighboring polar entities. This effect can be estimated for the current periodic systems by comparing the dipole moment of a monomer to that of the dimer, see Tab. 1. For the *BN* system without a central metal in the porphyrin segment, the dipole moment amounts to $8.18 Debye$. In the corresponding dimer the dipole per layer gets reduced to $6.32 Debye$. As can also be seen in Tab.1, the degree of depolarization is only slightly influenced by the type of metal contained in the porphyrin segments.

2.3.5 Appendix B - Additional Systems

In PUBLICATION III several different 3D covalent organic networks in a variety of architectures are discussed. In contrast to these porphyrin based networks, here, additional systems based on coronene segments in triangular architecture are presented. Again, collective electrostatic effects are exploited by incorporating polar elements in order to manipulate the electronic landscape in a desired way. All the calculations shown in this section are obtained at the level of PBE.

The structure of the systems presented in this section are motivated by the recently experimentally realized 2D COFs shown in Fig. 19, *i.e.* imine linked hexaphenylbenzene and hexabenzocoronene in triangular architecture. These COFs are highly conducting along the π-stacked columns. The triangular topology features pore sizes down to $12\overset{\circ}{A}$ which is
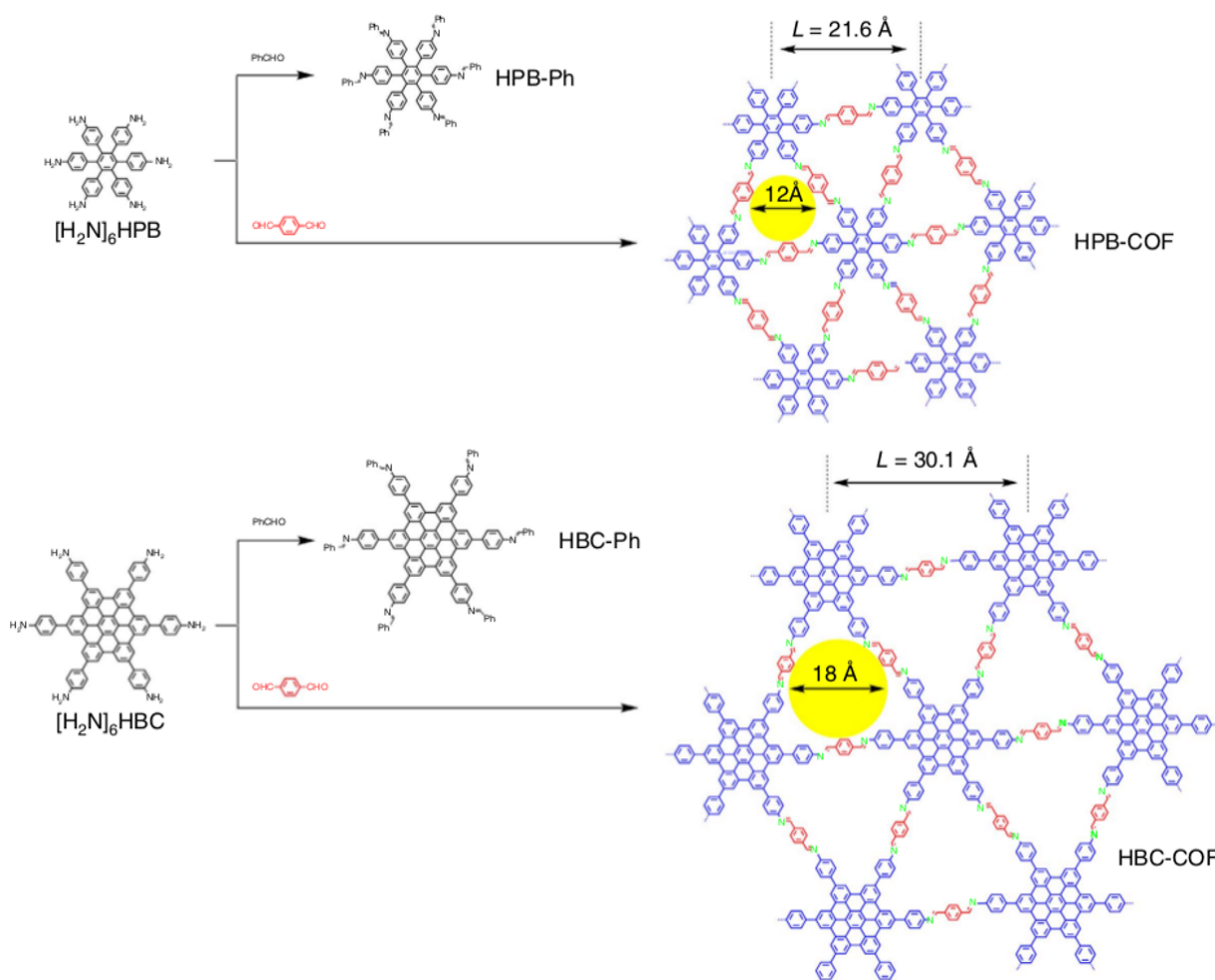
Figure 19: Experimentally Realized COFs with Triangular Topology. Schematic representation of the synthesis of imine linked triangular hexaphenylbenzene **(a)** and hexabenzocoronene **(b)** COFs. Reproduced from ref. [187].

among the smallest pores reported to date. The model systems based on these materials are shown in Fig. 20. As can be seen, coronene and hexabenzocoronene segments are
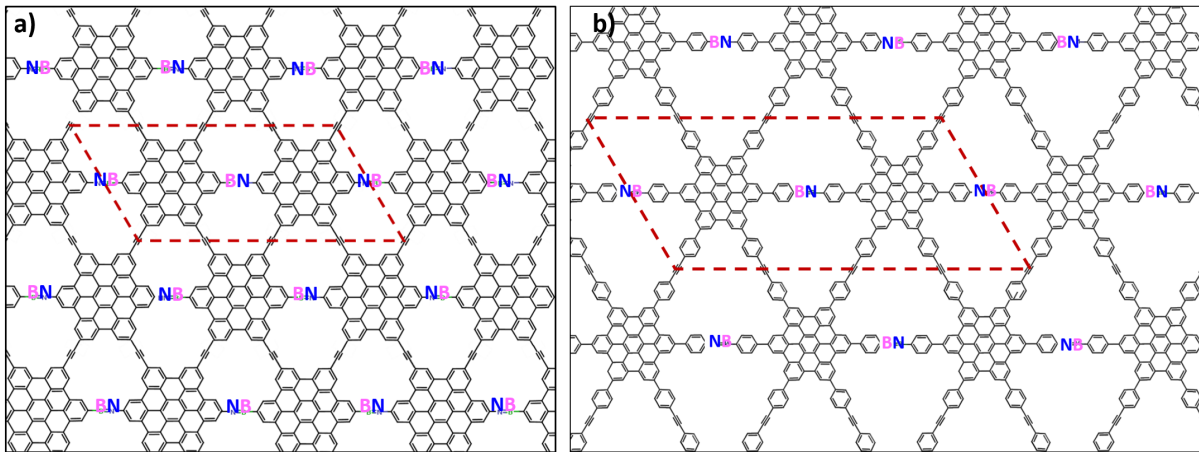
Figure 20: Triangular Model Systems. Chemical structure of π-stacked coronene **(a)** and hexabenzocoronene **(b)** based COFs in stripe architecure connected via polar boron nitride (BN) linkers. The unit cell is indicated as dashed red box.

covalently linked to each other and again BN groups are inserted into the linking groups in a stripe architecture. While the $B \equiv N$ linker is of somewhat hypothetical nature, it is used in this conceptional study to show that very large shifts are feasible for large dipole moments. However, in the spirit of the electrostatic design concept proposed in PUBLICATION III, also here, the type and number of polar linkers can be varied in order to tune the electronic landscape of these materials. For the systems presented in this section, the layers are stacked directly on top of each other via π-stacking. Note that this again leads to strongly dispersing bands in stacking direction (*cf.* section 2.3.4). The systems are optimized at the level of PBE applying the same procedure as described in the Supporting Information of PUBLICATION III.

Figure 21 shows the contour plot of the electrostatic energy for an electron in a plane perpendicular to the stacking direction for the hexabenzocoronene based system including BN linkers. One clearly sees the expected division into stripes of high (red) and low (blue) energy due to the superposition of the electric fields of the dipolar BN linkers. Figure 22 and 23 show the isodensity plots of the Gamma-point states of the valence and conduction bands for both of the systems. For both, the conduction band minima and the valence band minima, we see nice localization to the individual stripes. This demonstrates that the electrostatic design concept proposed in PUBLICATION III can in principle be extended to all kind of structures and topologies with diverse electrostatic pattering motifs.
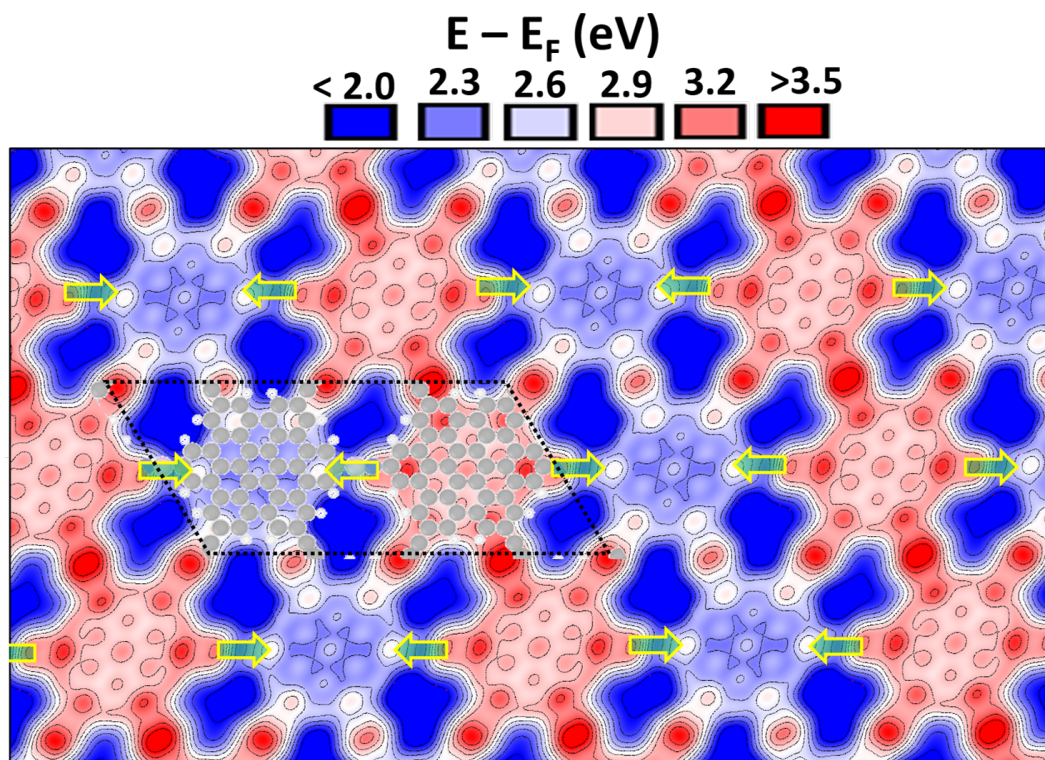
Figure 21: Electrostatic Energy.Contour plot of the electrostatic energy of an electron for the π-stacked coronene based COF (see Fig. 20a) in a plane perpendicular to the stacking direction (approximately 1.8 Å away from the molecular plane to avoid extensive variations near the nuclei). Isolines are drawn every 0.1 eV. The arrows represent the directions of the dipole moments of the linking BN elements. The unit cell is indicated as dashed black box.
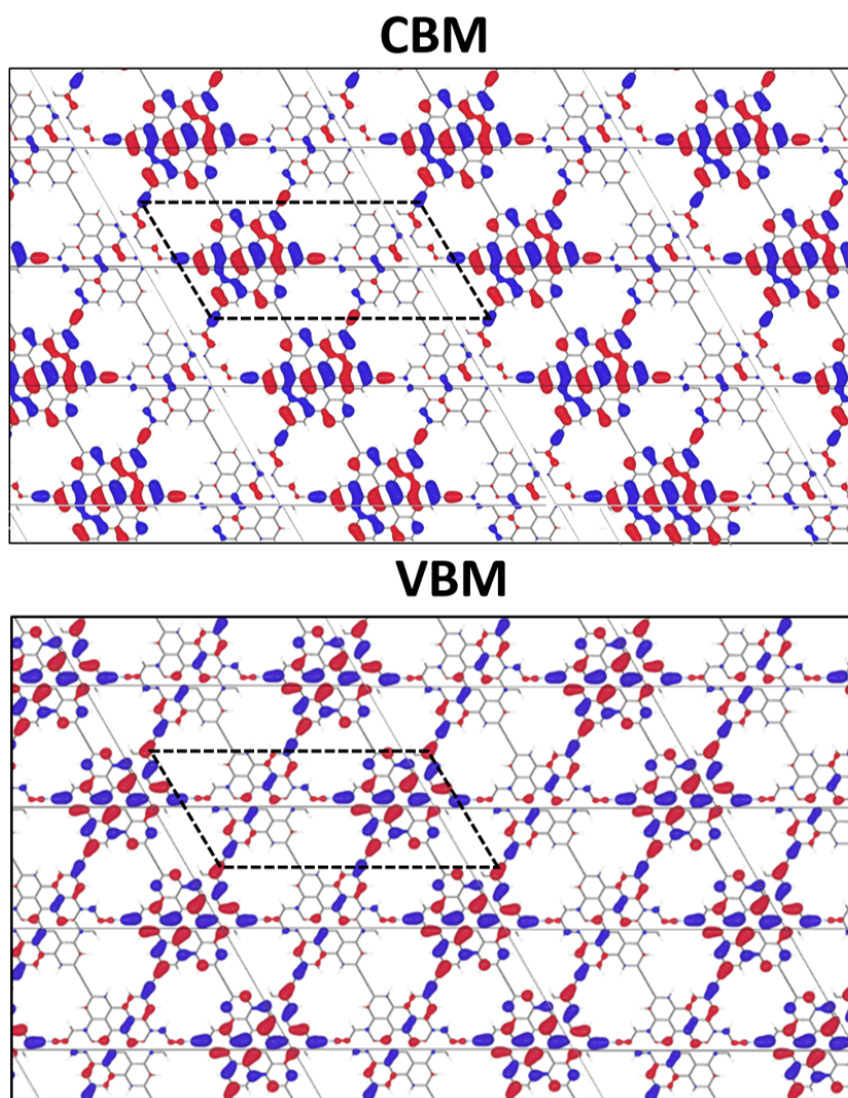
Figure 22: Localization of Coronene-Based COFs. 3D isodensity plots of the Gamma-point states of the valence and conduction bands for the coronene-based COF shown in Fig. 20a. An isovalue of 0.05 states per $\mathring{A}^3$ is applied.

CBM

VBM
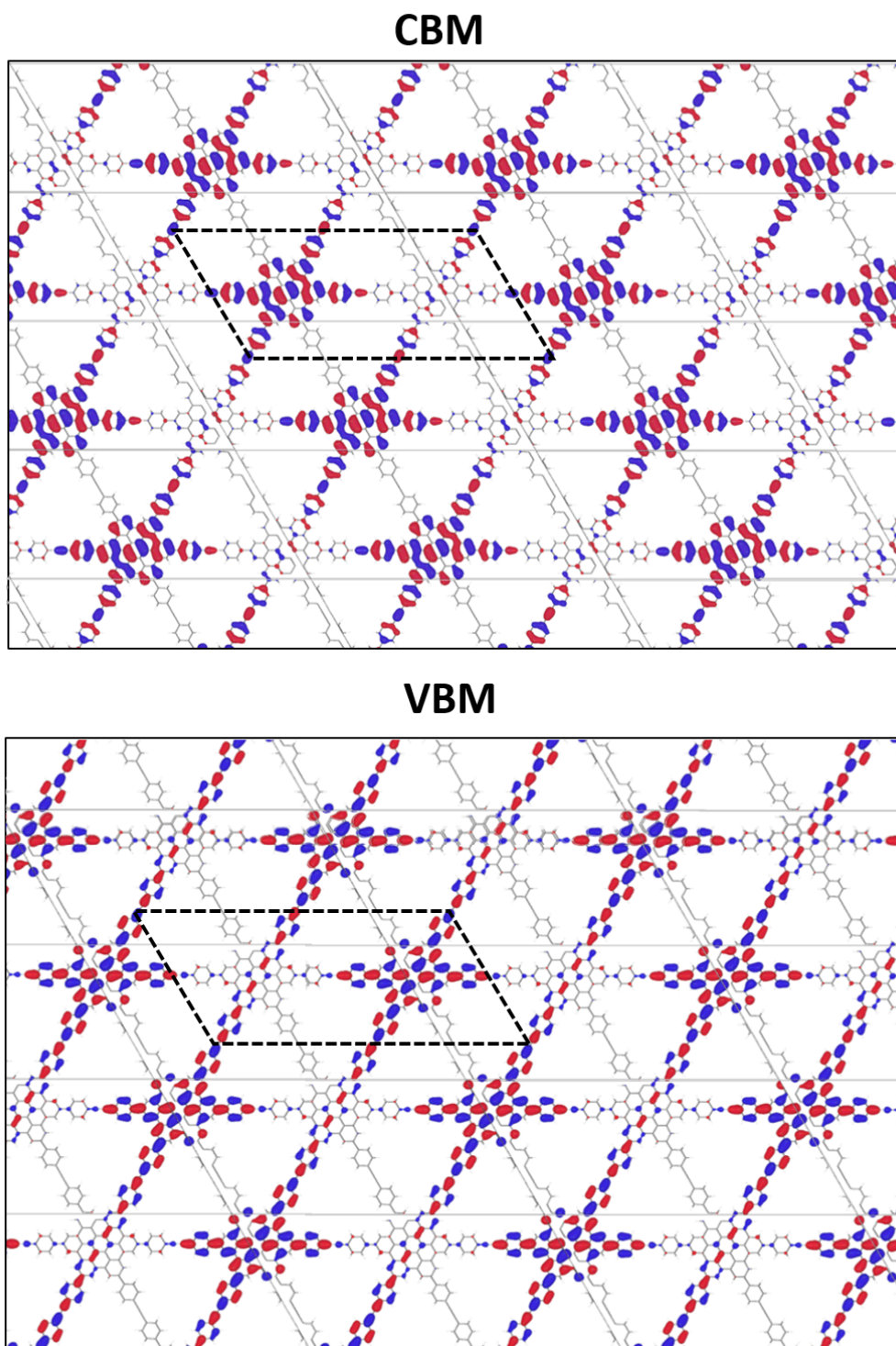
Figure 23: Localization of Hexabenzocoronene-Based COFs. 3D isodensity plots of the Gamma-point states of the valence and conduction bands for the hexabenzocoronene-based COF shown in Fig. 20b. An isovalue of 0.05 states per $\mathring{A}^3$ is applied.

2.4 Global Structure Search at Organic-Inorganic Interfaces

2.4.1 Author Contribution

O. T. Hofmann conceived the idea to perform global structure search at organic-inorganic interfaces. V. Obersteiner and O. T. Hofmann wrote a first version of the SAMPLE code, which was then improved by M. Scherbela and L. Hörmann. V. Obersteiner wrote the Basin-Hopping based routine and performed the first-principles calculations and data analysis. D. Wegner provided the experimental input and helped with the interpretation. E. Zojer and all co-authors intensively contributed to the interpretation of the results. V. Obersteiner and O. T. Hofmann designed the storyboard of the manuscript and V. Obersteiner wrote the first version of the manuscript and prepared all figures. The manuscript was then improved in close cooperation with O.T. Hofmann. The project was supervised by O. T. Hofmann.

The following paper has been submitted and is inserted here as original publication together with the Supporting Information. "Obersteiner, V. Scherbela, M., Hörmann, L., Wegner, D. and Hofmann, O. T. Structure Prediction for Surface-Induced Phases of Organic Monolayers."

2.4.2 Original Article

Structure Prediction for Surface-Induced Phases of Organic Monolayers

Veronika Obersteiner[1], Michael Scherbela[1], Lukas Hörmann,[1] Daniel Wegner[2] and Oliver T. Hofmann[1],*

[1] Institute of Solid State Physics, NAWI Graz, Graz University of Technology, Petersgasse 16, 8010 Graz, Austria

[2] Institute for Molecules and Materials, Radboud University, Heyendaalseweg 135, 6525 AJ Nijmegen, The Netherlands

Corresponding Author

*oliver.hofmann@tugraz.at

ABSTRACT

Structure determination and prediction pose a major challenge to computational material science, demanding efficient global structure search techniques tailored to identify promising and relevant candidates. Here, an innovative computational approach to explore the potential energy landscape of organic/inorganic interfaces is presented. It is specifically designed to sample the energetically lowest lying structures, including the thermodynamic minimum, in order to survey the particularly rich and intricate polymorphism in such systems. The approach combines a systematic discretization of the configuration space with an efficient exploration of the potential energy surface inspired by the Basin-Hopping method. Interfacing the algorithm with first-principles calculations, the power and efficiency of this approach is demonstrated for the example of the organic molecule TCNE (tetracyanoethylene) on Au(111). The predicted global minimum is validated by comparison to scanning tunneling microscopy experiments.

TOC
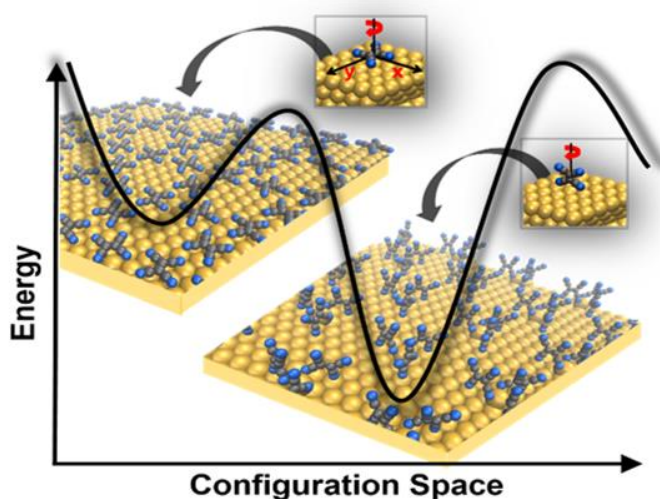
Introduction

The specific structure of any material constitutes the key to its functionality. Besides the chemical composition of a material, the way its individual constituents arrange, i.e. the polymorph it assumes, strongly influences the material's thermal[1], mechanical, optical[2], and electronic[3] properties. Structure determination and prediction is, therefore, the very fundament of material science. Determining polymorphs is particularly challenging for systems with more than one component, such as organic/inorganic interfaces that are prevalent in many applications, ranging from catalysis to organic electronics. Due to the interplay between intermolecular and molecule-substrate interactions, organic molecules on inorganic substrates are prone to form surface-induced phases, giving rise to a particularly rich and intricate polymorphism.[4,5] Such surface-induced phases often contain multiple molecules per unit cell and can display properties that are vastly superior to those of the bulk phase.[6] However, it is commonly *a priori* not assessable which polymorph the material will assume. Hence, predicting the structure of a material, ideally even before it is synthesized, is of crucial importance to pave the way towards computational materials design.

From a computational point of view, structure prediction can be considered as a global optimization problem, i.e. the problem of finding the global minimum of the energy landscape. The principle difficulty in treating nontrivial global optimization problems arises from the huge number of possible minima on the multidimensional potential energy surface (PES), which increases exponentially with the size of the system.[7] In practice, it is furthermore complicated by the fact that polymorphs can be kinetically trapped, i.e. also other minima besides the global minimum may play a decisive role for the structure formation at interfaces. Exhaustively sampling the corresponding vast configuration space demands an unfeasible amount of computational resources. Still a variety of different techniques, ranging from Monte Carlo or Molecular Dynamics based techniques such as simulated annealing,[19,20] Basin-Hopping[21–23] or minima hopping[24,25], to evolutionary approaches such as genetic algorithms[8,15,26–28] have been successfully applied to crystals[8–12], clusters[13–15], biomolecules[16,17] or multicomponent systems[18].

Although most of these efforts were dedicated to gas-phase structures or bulk crystals, recently, structure search was extended to organic/inorganic interfaces.[29–32] However, these methods often rely on elaborate data fitting or force fields to describe intermolecular interactions.

In this article we present a powerful and efficient computational structure search algorithm that allows to employ fully converged first-principles calculations throughout. It is specifically designed to explore the potential energy landscape of organic/inorganic interfaces with large unit cells containing multiple molecules and to efficiently and accurately locate low-energy polymorphs. This allows us to predict global minima (in cases where the experimental growth process in thermodynamically controlled), and furthermore also provides a set of relevant, low-energy structures that are useful to verify the interpretation of experiments. In short, the approach (which we call SAMPLE, surface adsorbate polymorph prediction with little effort) combines a systematic discretization of the PES with an efficient exploration inspired by a Basin-Hopping algorithm. Interfacing SAMPLE with dispersion-corrected density-functional theory (DFT), we demonstrate the power and efficiency of our algorithm by application to the strong electron-accepting molecule tetracyanoethylene (TCNE) adsorbed on the Au(111) surface. TCNE is particularly interesting for computational structure search studies, as it forms very different surface-induced phases on various metallic substrates,[33–35] with structures that are markedly different to those observed in the bulk.[36,37] Employing the SAMPLE approach to TCNE/Au(111) we find that a "naïve" evaluation of the structure on the basis of the scanning tunneling microscopy (STM) image does not yield the global minimum geometry, and we provide an alternative interpretation that cannot be inferred from experimental data alone.

Results

The SAMPLE approach

To present our method, we will first provide a general overview of the SAMPLE procedure and introduce the core concepts. Then, the individual steps of the procedure are discussed in detail on the specific example of TCNE adsorbed on Au(111). As illustrated in Fig. 1, the SAMPLE approach divides the structure search problem at organic/inorganic interfaces into two main

parts: first, a systematic discretization of the configuration space and second, an efficient exploration of the PES. The outcome is a set of energetically lowest lying polymorphs.
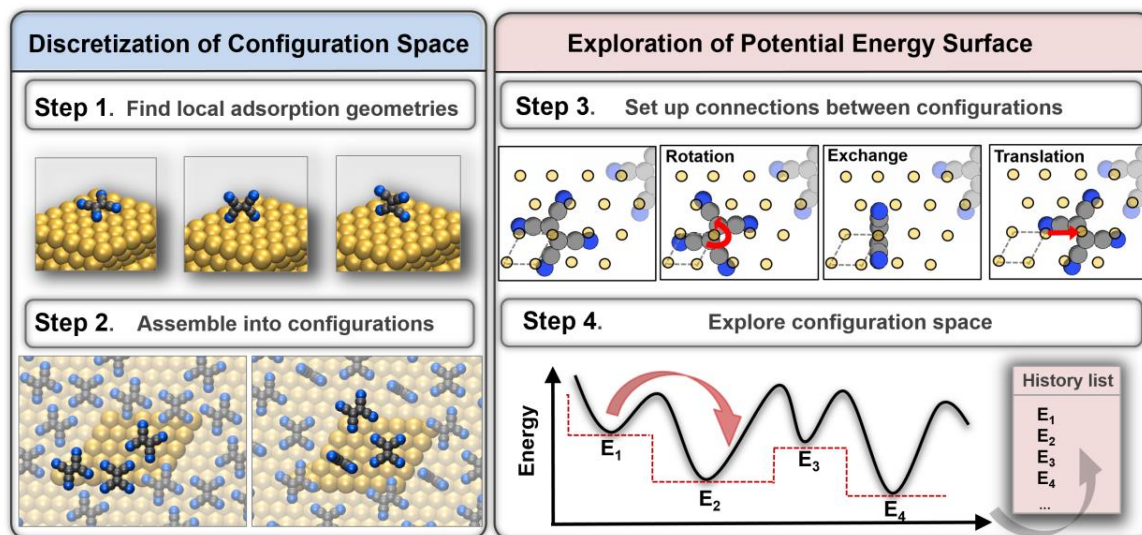
Figure 1. The SAMPLE approach. *A systematic discretization of the configuration space consisting of an extensive set of supramolecular configurations (left) is followed by an exploration of the PES, where efficiently chosen configurations are relaxed to the corresponding polymorphs, i.e. the nearest local minima on the PES (right). The outcome is a set of energetically lowest lying polymorphs. Specifically, **Step 1** shows three out of the nine stable local adsorption structures for TCNE/Au(111), i.e. a flat-lying TCNE molecule, an upright-standing TCNE molecule with the central C=C bond parallel to the surface and equivalently perpendicular to the surface. **Step 2** depicts two possible configurations generated by the assembly process. In **Step 3**, exemplary trial moves are illustrated, i.e. translation by one primitive surface unit cell (which is indicated by the dashed box), rotation and exchange by another local adsorption geometry. **Step 4** shows a schematic PES (black line) and the corresponding transformation into a set of interpenetrating staircases (red dashed line) by performing local geometry optimizations. Due to the unique labeling of all configurations, a history list containing all visited polymorphs can be provided. For details see main text.*

As visualized in Fig. 1, the discretization is performed in two consecutive steps. First, the adsorption geometries that isolated molecules on the surface would assume are determined.

This allows us to establish which adsorption sites are adopted and, in a subsequent assembly process, use the substrate as discrete registry to combine these local adsorption geometries into supramolecular configurations. Here, the term "configuration" denotes a specific arrangement of several molecules in the unit cell that serve as a starting point from which later the corresponding polymorph, i.e. the closest local minimum on the PES, will be determined via a local geometry optimization. These steps are fully deterministic and performed only once for a given interface. In notable contrast to commonly applied global structure search techniques, thereby an enclosed configuration space with a well-defined and reproducible number of possible configurations is generated a priori.

In principle, one could perform a local geometry optimization for each of these starting configurations to their nearest local minimum, and thereby obtain a complete energy ranking. However, the number of polymorphs increases exponentially with the number of molecules in the unit cell. Hence, in many cases, even after the aforementioned discretization procedure, the configuration space is too large to perform an exhaustive search within reasonable time. This demands, as the second part of the SAMPLE procedure, an efficient exploration of the PES.

To sample the PES we explore the configuration space generated in the first part in consecutive Monte Carlo steps by iteratively suggesting new configurations followed by a local geometry optimization. The discretization of the configuration space allows us to define connections between the configurations with the main advantage of performing a selective search along the PES. As illustrated as Step 3 in Fig. 1, we define specific trial moves for the molecules on the surface (i.e. translation, rotation and exchange by a different local adsorption geometry) and thereby set up a neighbor list for each configuration from which the next one is chosen randomly. Each suggested configuration is followed by a local structure relaxation into the closest local minimum. These minima (which can be uniquely identified by the molecular configurations and their positions) and their energies are stored for later reference and analysis. The outcome of the SAMPLE procedure is a set of energetically lowest lying polymorphs.

We note that the SAMPLE approach can be linked to any suitable electronic structure method that provides an accurate energy ranking. For all calculations in this article, we optimize the

geometry using PBE+vdW^{surf} [38] and report adsorption energies using the (supposedly) more accurate many-body dispersions correction scheme[39]. For full details on the methodology, see the Computational Methods section and the Supplementary Methods.

Application to TCNE/Au(111)

To convey a more detailed explanation of the SAMPLE approach and to benchmark its efficiency, in the following, we will apply it to the specific example of TCNE (tetracyanoethylene, see Fig. 2a) adsorbed on Au(111). As mentioned in the introduction, TCNE forms very different surface-induced phases on various metallic substrates.[33–35] In the specific case of Au(111), STM experiments performed at low temperature (T = 7 K, see Methods Section) reveal a triangular pattern in a non-orthogonal unit cell containing three TCNE molecules, as shown in Fig. 2b. (Note that these structures have already previously been reported in Ref. 33.) Interestingly, in contrast to many other conjugated molecules as well as to the adsorption of TCNE on, e.g., low-index Ag surfaces[33–35] or Cu(100)[33,40], the molecules do not appear in the expected flat-lying fashion. Rather, from the STM experiment they appear to be tilted onto their sides. This peculiarity makes TCNE/Au(111) an exciting candidate for employing our SAMPLE approach.
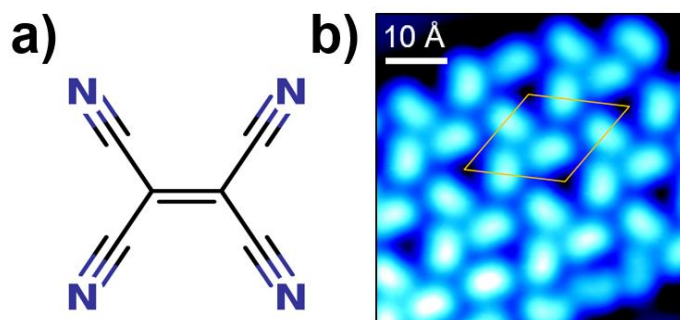
Figure 2. Molecular structure of TCNE and experimental STM image of TCNE/Au(111). (a) Chemical structure of tetracyanoethylene (TCNE, C_6N_4) (b) Experimental STM topography of TCNE adsorbed on Au(111). The image was taken in constant-current mode (V_s = 0.1 V, I = 5 pA, T = 7 K) and the film was grown at room temperature. TCNE arranges in ordered triangular structures with a unit cell containing three molecules that are tilted onto their sides.

Step 1: Evaluating the Local Adsorption Geometries

All band-structure calculations require a unique set of lattice vectors as input. In other words, *any* computational structure search for interfaces is limited to structures that are commensurable. As such, each molecule can be assigned a specific adsorption site on the substrate. For SAMPLE, we assume that the adsorption site is mostly independent of the molecular coverage, i.e. that the geometry of a molecule with respect to its position on the substrate is only slightly perturbed by the presence of other molecules on the surface. This means, for example, that an individual TCNE molecule might adopt a bridge or an on-top position (besides others). These are then likely also local minima (for each molecule) at high coverage (although the exact position may change, but this will be captured during geometry optimization) and thus suitable starting points for setting up the configuration space. Hence, we systematically discretize the configuration space in two consecutive steps. First, we only consider the metal-molecule interactions of single molecules, while intermolecular interactions are accounted for in a consecutive assembly process including several molecules per unit cell. This procedure significantly reduces the conformational complexity. We note that such a "divide and conquer" approach has also very recently been attempted for interfaces.[32] However, in contrast to ref. 32, in our work, the intermolecular interactions are not fitted from gas-phase calculations. Rather, they are directly obtained from first principles calculations of the molecules on the surface. Indeed, we emphasize that for the present system, which undergoes metal-to-molecule charge transfer, the intermolecular interaction even qualitatively changes between the gas phase and the adsorbed molecules.

Hence, in Step 1 we neglect the impact of intermolecular interactions and determine the stable geometries that an isolated, single molecule on the surface can adopt. In the present case, this is done by performing multiple local geometry optimizations from systematically chosen initial guesses with different molecular orientations and positions relative to the substrate (see Supplementary Methods for details). Altogether, we find nine possible local adsorption

geometries for TCNE/Au(111), three of which are exemplarily shown in Step 1 of Fig. 1. They differ in their particular adsorption site with respect to the substrate as well as in their orientation, i.e. they are flat-lying or upright-standing. Due to the hexagonal lattice of the gold surface and the mirror symmetries to TCNE each of the nine stable local adsorption geometries has three symmetry-equivalent isomers, which need to be considered in the second assembly step. A comprehensive list of all structures together with their adsorption energies can be found in the Supplementary Fig. 1 and 2.

Step 2: Assembling the Configurations

One of the major challenges in any structure search algorithm is the exponential explosion of the configuration space, i.e. the exponentially increasing number of configurations with system size. Exemplarily, for a unit cell containing three molecules, considering five degrees of freedom for each molecule on the surface and four different values per degree of freedom, an unfeasible number of $4^{(3 \cdot 5)} > 1$ billion configurations would be generated. Applying our discretization procedure, this problem is greatly mitigated. After evaluating the local adsorption geometries in Step 1, we assemble them into supramolecular configurations, as exemplarily illustrated in Step 2 of Fig. 1. In other words, the systematic pre-optimization allows us to "freeze out" the internal coordinates during the assembly step, where then only intermolecular interactions have to be considered.

For this assembly procedure, we use the primitive surface cell of the substrate, i.e. the p(1x1) (equivalent to $\sqrt{3}$ x $\sqrt{3}$ R30) unit cell of Au(111), as registry. In principle, we try all combinations of all possible local adsorption geometries in all rotations on each surface unit cell and discard all configurations that do not have the desired coverage or that are symmetry-equivalent to another configuration. Additionally, we remove configurations that are unphysical, because they interpenetrate or come too close to each other. Specifically, we exclude all configurations where the minimum distance between two atoms of adjacent molecules is smaller than a predefined threshold. Here we use 2.4 Å, but we note that for the present system, the number of configurations is not overly sensitive to the exact choice of this parameter, as shown in the

Supplementary Fig. 3. For details on our technical implementation, which avoids the configurational explosion associated to this assembly procedure, see Supplementary Fig. 4.

The extent of the generated configuration space, i.e. the number of possible configurations, depends on the number of local adsorption geometries that are determined in Step 1 as well as the molecular packing density, i.e. the size and shape of the unit cell together with the number of molecules it contains. In principle one could generate a configuration space for different unit cell shapes, sizes, and coverages. For the present case, we focus on the packing density which can be unambiguously obtained from the experimental STM shown in Fig. 2b, i.e. we generate the configuration space with the measured experimental unit cell containing three molecules. With this input, the assembly procedure generates approximately 200000 different configurations.

The discretization of the configuration space allows us to introduce a unique labeling for each of these configurations by storing the local adsorption site and position for each molecule in the unit cell using the substrate as registry. This leads to a major advantage in the exploration step, as discussed below.

Step 3: Setting up the Connections between Configurations

To explore the PES in a stepwise Monte Carlo procedure we sample the configuration space generated in the first part in consecutive steps by iteratively suggesting new configurations followed by a local geometry optimization. This is in principle similar to traditional Basin-Hopping, where the complex PES is transformed into a set of staircases by consecutive hops followed by geometry relaxations into the closest local minimum. Hopping between the configurations is performed by randomly choosing trial moves along certain trajectories, typically Cartesian or internal coordinates.[22,23] In contrast to this, in SAMPLE, a more efficient approach is pursued by exploiting the fact that each configuration in the discretized configuration space can be systematically connected to a certain number of neighboring configurations by performing selective trial moves. Specifically, the neighborhood for a certain configuration is generated according to the selection rules illustrated in Step 3 of Fig. 1: we allow each molecule in the cell

to (i) move to an adjacent space of the substrate, i.e. *translation* by one primitive p(1x1) surface cell (i.e., shift to the next possible equivalent adsorption site on the substrate), (ii) *rotate* on the spot to a symmetry-equivalent structure or (iii) adopt a different adsorption site, i.e., *exchange* to a different local adsorption geometry. Thereby, each configuration obtains an individual neighbor list defining all connections within the configuration space.

Step 4: Exploring the Configuration Space

The iterative procedure to explore the PES is illustrated in the flowchart depicted in Fig. 3. Starting from a certain configuration we suggest a random neighbor according to the neighbor list defined in Step 3. Depending on whether this neighboring configuration has already been visited or not, we would either just look up its energy in a history list or perform a local geometry optimization to the nearest local minimum on the PES. Note that this relaxation is comparably inexpensive as we start from a combination of already optimized local adsorption geometries (convergence is reached after 3-4 geometry steps on average). The suggested polymorph is accepted or rejected on the basis of the Metropolis-Hastings scheme: [41]

$$p_{acc} = min\left(1, e^{-\beta \Delta E}\right) \tag{1}$$

If the new energy is lower than the one of the current polymorph, it is accepted; in case of a higher energy it will be accepted depending on a probability that considers the energy difference to the last accepted polymorph, ΔE, as well as an effective temperature via a Boltzmann factor, β. In case of rejection, a different neighbor is chosen. The initial temperature was set to 300 K and was varied upon iterations, i.e. the temperature was decreased (increased) by 100 K in case of acceptation (rejection). Due to the unique labeling of each polymorph, all visited structures (accepted or rejected) can be added to a history list and need not to be recalculated in case of revisiting. As in traditional Basin-Hopping, this exploration run (as depicted in Fig. 3) is repeated several times for different starting configurations in order to ensure an unbiased structure search on the PES. However, in SAMPLE the history list of visited structures can be easily transferred from one run to the other, and as we will show in the following, this enormously increases the overall performance.
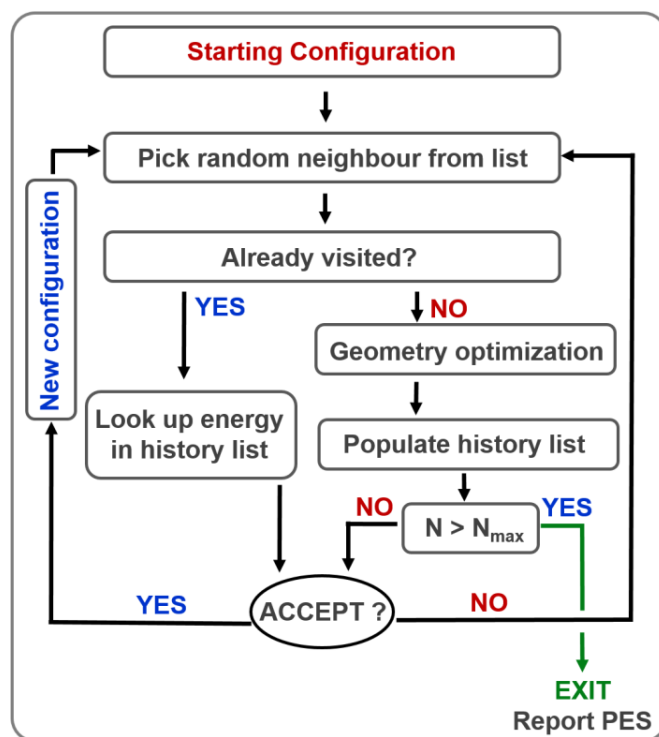
Figure 3. Exploration of the Potential Energy Surface. *Flowchart representing the iterative Monte Carlo procedure to explore the PES. The iterative process is stopped after a pre-determined number of geometry optimizations with DFT. For details, see main text.*

Benchmark, validation and performance.

In order to validate the performance of the exploration aspect of the SAMPLE approach, it is useful to reduce the conformation space to a size where a comprehensive search is possible, i.e., to a system where we can calculate, from first principles, all configurations that are created in the assembly procedure of the SAMPLE approach and see how efficiently the global minimum is found. Although SAMPLE does not necessarily rely on experimental input at all, it straightforwardly allows to incorporate information if available. We note that in principle such structural information could also be obtained from any experimental method, such as low energy electron diffraction techniques. For the case of TCNE/Au(111), it suggests itself to incorporate the information that TCNE forms triangular structures (cf. Fig. 2b).

Discarding all conformations where this is not the case (i.e., automatically rejecting all trial moves that lead to non-triangular structures in Step 3 of Fig. 1) reduces the complexity from about 200k to 144 configurations. The corresponding Sub-PES, i.e. the total energy of each of these polymorphs *after optimization to their local minimum* is shown in Fig. 4a. Each box of this PES represents one of the 144 triangular polymorphs. The global minimum is indicated by the red box.
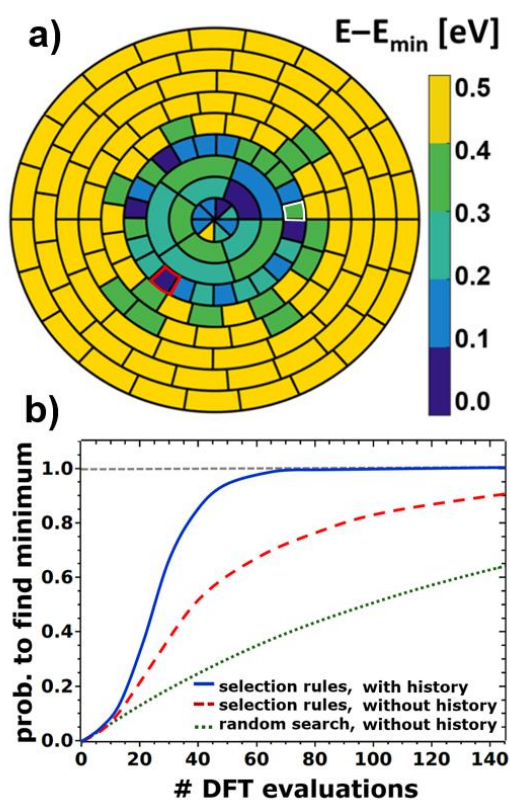
Figure 4. Benchmark and performance of SAMPLE. *(a)* *Sub-PES for TCNE/Au(111) comprising 144 triangular polymorphs. Each of the 144 boxes refers to one of the possible polymorphs generated by the assembly procedure. The color represents the total energy obtained after geometry optimization. Energies are given relative to the global minimum. The global minimum is indicated by a red box, while the polymorph with rank 30 (i.e. 0.35 eV higher in energy than the global minimum) is highlighted by the white box. The arrangement of the boxes is described*

*in detail in Supplementary Fig. 5 and 6. **(b)** Probability to find the global minimum on the PES*

shown in (a) for an increasing number of DFT evaluations. For details see main text.

On basis of this Sub-PES we evaluate the efficiency of our SAMPLE approach by estimating the probability to find the global minimum within a certain number of first-principles evaluations, i.e. the number of geometry optimizations, independent of how SAMPLE cycles where the energy is just looked up (which is essentially free) have been performed. To ensure an unbiased structure search we start the exploration (as described in Fig. 3) from a completely random starting configuration on the PES and stop it after a finite number (N_{max}) of geometry optimizations. As described above, the peculiarity of our approach is the fact that we explore the PES within a finite configuration space consisting of unique configurations that can be labeled and stored for re-visiting. Hence, we provide the energies of already calculated polymorphs in form of a history list, thereby avoiding expensive recalculation of already visited parts of the PES. Due to the stochastic nature of our approach the whole procedure is repeated 10.000 times to obtain accurate statistics, each time choosing a new random seed for the Metropolis-Hastings evaluation as well as for the starting configuration. Figure 4b shows the probability to find the global minimum on the Sub-PES as function of the performed geometry optimizations. When applying the SAMPLE procedure (blue line), the global minimum is found with a probability of approximately 85% already after 40 DFT evaluations (which corresponds to visiting 28% of the PES). In the present case, after 70 DFT evaluations (ca. 50% of the PES) the global minimum is practically guaranteed to be found. If we did not have a history list (which would be the case in traditional Basin-Hopping that cannot label configurations), the performance is considerably decreased. As shown in the red line in Fig. 4b, the probability to find the global minimum after 40 DFT evaluations only amounts to 50%. Furthermore, for a completely random search, i.e., if we did not employ system-specific selection rules and did not have a history list either, the probability would decrease to 25% after 40 DFT evaluations (see green line in Fig. 4b).

Comparison to Experiment

While the evaluation clearly shows that our approach is capable of efficiently determining the global minimum structure on the PES, it is also substantial to validate the results by comparison to the experimentally obtained structure. Applying SAMPLE to TCNE/Au(111), we find a global minimum that is indicated by the red box in the PES of Fig. 4a with the geometric structure shown in Fig. 5a. Although, as isolated species, the flat-lying TCNE molecule is found to be the most stable structure, indeed, among the triangular structures a configuration consisting of upright-standing molecules is obtained. The agreement between the global minimum and the experimental minimum looks, in principle, very reasonable.
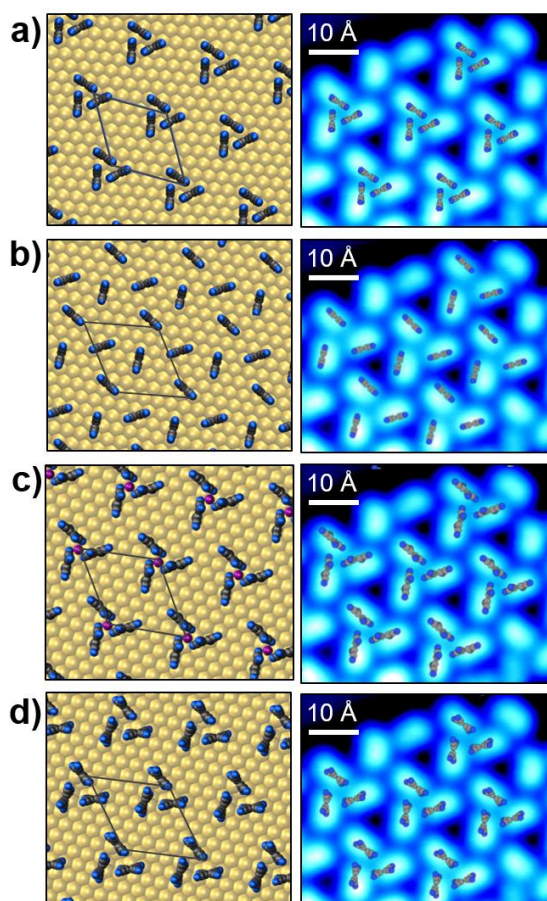
Figure 5. Predicted Polymorphs for TCNE/Au(111). *Geometric structure and overlay to the experimental STM of **(a)** the predicted global minimum on the in Fig. 4a (red box) shown sub-*

*PES consisting of triangular polymorphs of TCNE/Au(111), **(b)** the polymorph obtained from a "naïve" starting point where the molecules where placed in the middle of the spots in the STM image, corresponding to rank 30 in our PES evaluation, **(c)** the predicted global minimum including a gold adatom (pink) in the center of the triangular structures and **(d)** the predicted global minimum with a vacancy in the center of the triangular structures.*

However, if we start a geometry optimization based on the experimental picture alone, i.e. a geometry where we place all TCNE molecules in the middle of the spots in the STM image (Fig. 2b), we do arrive at a polymorph that is also covered by our SAMPLE approach. Surprisingly, this structure, shown in Fig. 5b and highlighted in Fig. 4a by the white border, is 0.35 eV higher in energy than the global minimum. It is thus only at rank 30 in the overall hierarchy of all calculated polymorphs. Compared to this polymorph, the molecules in the predicted global minimum polymorph appear to be too close to each other.

It is, in principle, conceivable that the reason for this apparent discrepancy is rooted in the inability of the employed electronic structure theory method (i.e., PBE+MBD) to correctly reproduce the real potential energy surface. Indeed, it is well known that the PBE functional generally misjudges the amount of charge transfer,[42–44] and tends to overdelocalize charge at interfaces.[45,46] Furthermore, we neglected the energy contribution from vibrations, which may change the ordering of the free energy relative to the DFT energies. On the other hand, the same method that we employ here has been recently used to gauge the hierarchy of organic bulk crystals in a blind test[12] with outstanding success, and also reproduces desorption energies of organic molecules on coinage metals very well.[47] We therefore expect that it is unlikely that the polymorph at rank 30 would actually be the true global minimum if we had used an even more accurate method.

Another possible interpretation of our results is that the experimentally observed structure is not in thermodynamic equilibrium. According to Ostwald's rule of stages,[48] many crystals go through higher-energy polymorphs before assuming the thermodynamic equilibrium arrangement. Indeed, the preparation of the sample was performed at room temperature, while the measurements were done at 7K, which could potentially "freeze" the prevalent conformation at that stage. On the other hand, most polymorphs of organic molecules that are experimentally

observed exhibit energy differences of less than 0.075 eV,[49] much less than the difference between our global minimum and the rank 30 polymorph. Also, the cool-down procedure prior to insertion of the sample into the liquid helium cooled STM involved a relatively slow (ca. 40 minutes) precooling from 300 K to 80 K using liquid nitrogen, which makes kinetic trapping unlikely.

A possibly more plausible scenario is that an implicit assumption in the interpretation of the STM data, namely that the system solely consists of TCNE molecules on a pristine Au(111) surface, is misleading. Especially the fact that the molecules seem to appear too close with respect to each other in the calculations (compared to experiment) suggests that the system may contain aspects that are not easily imaged with STM. These could be vacancies[50,51] or surface adatoms[35,52–54] both of which have been observed in several experimental studies. Therefore, we chose also to explore these possibilities and apply SAMPLE to predict the global minimum for these two scenarios. To this aim, we repeated the discretization and exploration procedure for triangular structures including a central adatom or a central vacancy. The corresponding Sub-PESs are shown in the Supplementary Fig. 7-9. The polymorphs of the most stable structures are depicted in Fig. 5c and d. Indeed, the presence of either an adatom or a vacancy increases the relative distances between the molecules to roughly the experimentally observed positions. We note that since the three scenarios (pristine surface, adatom and vacancy) contain a different number of atoms, their energies are not directly comparable in our calculations (unless an assumption about the chemical potential of Au is made, which is not viable here). However, in particular for the polymorph including the adatom an excellent agreement to the experimental STM is observed, which makes us confident that this adatom structure reflects the actual situation. This situation nicely illustrates that computational structure search is a powerful tool to verify and augment the interpretation of experiments and to pinpoint "hidden" aspects that might not be covered by a particular experimental technique. The concluding interpretation, of course, still lies in the hand of experimentalists, which can confirm – or refuse – the options presented by theory.

Conclusions

We have introduced SAMPLE, an innovative computational structure search algorithm to explore the potential energy landscape of organic/inorganic interfaces upon first-principles. Our approach combines a systematic discretization of the PES with an efficient exploration realized as a Monte Carlo method inspired by the Basin-Hopping algorithm. In stark contrast to commonly applied global structure search techniques, in a first assembly process we a priori generate a complete and enclosed configuration space with a well-defined and reproducible number of possible configurations. In a subsequent exploration step, an efficiently chosen set of energetically low-lying polymorphs including the thermodynamic minimum is predicted. Our approach is inspired by traditional Basin-Hopping, but is generally more efficient. The discretization is designed such that the resulting configuration is already very close to a local minimum, ensuring that the consecutive local geometry optimization is highly efficient. Furthermore, our method allows to efficiently revisit and cross already known parts of the configuration space without any additional computational effort, as the first assembly process enables the unique labeling of each polymorph. The efficiency is particularly enhanced by applying systematic trial moves according to carefully chosen transition rules, instead of the commonly applied random trial moves. We benchmarked our approach on the example of TCNE/Au(111) by interfacing SAMPLE with dispersion-corrected DFT and validated the predicted global minimum by comparison to the experimental STM data. Besides demonstrating the efficiency and power of the SAMPLE approach we could moreover provide an alternative interpretation that cannot be inferred from pure experimental data. These aspects endow the SAMPLE approach with significant potential for refined structure determination and prediction of other interface materials far beyond the system discussed here.

Methods

Computational Section

All electronic structure calculations were performed within the framework of DFT using the Fritz-Haber-Institute ab initio molecular simulations (FHI-aims) package.[55] The Perdew-Burke-

Ernzerhof (PBE)[56] exchange-correlation functional was applied and dispersion correction was included using vdW^{surf} [38] for geometry optimizations and many body dispersion (MBD)[39] for subsequent single point calculations. When changing from vdW^{surf} to MBD, we observe qualitative differences in the energetic ordering of the local adsorption geometries as well as the polymorphs spanning the PES (see Supplementary Fig. 2 and 5 for more details). To obtain the local adsorption geometries, we used a (6x6) unit cell to avoid spurious interaction between neighboring cells. For all supramolecular polymorph calculations the experimental unit cell was measured from the representative STM image shown in Fig. 2b with an epitaxy matrix of $\begin{pmatrix} 5 & 1 \\ -1 & 6 \end{pmatrix}$. We employed a tier 1 basis for Au (excluding g and h basis functions) and tier 2 for N and C basis functions. A converged 4x4x1 k-point grid was applied for all calculations. Geometry optimizations were performed using the trust radius method enhanced version of the Broyden-Fletcher-Goldfarb-Shanno optimization algorithm until the remaining forces were less than 0.1 eV/Å. For the local adsorption structures as well as for the polymorphs we used four layers of gold and relaxed the uppermost two layers together with the monolayer. VMD[57], VESTA[58] and Matlab were used for graphical visualization, python was used to implement SAMPLE. For full details on the applied computational methodology and numerical parameters used in our calculations, see the Supplementary Methods.

Experimental Section

The experiments were performed in ultrahigh vacuum (UHV) using a home-built STM operated at $T = 7$ K. TCNE crystals (99% purity) were kept in a small vacuum container that was cleaned by repeated cycles of flushing with Ar gas and pumping. Its high vapor pressure of ~$2 \cdot 10^{-3}$ mbar at room temperature[59] permits controlled dosing of TCNE gas from the container into the UHV system through a leak valve. The purity of the TCNE gas was checked with quadrupole mass spectrometry. Prior to TCNE adsorption, the Au(111) single-crystal substrate was cleaned by repeated cycles of Ar sputtering and annealing. Afterward, TCNE was deposited through the leak valve onto the Au(111) substrate that was held at room temperature, leading to sub-monolayer amounts in fcc regions of the Au(111) herringbone reconstruction.[33] Then the sample was slowly (within about 40 minutes) precooled to about 80 K before the final transfer into the cryogenic

STM. The STM tip was made of PtIr, and topography images were taken in constant-current mode.

Acknowledgements

Author Contributions

O.T.H. conceived the project idea. V.O. and O.T.H. wrote a first version of the structure search code, which was then improved by M.S and L.H. V.O. wrote the Basin-Hopping based routine and performed the first-principles calculations and data analysis. D.W. provided the experimental input and helped with the interpretation. V.O. prepared the figures and compiled the manuscript in close cooperation with O.T.H.

Additional Information

Supplementary Information is available. Correspondence should be addressed to O.T.H.

Competing financial interest

The authors declare no competing financial interest.

References

1. David, W. I. F. *et al.* The structure, thermal properties and phase transformations of the cubic polymorph of magnesium tetrahydroborate. *Phys. Chem. Chem. Phys.* **14,** 11800–11807 (2012).
2. Tiago, M. L., Northrup, J. E. & Louie, S. G. \textit{Ab initio} calculation of the electronic and optical properties of solid pentacene. *Phys. Rev. B* **67,** 115212 (2003).
3. Ambrosch-Draxl, C., Nabok, D., Puschnig, P. & Meisenbichler, C. The role of polymorphism in organic thin films: oligoacenes investigated from first principles. *New J. Phys.* **11,** 125010 (2009).
4. Jones, A. O. F., Chattopadhyay, B., Geerts, Y. H. & Resel, R. Substrate-Induced and Thin-Film Phases: Polymorphism of Organic Materials on Surfaces. *Adv. Funct. Mater.* **26,** 2233–2255 (2016).
5. Chung, H. & Diao, Y. Polymorphism as an emerging design strategy for high performance organic electronics. *J. Mater. Chem. C* **4,** 3915–3933 (2016).
6. Diao, Y. *et al.* Understanding Polymorphism in Organic Semiconductor Thin Films through Nanoconfinement. *J. Am. Chem. Soc.* **136,** 17046–17057 (2014).
7. Stillinger, F. H. Exponential multiplicity of inherent structures. *Phys. Rev. E* **59,** 48–51 (1999).
8. Abraham, N. L. & Probert, M. I. J. A periodic genetic algorithm with real-space representation for crystal structure and polymorph prediction. *Phys. Rev. B* **73,** 224104 (2006).
9. Oganov, A. R. & Glass, C. W. Crystal structure prediction using ab initio evolutionary techniques: Principles and applications. *J. Chem. Phys.* **124,** 244704 (2006).
10. Woodley, S. M. & Catlow, R. Crystal structure prediction from first principles. *Nat. Mater.* **7,** 937–946 (2008).
11. Wang, Y., Lv, J., Zhu, L. & Ma, Y. Crystal structure prediction via particle-swarm optimization. *Phys. Rev. B* **82,** 094116 (2010).
12. Reilly, A. M. *et al.* Report on the sixth blind test of organic crystal structure prediction methods. *Acta Crystallogr. Sect. B Struct. Sci. Cryst. Eng. Mater.* **72,** 439–459 (2016).
13. Johnston, R. L. Evolving better nanoparticles: Genetic algorithms for optimising cluster geometries. *Dalton Trans.* 4193–4207 (2003). doi:10.1039/B305686D
14. Ferrando, R., Fortunelli, A. & Johnston, R. L. Searching for the optimum structures of alloy nanoclusters. *Phys. Chem. Chem. Phys.* **10,** 640–649 (2008).
15. Heiles, S. & Johnston, R. L. Global optimization of clusters using electronic structure methods. *Int. J. Quantum Chem.* **113,** 2091–2109 (2013).
16. Liwo, A., Lee, J., Ripoll, D. R., Pillardy, J. & Scheraga, H. A. Protein structure prediction by global optimization of a potential energy function. *Proc. Natl. Acad. Sci.* **96,** 5482–5485 (1999).
17. Olson, B., Hashmi, I., Molloy, K. & Shehu, A. Basin Hopping As a General and Versatile Optimization Framework for the Characterization of Biological Macromolecules. *Adv Artif Intell* **2012,** 3:3–3:3 (2012).
18. Chua, A. L.-S., Benedek, N. A., Chen, L., Finnis, M. W. & Sutton, A. P. A genetic algorithm for predicting the structures of interfaces in multicomponent systems. *Nat. Mater.* **9,** 418–422 (2010).
19. Pannetier, J., Bassas-Alsina, J., Rodriguez-Carvajal, J. & Caignaert, V. Prediction of crystal structures from crystal chemistry rules by simulated annealing. *Nature* **346,** 343–345 (1990).
20. Schön, J. C. & Jansen, M. in *Modern Methods of Crystal Structure Prediction* (ed. Oganov, A. R.) 67–105 (Wiley-VCH Verlag GmbH & Co. KGaA, 2010).
21. Wales, D. J. & Doye, J. P. K. Global Optimization by Basin-Hopping and the Lowest Energy Structures of Lennard-Jones Clusters Containing up to 110 Atoms. *J. Phys. Chem. A* **101,** 5111–5116 (1997).
22. Panosetti, C., Krautgasser, K., Palagin, D., Reuter, K. & Maurer, R. J. Global Materials Structure Search with Chemically Motivated Coordinates. *Nano Lett.* **15,** 8044–8048 (2015).

23. Krautgasser, K., Panosetti, C., Palagin, D., Reuter, K. & Maurer, R. J. Global structure search for molecules on surfaces: Efficient sampling with curvilinear coordinates. *J. Chem. Phys.* **145,** 084117 (2016).
24. Goedecker, S. Minima hopping: An efficient search method for the global minimum of the potential energy surface of complex molecular systems. *J. Chem. Phys.* **120,** 9911–9917 (2004).
25. Goedecker, S. in *Modern Methods of Crystal Structure Prediction* (ed. Oganov, A. R.) 131–145 (Wiley-VCH Verlag GmbH & Co. KGaA, 2010).
26. Hartke, B. Global geometry optimization of clusters using genetic algorithms. *J. Phys. Chem.* **97,** 9973–9976 (1993).
27. Deaven, D. M. & Ho, K. M. Molecular Geometry Optimization with a Genetic Algorithm. *Phys. Rev. Lett.* **75,** 288–291 (1995).
28. Supady, A., Blum, V. & Baldauf, C. First-Principles Molecular Structure Search with a Genetic Algorithm. *J. Chem. Inf. Model.* **55,** 2338–2348 (2015).
29. Copie, G. *et al.* Atomic Scale Modeling of Two-Dimensional Molecular Self-Assembly on a Passivated Si Surface. *J. Phys. Chem. C* **118,** 12817–12825 (2014).
30. J. Roussel, T., Barrena, E., Ocal, C. & Faraudo, J. Predicting supramolecular self-assembly on reconstructed metal surfaces. *Nanoscale* **6,** 7991–8001 (2014).
31. Copie, G. *et al.* Surface-Induced Optimal Packing of Two-Dimensional Molecular Networks. *Phys. Rev. Lett.* **114,** 066101 (2015).
32. Packwood, D. M., Han, P. & Hitosugi, T. Chemical and entropic control on the molecular self-assembly process. *Nat. Commun.* **8,** (2017).
33. Wegner, D. *et al.* Single-Molecule Charge Transfer and Bonding at an Organic/Inorganic Interface: Tetracyanoethylene on Noble Metals. *Nano Lett.* **8,** 131–135 (2008).
34. Wegner, D. *et al.* Adsorption Site Determination of a Molecular Monolayer via Inelastic Tunneling. *Nano Lett.* **13,** 2346–2350 (2013).
35. Rodríguez-Fernández, J. *et al.* Temperature-controlled metal/ligand stoichiometric ratio in Ag-TCNE coordination networks. *J. Chem. Phys.* **142,** 101930 (2015).
36. Bekoe, D. A. & Trueblood, K. N. The crystal structure of tetracyanoethylene*. *Z. Krist.* **113,** 1–22 (1960).
37. Khazaei, M., Arai, M., Sasaki, T. & Kawazoe, Y. Polymerization of Tetracyanoethylene under Pressure. *J. Phys. Chem. C* **117,** 712–720 (2013).
38. Ruiz, V. G., Liu, W., Zojer, E., Scheffler, M. & Tkatchenko, A. Density-Functional Theory with Screened van der Waals Interactions for the Modeling of Hybrid Inorganic-Organic Systems. *Phys. Rev. Lett.* **108,** 146103 (2012).
39. Tkatchenko, A., DiStasio, R. A., Car, R. & Scheffler, M. Accurate and Efficient Method for Many-Body van der Waals Interactions. *Phys. Rev. Lett.* **108,** 236402 (2012).
40. Bedwani, S., Wegner, D., Crommie, M. F. & Rochefort, A. Strongly Reshaped Organic-Metal Interfaces: Tetracyanoethylene on Cu(100). *Phys. Rev. Lett.* **101,** 216105 (2008).
41. Metropolis, N., Rosenbluth, A. W., Rosenbluth, M. N., Teller, A. H. & Teller, E. Equation of State Calculations by Fast Computing Machines. *J. Chem. Phys.* **21,** 1087–1092 (1953).
42. Atalla, V., Yoon, M., Caruso, F., Rinke, P. & Scheffler, M. Hybrid density functional theory meets quasiparticle calculations: A consistent electronic structure approach. *Phys. Rev. B* **88,** (2013).
43. Fonari, A., Sutton, C., Brédas, J.-L. & Coropceanu, V. Impact of exact exchange in the description of the electronic structure of organic charge-transfer molecular crystals. *Phys. Rev. B* **90,** 165205 (2014).
44. Cohen, A. J., Mori-Sánchez, P. & Yang, W. Challenges for Density Functional Theory. *Chem. Rev.* **112,** 289–320 (2012).

45. Körzdörfer, T. & Brédas, J.-L. Organic Electronic Materials: Recent Advances in the DFT Description of the Ground and Excited States Using Tuned Range-Separated Hybrid Functionals. *Acc. Chem. Res.* **47,** 3284–3291 (2014).

46. Hofmann, O. T., Rinke, P., Scheffler, M. & Heimel, G. Integer versus Fractional Charge Transfer at Metal(/Insulator)/Organic Interfaces: Cu(/NaCl)/TCNE. *ACS Nano* **9,** 5391–5404 (2015).

47. Maurer, R. J. *et al.* Adsorption structures and energetics of molecules on metal surfaces: Bridging experiment and theory. *Prog. Surf. Sci.* **91,** 72–100 (2016).

48. Chung, S.-Y., Kim, Y.-M., Kim, J.-G. & Kim, Y.-J. Multiphase transformation and Ostwald's rule of stages during crystallization of a metal phosphate. *Nat. Phys.* **5,** 68–73 (2009).

49. Nyman, J. & Day, G. M. Static and lattice vibrational energy differences between polymorphs. *CrystEngComm* **17,** 5154–5165 (2015).

50. Wang, L. *et al.* Metal adatoms generated by the co-play of melamine assembly and subsequent CO adsorption. *Phys Chem Chem Phys* **18,** 2324–2329 (2016).

51. Azzam, W. Adlayer structures of anthracenthiol on Au(111) after removal of covering multilayers with probe scan. *Appl. Surf. Sci.* **371,** 562–570 (2016).

52. Lin, N. *et al.* Two-Dimensional Adatom Gas Bestowing Dynamic Heterogeneity on Surfaces. *Angew. Chem. Int. Ed.* **44,** 1488–1491 (2005).

53. Faraggi, M. N. *et al.* Bonding and Charge Transfer in Metal–Organic Coordination Networks on Au(111) with Strong Acceptor Molecules. *J. Phys. Chem. C* **116,** 24558–24565 (2012).

54. Meyer, J. *et al.* Tuning the formation of discrete coordination nanostructures. *Chem Commun* **51,** 12621–12624 (2015).

55. Blum, V. *et al.* Ab initio molecular simulations with numeric atom-centered orbitals. *Comput. Phys. Commun.* **180,** 2175–2196 (2009).

56. Perdew, J. P., Burke, K. & Ernzerhof, M. Generalized Gradient Approximation Made Simple. *Phys. Rev. Lett.* **77,** 3865–3868 (1996).

57. Humphrey, W., Dalke, A. & Schulten, K. VMD: Visual molecular dynamics. *J. Mol. Graph.* **14,** 33–38 (1996).

58. Momma, K. & Izumi, F. VESTA: a three-dimensional visualization system for electronic and structural analysis. *J. Appl. Crystallogr.* **41,** 653–658 (2008).

59. De Wit, H. G. ., Van Miltenburg, J. . & De Kruif, C. . Thermodynamic properties of molecular organic crystals containing nitrogen, oxygen, and sulphur 1. Vapour pressures and enthalpies of sublimation. *J. Chem. Thermodyn.* **15,** 651–663 (1983).

2.4.3 Supporting Information

Supporting Information to

Structure Prediction for Surface-Induced Phases of Organic Monolayers

Veronika Obersteiner[1], Michael Scherbela[1], Lukas Hörmann[1], Daniel Wegner[2] and Oliver T. Hofmann[1],*

[1]Institute of Solid State Physics, NAWI Graz, Graz University of Technology, Petersgasse 16, 8010 Graz, Austria

[2]Institute of Molecules and Materials, Radboud University, 6500 GL Nijmegen, The Netherlands

Corresponding Authors

*oliver.hofmann@tugraz.at

The Supplementary Information file includes:

I. Supplementary Methods

Details to the DFT Methodology

As described in the main text DFT calculations were performed applying the FHI-aims code. For the calculation of the different polymorphs that partly lie very close in energy a huge accuracy of the energies is required. Therefore, we thoroughly performed the following convergence tests. For both, the unit cell for the local adsorption geometries (6x6 the primitive √3x√3 R30 Au(111) surface unit cell) as well as for the polymorphs (the unit cell measured from the experimental STM with an epitaxy matrix of $\begin{pmatrix} 5 & 1 \\ -1 & 6 \end{pmatrix}$), we converged the adsorption energy per molecule with respect to the basis set, the k-point grid, the vacuum layer as well as the number of substrate layers within 0.01 eV per molecule. (For the local adsorption geometries we also converged the size of the unit cell to avoid spurious interactions between individual molecules.) The convergence criteria for the self-consistent cycles were set to 10^{-2} e/Å^3 for the charge density and 10^{-5} eV for the total energy. We included relativistic effects within the ZORA approximation due to the presence of the gold substrate. The repeated slab approach with a vacuum of 60 Å was applied together with a dipole correction perpendicular to the surface.

Geometry optimizations were performed at the PBE level using the trust radius method enhanced version of the Broyden-Fletcher-Goldfarb-Shanno optimization algorithm with a tolerance of 10^{-2} eV/ Å, until the remaining forces were less than 10^{-1} eV/ Å. For the evaluation of the local adsorption geometries, we started from 48 different initial guesses varying the orientation of the molecule as well as the position with respect to the surface. For each orientation, i.e. flat lying TCNE, upright standing with the central C=C bond parallel to the surface and equivalently normal to the surface, we place the molecule on the four symmetry inequivalent adsorption sites (on top, fcc hollow, hcp hollow and bridge position) and moreover rotate the whole molecule around the z-direction, i.e. perpendicular to the substrate, by 0°, 15°, 30° and 45°. During the optimization the uppermost Gold layer is relaxed together with the molecule. The 48 starting points converged into 9 distinct local adsorption geometries which are shown in Supplementary Fig.1.

II. Supplementary Figures
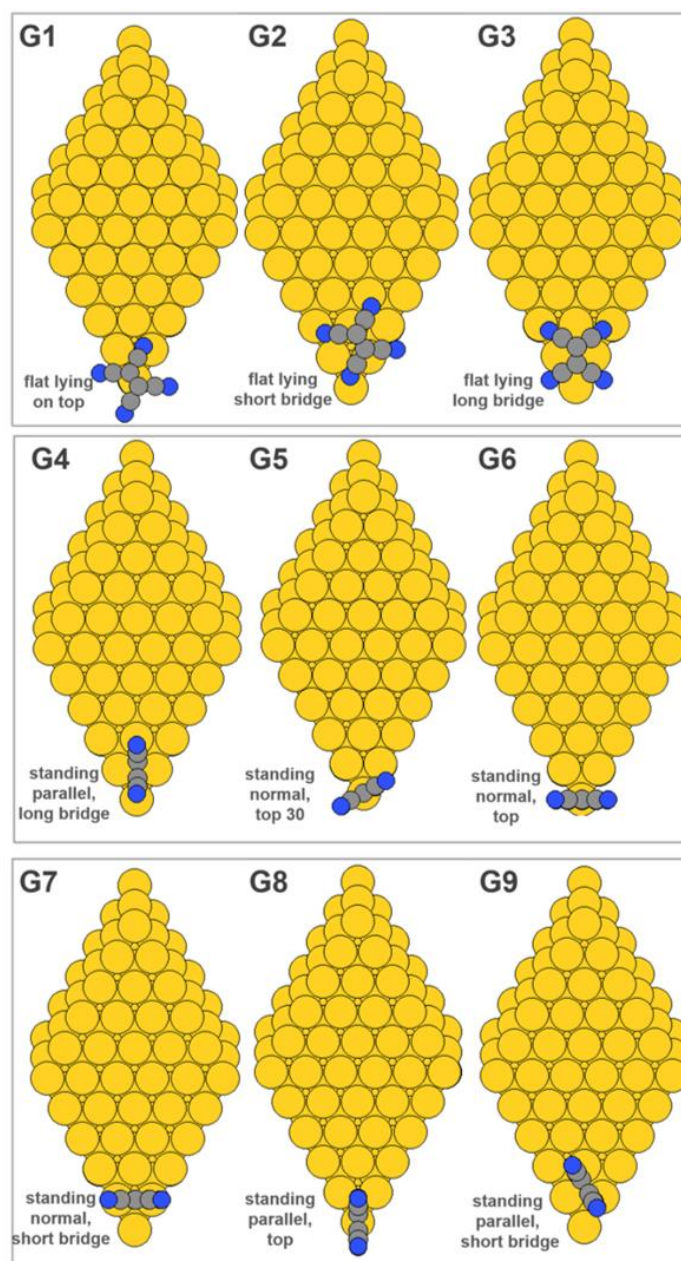
Supplementary Figure 1. *Local Adsorption Geometries of TCNE/Au(111). Structure of the nine stable local adsorption geometries ordered with respect to energy, i.e. structure G1 is the most stable local adsorption geometry (compare Supplementary Fig. 2). They differ in the orientation with respect to the surface, i.e. flat lying or upright standing, as well as in the particular binding site. As mentioned in the main text, we categorize them into three different groups: the flat lying adsorption geometries, the upright standing ones with the central C=C bond oriented parallel to the surface and equivalently normal to the surface.*
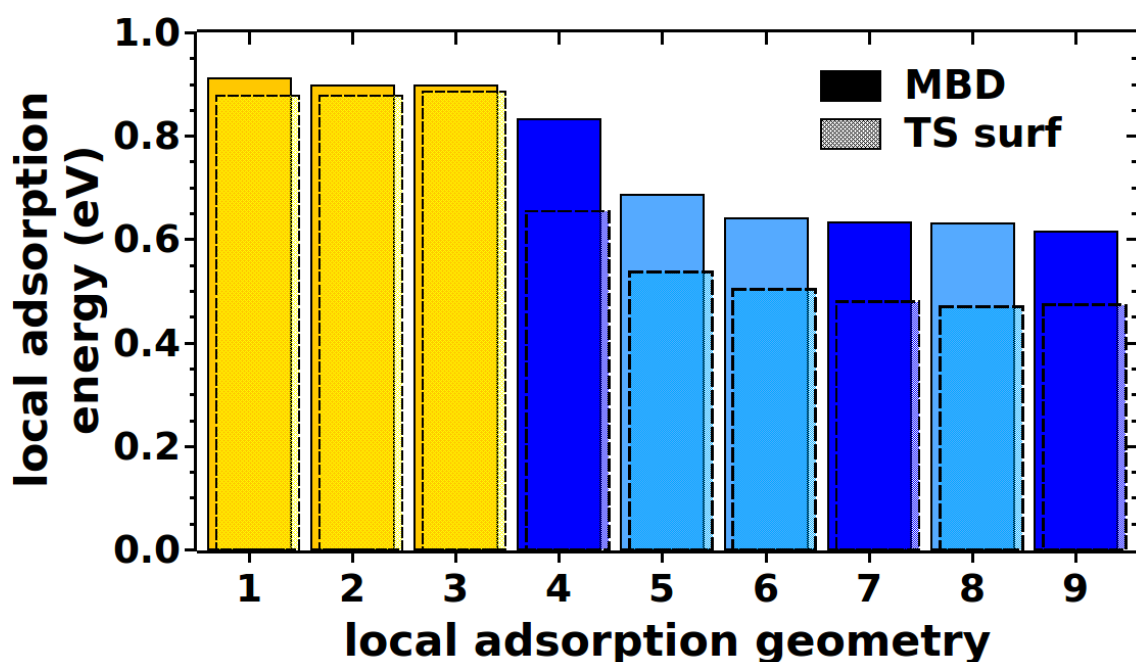
Supplementary Figure 2. *Local Adsorption Energies for TCNE/Au(111). Adsorption energies for the nine stable local adsorption geometries shown in Supplementary Fig.1 applying different dispersion schemes, i.e. vdW^{surf} energies (solid bars) and MBD energies (dashed bars). As explained in the main text, we categorize the local adsorption geometries into three groups: flat lying local adsorption geometries (yellow), upright standing with the central C=C bond oriented parallel to the surface (dark blue) and equivalently normal to the surface (light blue). Qualitative different results are observed when changing from vdW^{surf} to MBD: the energy ordering for the flat lying local adsorption geometries changes, i.e. the most stable structure changes from structure G3 to G1 (but is still flat lying). More importantly for this study, the upright standing local adsorption geometries are favored when applying MBD, reducing the energy difference between structure G4 and the most stable structure G1 from 0.24 eV (vdW^{surf}) to 0.06 eV (MBD). As a consequence, the PESs in Fig. 5, 7 and 9 also show qualitative different results when applying different dispersion correction schemes.*
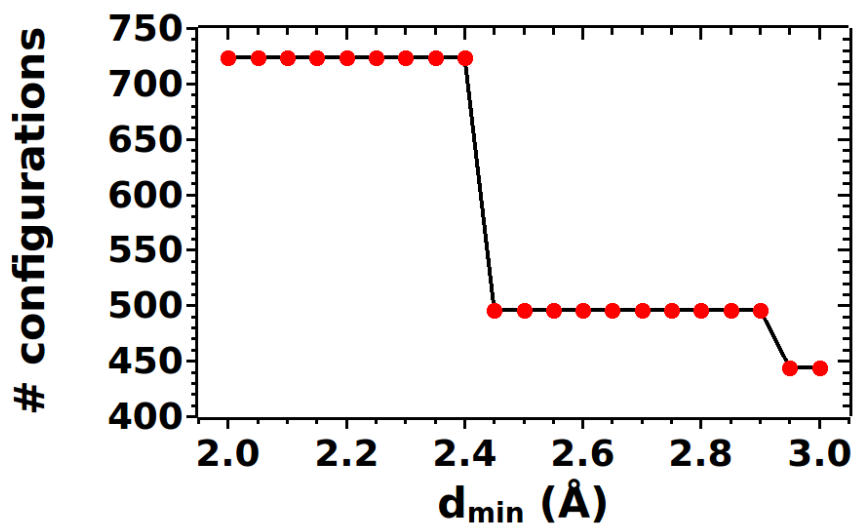
Supplementary Figure 3. *Threshold for the Assembly Procedure. Number of configurations generated in Step 2 of Fig. 1 obtained for different minimum distances between the atoms of two neighboring molecules. The threshold chosen for TCNE/Au(111) is* 2.4 Å.
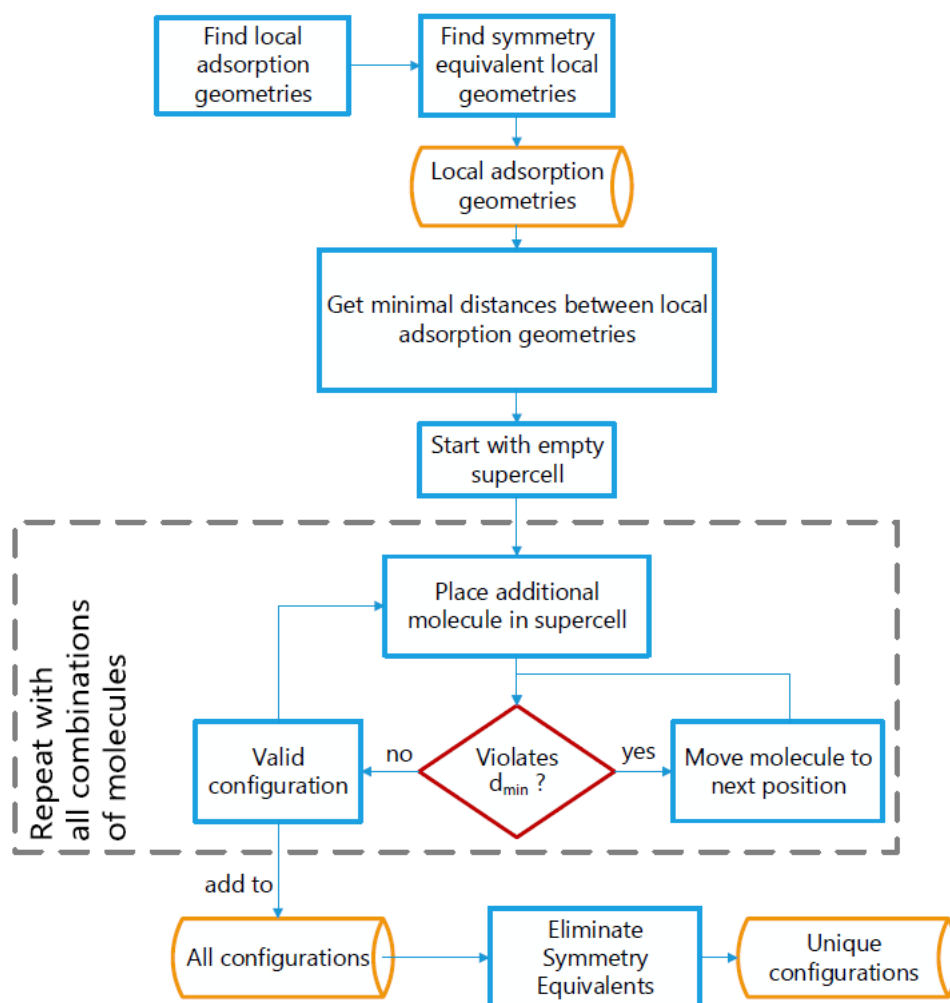
Supplementary Figure 4. *Flowchart for the Discretization of the Configuration Space.*

As described in the main text the discretization is performed in two consecutive steps where we first find the local adsorption geometries isolated molecules could assume on the surface and afterwards combine them into supramolecular configurations. As illustrated in the flowchart, after evaluating all local adsorption geometries and their symmetry equivalents, all physically sensible configurations with multiple molecules per supercell are generated. In contrast to a brute-force ansatz where each molecule is put on every possible position in each possible rotation, we start with an empty supercell and consecutively add additional molecules to the supercell. To avoid collisions between the molecules we define a threshold, i.e. a minimal distance between the local adsorption geometries. On basis of this threshold, d_{min} , we either move the molecule to the next position or keep this configuration. As shown in Supplementary Fig. 3 the number of configurations is not overly sensitive to the exact choice of this parameter. The consecutive adding of new molecules is stopped when a certain number of molecules in the unit cell (i.e. a certain molecular

coverage) is reached. The procedure (indicated by the grey box) is iteratively repeated with all combinations of molecules. Thereafter, all symmetry equivalent configurations are removed. In particular, translations as well as rotational and inversion symmetry are exploited to reduce the total number of configurations. This process of eliminating colliding structures and exploiting substrate symmetries can reduce the configuration space by orders of magnitude compared to a brute-force ansatz.
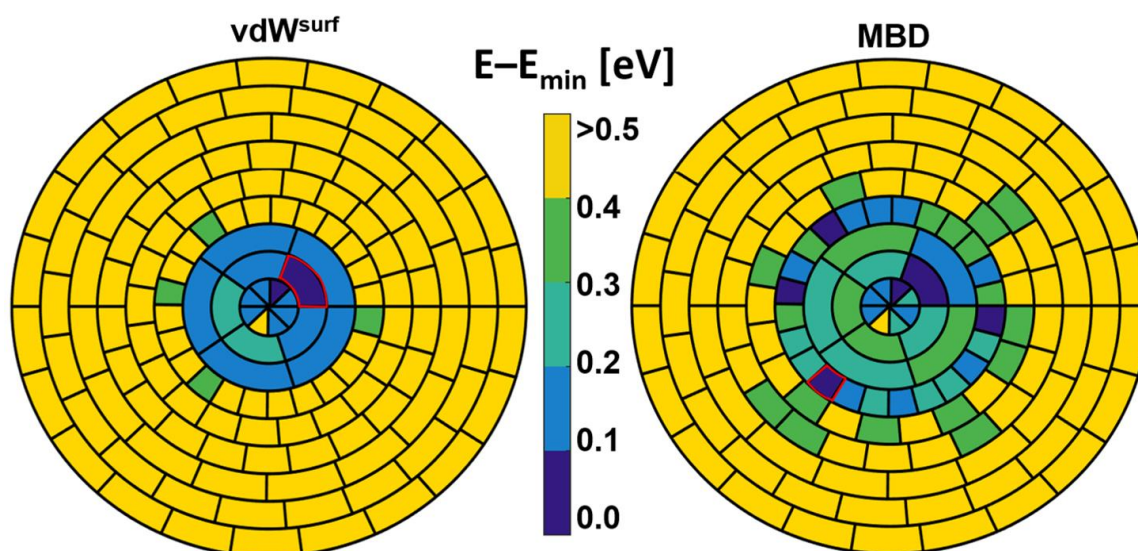
Supplementary Figure 5. *PES for TCNE/Au(111).* *Sub-PES for TCNE/Au(111) consisting of all possible triangular polymorphs applying different dispersion schemes, i.e. vdW^surf (left) and MBD (right). Energies are obtained after geometry optimization and are given with respect to the global minimum of the respective PES. We see qualitative differences in the energetic ordering of the polymorphs when applying different dispersion schemes, i.e. the global minimum (indicated by the red box) changes from a structures consisting of flat lying molecules (left) to the one comprising upright standing molecules. The geometric structure of some of the polymorphs are shown in the Supplementary Fig. 5. The boxes are arranged in the following way: starting from the center, each of the nine rings contains polymorphs consisting of three symmetry equivalent local adsorption geometries which are ordered according to their local adsorption energies as defined in Supplementary Fig. 2, i.e. the innermost three rings contain polymorphs comprising only flat lying molecules, while the outermost six rings comprise upright standing molecules.*
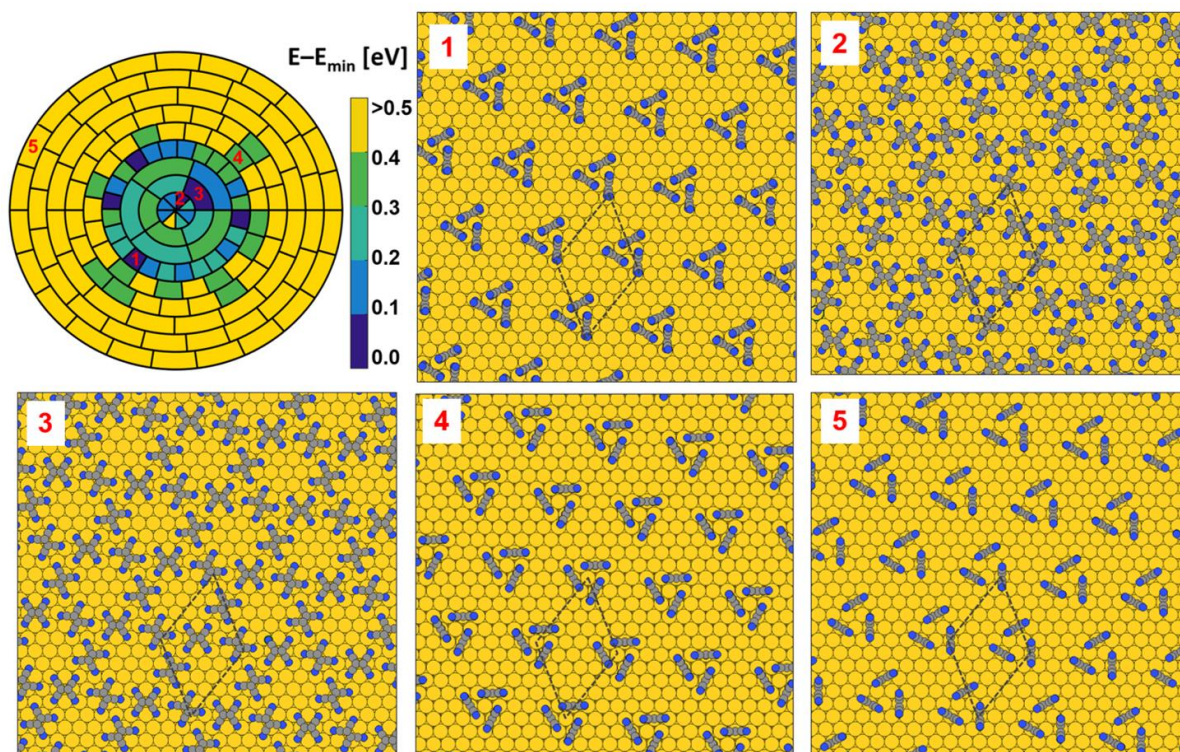
Supplementary Figure 6. *Exemplarily Structures of the PES for TCNE/Au(111). On the sub-PES for TCNE/Au(111) consisting of three-fold symmetric polymorphs, exemplarily, 5 different polymorphs with increasing energy are indicated and their structures are shown after geometry optimization.*
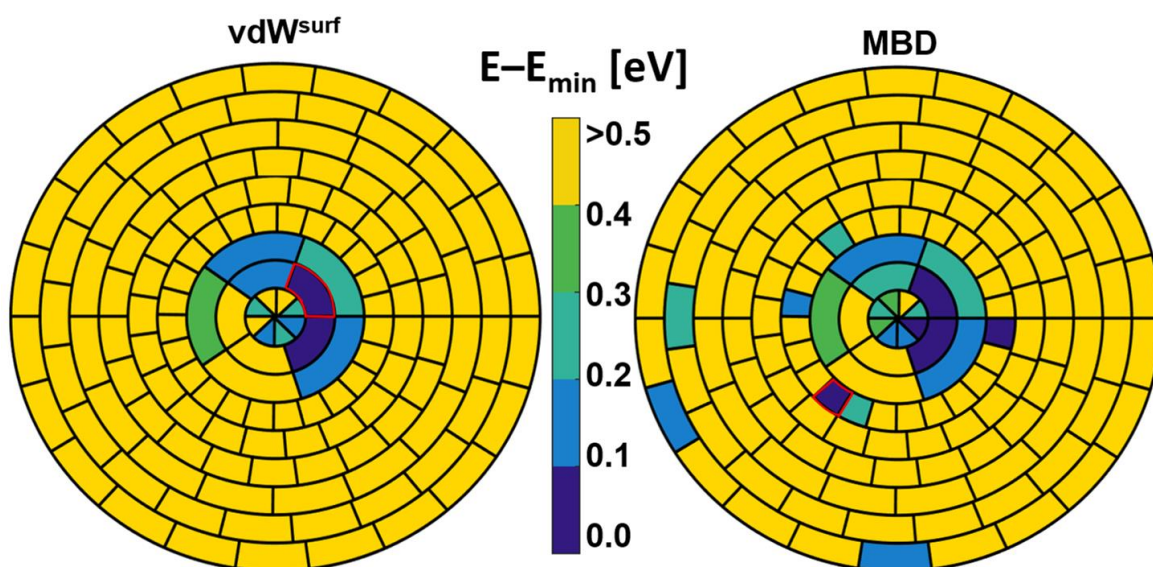
Supplementary Figure 7. *PES for TCNE/Au(111) with adatom. Sub-PES for TCNE/Au(111) consisting of all possible three-fold symmetric polymorphs including one gold adatom in the center, applying different dispersion schemes, i.e. vdW^surf (left) and MBD (right). Energies are obtained after geometry optimization and are given with respect to the global minimum of each PES. We see qualitative differences in the energetic ordering of the polymorphs when applying different dispersion schemes, i.e. the global minimum (as indicated by the red box) changes from a structures consisting of flat lying molecules (left) to the one comprising upright standing molecules. The geometric structure of some of the polymorphs are shown in the Supplementary Fig. 8.*
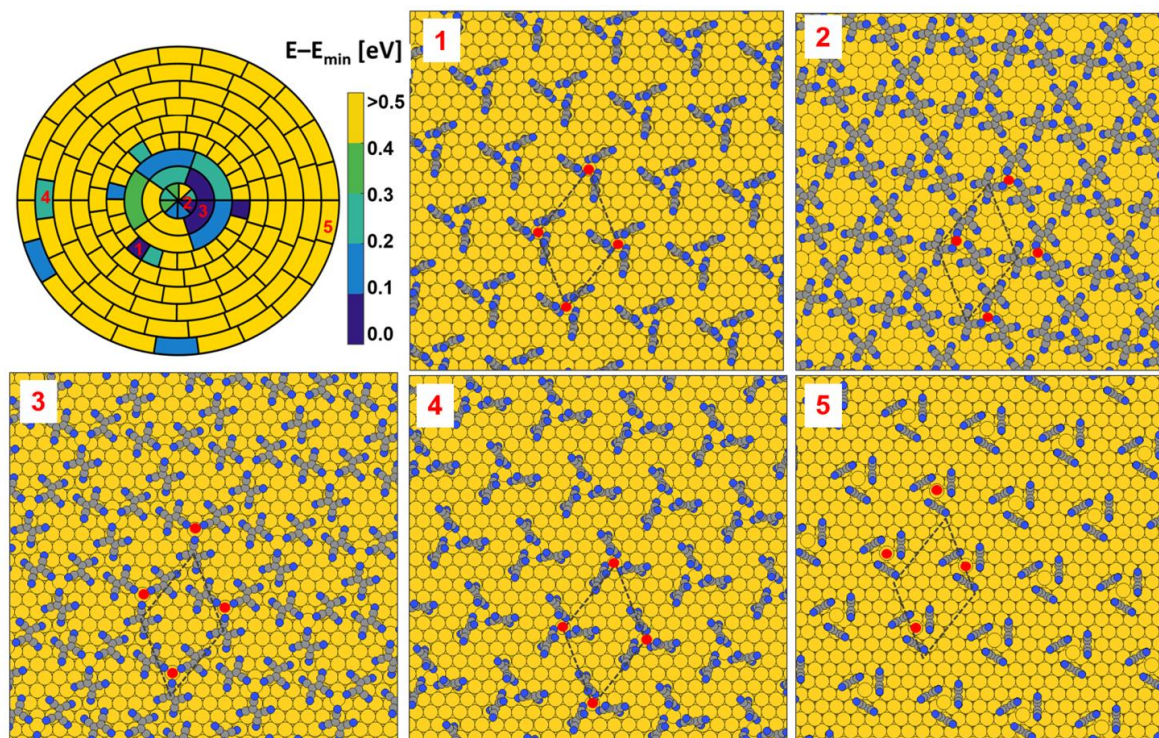
Supplementary Figure 8. *Exemplarily Structures of the PES for TCNE/Au(111) with adatom.* On the sub-PES for TCNE/Au(111) consisting of three-fold symmetric polymorphs with a gold adatom in the center, exemplarily, 5 different polymorphs with increasing energy are indicated and their structures are shown after geometry optimization. The red dots indicate the positions of the gold adatom.
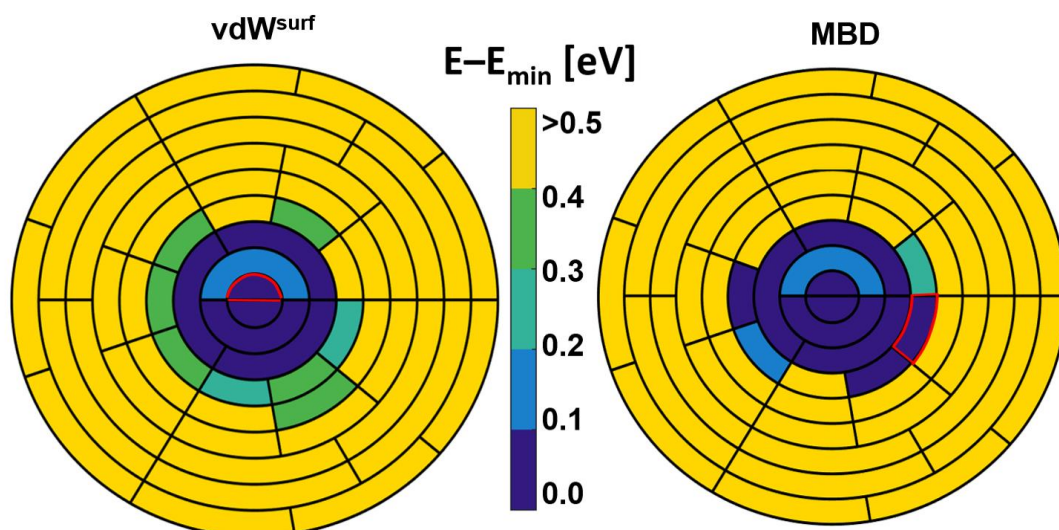
Supplementary Figure 9. *PES for TCNE/Au(111) with vacancy. Sub-PES for TCNE/Au(111) consisting of all possible three-fold symmetric polymorphs including a vacancy in the center, applying different dispersion schemes, i.e. vdW^{surf} (left) and MBD (right). Energies are obtained after geometry optimization and are given with respect to the global minimum of each PES. We see qualitative differences in the energetic ordering of the polymorphs when applying different dispersion schemes, i.e. the global minimum (as indicated by the red box) changes from a structures consisting of flat lying molecules (left) to the one comprising upright standing molecules.*

2.4.4 Appendix C - TCNE on Cu(111)

One of the model systems studied in this Thesis in order to apply global structure search at organic-inorganic interfaces is TCNE adsorbed on Cu(111). Its experimental STM image was provided by Daniel Wegner as a private communication and is shown in Fig. 24. As can be seen, in this STM image it is neither possible to assign certain features to individual molecules nor to determine whether the molecules are upright standing or flat lying. Rather, the molecules appear in a disordered fashion. This is in notable contrast to what has been observed for TCNE on other metallic substrates,[103–105] see Fig. 14. In the following, a brief introduction into disorder at organic-inorganic interfaces is given. Then, the SAMPLE approach is discussed in detail on the basis of the TCNE/Cu(111) interface, as this system was the primary model system the structure search was started with. The modifications compared to the approach published in PUBLICATION III are discussed in detail below. In the end of this chapter, a coverage-dependent study of TCNE/Cu(111) is
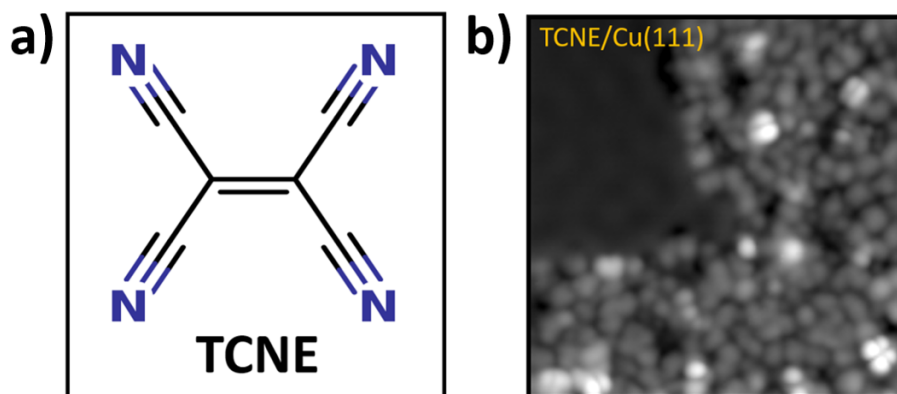
Figure 24: STM of TCNE/Cu(111). **(a)** Chemical structure of tetracyanoethylene TCNE. **(b)** Experimental STM image of TCNE adsorbed on Cu(111). STM was operated in constant current mode at 7K and the film was grown at room temperature. Taken from a private communication with Daniel Wegner.

presented by applying the SAMPLE approach. The main motivation of this is to find the coverage at which the TCNE molecules start to become upright standing. This is driven by experimental EELS (energy electron loss spectroscopy) measurements,[141] as in detail discussed below.

Disorder at Organic-Inorganic Interfaces

In many practical applications in organic electronics or photovoltaics, organic semiconductors are used as amorphous or disordered materials, rather than as single crystals. In disordered materials, macroscopic properties are no longer single numbers but rather a function reflecting a property distribution including the global minimum and its energetically higher lying polymorphs. This is indicated in Fig. 25 where the thermal distribution of TCNE/Cu(111) polymorphs is plotted applying a Boltzmann statistic. Upon approaching zero temperature, thermodynamically the organic material on top of the inorganic substrate would consist exclusively of the most stable adsorption geometry.

However, at finite temperature, the different adsorption geometries will be populated according to Boltzmann statistics and polymorphs including defects will be stabilized over perfectly crystalline layers by configuration entropy. Hence, the polymorphs that are in the most stable configuration (red) decreases with increasing temperature while energetically higher lying polymorphs (blue) increase. At room temperature ($300K$) around two thirds of the organic material consists of energetically higher lying configurations.
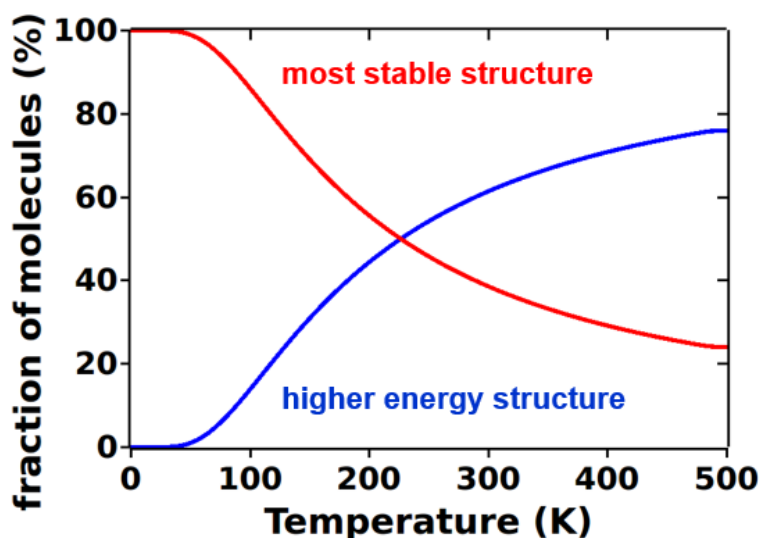
Figure 25: Thermal Distribution of TCNE/Cu(111) Polymorphs. Fraction of molecules that are in the most stable configuration (red) or in energetically higher lying structures (blue) as a function of temperature according to a Boltzmann statistic calculated for the example of TCNE/Cu(111) polymorphs.

In inorganic materials, the impact of disorder and defects on bulk properties is well known, as for example demonstrated by F-centers determining gem colors or charged vacancies being responsible for the catalytic activity in MgO.[188] Also in bulk organic materials, the impact of defects on conduction is well documented.[189] At organic-inorganic interfaces, these effects are expected to be as desisive when for example considering charge transport across the interface. As recently demonstrated for the example of pentacene thin film transistors, even slight changes in the molecular packing largely affect the electronic properties such as the carrier mobility.[102] The hole mobility was measured as high as $11 cm^2/Vs$ in an non-equilibrium polymorph, whereas the equilibrium form yielded hole mobility in the order of $1 cm^2/Vs$, *i.e.* one order of magnitude lower.[102]

Common defect types at organic-inorganic interfaces are shown in Fig. 26 for the example of TCNE/Cu(111). They can be classified into four different groups: Orientational disorder, where all molecules show the same adsorption geometry (*e.g.* flat lying) but are differently oriented with respect to the surface (*i.e.* they exhibit a different binding site). Topological defects, where individual molecules or groups of molecules exhibit a fundamentally different adsorption geometry than the majority species. Grain boundaries or islands and structural defects such as vacancies, interstitials or substitutions by different

160
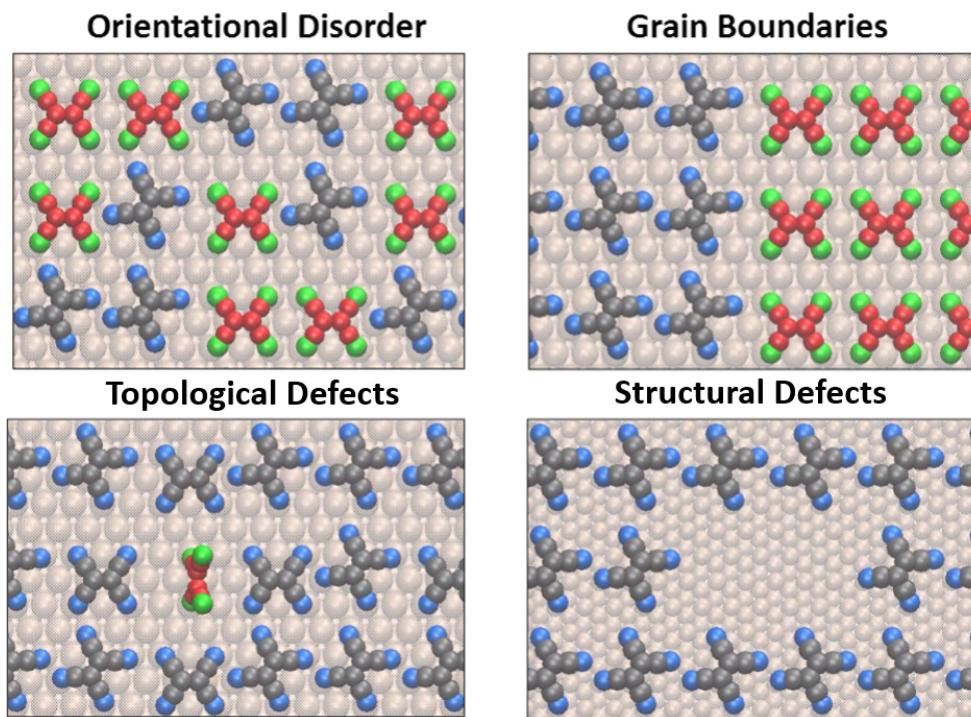
Figure 26: Defects at Organic-Inorganic Interfaces. On the example of TC-NE/Cu(111) some examples for disorder at organic-inorganic interfaces are shown: orientational disorder, grain boundaries, topological defects and vacancies.

adsorbates (*e.g.* a fraction of the molecule, hydrogen or water).

Still, up to date most first-principles studies focus on highly ordered, crystalline materials. Within this Thesis, first steps towards the description of disordered materials are done with the main goal of finding a set of energetically lowest lying polymorphs including the thermodynamic minimum. Particularly interesting are the structural differences as well as the relative energetic differences of this set of most stable polymorphs. In these first steps, only orientaional disorder is accounted for. The developed approach is discussed in the following for the example of TCNE/Cu(111).

The SAMPLE approach for TCNE/Cu(111)

The SAMPLE approach was already introduced in PUBLICATION IV for the example of TCNE/Au(111). Due to the limited space that is typically available in publications, here, the SAMPLE approach is discussed in detail for the example of TCNE/Cu(111). This was the system that SAMPLE was originally developed on. Compared to PUBLICATION IV this version of SAMPLE exhibits slight modifications, which are discussed in detail below.

As illustrated in the flow chart in Fig. 27, the SAMPLE approach consists of two consecutive steps. First, SAMPLE generates a systematic set of sensible starting configurations for any organic-inorganic interface. These configurations represent specific arrangements of several molecules per unit cell and serve as starting points from which later the PES, *i.e.*

161
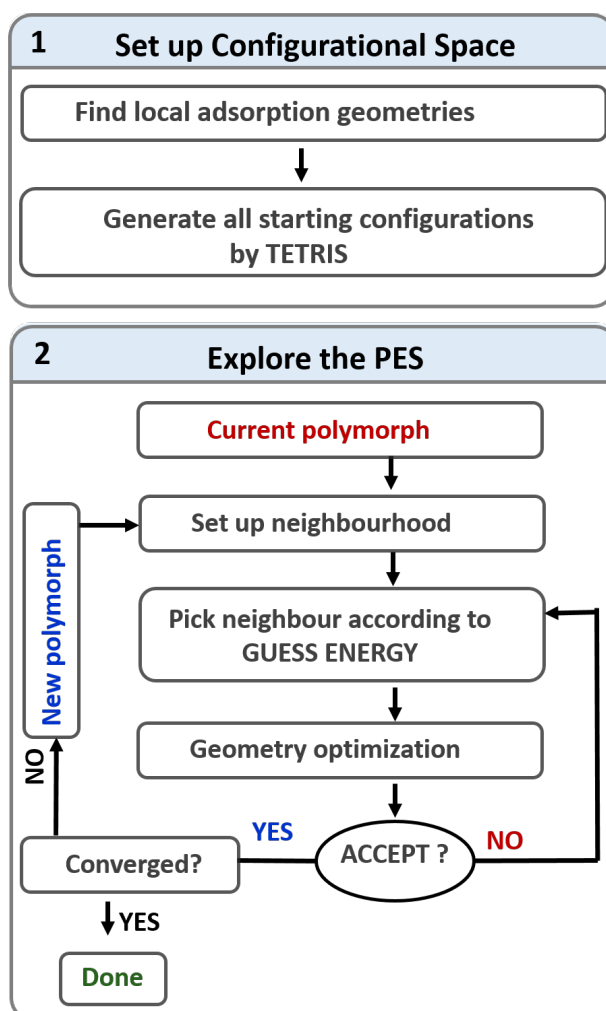
Figure 27: Flowchart Diagram of the Sample Approach. A systematic generation of the configuration space consisting of an extensive set of starting configurations for a specific organic-inorganic interface (step 1) is followed by an exploration of the PES in which efficiently chosen starting configurations are relaxed to their nearest local minimum (step 2). In contrast to the in PUBLICATION III presented SAMPLE approach for TCNE/Au(111), for TCNE/Cu(111) a neighbourhood for each polymorph is generated according to the in Fig. 34 illustrated selection rules. Within this neigbourhood the next polymorph is suggested on the basis of a guess energy. For details see main text.

the stable polymorphs, will be determined via full local geometry optimization. To generate these configurations, we exploit the fact that our interfaces must be commensurable. This allows us to use the substrate as discrete registry on which molecules are (initially) adsorbed on specific, well defined adsorption sites. In notable contrast to commonly applied global structure search techniques, thereby a complete and enclosed configuration space with a well-defined and reproducible number of possible configurations (including the global minimum) is generated a-priori.

In principle one could perform a local geometry optimization in each of these starting configurations to their nearest local minimum in order to achieve a complete energy ranking. However, the number of polymorphs increases exponentially with the number of molecules in the unit cell. Hence, in many cases, even after the aforementioned discretization procedure, the configuration space is too large to perform an exhaustive search within reasonable time. This demands the second step, an efficient exploration of the PES. As illustrated in the bottom box of Fig. 27, in SAMPLE , this is implemented as an iterative Monte Carlo algorithm inspired by the Basin-Hopping method (*cf.* section 1.2). The principle idea of the Basin-Hopping method is to transform the complex PES into a set of interpenetrating staircases by consecutive trial moves along the PES followed by a local optimization into the closest local minimum. Similarly, in SAMPLE, we explore a fraction of the PES by performing trial moves between the starting configurations generated in the first step followed by a local geometry relaxation. These moves are not randomly chosen as in classical Basin-Hopping,[120,121] but according to system-specific selection rules. This leads to distinct advantages over a classical Basin-Hopping procedure. Displacements that would generate unphysical structures are prevented. Furthermore, we assume that each of the starting configurations relaxes to a distinct polymorph enabling the identification and labeling of all polymorphs. On the basis of a history list, in this way, recalculations of already visited basins can be avoided.

The SAMPLE approach can be linked to any suitable electronic structure method that provides an energy ranking that is accurate enough. For all calculations in this section, we apply dispersion corrected density functional theory (DFT) using the `FHI-aims` code.

Generation of the Configuration Space

In the following, the individual steps for generating the configuration space are discussed in detail for the example of TCNE/Cu(111). The creation of the starting configurations is based on a systematic discretization in two consecutive steps, as illustrated in the upper box of the flow chart in Fig. 27. First, we determine the local adsorption geometries, *i.e.* the different possibilities in which a single, isolated molecule can adsorb on the substrate. For conjugated organic molecules, such as TCNE, the most important degrees of freedom are the translation along and orientation with respect to the surface, as illustrated in Fig. 28a and b. Considering the resulting five degrees of freedom we perform geometry optimization from multiple, systematically chosen starting points for a single molecule in a large supercell. Specifically, we start from 48 different initial guesses varying the orientation of the molecule as well as the position with respect to the surface. For each orientation, *i.e.* flat lying TCNE, upright standing with the central C=C bond parallel to the surface and, equivalently, normal to the surface, we place the molecule on the four
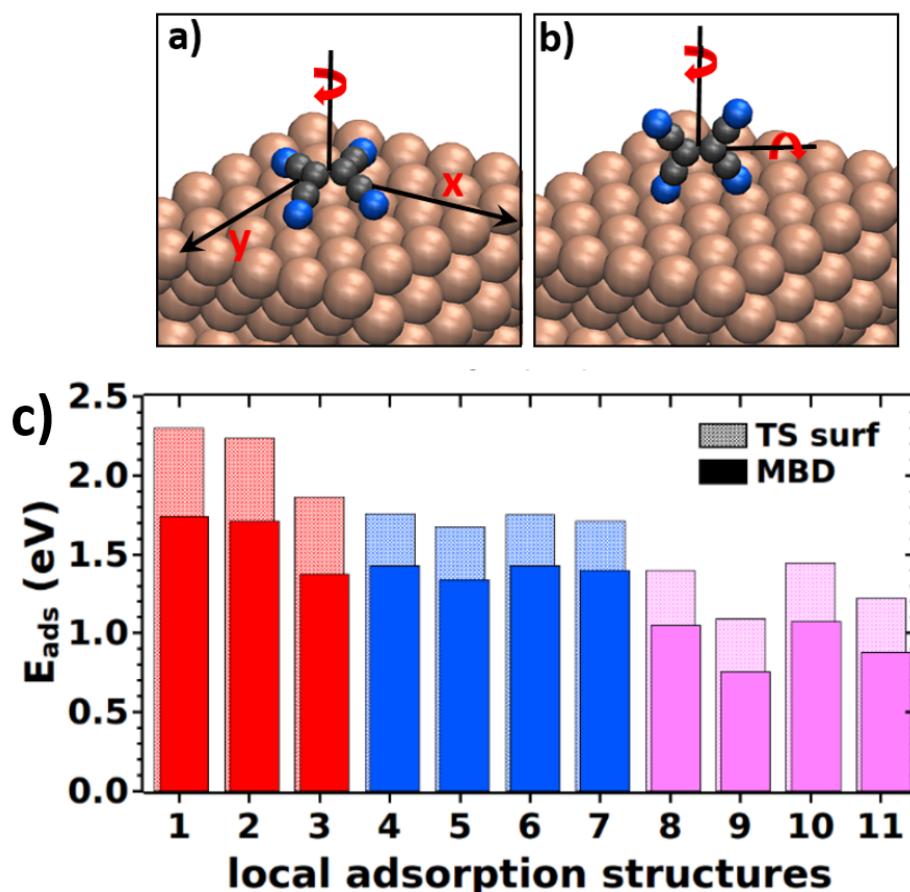
Figure 28: Local Adsorption Energies for TCNE/Cu(111). Individual flat lying **(a)** and upright standing **(b)** TCNE molecule on the Cu(111) surface illustrating the translation along x and y direction on the surface as well as the rotation along the three molecular axis, resulting in 5 degrees of freedom considered for the evaluation of the local adsorption geometries. **(c)** Adsorption energies for the eleven stable local adsorption geometries shown in Fig. 29 applying different dispersion schemes, *i.e.* vdW^{surf} energies (solid bars) and MBD energies (dashed bars). We categorize the local adsorption geometries into three groups: flat lying local adsorption geometries (red), upright standing with the central C=C bond oriented parallel to the surface (blue) and equivalently normal to the surface (pink).

164

symmetry inequivalent adsorption sites (on top, fcc hollow, hcp hollow and bridge position) and, moreover, rotate the whole molecule around the z-direction, *i.e.* perpendicular to the substrate, by 0°, 15°, 30° and 45°. Employing this procedure to TCNE on Cu(111), we find 11 stable local adsorption geometries, as shown in Fig. 29. (For almost all of them we performed frequency calculations in order to validate that the found minimum is a local minimum rather than a saddle point.) They differ in their particular binding site with respect to the surface as well as in their orientation, *i.e.* they are flat lying or upright standing. We categorize them into three different groups: the flat lying adsorption geometries (G1-G3), the upright standing ones with the central C=C bond oriented parallel to the surface (G4-G7), and equivalently normal to the surface (G8-G11). Due to the C3 symmetry induced uppon adsorption of TCNE on the Cu(111) surface each of the nine stable local adsorption geometries has three symmetry equivalent isomers, which need to be considered in the second step.

The adsorption energies of all local adsorption geometries are shown in Fig. 28b and together with their adsorption heights summarized in Tab. 2. The adsorption energies E_{ads} are defined as

$$E_{ads} = (E_{mol} + E_{slab}) - E_{sys} \qquad (26)$$

where E_{sys} is the total energy of the TCNE/Cu(111) system, while E_{mol} and E_{subst} refer to the total energies of the individual components, *i.e.* the molecule in gas phase and the pristine copper slab. The adsorption energies are obtained applying different vdW schemes, namely the vdW^{surf} method[190] that is commonly applied to organic molecules on metallic substrates and the many-body disperion scheme (MBD)[171] that goes beyond the pairwise interaction of vdW^{surf} and was just recently demonstrated to show even nicer agreement with experiments[166]. While originally, the vdW^{surf} method was used, in PUBLICATION IV, we showed that MBD qualitatively changes the energetic orderings in the local adsorption geometries and also in the energetically lowest lying polymorphs. Hence, we also investigated these effects here for the local adsorption geometries, but for the evaulation of the PES we stayed with the vdW^{surf} methods. As can be seen in Fig. 28b, MBD reduces the adsorption energies of all adsorption structures, which is not unexpected, as vdW^{surf} typically overestimates the binding energies at interfaces.[166,191]

As can be seen in Tab. 2, the most stable local adsorption structure is a flat lying TCNE molecule adsorbed in the fcc hollow position (independent of the applied vdW scheme). A notable bending of the outer cyano groups towards the Cu surface is observed upon geometry optimization. All upright standing geometries are more than $0.5eV$ less binding. Also in experiments, for TCNE/Cu(111) several different local adsorption structures have been observed.[142] On the basis of STM measurements, Choi et al. found 5 different flat lying states (with a population of 44:19:24:10:3), between which they could switch by applying voltage pulses along the STM tip. Two of them (the α and the β-TCNE[142]) can be clearly associated to G1 and G2 being the energetically lowest lying adsorption geometries in our calculations. In experiments, they were also shown to be more stable than the other observed geometries.[142] For the current study these observations are important as the existence of several energetically similar local adsorption structures endorses the supposed disordered morphology for TCNE/Cu(111).
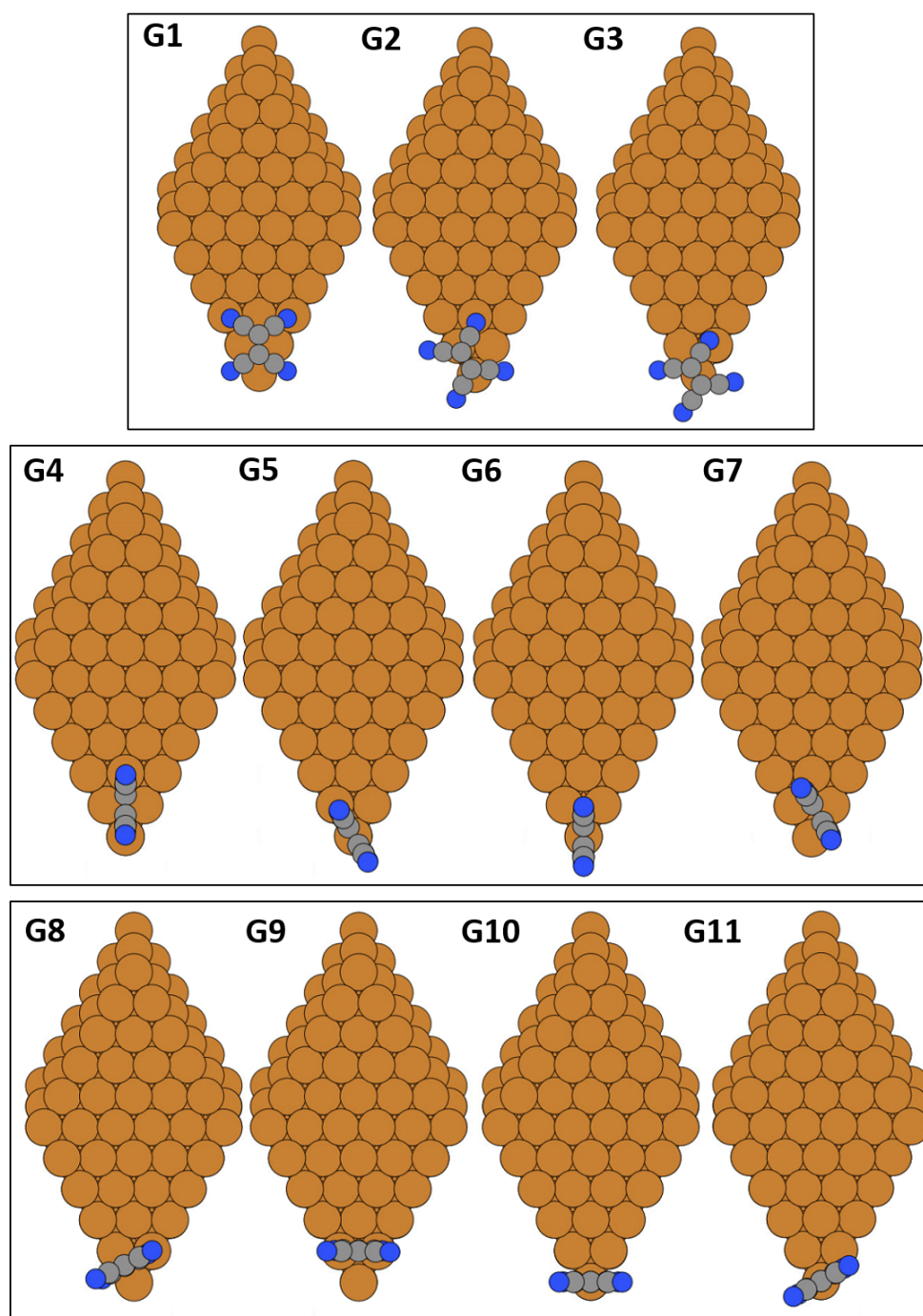
Figure 29: Local Adsorption Geometries for TCNE/Cu(111). Structure of the eleven stable local adsorption geometries for TCNE/Cu(111). They differ in the orientation with respect to the surface, *i.e.* flat lying or upright standing, as well as in the particular binding site. They are categorized into three different groups: the flat lying adsorption geometries (G1-G3), the upright standing ones with the central C=C bond oriented parallel to the surface (G4-G7) and equivalently normal to the surface (G8-G11).

Table 2: Structural and Electronic Properties of TCNE/Cu(111). Adsorption height, h_{ads}, adsorption energy, E_{ads}, and energy difference, ΔE_{ads}, to the most stable local adsorption structure (G1) for the eleven different local adsorption geometries of TCNE/Cu(111). The adsorption height is given as the distance between the N atoms of TCNE (averaged) and the average of the uppermost Cu layer. (For upright standing TCNE molecules only the lowermost N atoms are taken into account.) Adsorption energies were determined applying vdW^{surf} as well as MBD. For some of the local adsorption geometries, zero-point energies, ZPE, were obtained from frequency calculations applying the `FHI-aims` code in conjunction with a finite displacement method using the `aims.vibrations.pl` script with a displacement value of $0.0025 \mathring{A}$.

	$\mathbf{h_{ads}[\mathring{A}]}$	$\mathbf{E^{surf}_{ads}[eV]}$	$\mathbf{\Delta E^{surf}_{ads}[eV]}$	$\mathbf{E^{MBD}_{ads}[eV]}$	$\mathbf{\Delta E^{MBD}_{ads}[eV]}$	$\mathbf{ZPE[eV]}$
G1	2.15	2.30	0.00	1.74	0.00	1.23
G2	2.16	2.24	0.06	1.71	0.02	1.22
G3	2.16	1.86	0.44	1.37	0.36	1.20
G4	1.98	1.76	0.54	1.43	0.31	1.23
G5	1.97	1.67	0.63	1.34	0.40	1.23
G6	1.61	1.75	0.55	1.42	0.31	-
G7	1.62	1.71	0.59	1.40	0.34	-
G8	2.00	2.01	0.90	1.05	0.69	1.22
G9	2.01	1.09	1.21	0.75	0.98	-
G10	2.00	1.44	0.86	1.07	0.66	1.22
G11	1.71	1.22	1.08	0.88	0.86	-

As illustrated in Fig. 27, after finding the geometric structure that isolated TCNE molecules can assume on the Cu(111) surface, in a subsequent 'TETRIS'-like assembly process, we combine these local adsorption structures into supramolecular starting configurations. These span the configuration space and serve as starting points for subsequent geometry optimizations. The extent of the configuration space, *i.e.* the number of possible starting configurations, depends on the number of local adsorption geometries that are generated in the first step and the molecular packing density, *i.e.* the size and shape of the unit cell together with the number of molecules it contains. While a detailed technical description of the TETRIS procedure is given in the Supporting Information of PUBLICATION III, here, the general idea is outlined.

The TETRIS assembly procedure is visualized in Fig. 30. Inspired by a bottom-up approach, we start from disassembling the surface into its smallest natural building blocks. These are the primitive surface unit cells of the substrate, indicated by the solid black box in Fig. 30a. After defining the supercell size (*e.g.*, the larger dashed black box), the assembling process starts by consecutively adding substrate unit cells that may contain one of the previously determined local adsorption structures, or remain empty. Every time such a building block is added, the whole geometry is checked against collisions and symmetry. Collisions are validated on basis of a predefined threshold, *i.e.* the minimum distance between the atoms of two neighboring molecules. For TCNE/Cu(111) it is set to $2.5\mathring{A}$ (approximately two times the vdW radius of Nitrogen). Unphysical structures with
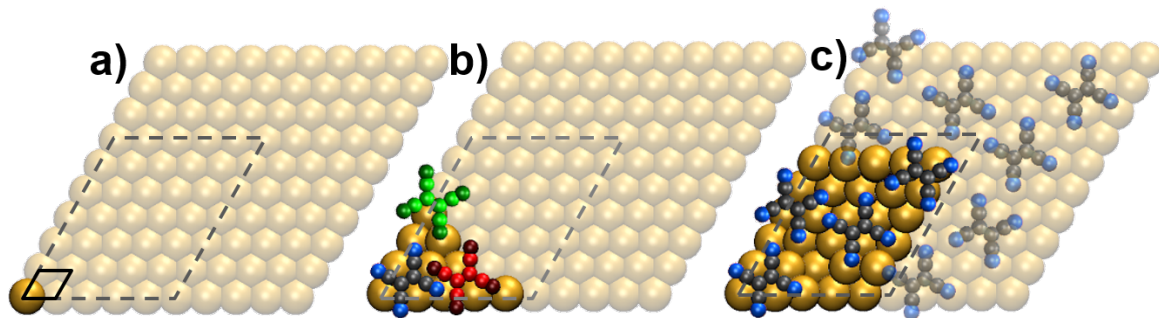
Figure 30: Visualization of the Tetris procedure. (a) Disassembly of the surface into primitive unit cells (solid box) and selection of supercell size (dashed box). (b) Consecutive adding of substrate unit cells containing local adsorption structures. Unphysical structures (red molecule) with atomic distances below the threshold are discarded. For all sensible structures (green molecule) substrate unit cells are added until the molecular coverage is met. (c) One possible polymorph generated by the Tetris procedure. For details, see main text.

atomic distances below the threshold (as indicated by the red molecule in Fig. 30b) are discarded. For all reasonable structures (indicated by the green molecule), the described process is repeated by adding further substrate unit cells until the molecular coverage is reached. A possible final polymorph is shown in Fig. 30c. The outcome of the Tetris procedure is a complete and enclosed configuration space consisting of a well-defined number of possible starting configurations that serve as starting points for later geometry optimizations. Our way to represent the associated configuration space is introduced in Fig. 31 for the example of a very small Sub-Pes of TCNE/Cu(111). Exemplarily, for a 2x2 supercell and 3 local adsorption geometries (1-3), Sample generates 27 symmetry inequivalent configurations. We arrange them in a pie plot, where each of the boxes represents one possible configuration. We order the local adsorption geometries according to their adsorption energies, where 1 would be the most stable one. Hence, with increasing ring diameter, the local adsorption energies decrease. Counterclockwise, the degree of disorder increases. Upon geometry optimization in the exploration step, the boxes are colored according to their relative energies. Innermost rings are expected to be lowest in energy.

For the specific case of TCNE/Cu(111), when incorporating all eleven found local adsorption geometries with three symmetry equivalent isomers each, the configuration space for a (6x6) unit cell with a coverage of 3 molecules, exponentially explodes to several hundreds of thousands different configurations. Here, we want to keep the configuration space small in order to afford the calculation of all configurations with DFT and test our exploration approach on a small sub-Pes. Hence, we only include the two most stable local adsorption structures G1 and G2 (with all symmetry equivalent isomers for G1 and only one for G2). This choice is strengthened by the fact that G1 and G2 are the most stable local adsorption structures (only differing by $0.06eV$) while the rest of the local adsorption structures are less stable by at least $0.44eV$, as can be inferred from Tab. 3. When applying the Tetris procedure with a threshold of 2.5Å, choosing a unit cell
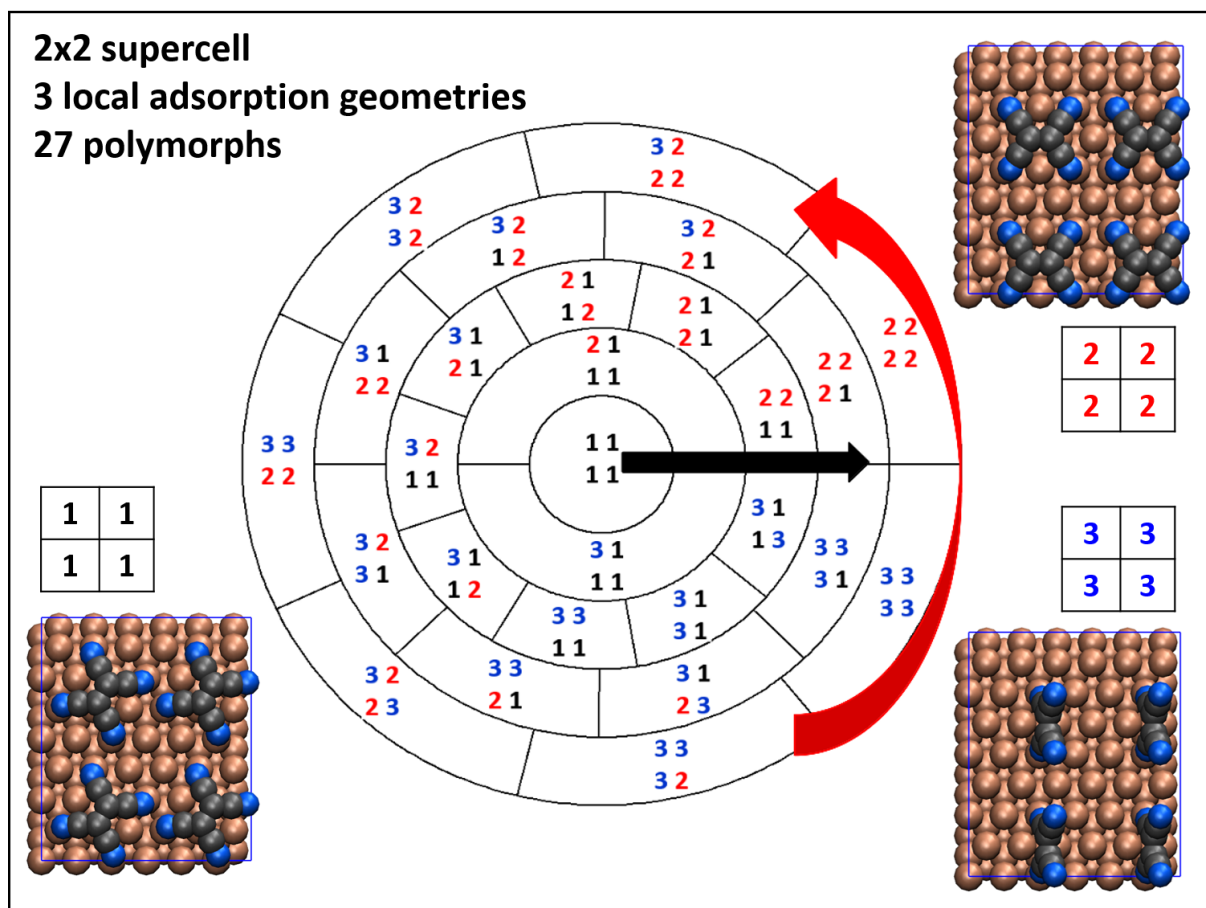
Figure 31: Configuration Space for Organic-Inorganic Interfaces. Pie plot to illustrate the configuration space at organic-inorganic interfaces for the example of a small Sub-Pes of TCNE/Cu(111). For a 2x2 supercell and 3 local adsorption geometries (1-3), Sample generates 27 symmetry inequivalent configurations. Each of them is represented by a box. For details, see main text.

169

which is 6x6 the primitive substrate unit cell of Cu(111) including 3 molecules, we get 118 different configurations. Figure 32 shows the PES comprising all of these 118 different structures after geometry optimization with DFT + vdW^{surf}. As mentioned above, each
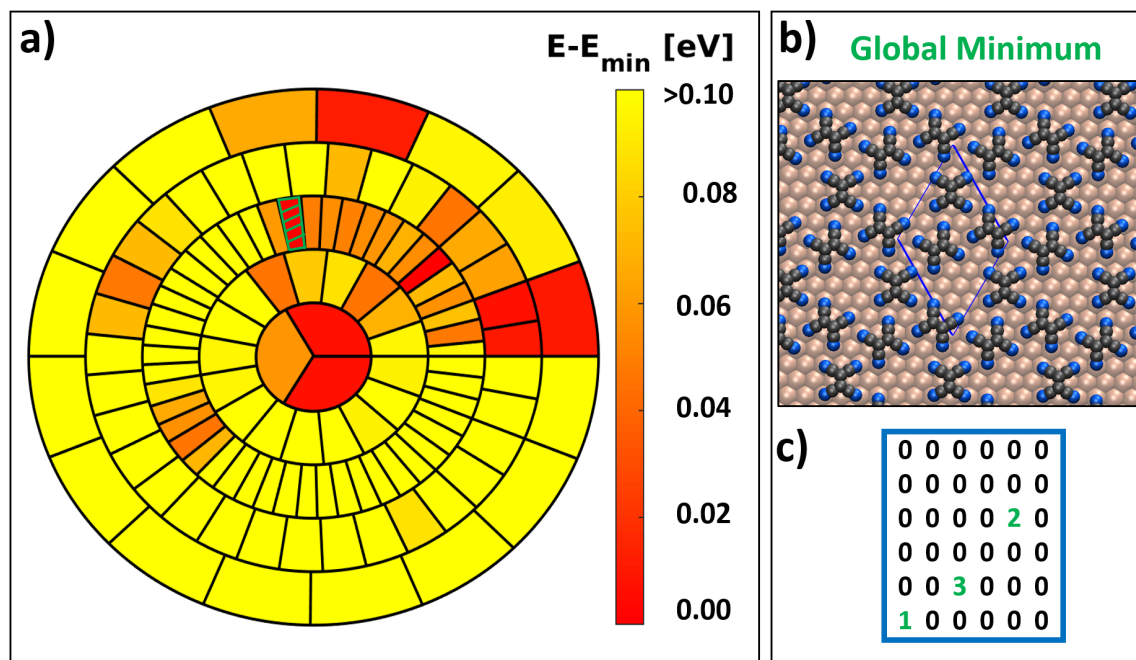
Figure 32: PES for TCNE/Cu(111). **(a)** Sub-PES for TCNE on Cu(111) comprising 118 polymorphs (colored boxes). The color represents the total energy after geometry optimization with `FHI-aims`. Energies are aligned to the global minimum which is indicated by the green dashed box. **(b)** Geometric structure of the global minimum of the in (a) shown PES. **(c)** Corresponding notation of the global minimum in the corresponding 6x6 supercell. Each number represents a lattice site. Zeros represent empty substrate lattice sites; numbers represent lattice sites occupied by different local adsorption geometries 1 to 3. (In this case 1-3 are the three symmetry equivalents of the local adsorption geometry G1 shown in Fig. 29.)

of the boxes represents one of the 118 polymorphs. The energies are given with respect to the global minimum. As can be seen, a distinct number of the polymorphs are energetically very close, *i.e.* the energy difference to the global minimum is smaller than $100 meV$. Especially for the dark red colored boxes, *i.e.* for the set of energetically lowest lying polymorphs, the computed energy differences are within $1 k_b T$, which clearly points towards a disordered morphology for TCNE/Cu(111). The global minimum within this Sub-PES is indicated in Fig. 32a with a green shaded box and the geometric structure is shown in (b). As can be seen, a hexagonal arrangement of flat lying TCNE molecules is obtained. This structure appears in principle quite reasonable, as also for TCNE/Ag(111) a hexagonal structure of flat lying molecules is seen in experiments (*cf.* Fig. 14).

Exploration of the Potential Energy Surface

After generating starting points from which we explore the configuration space, in the subsequent exploration step only a fraction of the PES is scanned to find the global minimum. For this task we apply an iterative Monte Carlo algorithm inspired by the Basin-Hopping method (*cf.* 1.2). As shown in the lower box of Fig. 27, similar to a generic BH scheme applied to molecules[109] or clusters[121], we SAMPLE the PES by consecutive hops from one configuration to the next. Each hop is followed by a local geometry optimization, which is comparably inexpensive as we start from a combination of already optimized local adsorption geometries (a converged geometry is found after 3-4 geometry optimization steps with textscDft). In contrast to classical Basin-Hopping these hops are not performed via randomly chosen trial moves. We rather set up a neighborhood for each polymorph from which the next polymorph is suggested according to a certain 'guess energy', which is introduced below. After geometry optimization, the suggested polymorph is accepted or rejected according to the Metropolis-Hastings scheme.[114]

$$p_{acc} = min(1, e^{\frac{\Delta E}{k_B T}}) \tag{27}$$

If the suggested polymorph has a lower energy than the last polymorph, it is accepted; in case of a higher energy it will be accepted depending on a probability that considers the energy difference to the last accepted polymorph as well as an effective temperature via a Boltzmann factor. The initial temperature is set to $300K$ and is varied during iterations according to the flooding technique, *i.e.* the temperature is decreased by $100K$ in case of acceptance, respectively increased for rejection. In case of rejection, a different neighbor is chosen. Due to the unique labeling of each polymorph, all visited structures (accepted or rejected) can be added to a history list and need not to be recalculated in case of revisiting. The procedure is iteratively repeated until a certain convergence criterion is met.

The neighborhood for a certain polymorph is generated according to system-specific selection rules, see Fig. 33. On the basis of the discrete registry of the adsorbed molecules
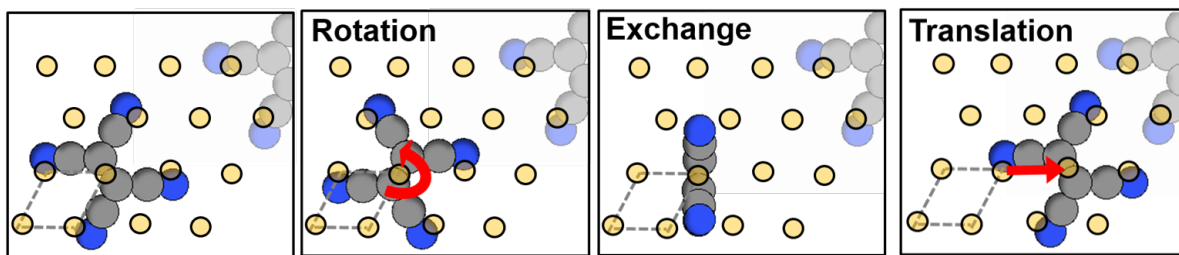
Figure 33: Selection Rules for SAMPLE. A neighborhood for each configuration is generated according to pre-defined selection rules: each molecule in the cell is allowed to (i) move to an adjacent space of the substrate, *i.e. translation* by one primitive $\sqrt{3}x\sqrt{3}R30$ surface cell (*i.e.*, shift to the next possible equivalent adsorption site on the substrate), (ii) *rotate* on the spot to a symmetry equivalent structure or (iii) adopt a different adsorption site *i.e.*, *exchange* to a different local adsorption geometry.

with the substrate, we either exchange the local adsorption geometry at a certain site to one of the other local adsorption geometries, move it along x or y by the distance of a

primitive surface unit cell of the substrate, or rotate it by 120° degrees to a symmetry equivalent isomer. We allow one or more molecules to change at the same time. Applying this procedure, each configuration obtains a well-defined neighborhood, *i.e.* a finite number of neighboring configurations, which altogether define the connections within the configuration space. The selection rules can be customized to the specific system at hand (as for example done in PUBLICATION IV where the configuration space is limited to triangular structures). Exemplarily, Fig. 34 shows a small section of the whole connectivity within the PES in form of a tree diagram, where each configuration is illustrated by a (6x6) matrix with each matrix element representing the position in the unit cell in units of to the primitive surface cell. 0 represents an empty adsorption site, while
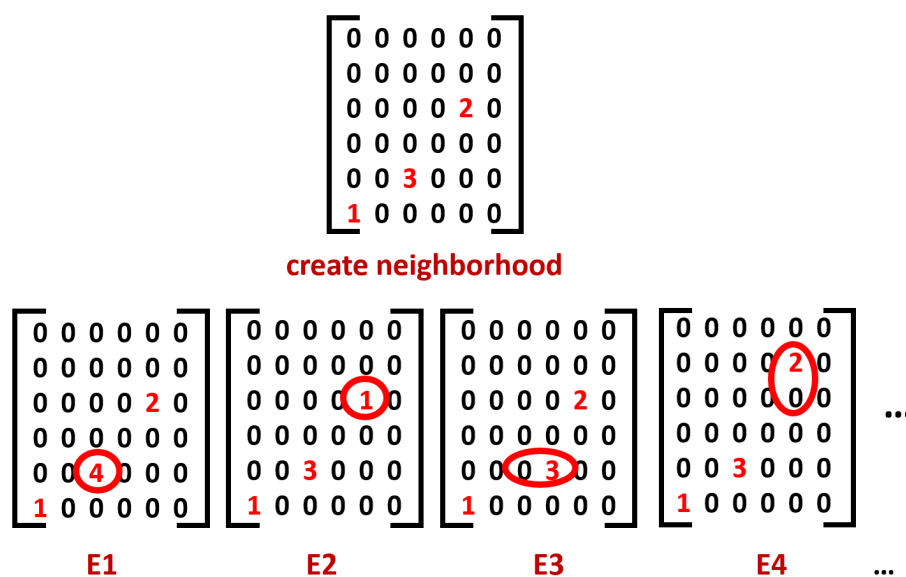
Figure 34: Generation of Neighbourhood. Exemplary part of the tree diagram generated by applying the selection rules to TCNE/Cu(111). For every polymorph a specific notation is used where zeros represent empty substrate lattice sites and numbers represent lattice sites occupied by different local adsorption geometries 1 to 4. For every polymorph a set of neighbors is generated according to the following selection rules: (i) an individual molecule can change its local adsorption geometry (exemplarily indicated by neighbor 1 and 2), (ii) two neighboring lattice sites can be switched (exemplarily indicated by neighbor 3 (vertical switch) and 4 (horizontal switch). Diagonal switches are not included.

all other numbers reflect the local adsorption geometries found in the first step of the discretization procedure. For TCNE/Cu(111) each configuration is associated to a certain number of neighboring configurations applying the following selection rules: (i) an individual molecule can change its local adsorption geometry (exemplarily indicated by neighbor 1 and 2), (ii) two neighboring lattice sites can be switched (exemplarily indicated by neighbor 3 (vertical switch) and 4 (horizontal switch). Diagonal switches are not included. From this kind of plot, one can clearly see the possible paths along the PES along which the MC steps can be performed.

<u>Guess Energy</u>
The generation of the connections within the configuration space allows us to suggest new configurations in a more directed way than just performing random trial moves (as usually done in Basin-Hopping). For each of the configurations within a neighborhood we set up a 'guess energy', which consists of two contributions: the sum of adsorption energies, E_{ads}, of all involved local adsorption geometries in the unit cell, and the Coulomb energy, $E_{coulomb}$, associated to the (charged) molecules on the surface.

$$E_{guess} = \sum E_{ads} + \sum E_{coulomb} \tag{28}$$

$$E_{coulomb} = \frac{1}{4\pi\epsilon_0} \frac{1}{2} \sum_i q_i \sum_{j \neq i} q_j \frac{1}{r_{ij}} \tag{29}$$

Here, r_{ij} is the distance between two molecules on the surface (strictly speaking, the distance between the two lattice sites the molecules are associated to within the unit cell) and $q_{i,j}$ is the charge of the molecule (upon adsorption on the surface, the strong accepting TCNE molecules get differently charged depending on their orientation with respect to the surface, i.e. the flat lying TCNE reflects a dianion and the upright standing an anion, see next section for details). For each configuration, a neighborhood according to the above mentioned selection rules, is generated. For each of these neighbors the guess energy is calculated. The neighbor with the lowest guess energy is picked. To test how well this guess energy would reflect the actual DFT results, we compare the corresponding PES of the 118 configurations for the (6x6) unit cell comprising 3 molecules, see Fig. 35 and 36. When only accounting for the sum of the local adsorption energies (upper panel in Fig. 35, red squares in Fig. 36) the agreement of the guess energy to the DFT energies is quite bad. The inclusion of the Coulomb contribution (lower panel in Fig. 35, blue dots in Fig. 36) considerably improves the performance of the guess energy. A major part of the 'real' PES calculated with DFT is recovered when using this guess energy.
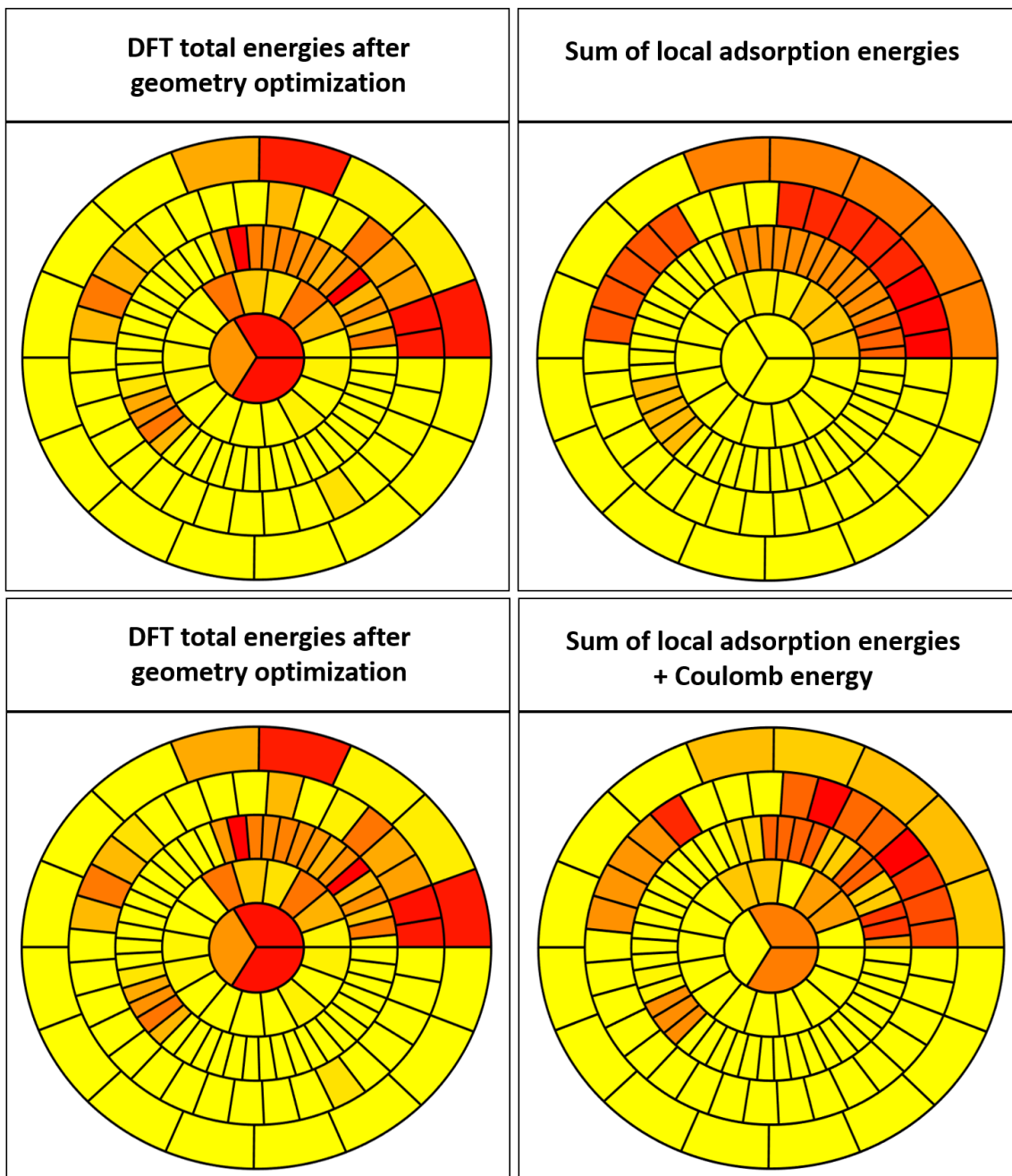
Figure 35: Guess Energy for TCNE/Cu(111). The Sub-Pes as introduced in Fig. 32 is here plotted again (see *DFT total energies after geometry optimization*) in order to compare it to the Pes obtained from the guess energy described in Eq.28 and 29. The upper panels show the comparison when only accounting for the *sum of the local adsorption energies* while in the lower panels additionally the *coulomb* contribution is included in the guess energy. The energy scale is the same as in Fig. 32.
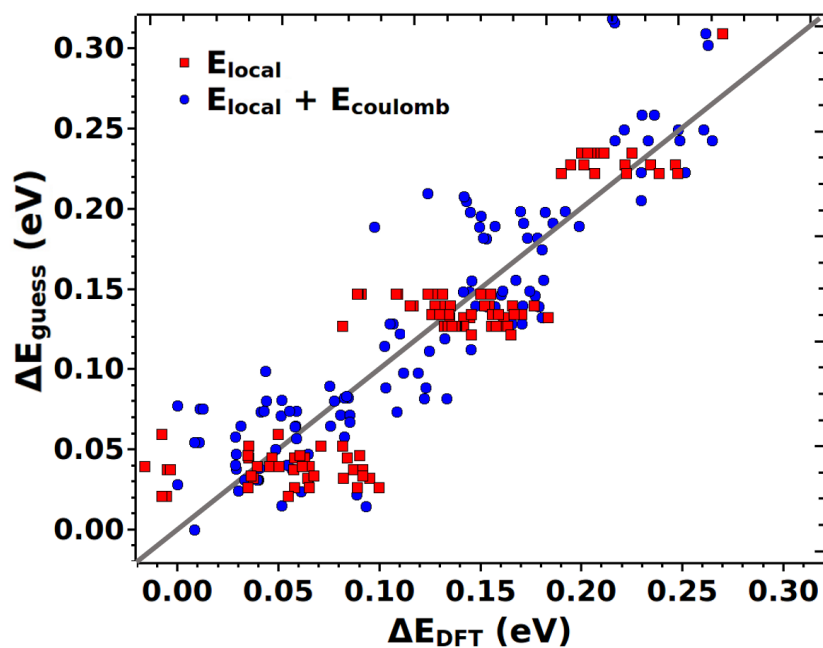
Figure 36: Guess Energy for TCNE/Cu(111). The guess energy with respect to the minimum, ΔE_{guess}, is compared to the real DFT energy with respect to the minimum, ΔE_{DFT}, for the Sub-PES of TCNE/Cu(111). Red squares only include the contribution from the local adsorption energies; blue dots additionally include the Coulomb contribution, see Eq.29.

Coverage-Dependent Study of TCNE/Cu(111)

In 1987, W. Erley et al. studied the adsorption of TCNE on Cu(111) by high-resolution electron energy loss spectroscopy (EELS) with the main observation that TCNE adsorbs in multiply ionized molecular species on the copper surface.[141] The corresponding spectra are shown in Fig. 37 a-c for increasing coverage. As a measure of the relative coverage of adsorbed TCNE molecules the ratios of C_{272} and Cu_{928} Auger transitions (C/Cu) are indicated in the figure. The monolayer coverage is represented by an Auger value of C/Cu=0.11, from which a coverage of 13 copper surface atoms per TCNE molecule is estimated.[141] The colored boxes indicate the frequencies that are associated to the symmetric CN stretching mode (region around $2100 cm^{-1}$) as well as to the symmetric C=C stretching vibration (at around $1300 cm^{-1}$). One can see in Fig. 37a that for each of these ranges two distinct peaks occur. These are assigned to the singly charged species, *i.e.* anions (blue boxes) as well as to the doubly charged species , *i.e.* dianions (red boxes). For the full monolayer (a) the dianion represents the dominant species and only a small concentration of anions are apparent. Interestingly, the loss features characteristic to the anions cannot be observed for very low coverage (not shown here) and are, therefore, not formed initially on the Copper surface. When increasing the coverage (see Fig. 37 b and c), the peak associated to the anion gets more and more pronounced. Erley at al. provide the following interpretation for these observations. "Most likely TCNE anions are adsorbed above the dianions in a second layer", thereby assigning the anions to molecules in the second layer. They also state that "anions start to adsorb on top of the dianions long before the first layer is completed". However, based on the investigations on TCNE/Cu(111) performed within this Thesis, an alternative interpretation is provided. A detailed analysis based on vibrational frequency calculations as well as on applying the SAMPLE approach for different coverages, makes us confident that what Erley et al. refer to as anion is rather an upright standing TCNE molecule in the first layer and not related to a molecule in the second layer.

First, a vibrational analysis is performed and the resulting frequencies are compared to Erley's EELS experiment.[141] Therefore, frequency calculations for the local adsorption structures of TCNE/Cu(111) are performed. This is done applying `FHI-aims` together with a finite displacement method, *i.e.* each atom is displaced in the direction of each Cartesian coordinate and the Hesse matrix is determined from the forces (using the `aims.vibrations.pl` script). For simplicity, all Cu layers are kept fixed to reduce the number of calculations. The default displacement value of $0.0025 Å$ is used. The symmetric C≡N and C=C stretching modes are summarized in Tab. 3 for the majority of the local adsorption structures shown in Fig. 29. G1 to G3 are flat lying geometries, while G4 to G10 represent upright standing structures. The frequencies associated to the neutral, singly and doubly charged TCNE/Cu(111), as obtained from the EELS experiments shown in Fig. 37 are summarized in Tab. 4. When comparing the theoretically as well as experimentally obtained values of Tab. 3 and 4, we see an interesting correlation. The frequencies for the CN stretching mode, ν_{CN}, obtained for the flat lying local adsorption geometries (G1-G3) in the range of $\approx 2090 cm^{-1}$ nicely agree with the energy loss frequency associated to the dianion (which is $2035 cm^{-1}$). Moreover, the frequencies obtained for the upright standing TCNE molecules (G4-G10) which are in the
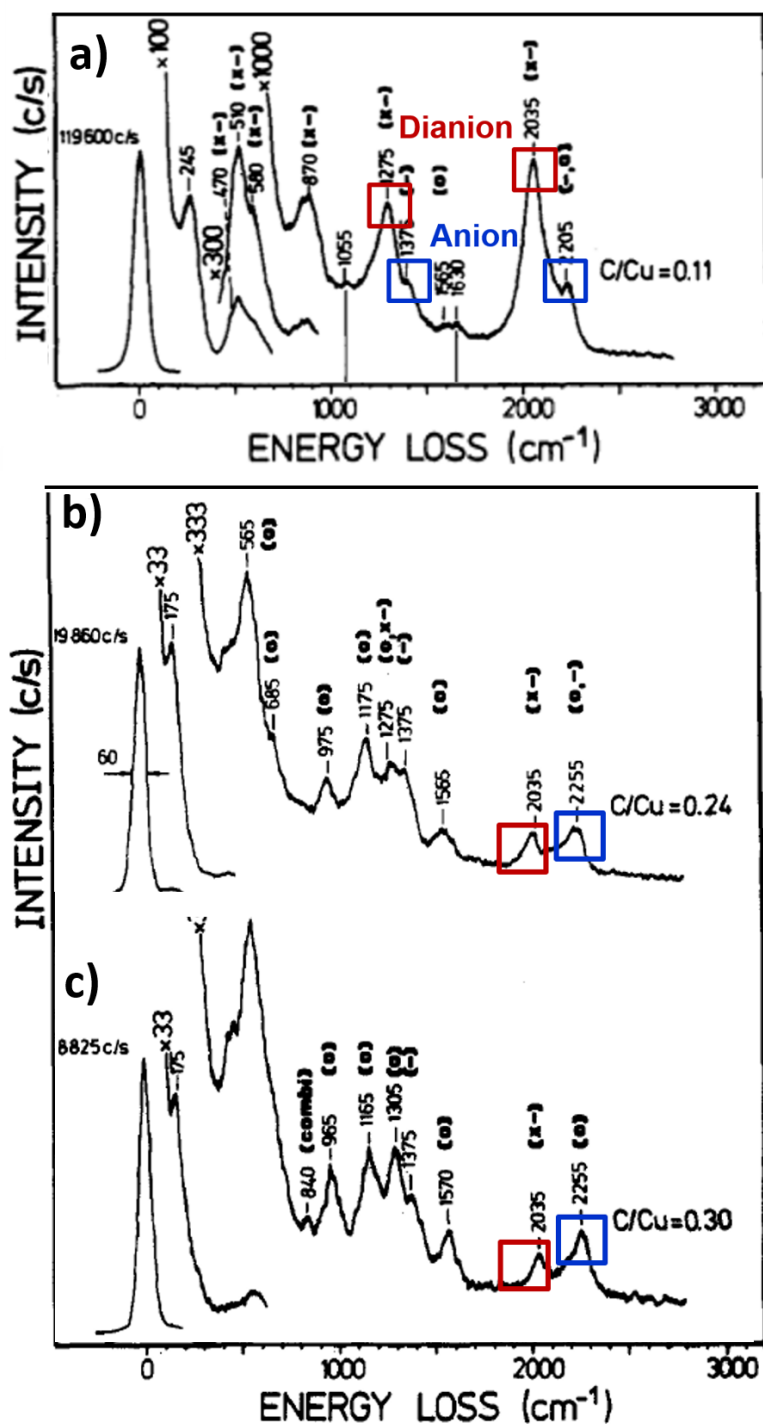
Figure 37: Electron Energy Loss Spectra for TCNE/Cu(111). EELS spectrum for TCNE adsorbed on Cu(111) at $100K$ for monolayer coverage **(a)** and below monolayer coverage **(b)** and **(c)**. As a measure of the relative coverage of adsorbed TCNE molecules the ratios of C_{272} and Cu_{928} Auger transitions (C/Cu) are indicated in the figure. The monolayer coverage is represented by an Auger ration of C/Cu=0.11. Frequencies assigned to singly (blue boxes) and doubly (red boxes) charged TCNE species are marked. Adapted with permission from ref. [141]. Copyright 1987 American Chemical Society.

177

Table 3: Vibrational Analysis of TCNE/Cu(111) - Theory. Calculated vibrational frequency of the symmetric C=N and C=C stretching modes (ν_{CN} and ν_{CC}) and bond length of central C=C bond d_{CC} for some of the eleven local adsorption geometries of TCNE/Cu(111).

Theory	**G1**	**G2**	**G3**	**G4**	**G5**	**G8**	**G10**
$\nu_{CN}[\mathbf{cm^{-1}}]$	2099	2098	2094	2225	2226	2213	2209
$\nu_{CC}[\mathbf{cm^{-1}}]$	1270	1283	1294	1395	1419	1340	1338
$\mathbf{d_{CC}}[\mathbf{\mathring{A}}]$	1.49	1.50	1.50	1.44	1.44	1.42	1.42

Table 4: Vibrational Analysis of TCNE/Cu(111) - Experiment. Experimentally obtained vibrational frequency of the symmetric C=N and C=C stretching modes (ν_{CN} and ν_{CC}) associated to the neutral TCNE, the anion and the dianion. Taken from ref. [141].

Experiment	**neutral**	**anion**	**dianion**
$\nu_{CC}[\mathbf{cm^{-1}}]$	1565	1375	1275
$\nu_{CN}[\mathbf{cm^{-1}}]$	2255	2205	2035

range of $\approx 2220 cm^{-1}$ perfectly agree with the anion frequency of $\approx 2205 cm^{-1}$. The same is true for the symmetric CC vibrations. (An absoulte error of around $20 - 50 cm^{-1}$ is reasonable for this kind of calculations while relative shifts should be well reproduced.) Hence, contradicting to what was argued in ref. [141], these observations suggest that the "TCNE anion" corresponds to an upright standing molecule in the first layer, rather than a molecule in the second layer.

We further investigated this argument by performing a vibrational analysis of TCNE in gasphase employing the `Gaussian09` code[192], see Tab. 5. For comparison, the experimentally obtained values are taken from ref. [193], where Infrared (IR) as well as Raman results for TCNE in gas phase are summarized (averaged over several literature values). The symmetric C=C stretching vibration (which is IR- inactive, because the dipole moment does not change, but Raman active) as well as the N=C symmetric vibration (which is IR-active) are summarized in Tab.6. Again, a very nice agreement to the calculated frequencies is observed. Another quantity that is very sensitive to the charge state of the TCNE molecule is the bond length of the central C=C bond, which increases for increasing charge. The values are also tabulated as d_{CC} in the aforementioned tables and show very nice agreement between the experimental and theoretically obtained values, which clearly strengthens the previous observations. The bond lengths slightly increase when TCNE is adsorbed on the surface, see Tab.3, and the overall trends prevail.

Another possibility to support our findings, is to calculate the density of states (DOS) of a system with two layers of TCNE adsorbed on Cu(111) and project it onto the individual layers, see PDOS in Fig. 38. A (2x2) unit cell was used and for this simple test case the unit cell was not fully relaxed. As can be seen, the LUMO (lowest unoccupied molecular orbital) for the first layer (red) is completely filled (as the peak associated to the LUMO lies below the Fermi level), while the LUMO for the second layer (blue) stays more or less empty. Hence, no charge transfer into the second layer is observed in our calculations,

Table 5: Vibrational Analysis of TCNE - Theory. Calculated gasphase frequencies for neutral TCNE, anion and dianion together with the central C=C distance as obtained from the GAUSSIAN09 code applying the PBE functional and the 6-31G* basis set.

Theory	$\nu_{\mathbf{CC}}[\mathbf{cm^{-1}}]$	$\nu_{\mathbf{CN}}[\mathbf{cm^{-1}}]$	$\mathbf{d_{CC}[\mathring{A}]}$
neutral	1517	2249	1.39
anion	1390	2212	1.45
dianion	1260	2173	1.52

Table 6: Vibrational Analysis of TCNE - Experiment. Experimental gasphase frequencies for neutral TCNE, anion and dianion together with the measured central C=C distance taken from ref.[193].

Experiment	$\nu_{\mathbf{CC}}[\mathbf{cm^{-1}}]$	$\nu_{\mathbf{CN}}[\mathbf{cm^{-1}}]$	$\mathbf{d_{CC}[\mathring{A}]}$
neutral	1570	2250	1.35
anion	1421	2164	1.43
dianion	1260	2142	1.49
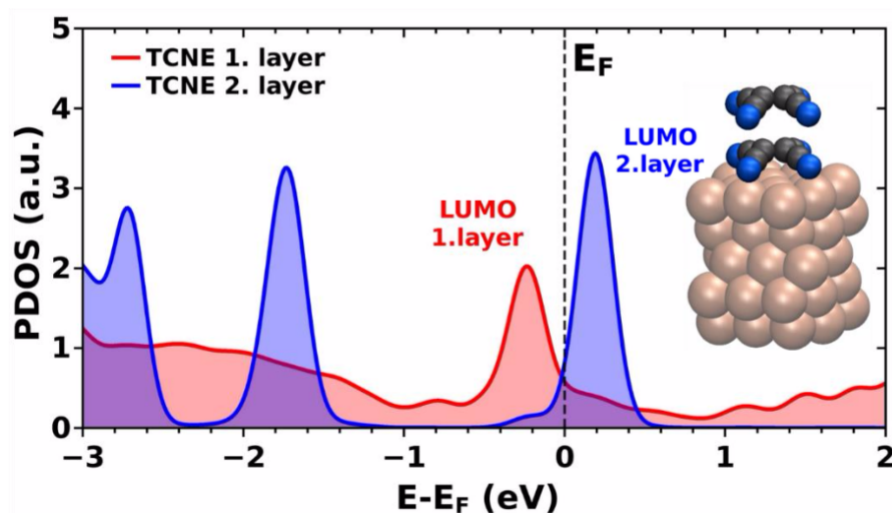
Figure 38: Density of States for TCNE/Cu(111). DOS projected onto the first (red) and second (blue) TCNE layer on Cu(111) obtained at the level of HSE. Energies are aligned to the Fermi level. While the first TCNE layer experiences pronounced charge transfer filling its LUMO, for the second layer the LUMO stays more or less empty.

which makes it very unlikely that anions are formed in the second layer. With these observations at hand, we are confident to interpret the "dianions" and "anions" from EELS experiments, as flat lying and upright standing TCNE molecules in the first layer. Note that this interpretation is insofar strengthened by the EELS measurements as the loss features characteristic of the anions are not observed for very low coverage.[141] Hence, upright standing molecules are not formed initially on the copper surface, but should start to appear when a certain coverage, *i.e.* packing density, is reached.

Applying SAMPLE for different coverages

What needs to be clarified, is the molecular coverage at which the TCNE molecules start to adsorb in an upright standing manner. While we cannot describe the associated dynamical process, with the SAMPLE code at hand, we can at least predict the energetically lowest lying polymorphs for different coverages. It has to be emphasized here that the following is preliminary data based on a very small Sub-PES applying not fully converged settings in the DFT calculations. Hence, the following is only meant to provide first qualitative trends. On the basis of the (6x6) unit cell used above, we apply the SAMPLE procedure for different coverages, *i.e.* the unit cell comprising 1, 2, 3 and 4 molecules. Experimentally, a coverage of 13 Cu atoms per TCNE molecule is found.[141] The coverages investigated here correspond to 36, 18, 12 and 9 Cu atoms per TCNE molecule. The global minimum for each coverage is depicted in Fig. 39. For each coverage the adsorption energy per molecule, E_{ads}^{mol}, is determined according to

$$E_{ads}^{mol} = \frac{1}{N}\Big(E_{sys} - (E_{slab} + NE_{mol})\Big) \tag{30}$$

where E_{sys} is the total energy of the TCNE/Cu(111) system, while E_{mol} and E_{subst} are referred to the total energies of the individual components and N is the number of molecules in the unit cell. The values are summarized in Tab. 7 applying vdW^{surf} as well as MBD (more negative is more binding). As can be seen, the adsorption energy per molecule is increasing with the number of molecules up to the most densely packed situation of 4 flat lying molecules in the unit cell which corresponds to a coverage of only 9 Cu atoms per TCNE molecule. This is a slightly higher packing density than the experimentally predicted coverage of around 13 Cu atoms per molecule. In order to elucidate this situation, one would need to (i) increase the unit cell and number of molecules in order to simulate higher packing densities, (ii) test this behavior for different unit cell shapes and sizes or (iii) potentially recalculate the obtained minima with HSE in order to better account for the charge transfer to the molecules.

What needs to be clarified, is whether a structure with an additional upright standing molecule would be more stable than a structure with a flat lying molecule in the second layer, see Fig. 40. As can be seen from Tab. 7 the structure including the upright standing molecule in the first layer is more stable by $0.4eV$ per molecule. Further investigations in this direction need to be done to clarify the situation.
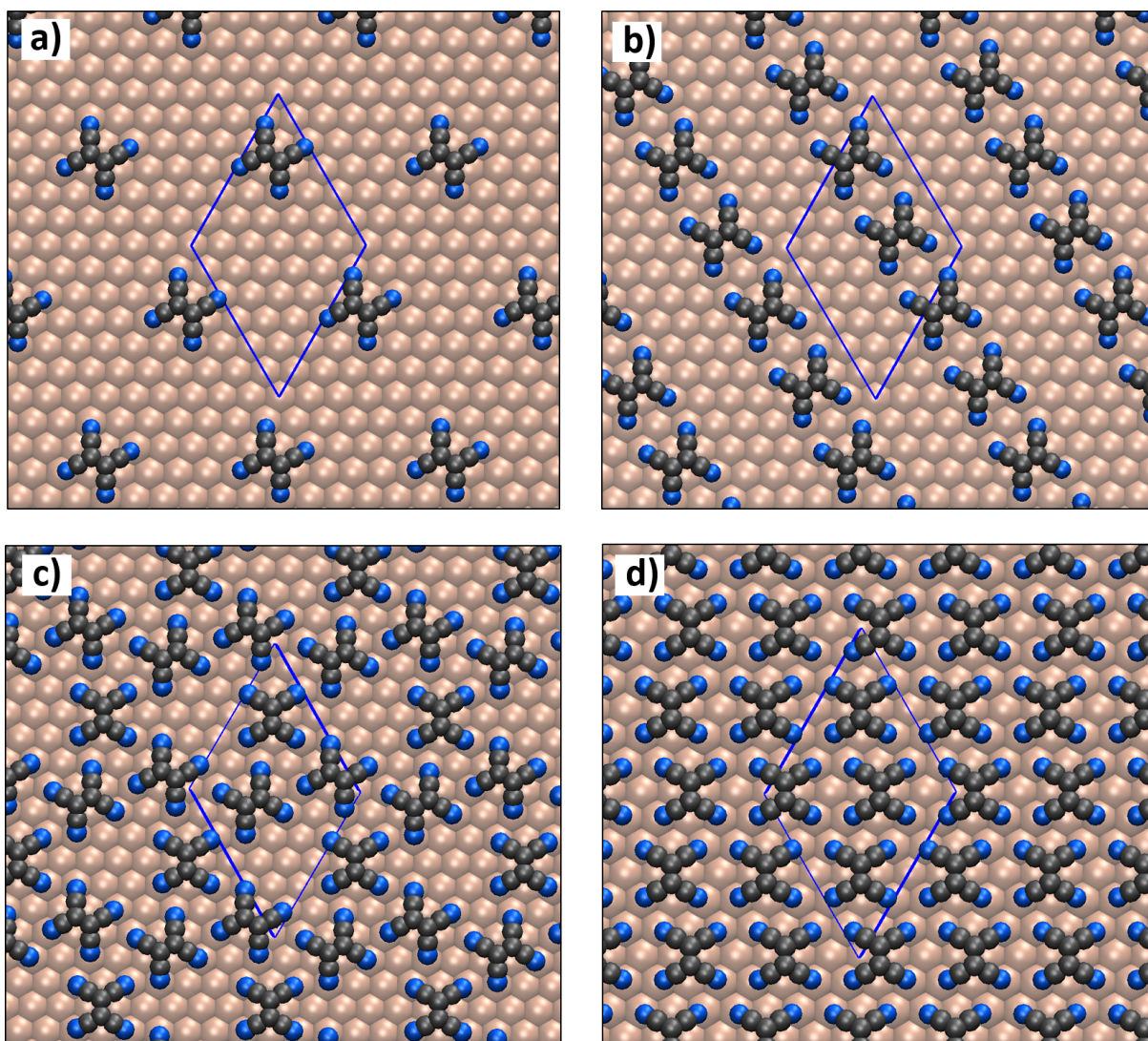
Figure 39: Coverage Study of TCNE/Cu(111). Geometric structure of the global minimum for one **(a)**, two **(b)**, three **(c)** and four **(d)** TCNE molecules per 6x6 supercell, corresponding to a coverage of 36, 18, 12 and 9 Cu atoms per TCNE molecule. Experimentally a coverage of 13 Cu atoms per TCNE molecule is found.[141]

Table 7: Coverage Study of TCNE/Cu(111). Adsorption energies per molecule obtained with vdW$^{\text{surf}}$ and MBD for varying coverage, *i.e.* within a (6x6) unit cell containing 1 to 4 molecules as shown in Fig. 39 a-d and Fig. 40 a-b. The energies are obtained according to Eq.30, *i.e.* more negative is more binding. Note that the parameters like the size for the unit cell as well as the number of k-points is not fully converged.

	1 lying	2 lying	3 lying	4 lying	3 lying 1 standing	3 lying 1 in 2nd layer
coverage	1	2	3	4	4	4
Cu atoms/mol	36	18	12	9	9	9
structure	Fig. 39a	Fig. 39b	Fig. 39c	Fig. 39d	Fig. 40a	Fig. 40b
$\mathbf{E_{ads}^{surf}/mol[eV]}$	-2.63	-2.65	-2.67	-2.70	-2.53	-2.16
$\mathbf{E_{ads}^{MBD}/mol[eV]}$	-1.95	-1.97	-2.03	-2.08	-2.00	-1.65
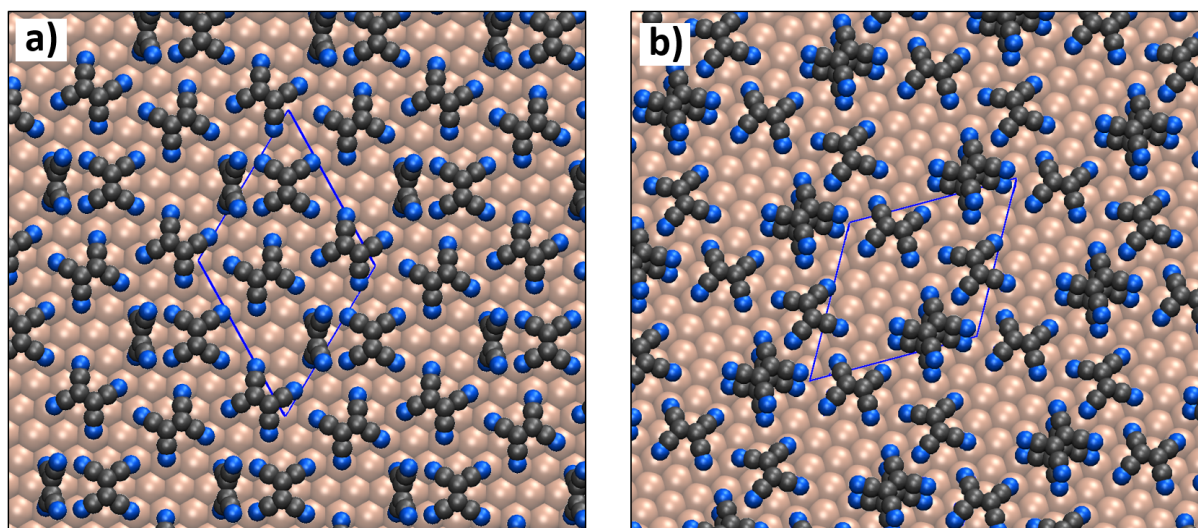
Figure 40: Coverage Study for TCNE/Cu(111). Geometric structure of TCNE/Cu(111) with an upright standing molecule in the first layer **(a)** compared to a flat lying molecule in the second layer **(b)**.

2.4.5 Appendix D - Density Functional Tight Binding

The major limiting factor for *any* global structure search algorithm is the computational cost associated to the underlying electronic structure method. SAMPLE is currently interfaced to the DFT code `FHI-aims`. A typical geometry optimization of a system containing 190 atoms (*e.g.* a single TCNE molecule on Cu(111) in a (6x6) unit cell) requires around 40 steps to converge, where each step, *i.e.* each single point calculation, consumes 2 hours on 64 CPU. Hence, in total, around 5000 CPU hours per geometry optimization are needed. As structure search as such intrinsically demands for a large number of consecutive calculations, the resulting computational cost is huge. In search of computationally less expensive alternatives, the DFTB (Density Functional Tight Binding) approach sounds promising. In comparison to DFT, the above mentioned single-point calculation for TCNE/Cu(111) requires only 10 minutes on 16 CPU. However, this enormous increase in efficiency is payed by a loss in accuracy. Still, DFTB could be used in conjunction withe the SAMPLE approach either as a potential 'guess energy' (compare Appendix C) or for a pre-screening of the PES, upon which accurate DFT calculations for a selection of energetically lowest lying configurations could be performed.

Density Functional Tight Binding (DFTB) is based on DFT as formulated by KOHN and SHAM, but keeps efficiency by using also ideas from the semiempirical tight-binding methods. The DFTB approach is evidently not *ab-initio*, since it contains parameters. However, with the right parameters at hand, a reasonable accuracy can be achieved, while the computational effort is enormously reduced compared to DFT. Still, absolute transferability cannot be found since the very fundament of DFTB are tightly bound electrons with interactions ultimately treated perturbatively. DFTB is currently succesfully applied to large organic and biological molecules or clusters[194–196] but also for evaluating the structural properties of nanostructures such as COFs[197] or MOFs[198] with a wide range of different elements. DFTB starts with considering the system as an ensemble of isolated atoms, where the reference density, n_0, is expressed as a superposition of atomic densities, which is an approximation to the real density of the system, n. The general idea is then to perform a Taylor series expansion of the KOHN-SHAM total energy in DFT, *i.e.* the actual density and the corresponding energy, in terms of fluctuations δn around n_0. Depending on the inclusion of terms in the Taylor expansion different models appear, which build successively on top of each other, ranging from first-order non-self-consistent DFTB[199,200] (originally called DFTB) to the self-consistent, second order DFTB2[194] (originally called SCC-DFTB) and the recent extension to the third order DFTB3[201]. For details on the methodology, the interested reader is referred to very recommendable reviews such as ref. [195], [202] or [203].

The most common DFTB implementation is the DFTB+ code[204], which was also used in this Thesis. In general, apart from the usual input files defining geometry and settings for the calculations, SLATER-KOSTER files (SK-files) have to be provided for each atom pair ($I-I$, $I-J$, $J-I$, $J-J$). The DFTB parameters entering these SK-files consist of two parts, the electronic part and the repulsive part. The electronic part contains the atomic and diatomic contributions calculated from DFT, *i.e.* the atomic s, p, d KOHN-SHAM eigenenergies, which enter as diagonal elements the Hamilton matrix. Moreover, the non-diagonal matrix elements (overlap and Hamilton matrix) are calculated in a two-center approximation for a neutral atomic reference density. They are distance dependent and stored as a table. Using these parameters, the DFTB program does not have to evaluate

any integration during runtime. The repulsive energy contribution is approximated as sum of pair potentials, which are represented either by spline functions or polynomials. The generation of the SK-files is clearly somewhat involved and moreover a N^2 process with N being the number of species. Therefore, these files are typically shared online (*dftb.org*). Still, up to now only a fraction of the desirable element combinations are available. Very recently, DFTB in conjunction with a vdW^{surf} implementation was applied to an organic-inorganic interace, namely bisphenol A adsorbed on Ag(111)[205], showing very nice agreement to experiments. In general, vdW contributions like vdW^{TS} (ref. [167]), vdW^{surf} (ref.[190]) and MBD[171,206] (see chapter 1.3.1 for methodological details) have been implemented only recently in DFTB + by the group of Karsten Reuter and Reinhard Maurer[207] and are, therefore, not contained in the latest official version. Still, an unreleased version of DFTB + including these implementations was provided by Reinhard Maurer for benchmarking against DFT. In this chapter, first, a general description of the parameters entering the DFTB + code is presented which is then followed by a comparison to DFT (`FHI-aims`) on the example of TCNE/Cu(111).

DFTB+ Parameters

The input for DFTB + calculations consists of a geometry file `geo_in.gen` containing the coordinates of all involved atoms in the unit cell, the `dftb_in.hsd` input file comprising all settings for the calculation and a set of Slater-Koster (SK)-files for each element pair including all diatomic parameters for the given interaction. The SK-files used here, were provided by Martin Stöhr (*i.e.* C-N, C-C as well as N-N parameters were taken from mio-1-1-set, see *www.dftb.org/parameters/download*); the other interactions were fitted using the `Hotbit`[202] code: Cu-Cu parameters were fitted to Cu_2, Cu_3 (D3h) and Cu_4 (Td); Cu-N interactions were fitted to CuN, CuN_2, Cu_2N and Cu_{4N}; Cu-C interactions were fitted to CuC, CuC_2, Cu_2C and Cu_4C; PBE-DFT reference calculations were performed using the `FHI-aims` code). In the following the input file, `dftb_in.hsd`, used for a periodic DFTB + calculation (for a single-point calculation of the flat lying local adsorption geometry G1 for TCNE/Cu(111), see Fig.29) is given with a short description of the individual parameters. For detailed information, see the DFTB + manual.

```
Geometry = GenFormat {
    <<< "geo_in.gen"                      # location of geometry file
}
Hamiltonian = DFTB{
    Charge = 0                            # overall charge in the system
    Filling = MethfesselPaxton}           # occupation scheme
        Temperature = 0.0036
        Order = 1                         # Gaussian Filling
    }
    KPointsAndWeights = SupercellFolding{   # k-point grid
    4 0 0
    0 4 0
    0 0 1
    0 0 0
    }
    MaxAngularMomentum = {                # basis set
```

```
        C = "p"
        Cu = "d"
        N = "p"
    }
    SCC = YES                              # self-consistent calculation
    SCCTolerance=3.7E-07                   # conv. crit. total energy,
                                               unit is Hartree
    SlaterKosterFiles = Type2FileNames{    # location of SK-files
        Prefix = ~/DFTB/parameters/new/
        Separator = "-"
        Suffix = ".skf"
    }
    EwaldParameter=0                       # for coulomb solver
                                               in periodic calculations
}
Options {
    WriteResultsTag = Yes
}
```

Moreover, in the following the converged parameters for vdW$_{surf}$, vdW$_{TS}$, as well as MBD calculations are given:

```
    ManyBodyDispersion = TS{        # vdW TS / surf
     TSEnergyAccuracy = 1e-10       #
     Params = tssurf                 # C6 parameters: ts or tssurf
     }
```

```
    ManyBodyDispersion = MBD{        # Many Body Dispersion
     Params = tssurf                 # C6 parameters: ts or tssurf
     doReciprocal = Yes              # calculation of MBD energy
                                         via reciprocal k-integration
     NomegaGrid = 10                 # grid for calculating the
                                     freq. dependent polarizability
                                     default 25, recommended 5
     SCSRealCutoffScaling = 0.6      # real Ewald cutoff, default 1
     SCSRecCutoffScaling = 0.6       # reciprocal Ewald cutoff, default 1
     KGrid = { 8 8 1 }               # for doReciprocal, MP grid to
                                     calculate the MBD energy
     VacuumAxis = { 0 0 1 }          # axis for vacuum insertion
                                     in case of  slab-type calculation.

     }
```

The settings given above are already the converged parameters for TCNE/Cu(111). Specifically, the k-grid, basis set, the Ewald parameter, as well as the cutoff parameters and the kGrid in case of MBD, were converged to an energy difference of 0.01eV with respect to the total energy.

Results for TCNE/Cu(111)

In the following, we compare DFT results obtained with `FHI-aims` to DFTB results obtained with DFTB+. For comparison, also the settings used in the `control.in` input for `FHI-aims` are given here.

```
xc pbe                                # exchange correlation functional
vdw_correction_hirshfeld .true.       # van der Waals corrections
vdw_pair_ignore Cu Cu
relativistic atomic_zora scalar       # relativistic effects for Cu
RI_method lvl_fast
charge 0                              # overall charge in the system
spin none                             # spin−polarization
use_dipole_correction .true.          # slab type − dipole correction
compensate_multipole_errors .true.

# Define convergence
sc_accuracy_rho 1e−2                  # conv. crit. charge density
sc_accuracy_etot 1e−5                 # conv. crit. total energy
sc_accuracy_forces 1e−3               # conv. crit. forces


occupation_type gaussian 0.01         # occupation scheme


# K−point grid
k_grid 4 4 1                          # k−point grid
```

In `FHI-aims` vdW^{surf} is included by manually providing the C6 parameters in the `control.in` file. For MBD the following parameters need to be set.

```
many_body_dispersion
mbd_scs_vacuum_axis .false. .false. .true.
mbd_cfdm_dip_cutoff 1800
```

In order to compare the results of DFTB to DFT, we first check the energetic ordering within the local adsorption geometries for TCNE/Cu(111) (see G1-G11 shown in Fig. 29). Figure 41a shows the total energy for all local adsorption structures with respect to the minimum G1. As can be seen, the relative energetic differences obtained from DFT are not at all reproduced by DFTB. Moreover, a huge spread in the DFTB results is observed. To further analyze this observation the vdW contributions are investigated, see Fig. 41b. The implementation of vdW^{surf} as well as MBD nicely agrees with the DFT results. When excluding vdW contributions, see Fig. 41c, we see no agreement between DFT and DFTB. This can furthermore be inferred from the binding curve, *i.e.* the total energy as a function of the adsorption distance for the most stable configuration G1 as shown in Fig. 42. Following on a recommendation of Reinhard Maurer, DFTB3[201] was also applied to the current system, as this should increase the performance for charge-transfer systems. DFTB3 additionally includes third order corrections, *i.e.* it corrects the SCC-Hamiltonian with the derivatives of the Hubbard U parameters. In the `dftb-hsd.in` file the following lines need to be included.
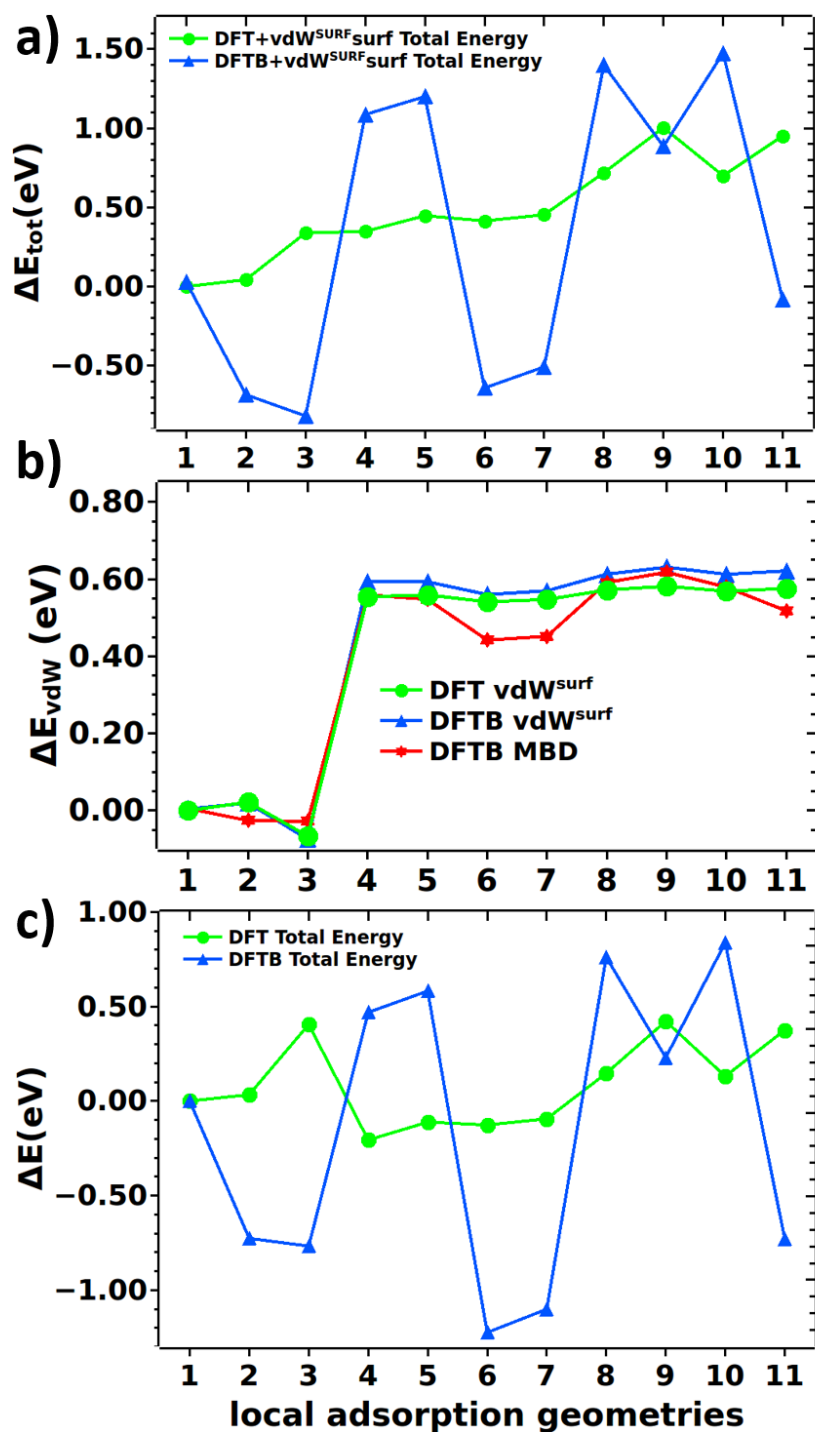
Figure 41: DFTB vs DFT for TCNE/Cu(111). Total energies for DFT and DFTB with respect to the minimum structure G1 for all found local adsorption geometries G1-G11 for TCNE/Cu(111) as shown in Fig. 29 when applying different dispersion schemes, *i.e.* vdW^{surf} and MBD. Comparison is done between DFT and DFTB. **(a)** shows the total energies including vdW^{surf} contributions, **(b)** shows only vdW contributions and **(c)** shows total energies without vdW contributions. See main text for details.
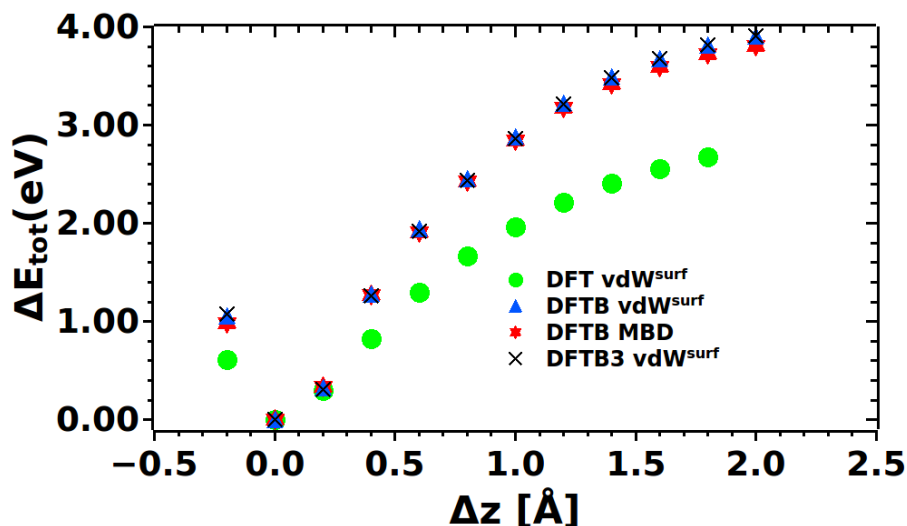
Figure 42: Binding curve for TCNE/Cu(111). Total energy for different adsorption heights Δz (in steps of $0.2\mathring{A}$) for the local adsorption structure G1 (see Fig. 29) applying different dispersion schemes, *i.e.* vdW$^{\text{surf}}$ and MBD. Comparison is done between Dft, Dftb2 as well as Dftb3. See main text for details.

```
ThirdOrderFull = Yes
   HubbardDerivs {
     C=−0.23
     N=−0.13
     Cu=−0.20
   }
```

The Hubbard derivatives need to be specified for every element. In principle these values should be optimized for the system at hand. However, for a quick testing, the values for N and C were taken from ref. [208] while the one for Cu is taken from ref. [209]. As can be seen in Fig. 42, at least for the chosen parameters, no improvement is found compared to Dftb2.

Within this Thesis, the enormous mismatch between Dft and Dftb results could not be resolved but it might be rooted in the Sk-files, *i.e.* the parametrization applying `hotbit` on the PBE reference. This needs to be further investigated for potential future applications.

3   Summary

In this Thesis, several approaches towards modeling and predicting organic-inorganic nanomaterials have been presented using atomistic simulations based on density-functional theory (DFT). In the following, the most relevant findings are summarized and an outlook for potential future efforts is given.

A thorough understanding of charge transport through metal-molecule-metal junctions is a prerequisite for advancing the field of molecular electronics. In this Thesis, a special emphasis was put on illustrating the tremendous difference in current-voltage characteristics of molecular junctions that comprise either a single molecule or a molecular assembly. As discussed in the introduction, the responsible effects are termed as *collective electrostatic effects*.[4–8] As was already shown in my Master Thesis for the example of 'Tour-wire'-based molecular junctions, *i.e.* 1,2-bis(2-phenylethynyl)benzene bonded to Au electrodes with thiolate docking groups (see Fig.43a), collective electrostatic effects emerge naturally from the bonding of the molecules to the leads and change transport characteristics of molecular ensembles even qualitatively as they strongly affect the total current as well as its polarity.[1,22] It was moreover demonstrated that the collective effects of polar groups
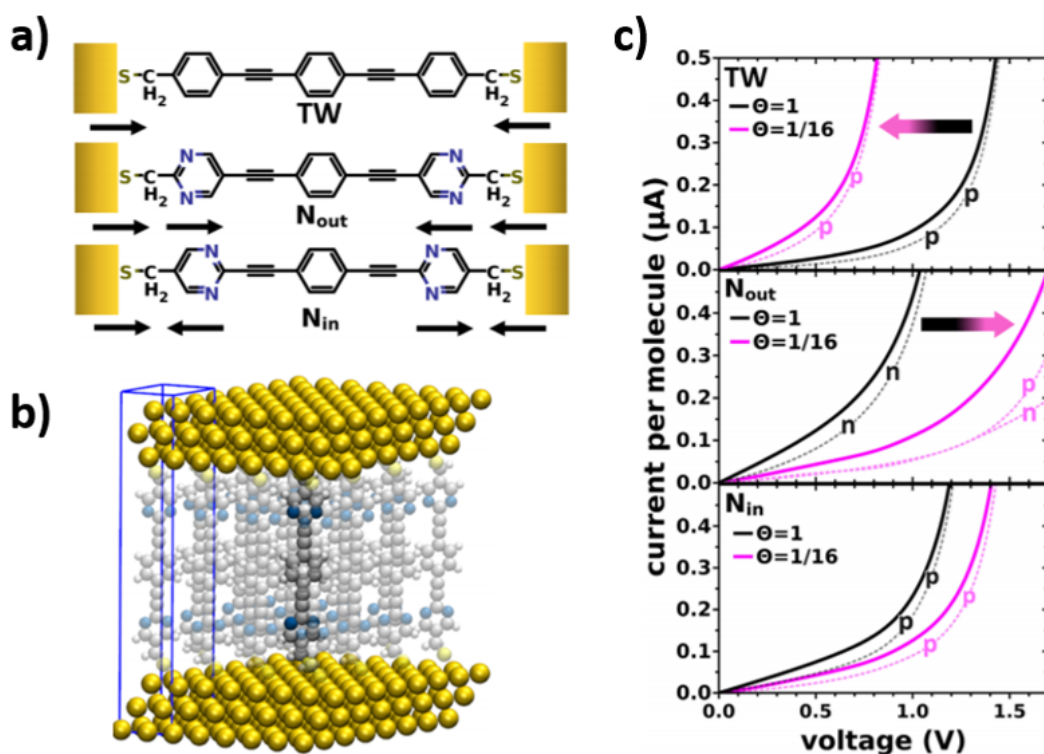
Figure 43: Current-Voltage Characteristics of Molecular Junctions. **(a)** Chemical structures of the *TW*, N_{out} and N_{in} molecular junctions. The arrows represent the local dipoles present in these systems. **(b)** Structure for the monolayer system (all molecules, blue unit cell, coverage $\Theta = 1$) and the single molecule junction (dark molecule, coverage $\Theta = 1/16$) **(c)** Corresponding current-voltage characteristics for the respective monolayer junctions (coverage, $\Theta = 1$) and the single molecule limit (coverage, $\Theta = 1/16$). Reprinted with permission from ref. [1]. Copyright 2014 American Chemical Society.

embedded into the backbones of the molecules (N_{out} and N_{in} in Fig. 43a) can significantly increase or decrease the current per molecule depending on the magnitude, location and orientation of the associate dipoles, see Fig.43b. For the *TW* molecular junction (without embedded dipoles) the current per molecule distinctively increases when reducing the molecular packing density from the monolayer ($\Theta = 1$) to the single molecule ($\Theta = 1/16$). In contrast, for N_{out}, a marked decrease is observed. For N_{in}, the effects of the bond dipole and the embedded dipole almost cancel and the current per molecule in the single molecule and the respective SAM almost equals. While these investigations clearly demonstrated that collective electrostatic effects are expected to occur in essentially every multimolecular junction, in PUBLICATION I enclosed in this Thesis, the impact of anchoring groups on ballistic transport has been investigated by extending the coverage dependent transport study to differently docked metal-molecule-mezal junctions, see Fig. 44a. Transmission functions and current-voltage characteristics were obtained within the framework of DFT in conjunction with non-equilibrium Greens function techniques. As discussed in the in-
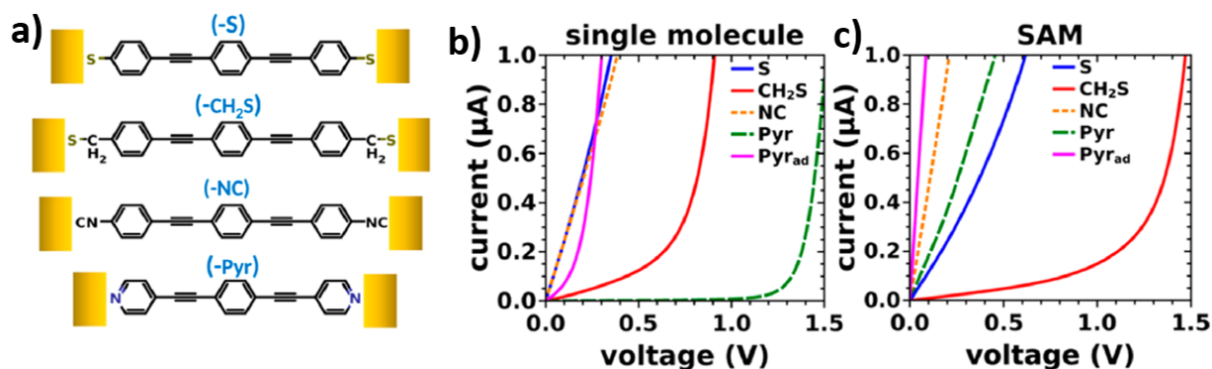
Figure 44: Current-Voltage Characteristics of Differently Linked Molecular Junctions. **(a)** Checmial structures of thiol (-SH) to methylthiol (-CH$_2$SH), isocyanide (-NC) and pyridine (-Pyr) linkedmethy molecular junctions. The corresponding current-voltage characteristics for the respective single molecule and monolayer junctions are shown in **(b)** and **(c)**. Reprinted with permission from ref. [2]. Copyright 2017 American Chemical Society.

troduction, it is well known that the type of docking group has a large impact on the final current-voltage characteristics.[48,49] The docking groups investigated in this work range from the commonly used thiol (-SH) to methylthiol (-CH$_2$SH), isocyanide (-NC) and pyridine (-Pyr), *cf.* Fig.44a. The current-voltage characteristics of these junctions were explicitly calculated considering different molecular packing densities spanning the range between the two limiting cases of the single molecule and the molecular monolayer. As can be seen from Fig. 44b, significant differences in the current through single molecule junctions have been found when varying the docking chemistry, with an overall sequence of S $\approx$ NC > CH$_2$SH >> Pyr. Interestingy, for the corresponding monolayer junction, a markedly different sequence is observed: NC > Pyr > S >> CH$_2$SH. These trends are also reflected in the corresponding zero-bias conductance. This clearly demonstrates that it strongly depends on the molecular packing density, which anchoring group yields the highest conductance.[2] As discussed in the methods section, current-voltage characteristics are related to transmission functions via the Landauer-Büttiker formalism.[180] Hence, the

observed (I-V)-trends can be directly traced back to the respective transmission functions. In this context, it could be found that the type of docking group strongly affects the level alignment of the transmissive states with respect to the Fermi level of the electrodes. Moreover, the interfacial coupling, which can be related to the width of the transmissive features,[210] drastically changes when changing the anchoring group. Collective electrostatic effects were found to lower the energies of the relevant transmission features in all studied systems. The exact amount of that shift depends on two highly system-dependent contributions.(i) The bonding-induced shifts as a consequence of charge-rearrangements at the interface (termed as *bond dipole*) and (ii) the energetic shift due to the formation of the free-standing monolayer which is attributed to the collective electrostatic effects of local dipoles within the molecule. Whether this energetic downwards shift then results in a decrease or increase in the current per molecule depends on whether the transmissive states arise from occupied or unoccupied states. In terms of chemical design of molecular junctions, it can be concluded that the ideal choice of anchoring group is clearly different for monolayer and single molecule junctions.

As discussed in the introduction, there is a strong dispute on the scaling of charge transport with the *number* of molecules contained in a molecular junction. While the work discussed so far, provides tremendous insights in the possible source of different (I-V)-characteristics between single molecule and monolayer, namely collective electrostatic effects, it needs to be clarified *how* the single molecule limit approaches the monolayer. Hence, in Publication II, transport studies were extended to differently sized clusters of molecules, *i.e.* 1, 2, 3, 4, 9 and 16 molecules in the cluster. Based on elaborate transport calculations for these comparably large systems (a cluster of 16 molecules sandwiched between three gold layers on each side of the junction results in ≈ 1700 atoms per unit cell) together with simple electrostatic considerations for much larger clusters, it was discussed in detail, how the single molecule limit approaches the monolayer. We found profound collective electrostatic effects already for very small cluster sizes. Moreover, the scaling of charge-transport with the number of molecules was found to be far from linear with the actual evolution depending significantly on the system at hand. Finally, we showed that transport in clusters becomes highly inhomogeneous with pronounced edge effects due to molecules in different electrostatic environments. The latter could be nicely demonstrated for the (-Pyr) linked cluster, see Fig. 45. For a cluster comprising 9 molecules the corresponding transmission features group into three main peaks, see Fig. 45b. These individual transport channels could be associated to molecules or molecular groups in different local electrostatic environments, as can be seen from the local density of states for the three lowest unoccupied states.

After illustrating the importance of collective electrostatic effects in molecular junctions, in Publication III, we went a decisive step beyond that and exploited these effects to design entirely new materials systems with exceptional properties. The basic idea of the proposed electrostatic design principle is to deliberately incorporate periodic arrangements of polar segments into materials in order to get control over the electronic levels and charges at the nanoscale. This was demonstrated by introducing polar linking groups into 3D bulk materials similar to covalent organic frameworks (Cofs), see Fig. 46a. As can be seen, porphyrin segments are linked via 1,3-difluorobenzene groups. Due to the

191
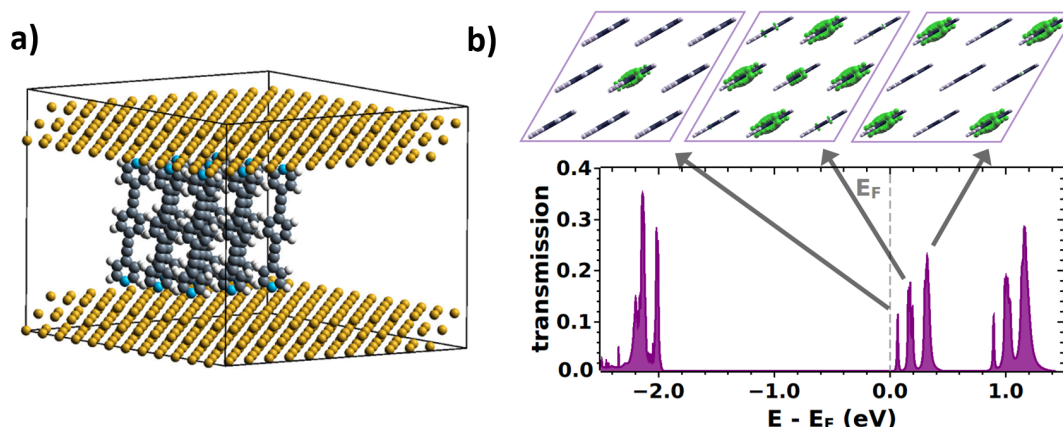
Figure 45: Transport Channels for Pyridine-linked Molecular Clusters.(a) Structure of the molecular cluster comprising 9 (-Pyr) linked molecules and (b) corresponding transmission function. Energies are aligned to the Fermi level. The insets show the local density of states projected onto the indicated transmission channels.

collective electrostatic effects of the introduced dipoles the porphyrin stripes are expected to shift in energy with respect to each other. This could, indeed, be demonstrated by first-principle calculations with DFT, as is shown for the electrostatic potential in Fig. 46b. The targeted manipulation of the electronic landscape is accompanied by a localization of the charge carriers, such that electrons and holes are localized to spatially confined pre-defined pathways. This was shown by analyzing the local density of states of the frontier orbitals. The level alignment achieved in these electrostatically designed systems is equivalent to the one occuring in donor-acceptor bulk heterojunctions. The level offset as driving force for exciton dissociation is the electrostatically induced shift between the porphyrin stripes. The exceptional broad and ordered interface between donor and acceptor phases in these materials together with the ideal pathways for electrons and holes turn them into promising candidates for solar cells. Indeed, as discussed in the introduction, very recently, the first solar cell was build using COFs covalently linking donor and acceptor molecules.[87] Compared to this conventional design principle, termed as "chemical design", the "electrostatic design" strategy proposed in this Thesis offers several advantages. Most importantly, the level offset as driving force for exciton dissociation is not determined by the chemical properties of the different donating and accepting materials. Rather, it is determined by the collective electrostatic effects induced by the polar segments that link chemically identical porphyrin units. In turn, this offers a tuning handle by varying the dipole density as well as dipole moment of the used linking segments. By investigating a variety of different linkers (such as 1,3-dichlorobenzene, pyrimidine or boron nitride) as well as different dipole densities (by varying the number of polar linkers as well as the distance between the layers), it was shown that the band offset can be tuned between 0.1 and $0.4 eV$. Another striking advantage of the electrostatic design is the fairly simple realization of much more complex architectures, as was discussed for the example of quantum checkerboards and quantum cascades. The latter is in particular promising for photovoltaics application, as the generated paths for electrons and holes are not only energetically separated but also in space which could potentially reduce recombination
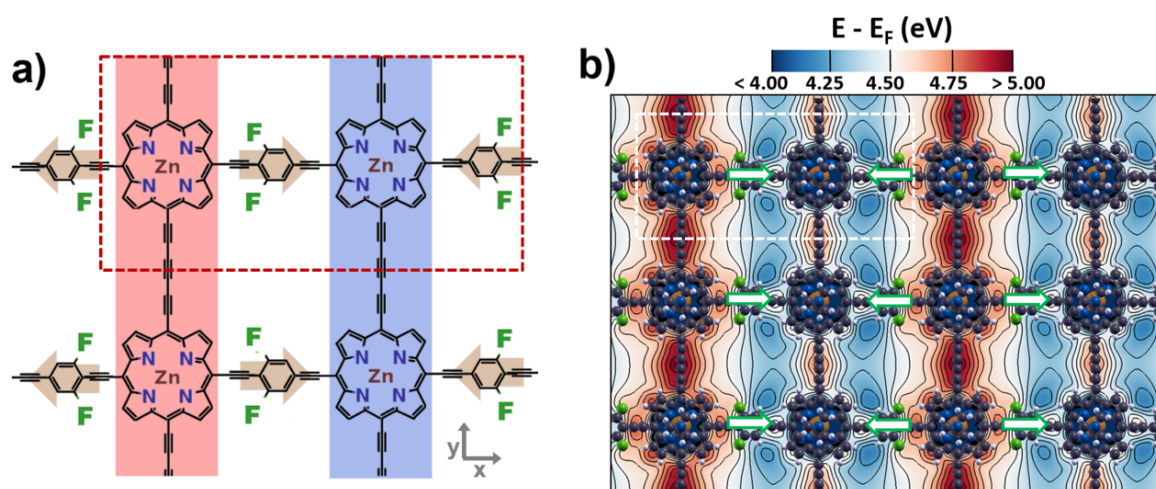
Figure 46: Electrostatic Design of 3D Covalent Organic Networks. (a) Top view of the electrostatically designed covalent organic networks consisting of porphyrin segments linked via polar 1,3-difluorobenzene groups. The arrows represent the direction of the dipole moment while the red and blue shaded areas indicate the expected division into high and low energetic stripes. (b) Corresponding contour plot of the electrostatic energy of an electron in a plane perpendicular to the stacking direction. The energy is given with respect to the Fermi level and isolines are drawn every $0.15 eV$. Reprinted with permission from ref. [3]. Copyright 2017 WILEY-VCH Verlag GmbH & Co. KGaA.

effects in these systems. In terms of future efforts, it has to be emphasized, that the proposed electrostatic design approach is not restricted to a specific class of materials.

Computational simulations cannot only be used to design entirely new materials systems but also to illuminate experimental investigations in the course of computational structure prediction. Many device properties depend heavily on the exact geometry of the underlying material. As discussed in the introduction, especially for organic electronics or photovoltaics applications, the interface between the organic molecules and the metal plays the most decisive role. In this context, in PUBLICATION IV, a new computational structure search algorithm to predict low-energy polymorphs at organic-inorganic interfaces, namely SAMPLE (Surface Polymorph Prediction with Little Effort), was developed and applied to TCNE/Au(111). SAMPLE consists of a systematic discretization of the configuration space followed by an efficient exploration of the potential energy surface inspired by the Basin-Hopping method. It is specifically designed to treat several molecules per unit cell and as an outcome provides a set of energetically low-lying polymorphs in order to provide the most relevant structures to verify the interpretation of experiments. A major advantage compared to common structure prediction methods is the discretization of the configuration space in two consecutive steps. First, the local adsorption geometries of individual molecules on the surface are determined which are then arranged into supramolecular configurations in the course of a 'Tetris-like' assembly procedure. Compared to traditional Basin-Hopping, the SAMPLE method exhibits certain peculiarities: (i) The disretization allows to set up the entire configuration space consisting of all possible, physically sensible starting configurations *a priori*. (ii) The geometry optimization for each configuration is comparably cheap as the starting configurations are already very close to the local minimum. (iii) A directed search along the potential energy surface is possible by connecting all configurations applying system-specific selection rules. (iv) A history list of all visited polymorphs can be generated from which the energy in case of revisiting is just looked up for free. The directed search and the history list enormously increase the overall performance. In PUBLICATION IV, SAMPLE was interfaced to dispersion-corrected DFT in order to predict the structure of TCNE/Au(111). As was shown in experimental STM measurements by Daniel Wegner,[103] TCNE orders in triangular structures on Au(111) consisting of essentially upright standing molecules. By validation of the predicted global minimum to experiments, an interpretation could be provided that cannot be directly inferred from experimental data alone: while for triangular structure on a pristine Au(111) surface the global minimum shown in Fig.47a was predicted, the agreement with experiments could be strongly improved by including a central gold adatom into the search, which resulted in the structure shown in 47b. As can be seen, due to the presence of the central gold adatom, the relative distance between the TCNE molecules got distinctively increased and a perfect agreement to experiments was observed.

For this benchmark study on TCNE/Au(111) it has been clearly demonstrated that based on the discretization of the configuration space, SAMPLE is definitely capable of predicting experimental structures at organic-inorganic interfaces. In terms of future perspectives, it has to be emphasized that SAMPLE is neither restricted to the Basin-Hopping method as a tool to explore the potential energy surface, nor to a specific electronic structure
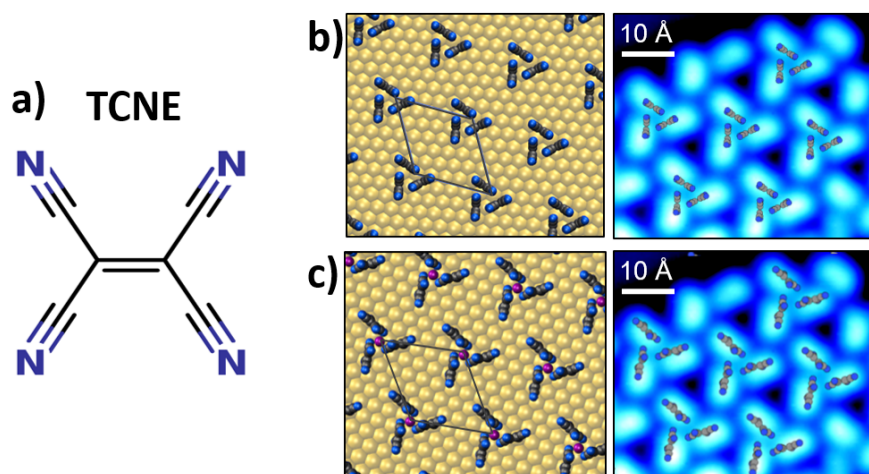
Figure 47: Predicted Global Minimum for TCNE/Au(111). (a) Chemical Structure of tetracyanoethylene (TCNE). Geometric structure and overlay to experimental STM[103] of **(b)** the global minimum predicted by SAMPLE for triangular polymorphs of TCNE/Au(111) and **(c)** the predicted global minimum including a gold adatom in the center of the triangular structure.

method (which is here DFT). Hence, on the one hand, more efficient exploration methods could be used, such as for example machine learning, which is currently developed in our group. While learning interactions for small unit cells, this technique allows to very efficiently predict the structure for larger unit cells. On the other hand, computationally less expensive electronic structure methods could be applied, such as DFTB which was also tested in the course of this PhD thesis. Applying SAMPLE to differently sized unit cells and different molecular coverages, finally allows to computationally predict phase transitions for organic monolayers on metal surfaces.

In summary, in the course of this PhD thesis, quantum-mechanical computer simulations have been performed to model and predict organic-inorganic nanomaterials. By highlighting collective electrostatic effects for multimolecular molecule-metal-molecule junctions, new insight into the field of molecular electronics was provided. An innovative electrostatic design strategy was proposed for controlling the electronic landscape of 3D bulk materials with potential application in photovoltaics. Finally, a novel algorithm to predict surface-induced phases of organic monolayers was developed.

References

(1) V. Obersteiner, D. A. Egger, G. Heimel, E. Zojer *The Journal of Physical Chemistry C* **2014**, **118**(38), 22395–22401, DOI: 10.1021/jp5084955.

(2) V. Obersteiner, D. A. Egger, E. Zojer *The Journal of Physical Chemistry C* **2015**, **119**(36), 21198–21208, DOI: 10.1021/acs.jpcc.5b06110.

(3) V. Obersteiner, A. Jeindl, J. Götz, A. Perveaux, O. T. Hofmann, E. Zojer *Advanced Materials* **2017**, in press.

(4) H. Ishii, K. Sugiyama, E. Ito, K. Seki *Advanced Materials* **1999**, **11**(8), 605–625, DOI: 10.1002/(SICI)1521-4095(199906)11:8<605::AID-ADMA605>3.0.CO;2-Q.

(5) D. Cahen, R. Naaman, Z. Vager *Advanced Functional Materials* **2005**, **15**(10), 1571–1578, DOI: 10.1002/adfm.200500187.

(6) A. Natan, Y. Zidon, Y. Shapira, L. Kronik *Physical Review B* **2006**, **73**(19), 193310, DOI: 10.1103/PhysRevB.73.193310.

(7) G. Heimel, F. Rissner, E. Zojer *Advanced Materials* **2010**, **22**(23), 2494–2513, DOI: 10.1002/adma.200903855.

(8) O. L. A. Monti *The Journal of Physical Chemistry Letters* **2012**, **3**(17), 2342–2351, DOI: 10.1021/jz300850x.

(9) G. Heimel, L. Romaner, E. Zojer, J.-L. Bredas *Accounts of Chemical Research* **2008**, **41**(6), 721–729, DOI: 10.1021/ar700284q.

(10) A. Natan, L. Kronik, H. Haick, R. T. Tung *Advanced Materials* **2007**, **19**(23), 4103–4117, DOI: 10.1002/adma.200701681.

(11) L. Romaner, G. Heimel, C. Ambrosch-Draxl, E. Zojer *Advanced Functional Materials* **2008**, **18**(24), 3999–4006, DOI: 10.1002/adfm.200800876.

(12) E. Verwüster, O. T. Hofmann, D. A. Egger, E. Zojer *The Journal of Physical Chemistry C* **2015**, **119**(14), 7817–7825, DOI: 10.1021/acs.jpcc.5b00992.

(13) G. Heimel, L. Romaner, J.-L. Brédas, E. Zojer *Physical Review Letters* **2006**, **96**(19), 196806, DOI: 10.1103/PhysRevLett.96.196806.

(14) J. C. Love, L. A. Estroff, J. K. Kriebel, R. G. Nuzzo, G. M. Whitesides *Chemical Reviews* **2005**, **105**(4), 1103–1170, DOI: 10.1021/cr0300789.

(15) G. Heimel, L. Romaner, E. Zojer, J.-L. Brédas *Nano Letters* **2007**, **7**(4), 932–940, DOI: 10.1021/nl0629106.

(16) T. Abu-Husein, S. Schuster, D. A. Egger, M. Kind, T. Santowski, A. Wiesner, R. Chiechi, E. Zojer, A. Terfort, M. Zharnikov *Advanced Functional Materials* **2015**, **25**(25), 3943–3957, DOI: 10.1002/adfm.201500899.

(17) A. Kovalchuk, T. Abu-Husein, D. Fracasso, D. A. Egger, E. Zojer, M. Zharnikov, A. Terfort, R. C. Chiechi *Chemical Science* **2016**, **7**(1), 781–787, DOI: 10.1039/C5SC03097H.

(18) I. Hehn, S. Schuster, T. Wächter, T. Abu-Husein, A. Terfort, M. Zharnikov, E. Zojer *The Journal of Physical Chemistry Letters* **2016**, **7**(15), 2994–3000, DOI: 10.1021/acs.jpclett.6b01096.

(19) T. C. Taucher, I. Hehn, O. T. Hofmann, M. Zharnikov, E. Zojer *The Journal of Physical Chemistry C* **2016**, **120**(6), 3428–3437, DOI: 10.1021/acs.jpcc.5b12387.

(20) B. Kretz, D. A. Egger, E. Zojer *Advanced Science* **2015**, **2**(3), n/a–n/a, DOI: 10.1002/advs.201400016.

(21) G. J. Kraberger, D. A. Egger, E. Zojer *Advanced Materials Interfaces* **2015**, **2**(17), n/a–n/a, DOI: 10.1002/admi.201500323.

(22) D. A. Egger, F. Rissner, E. Zojer, G. Heimel *Advanced Materials* **2012**, **24**(32), 4403–4407, DOI: 10.1002/adma.201200872.

(23) B. Mann, H. Kuhn *Journal of Applied Physics* **1971**, **42**(11), 4398–4405, DOI: 10.1063/1.1659785.

(24) A. Aviram, M. A. Ratner *Chemical Physics Letters* **1974**, **29**(2), 277–283, DOI: 10.1016/0009-2614(74)85031-1.

(25) M. A. Reed, C. Zhou, C. J. Muller, T. P. Burgin, J. M. Tour *Science* **1997**, **278**(5336), 252–254, DOI: 10.1126/science.278.5336.252.

(26) D. Xiang, X. Wang, C. Jia, T. Lee, X. Guo *Chemical Reviews* **2016**, **116**(7), 4318–4440, DOI: 10.1021/acs.chemrev.5b00680.

(27) J. C. Cuevas, E. Scheer, *Molecular electronics: an introduction to theory and experiment*; World Scientific series in nanoscience and nanotechnology v. 1, OCLC: ocn428025897; World Scientific: Singapore ; Hackensack, NJ, 2010.

(28) J. Moreland, J. W. Ekin *Journal of Applied Physics* **1985**, **58**(10), 3888–3895, DOI: 10.1063/1.335608.

(29) C. J. Muller, J. M. van Ruitenbeek, L. J. de Jongh *Physical Review Letters* **1992**, **69**(1), 140–143, DOI: 10.1103/PhysRevLett.69.140.

(30) H. Park, A. K. L. Lim, A. P. Alivisatos, J. Park, P. L. McEuen *Applied Physics Letters* **1999**, **75**(2), 301–303, DOI: 10.1063/1.124354.

(31) D. Xiang, H. Jeong, T. Lee, D. Mayer *Advanced Materials* **2013**, **25**(35), 4845–4867, DOI: 10.1002/adma.201301589.

(32) B. Xu, N. J. Tao *Science* **2003**, **301**(5637), 1221–1223, DOI: 10.1126/science.1087481.

(33) D. J. Wold, C. D. Frisbie *Journal of the American Chemical Society* **2000**, **122**(12), 2970–2971, DOI: 10.1021/ja994468h.

(34) J. G. Kushmerick, J. Naciri, J. C. Yang, R. Shashidhar *Nano Letters* **2003**, **3**(7), 897–900, DOI: 10.1021/nl034201n.

(35) H. B. Akkerman, P. W. M. Blom, D. M. de Leeuw, B. de Boer *Nature* **2006**, **441**(7089), 69–72, DOI: 10.1038/nature04699.

(36) F. Anariba, H. Tiznado, J. R. Diers, I. Schmidt, A. Z. Muresan, J. S. Lindsey, F. Zaera, D. F. Bocian *The Journal of Physical Chemistry C* **2008**, **112**(25), 9474–9485, DOI: 10.1021/jp802428y.

(37) N. Robertson, C. A. McGowan *Chemical Society Reviews* **2003**, **32**(2), 96–103, DOI: 10.1039/b206919a.

(38) R. L. McCreery *Chemistry of Materials* **2004**, **16**(23), 4477–4496, DOI: 10.1021/cm049517q.

(39) I. Díez-Pérez, J. Hihath, Y. Lee, L. Yu, L. Adamska, M. A. Kozhushner, I. I. Oleynik, N. Tao *Nature Chemistry* **2009**, **1**(8), 635–641, DOI: 10.1038/nchem.392.

(40) G. J. Ashwell, J. R. Sambles, A. S. Martin, W. G. Parker, M. Szablewski *Journal of the Chemical Society, Chemical Communications* **1990**(, 19), 1374, DOI: 10.1039/c39900001374.

(41) A. Batra, P. Darancet, Q. Chen, J. S. Meisner, J. R. Widawsky, J. B. Neaton, C. Nuckolls, L. Venkataraman *Nano Letters* **2013**, **13**(12), 6233–6237, DOI: 10.1021/nl403698m.

(42) E. Lörtscher, J. W. Ciszek, J. Tour, H. Riel *Small* **2006**, **2**(8-9), 973–977, DOI: 10.1002/smll.200600101.

(43) S. J. v. d. Molen, P. Liljeroth *Journal of Physics: Condensed Matter* **2010**, **22**(13), 133001, DOI: 10.1088/0953-8984/22/13/133001.

(44) Y. Kim, T. J. Hellmuth, D. Sysoiev, F. Pauly, T. Pietsch, J. Wolf, A. Erbe, T. Huhn, U. Groth, U. E. Steiner, E. Scheer *Nano Letters* **2012**, **12**(7), 3736–3742, DOI: 10.1021/nl3015523.

(45) C. Jia, J. Wang, C. Yao, Y. Cao, Y. Zhong, Z. Liu, Z. Liu, X. Guo *Angewandte Chemie International Edition* **2013**, **52**(33), 8666–8670, DOI: 10.1002/anie.201304301.

(46) H. Song, Y. Kim, Y. H. Jang, H. Jeong, M. A. Reed, T. Lee *Nature* **2009**, **462**(7276), 1039–1043, DOI: 10.1038/nature08639.

(47) L. Gao, L.-L. Li, X. Wang, P. Wu, Y. Cao, B. Liang, X. Li, Y. Lin, Y. Lu, X. Guo *Chemical Science* **2015**, **6**(4), 2469–2473, DOI: 10.1039/C4SC03612C.

(48) L. A. Zotti, T. Kirchner, J.-C. Cuevas, F. Pauly, T. Huhn, E. Scheer, A. Erbe *Small* **2010**, **6**(14), 1529–1535, DOI: 10.1002/smll.200902227.

(49) W. Hong, D. Z. Manrique, P. Moreno-García, M. Gulcur, A. Mishchenko, C. J. Lambert, M. R. Bryce, T. Wandlowski *Journal of the American Chemical Society* **2012**, **134**(4), 2292–2304, DOI: 10.1021/ja209844r.

(50) C. M. Kim, J. Bechhoefer *The Journal of Chemical Physics* **2013**, **138**(1), 014707, DOI: 10.1063/1.4773436.

(51) A. Sen, C.-C. Kaun *ACS Nano* **2010**, **4**(11), 6404–6408, DOI: 10.1021/nn101840a.

(52) M. Kamenetska, S. Y. Quek, A. C. Whalley, M. L. Steigerwald, H. J. Choi, S. G. Louie, C. Nuckolls, M. S. Hybertsen, J. B. Neaton, L. Venkataraman *Journal of the American Chemical Society* **2010**, **132**(19), 6817–6821, DOI: 10.1021/ja1015348.

(53) M. Frei, S. V. Aradhya, M. S. Hybertsen, L. Venkataraman *Journal of the American Chemical Society* **2012**, **134**(9), 4003–4006, DOI: 10.1021/ja211590d.

(54) Y.-L. Lo, S.-J. Sun, Y.-J. Kao *Physical Review B* **2011**, **84**(7), 075106, DOI: 10.1103/PhysRevB.84.075106.

(55) X. D. Cui, A. Primak, X. Zarate, J. Tomfohr, O. F. Sankey, A. L. Moore, T. A. Moore, D. Gust, G. Harris, S. M. Lindsay *Science* **2001**, **294**(5542), 571–574, DOI: 10.1126/science.1064354.

(56) A. Salomon, D. Cahen, S. Lindsay, J. Tomfohr, V. Engelkes, C. Frisbie *Advanced Materials* **2003**, **15**(22), 1881–1890, DOI: 10.1002/adma.200306091.

(57) M. Magoga, C. Joachim *Physical Review B* **1999**, **59**(24), 16011–16021, DOI: 10.1103/PhysRevB.59.16011.

(58) N. D. Lang, P. Avouris *Physical Review B* **2000**, **62**(11), 7325–7329, DOI: 10.1103/PhysRevB.62.7325.

(59) M. G. Reuter, G. C. Solomon, T. Hansen, T. Seideman, M. A. Ratner *The Journal of Physical Chemistry Letters* **2011**, **2**(14), 1667–1671, DOI: 10.1021/jz200658h.

(60) M. G. Reuter, T. Seideman, M. A. Ratner *Nano Letters* **2011**, **11**(11), 4693–4696, DOI: 10.1021/nl202342a.

(61) C. M. Guédon, H. Valkenier, T. Markussen, K. S. Thygesen, J. C. Hummelen, S. J. van der Molen *Nature Nanotechnology* **2012**, **7**(5), 305–309, DOI: 10.1038/nnano.2012.37.

(62) H. Vazquez, R. Skouta, S. Schneebeli, M. Kamenetska, R. Breslow, L. Venkataraman, M. S. Hybertsen *Nature Nanotechnology* **2012**, **7**(10), 663–667, DOI: 10.1038/nnano.2012.147.

(63) M. Galperin, A. Nitzan *The Journal of Physical Chemistry B* **2013**, **117**(16), 4449–4453, DOI: 10.1021/jp308222q.

(64) X. Feng, X. Ding, D. Jiang *Chemical Society Reviews* **2012**, **41**(18), 6010, DOI: 10.1039/c2cs35157a.

(65) S.-Y. Ding, W. Wang *Chem. Soc. Rev.* **2013**, **42**(2), 548–568, DOI: 10.1039/C2CS35072F.

(66) M. Dogru, T. Bein *Chem. Commun.* **2014**, **50**(42), 5531–5546, DOI: 10.1039/C3CC46767H.

(67) P. J. Waller, F. Gándara, O. M. Yaghi *Accounts of Chemical Research* **2015**, **48**(12), 3053–3063, DOI: 10.1021/acs.accounts.5b00369.

(68) J. Jiang, Y. Zhao, O. M. Yaghi *Journal of the American Chemical Society* **2016**, **138**(10), 3255–3265, DOI: 10.1021/jacs.5b10666.

(69) H. Li, M. Eddaoudi, M. O'Keeffe, O. M. Yaghi *Nature* **1999**, **402**(6759), 276–279, DOI: 10.1038/46248.

(70) S. T. Meek, J. A. Greathouse, M. D. Allendorf *Advanced Materials* **2011**, **23**(2), 249–267, DOI: 10.1002/adma.201002854.

(71) J.-L. Zhuang, A. Terfort, C. Wöll *Coordination Chemistry Reviews* **2016**, **307**, 391–424, DOI: 10.1016/j.ccr.2015.09.013.

(72) A. Dhakshinamoorthy, H. Garcia *Chemical Society Reviews* **2014**, **43**(16), 5750–5765, DOI: 10.1039/C3CS60442J.

(73) N. Huang, P. Wang, D. Jiang *Nature Reviews Materials* **2016**, **1**(10), 16068, DOI: 10.1038/natrevmats.2016.68.

(74) O. Shekhah, H. Wang, S. Kowarik, F. Schreiber, M. Paulus, M. Tolan, C. Sternemann, F. Evers, D. Zacher, R. A. Fischer, C. Wöll *Journal of the American Chemical Society* **2007**, **129**(49), 15118–15119, DOI: 10.1021/ja076210u.

(75) B. Liu, O. Shekhah, H. K. Arslan, J. Liu, C. Wöll, R. A. Fischer *Angewandte Chemie International Edition* **2012**, **51**(3), 807–810, DOI: 10.1002/anie.201104240.

(76) H. Wang, H. Ding, X. Meng, C. Wang *Chinese Chemical Letters* **2016**, **27**(8), 1376–1382, DOI: 10.1016/j.cclet.2016.05.020.

(77) E. Klontzas, E. Tylianakis, G. E. Froudakis *The Journal of Physical Chemistry C* **2008**, **112**(24), 9095–9098, DOI: 10.1021/jp711326g.

(78) H. Furukawa, O. M. Yaghi *Journal of the American Chemical Society* **2009**, **131**(25), 8875–8883, DOI: 10.1021/ja9015765.

(79) C. J. Doonan, D. J. Tranchemontagne, T. G. Glover, J. R. Hunt, O. M. Yaghi *Nature Chemistry* **2010**, **2**(3), 235–238, DOI: 10.1038/nchem.548.

(80) S. Wan, J. Guo, J. Kim, H. Ihee, D. Jiang *Angewandte Chemie* **2009**, **121**(30), 5547–5550, DOI: 10.1002/ange.200900881.

(81) X. Ding, X. Feng, A. Saeki, S. Seki, A. Nagai, D. Jiang *Chemical Communications* **2012**, **48**(71), 8952, DOI: 10.1039/c2cc33929c.

(82) X. Feng, L. Chen, Y. Honsho, O. Saengsawang, L. Liu, L. Wang, A. Saeki, S. Irle, S. Seki, Y. Dong, D. Jiang *Advanced Materials* **2012**, **24**(22), 3026–3031, DOI: 10.1002/adma.201201185.

(83) S. Jin, K. Furukawa, M. Addicoat, L. Chen, S. Takahashi, S. Irle, T. Nakamura, D. Jiang *Chemical Science* **2013**, **4**(12), 4505, DOI: 10.1039/c3sc52034j.

(84) M. Dogru, M. Handloser, F. Auras, T. Kunz, D. Medina, A. Hartschuh, P. Knochel, T. Bein *Angewandte Chemie* **2013**, **125**(10), 2992–2996, DOI: 10.1002/ange.201208514.

(85) L. Chen, K. Furukawa, J. Gao, A. Nagai, T. Nakamura, Y. Dong, D. Jiang *Journal of the American Chemical Society* **2014**, **136**(28), 9806–9809, DOI: 10.1021/ja502692w.

(86) M. Calik, F. Auras, L. M. Salonen, K. Bader, I. Grill, M. Handloser, D. D. Medina, M. Dogru, F. Löbermann, D. Trauner, A. Hartschuh, T. Bein *Journal of the American Chemical Society* **2014**, **136**(51), 17802–17807, DOI: 10.1021/ja509551m.

(87) S. Jin, M. Supur, M. Addicoat, K. Furukawa, L. Chen, T. Nakamura, S. Fukuzumi, S. Irle, D. Jiang *Journal of the American Chemical Society* **2015**, **137**(24), 7817–7827, DOI: 10.1021/jacs.5b03553.

(88) K.-S. Liao, S. D. Yambem, A. Haldar, N. J. Alley, S. A. Curran *Energies* **2010**, **3**(6), 1212–1250, DOI: 10.3390/en3061212.

(89) C. W. Tang *Applied Physics Letters* **1986**, **48**(2), 183–185, DOI: 10.1063/1.96937.

(90) E.-Y. Choi, P. M. Barron, R. W. Novotny, H.-T. Son, C. Hu, W. Choe *Inorganic Chemistry* **2009**, **48**(2), 426–428, DOI: 10.1021/ic801677y.

(91) B. J. Burnett, P. M. Barron, W. Choe *CrystEngComm* **2012**, **14**(11), 3839–3846, DOI: 10.1039/C2CE06692K.

(92) A. Nagai, X. Chen, X. Feng, X. Ding, Z. Guo, D. Jiang *Angewandte Chemie International Edition* **2013**, **52**(13), 3770–3774, DOI: 10.1002/anie.201300256.

(93) X. Chen, M. Addicoat, E. Jin, L. Zhai, H. Xu, N. Huang, Z. Guo, L. Liu, S. Irle, D. Jiang *Journal of the American Chemical Society* **2015**, **137**(9), 3241–3247, DOI: 10.1021/ja509602c.

(94) M. L. Tiago, J. E. Northrup, S. G. Louie *Physical Review B* **2003**, **67**(11), 115212, DOI: 10.1103/PhysRevB.67.115212.

(95) C. Ambrosch-Draxl, D. Nabok, P. Puschnig, C. Meisenbichler *New Journal of Physics* **2009**, **11**(12), 125010, DOI: 10.1088/1367-2630/11/12/125010.

(96) W. I. F. David, S. K. Callear, M. O. Jones, P. C. Aeberhard, S. D. Culligan, A. H. Pohl, S. R. Johnson, K. R. Ryan, J. E. Parker, P. P. Edwards, C. J. Nuttall, A. Amieiro-Fonseca **2012**, **14**(33), 11800–11807, DOI: 10.1039/C2CP23439D.

(97) W. C. McCrone, D. Fox, M. Labes, A. Weissberger *Eds. Interscience* **1965**, **II**, 725–767.

(98)   T. L. Threlfall **1995**, **120**(10), 2435–2460, DOI: 10.1039/AN9952002435.

(99)   A. O. F. Jones, B. Chattopadhyay, Y. H. Geerts, R. Resel *Advanced Functional Materials* **2016**, **26**(14), 2233–2255, DOI: 10.1002/adfm.201503169.

(100) H. Chung, Y. Diao **2016**, **4**(18), 3915–3933, DOI: 10.1039/C5TC04390E.

(101) T. Djuric, T. Ules, H.-G. Flesch, H. Plank, Q. Shen, C. Teichert, R. Resel, M. G. Ramsey *Crystal Growth & Design* **2011**, **11**(4), 1015–1020, DOI: 10.1021/cg101230j.

(102) Y. Diao, K. M. Lenn, W.-Y. Lee, M. A. Blood-Forsythe, J. Xu, Y. Mao, Y. Kim, J. A. Reinspach, S. Park, A. Aspuru-Guzik, G. Xue, P. Clancy, Z. Bao, S. C. B. Mannsfeld *Journal of the American Chemical Society* **2014**, **136**(49), 17046–17057, DOI: 10.1021/ja507179d.

(103) D. Wegner, R. Yamachika, Y. Wang, V. W. Brar, B. M. Bartlett, J. R. Long, M. F. Crommie *Nano Letters* **2008**, **8**(1), 131–135, DOI: 10.1021/nl072217y.

(104) J. Rodríguez-Fernández, K. Lauwaet, M. Á. Herranz, N. Martín, J. M. Gallego, R. Miranda, R. Otero *The Journal of Chemical Physics* **2015**, **142**(10), 101930, DOI: 10.1063/1.4913326.

(105) M. N. Faraggi, N. Jiang, N. Gonzalez-Lakunza, A. Langner, S. Stepanow, K. Kern, A. Arnau *The Journal of Physical Chemistry C* **2012**, **116**(46), 24558–24565, DOI: 10.1021/jp306780n.

(106) J. Maddox *Nature* **1988**(, 335), 6187, DOI: 10.1038/335201a0.

(107) F. H. Stillinger *Physical Review E* **1999**, **59**(1), 48–51, DOI: 10.1103/PhysRevE.59.48.

(108) J. Pannetier, J. Bassas-Alsina, J. Rodriguez-Carvajal, V. Caignaert *Nature* **1990**, **346**(6282), 343–345, DOI: 10.1038/346343a0.

(109) D. J. Wales, J. P. K. Doye *The Journal of Physical Chemistry A* **1997**, **101**(28), 5111–5116, DOI: 10.1021/jp970984n.

(110) S. Goedecker *The Journal of Chemical Physics* **2004**, **120**(21), 9911–9917, DOI: 10.1063/1.1724816.

(111) B. Hartke *The Journal of Physical Chemistry* **1993**, **97**(39), 9973–9976, DOI: 10.1021/j100141a013.

(112) A. R. Oganov, *Modern Methods of Crystal Structure Prediction*; Wiley-VCH Verlag GmbH & Co. KGaA: Weinheim, Germany, 2010.

(113) J. C. Schön, M. Jansen *Modern Methods of Crystal Structure Prediction*, Oganov, A. R., Ed., DOI: 10.1002/9783527632831.ch4; Wiley-VCH Verlag GmbH & Co. KGaA: 2010, 67–105.

(114) N. Metropolis, A. W. Rosenbluth, M. N. Rosenbluth, A. H. Teller, E. Teller *The Journal of Chemical Physics* **1953**, **21**(6), 1087–1092, DOI: 10.1063/1.1699114.

(115) C. Tsallis *Journal of Statistical Physics* **1988**, **52**(1-2), 479–487, DOI: 10.1007/BF01016429.

(116) C. Shang, D. J. Wales *The Journal of Chemical Physics* **2014**, **141**(7), 071101, DOI: 10.1063/1.4893344.

(117) C. M. Baker *Wiley Interdisciplinary Reviews: Computational Molecular Science* **2015**, **5**(2), 241–254, DOI: 10.1002/wcms.1215.

(118)   L. Verlet *Physical Review* **1967**, **159**(1), 98–103, DOI: 10.1103/PhysRev.159.98.

(119)   H. E. A. Huitema, J. P. van der Eerden *The Journal of Chemical Physics* **1999**, **110**(7), 3267–3274, DOI: 10.1063/1.478192.

(120)   K. Krautgasser, C. Panosetti, D. Palagin, K. Reuter, R. J. Maurer *The Journal of Chemical Physics* **2016**, **145**(8), 084117, DOI: 10.1063/1.4961259.

(121)   C. Panosetti, K. Krautgasser, D. Palagin, K. Reuter, R. J. Maurer *Nano Letters* **2015**, **15**(12), 8044–8048, DOI: 10.1021/acs.nanolett.5b03388.

(122)   D. Goldberg, K. Deb, B. Korb *Complex Systems* **1989**(, 3), 493–530.

(123)   D. M. Deaven, K. M. Ho *Physical Review Letters* **1995**, **75**(2), 288–291, DOI: 10.1103/PhysRevLett.75.288.

(124)   D. E. Goldberg, J. H. Holland *Machine Learning* **1988**, **3**(2-3), 95–99, DOI: 10.1023/A:1022602019183.

(125)   A. Lipowski, D. Lipowska *Physica A: Statistical Mechanics and its Applications* **2012**, **391**(6), arXiv: 1109.3627, 2193–2196, DOI: 10.1016/j.physa.2011.12.004.

(126)   A. M. Reilly, R. I. Cooper, C. S. Adjiman, S. Bhattacharya, A. D. Boese, J. G. Brandenburg, P. J. Bygrave, R. Bylsma, J. E. Campbell, R. Car, D. H. Case, R. Chadha, J. C. Cole, K. Cosburn, H. M. Cuppen, F. Curtis, G. M. Day, R. A. DiStasio Jr, A. Dzyabchenko, B. P. van Eijck, D. M. Elking, J. A. van den Ende, J. C. Facelli, M. B. Ferraro, L. Fusti-Molnar, C.-A. Gatsiou, T. S. Gee, R. de Gelder, L. M. Ghiringhelli, H. Goto, S. Grimme, R. Guo, D. W. M. Hofmann, J. Hoja, R. K. Hylton, L. Iuzzolino, W. Jankiewicz, D. T. de Jong, J. Kendrick, N. J. J. de Klerk, H.-Y. Ko, L. N. Kuleshova, X. Li, S. Lohani, F. J. J. Leusen, A. M. Lund, J. Lv, Y. Ma, N. Marom, A. E. Masunov, P. McCabe, D. P. McMahon, H. Meekes, M. P. Metz, A. J. Misquitta, S. Mohamed, B. Monserrat, R. J. Needs, M. A. Neumann, J. Nyman, S. Obata, H. Oberhofer, A. R. Oganov, A. M. Orendt, G. I. Pagola, C. C. Pantelides, C. J. Pickard, R. Podeszwa, L. S. Price, S. L. Price, A. Pulido, M. G. Read, K. Reuter, E. Schneider, C. Schober, G. P. Shields, P. Singh, I. J. Sugden, K. Szalewicz, C. R. Taylor, A. Tkatchenko, M. E. Tuckerman, F. Vacarro, M. Vasileiadis, A. Vazquez-Mayagoitia, L. Vogt, Y. Wang, R. E. Watson, G. A. de Wijs, J. Yang, Q. Zhu, C. R. Groom *Acta Crystallographica Section B: Structural Science, Crystal Engineering and Materials* **2016**, **72**(4), 439–459, DOI: 10.1107/S2052520616007447.

(127)   A. L.-S. Chua, N. A. Benedek, L. Chen, M. W. Finnis, A. P. Sutton *Nature Materials* **2010**, **9**(5), 418–422, DOI: 10.1038/nmat2712.

(128)   X. Zhao, Q. Shu, M. C. Nguyen, Y. Wang, M. Ji, H. Xiang, K.-M. Ho, X. Gong, C.-Z. Wang *The Journal of Physical Chemistry C* **2014**, **118**(18), 9524–9530, DOI: 10.1021/jp5010852.

(129)   S. Kiyohara, H. Oda, T. Miyata, T. Mizoguchi *Science Advances* **2016**, **2**(11), e1600746, DOI: 10.1126/sciadv.1600746.

(130)   G. Copie, Y. Makoudi, C. Krzeminski, F. Chérioux, F. Palmino, S. Lamare, B. Grandidier, F. Cleri *The Journal of Physical Chemistry C* **2014**, **118**(24), 12817–12825, DOI: 10.1021/jp501955v.

(131)   T. J. Roussel, E. Barrena, C. Ocal, J. Faraudo *Nanoscale* **2014**, **6**(14), 7991–8001, DOI: 10.1039/C4NR01987C.

(132)   G. Copie, F. Cleri, Y. Makoudi, C. Krzeminski, M. Berthe, F. Cherioux, F. Palmino, B. Grandidier *Physical Review Letters* **2015**, **114**(6), 066101, DOI: 10.1103/PhysRevLett.114.066101.

(133)   J. van der Lit, J. L. Marsman, R. S. Koster, P. H. Jacobse, S. A. den Hartog, D. Vanmaekelbergh, R. J. M. Klein Gebbink, L. Filion, I. Swart *The Journal of Physical Chemistry C* **2016**, **120**(1), 318–323, DOI: 10.1021/acs.jpcc.5b09889.

(134)   D. M. Packwood, P. Han, T. Hitosugi *Nature Communications* **2017**, **8**, 14463, DOI: 10.1038/ncomms14463.

(135)   O. W. Webster, W. Mahler, R. E. Benson *Journal of the American Chemical Society* **1962**, **84**(19), 3678–3684, DOI: 10.1021/ja00878a017.

(136)   A. A. Shabaka, K. M. El-Behery, M. Fadly *Journal of Materials Science Letters* **1988**, **7**(7), 685–687, DOI: 10.1007/BF00722067.

(137)   D. A. Bekoe, K. N. Trueblood *Zeitschrift fur Kristallographie* **1960**, **113**, 1–22, DOI: 10.1524/zkri.1960.113.1-6.1.

(138)   M. Khazaei, M. Arai, T. Sasaki, Y. Kawazoe *The Journal of Physical Chemistry C* **2013**, **117**(1), 712–720, DOI: 10.1021/jp310747v.

(139)   R. Mukhopadhyay, S. K. Deb, A. Das, S. L. Chaplot *Solid State Communications* **2009**, **149**(43–44), 1914–1918, DOI: 10.1016/j.ssc.2009.07.048.

(140)   B. Schatschneider, J.-J. Liang, S. Jezowski, A. Tkatchenko *CrystEngComm* **2012**, **14**(14), 4656–4663, DOI: 10.1039/C2CE25321F.

(141)   W. Erley, H. Ibach *The Journal of Physical Chemistry* **1987**, **91**(11), 2947–2950, DOI: 10.1021/j100295a059.

(142)   T. Choi, S. Bedwani, A. Rochefort, C.-Y. Chen, A. J. Epstein, J. A. Gupta *Nano Letters* **2010**, **10**(10), 4175–4180, DOI: 10.1021/nl1024563.

(143)   M. Born, R. Oppenheimer *Annalen der Physik* **1927**, **389**(20), 457–484, DOI: 10.1002/andp.19273892002.

(144)   P. Hohenberg, W. Kohn *Physical Review* **1964**, **136**(3B), B864–B871, DOI: 10.1103/PhysRev.136.B864.

(145)   W. Kohn, L. J. Sham *Physical Review* **1965**, **140**(4A), A1133–A1138, DOI: 10.1103/PhysRev.140.A1133.

(146)   J. P. Perdew, K. Burke, M. Ernzerhof *Physical Review Letters* **1996**, **77**(18), 3865–3868, DOI: 10.1103/PhysRevLett.77.3865.

(147)   R. Peverati, D. G. Truhlar *Phil. Trans. R. Soc. A* **2014**, **372**(2011), 20120476, DOI: 10.1098/rsta.2012.0476.

(148)   S. Kümmel *Reviews of Modern Physics* **2008**, **80**(1), 3–60, DOI: 10.1103/RevModPhys.80.3.

(149)   J. P. Perdew *Physical Review B* **1981**, **23**(10), 5048–5079, DOI: 10.1103/PhysRevB.23.5048.

(150)   N. Dori, M. Menon, L. Kilian, M. Sokolowski, L. Kronik, E. Umbach *Physical Review B* **2006**, **73**(19), 195208, DOI: 10.1103/PhysRevB.73.195208.

(151)   N. Marom, O. Hod, G. E. Scuseria, L. Kronik *The Journal of Chemical Physics* **2008**, **128**(16), 164107, DOI: 10.1063/1.2898540.

(152) T. Körzdörfer, S. Kümmel, N. Marom, L. Kronik *Physical Review B* **2009**, **79**(20), 201205, DOI: 10.1103/PhysRevB.79.201205.

(153) A. D. Becke *The Journal of Chemical Physics* **1993**, **98**(7), 5648–5652, DOI: 10.1063/1.464913.

(154) C. Adamo, V. Barone *The Journal of Chemical Physics* **1999**, **110**(13), 6158–6170, DOI: 10.1063/1.478522.

(155) J. Heyd, G. E. Scuseria, M. Ernzerhof *The Journal of Chemical Physics* **2003**, **118**(18), 8207–8215, DOI: 10.1063/1.1564060.

(156) R. Baer, E. Livshits, U. Salzner *Annual Review of Physical Chemistry* **2010**, **61**(1), 85–109, DOI: 10.1146/annurev.physchem.012809.103321.

(157) L. Kronik, T. Stein, S. Refaely-Abramson, R. Baer *Journal of Chemical Theory and Computation* **2012**, **8**(5), 1515–1531, DOI: 10.1021/ct2009363.

(158) S. Refaely-Abramson, S. Sharifzadeh, N. Govind, J. Autschbach, J. B. Neaton, R. Baer, L. Kronik *Physical Review Letters* **2012**, **109**(22), 226405, DOI: 10.1103/PhysRevLett.109.226405.

(159) S. Refaely-Abramson, S. Sharifzadeh, M. Jain, R. Baer, J. B. Neaton, L. Kronik *Physical Review B* **2013**, **88**(8), 081204, DOI: 10.1103/PhysRevB.88.081204.

(160) D. A. Egger, S. Weissman, S. Refaely-Abramson, S. Sharifzadeh, M. Dauth, R. Baer, S. Kümmel, J. B. Neaton, E. Zojer, L. Kronik *Journal of Chemical Theory and Computation* **2014**, **10**(5), 1934–1952, DOI: 10.1021/ct400956h.

(161) A. Tkatchenko, L. Romaner, O. T. Hofmann, E. Zojer, C. Ambrosch-Draxl, M. Scheffler *MRS Bulletin* **2010**, **35**(06), 435–442, DOI: 10.1557/mrs2010.581.

(162) S. Ehrlich, J. Moellmann, S. Grimme *Accounts of Chemical Research* **2013**, **46**(4), 916–926, DOI: 10.1021/ar3000844.

(163) A. J. Cohen, P. Mori-Sánchez, W. Yang *Chemical Reviews* **2012**, **112**(1), 289–320, DOI: 10.1021/cr200107z.

(164) J. Klimeš, A. Michaelides *The Journal of Chemical Physics* **2012**, **137**(12), 120901, DOI: 10.1063/1.4754130.

(165) R. A. DiStasio, V. V. Gobre, A. Tkatchenko *Journal of Physics. Condensed Matter: An Institute of Physics Journal* **2014**, **26**(21), 213202, DOI: 10.1088/0953-8984/26/21/213202.

(166) R. J. Maurer, V. G. Ruiz, J. Camarillo-Cisneros, W. Liu, N. Ferri, K. Reuter, A. Tkatchenko *Progress in Surface Science* **2016**, **91**(2), 72–100, DOI: 10.1016/j.progsurf.2016.05.001.

(167) A. Tkatchenko, M. Scheffler *Physical Review Letters* **2009**, **102**(7), 073005, DOI: 10.1103/PhysRevLett.102.073005.

(168) F. L. Hirshfeld *Israel Journal of Chemistry* **1977**, **16**(2-3), 198–201, DOI: 10.1002/ijch.197700033.

(169) V. G. Ruiz, W. Liu, E. Zojer, M. Scheffler, A. Tkatchenko *Physical Review Letters* **2012**, **108**(14), 146103, DOI: 10.1103/PhysRevLett.108.146103.

(170) E. Zaremba, W. Kohn *Physical Review B* **1976**, **13**(6), 2270–2285, DOI: 10.1103/PhysRevB.13.2270.

(171) A. Tkatchenko, R. A. DiStasio, R. Car, M. Scheffler *Physical Review Letters* **2012**, **108**(23), 236402, DOI: 10.1103/PhysRevLett.108.236402.

(172) W. Liu, F. Maaß, M. Willenbockel, C. Bronner, M. Schulze, S. Soubatch, F. S. Tautz, P. Tegeder, A. Tkatchenko *Physical Review Letters* **2015**, **115**(3), 036104, DOI: 10.1103/PhysRevLett.115.036104.

(173) J. Neugebauer, M. Scheffler *Physical Review B* **1992**, **46**(24), 16067–16080, DOI: 10.1103/PhysRevB.46.16067.

(174) G. Kresse, J. Furthmüller *Physical Review B* **1996**, **54**(16), 11169–11186, DOI: 10.1103/PhysRevB.54.11169.

(175) J. M. Soler, E. Artacho, J. D. Gale, A. García, J. Junquera, P. Ordejón, Daniel Sánchez-Portal *Journal of Physics: Condensed Matter* **2002**, **14**(11), 2745, DOI: 10.1088/0953-8984/14/11/302.

(176) V. Blum, R. Gehrke, F. Hanke, P. Havu, V. Havu, X. Ren, K. Reuter, M. Scheffler *Computer Physics Communications* **2009**, **180**(11), 2175–2196, DOI: 10.1016/j.cpc.2009.06.022.

(177) P. E. Blöchl *Physical Review B* **1994**, **50**(24), 17953–17979, DOI: 10.1103/PhysRevB.50.17953.

(178) K. Stokbro, J. Taylor, M. Brandbyge, P. Ordejón *Annals of the New York Academy of Sciences* **2003**, **1006**(1), 212–226, DOI: 10.1196/annals.1292.014.

(179) K. Lejaeghere, G. Bihlmayer, T. Björkman, P. Blaha, S. Blügel, V. Blum, D. Caliste, I. E. Castelli, S. J. Clark, A. D. Corso, S. d. Gironcoli, T. Deutsch, J. K. Dewhurst, I. D. Marco, C. Draxl, M. Dułak, O. Eriksson, J. A. Flores-Livas, K. F. Garrity, L. Genovese, P. Giannozzi, M. Giantomassi, S. Goedecker, X. Gonze, O. Grånäs, E. K. U. Gross, A. Gulans, F. Gygi, D. R. Hamann, P. J. Hasnip, N. a. W. Holzwarth, D. Iuşan, D. B. Jochym, F. Jollet, D. Jones, G. Kresse, K. Koepernik, E. Küçükbenli, Y. O. Kvashnin, I. L. M. Locht, S. Lubeck, M. Marsman, N. Marzari, U. Nitzsche, L. Nordström, T. Ozaki, L. Paulatto, C. J. Pickard, W. Poelmans, M. I. J. Probert, K. Refson, M. Richter, G.-M. Rignanese, S. Saha, M. Scheffler, M. Schlipf, K. Schwarz, S. Sharma, F. Tavazza, P. Thunström, A. Tkatchenko, M. Torrent, D. Vanderbilt, M. J. v. Setten, V. V. Speybroeck, J. M. Wills, J. R. Yates, G.-X. Zhang, S. Cottenier *Science* **2016**, **351**(6280), aad3000, DOI: 10.1126/science.aad3000.

(180) R. Landauer *IBM Journal of Research and Development* **1957**, **1**(3), 223–231, DOI: 10.1147/rd.13.0223.

(181) M. P. L. Sancho, J. M. L. Sancho, J. M. L. Sancho, J. Rubio *Journal of Physics F: Metal Physics* **1985**, **15**(4), 851, DOI: 10.1088/0305-4608/15/4/009.

(182) M. Brandbyge, J.-L. Mozos, P. Ordejón, J. Taylor, K. Stokbro *Physical Review B* **2002**, **65**(16), 165401, DOI: 10.1103/PhysRevB.65.165401.

(183) V. Obersteiner, *Master Thesis: Impact of Collective Effects on Charge Transport Through Molecular Monolayers*; Master Thesis: 2014.

(184) B. T. Koo, W. R. Dichtel, P. Clancy *Journal of Materials Chemistry* **2012**, **22**(34), 17460, DOI: 10.1039/c2jm32009f.

(185) A. P. Côté, A. I. Benin, N. W. Ockwig, M. O'Keeffe, A. J. Matzger, O. M. Yaghi *Science (New York, N.Y.)* **2005**, **310**(5751), 1166–1170, DOI: 10.1126/science.1120411.

(186) E. L. Spitler, W. R. Dichtel *Nature Chemistry* **2010**, **2**(8), 672–677, DOI: 10.1038/nchem.695.

(187) S. Dalapati, M. Addicoat, S. Jin, T. Sakurai, J. Gao, H. Xu, S. Irle, S. Seki, D. Jiang *Nature Communications* **2015**, **6**, 7786, DOI: 10.1038/ncomms8786.

(188) I. Balint, K.-i. Aika *Applied Surface Science* **2001**, **173**(3–4), 296–306, DOI: 10.1016/S0169-4332(00)00908-9.

(189) M. Schrader, R. Fitzner, M. Hein, C. Elschner, B. Baumeier, K. Leo, M. Riede, P. Bäuerle, D. Andrienko *Journal of the American Chemical Society* **2012**, **134**(13), 6052–6056, DOI: 10.1021/ja300851q.

(190) A. Tkatchenko, A. Ambrosetti, R. A. D. Jr *The Journal of Chemical Physics* **2013**, **138**(7), 074106, DOI: 10.1063/1.4789814.

(191) R. J. Maurer, V. G. Ruiz, A. Tkatchenko *The Journal of Chemical Physics* **2015**, **143**(10), 102808, DOI: 10.1063/1.4922688.

(192) M. Frisch, G. Trucks, H. Schlegel, G. Scuseria, M. Robb, J. Cheeseman, G. Scalmani, V. Barone, B. Mennucci, G. Petersson, H. Nakatsuji, M. Caricato, X. Li, H. Hratchian, A. Izmaylov, J. Bloino, G. Zheng, J. Sonnenberg, M. Hada, M. Ehara, K. Toyota, R. Fukuda, J. Hasegawa, M. Ishida, T. Nakajima, Y. Honda, O. Kitao, H. Nakai, T. Vreven, J. Montgomery, J. Peralta, F. Ogliaro, M. Bearpark, J. Heyd, E. Brothers, K. Kudin, V. Staroverov, R. Kobayashi, J. Normand, K. Raghavachari, A. Rendell, J. Burant, S. Iyengar, J. Tomasi, M. Cossi, N. Rega, J. Millam, M. Klene, J. Knox, J. Cross, V. Bakken, C. Adamo, J. Jaramillo, R. Gomperts, R. Stratmann, O. Yazyev, A. Austin, R. Cammi, C. Pomelli, J. Ochterski, R. Martin, K. Morokuma, V. Zakrzewski, G. Voth, P. Salvador, J. Dannenberg, S. Dapprich, A. Daniels, Farkas, J. Foresman, J. Ortiz, J. Cioslowski, D. Fox *Gaussian 09, Revision B.01, Gaussian, Inc., Wallingford CT* **2009**.

(193) J. S. Miller *Angewandte Chemie International Edition* **2006**, **45**(16), 2508–2525, DOI: 10.1002/anie.200503277.

(194) M. Elstner, D. Porezag, G. Jungnickel, J. Elsner, M. Haugk, T. Frauenheim, S. Suhai, G. Seifert *Physical Review B* **1998**, **58**(11), 7260–7268, DOI: 10.1103/PhysRevB.58.7260.

(195) T. Frauenheim, G. Seifert, M. Elstner, T. Niehaus, C. Köhler, Marc Amkreutz, M. Sternberg, Z. Hajnal, A. D. Carlo, S. Suhai *Journal of Physics: Condensed Matter* **2002**, **14**(11), 3015, DOI: 10.1088/0953-8984/14/11/313.

(196) M. Gaus, Q. Cui, M. Elstner *Wiley Interdisciplinary Reviews: Computational Molecular Science* **2014**, **4**(1), 49–61, DOI: 10.1002/wcms.1156.

(197) B. Lukose, A. Kuc, T. Heine *Chemistry – A European Journal* **2011**, **17**(8), 2388–2392, DOI: 10.1002/chem.201001290.

(198) B. Lukose, B. Supronowicz, P. St. Petkov, J. Frenzel, A. B. Kuc, G. Seifert, G. N. Vayssilov, T. Heine *physica status solidi (b)* **2012**, **249**(2), 335–342, DOI: 10.1002/pssb.201100634.

(199) D. Porezag, T. Frauenheim, T. Köhler, G. Seifert, R. Kaschner *Physical Review B* **1995**, **51**(19), 12947–12957, DOI: 10.1103/PhysRevB.51.12947.

(200) G. Seifert, D. Porezag, T. Frauenheim *International Journal of Quantum Chemistry* **1996**, **58**(2), 185–192, DOI: 10.1002/(SICI)1097-461X(1996)58:2<185::AID-QUA7>3.0.CO;2-U.

(201) Yang, H. Yu, D. York, Q. Cui, M. Elstner *The Journal of Physical Chemistry A* **2007**, **111**(42), 10861–10873, DOI: 10.1021/jp074167r.

(202) P. Koskinen, V. Mäkinen *Computational Materials Science* **2009**, **47**(1), 237–253, DOI: 10.1016/j.commatsci.2009.07.013.

(203) M. Elstner, G. Seifert *Philosophical Transactions of the Royal Society of London A: Mathematical, Physical and Engineering Sciences* **2014**, **372**(2011), 20120483, DOI: 10.1098/rsta.2012.0483.

(204) B. Aradi, B. Hourahine, T. Frauenheim *The Journal of Physical Chemistry A* **2007**, **111**(26), 5678–5684, DOI: 10.1021/jp070186p.

(205) J. A. Lloyd, A. C. Papageorgiou, S. Fischer, S. C. Oh, Ö. Sağlam, K. Diller, D. A. Duncan, F. Allegretti, F. Klappenberger, M. Stöhr, R. J. Maurer, K. Reuter, J. Reichert, J. V. Barth *Nano Letters* **2016**, **16**(3), 1884–1889, DOI: 10.1021/acs.nanolett.5b05026.

(206) A. Ambrosetti, A. M. Reilly, R. A. D. Jr, A. Tkatchenko *The Journal of Chemical Physics* **2014**, **140**(18), 18A508, DOI: 10.1063/1.4865104.

(207) M. Stöhr, G. S. Michelitsch, J. C. Tully, K. Reuter, R. J. Maurer *The Journal of Chemical Physics* **2016**, **144**(15), 151101, DOI: 10.1063/1.4947214.

(208) M. Gaus, Q. Cui, M. Elstner *Journal of Chemical Theory and Computation* **2011**, **7**(4), 931–948, DOI: 10.1021/ct100684s.

(209) M. Gaus, H. Jin, D. Demapan, A. S. Christensen, P. Goyal, M. Elstner, Q. Cui *Journal of Chemical Theory and Computation* **2015**, **11**(9), 4205–4219, DOI: 10.1021/acs.jctc.5b00600.

(210) C. V. Dyck, V. Geskin, A. J. Kronemeijer, D. M. d. Leeuw, J. Cornil *Physical Chemistry Chemical Physics* **2013**, **15**(12), 4392–4404, DOI: 10.1039/C3CP44132F.